THÈSE DE DOCTORAT

DE L'UNIVERSITÉ DE BOURGOGNE FRANCHE-COMTÉ

PRÉPARÉE À L'UNIVERSITÉ DE BOURGOGNE

École doctorale n°37

Sciences Pour l'Ingénieur et Microtechniques

Doctorat d'Instrumentation et Informatique de l'image

par

Usama Bello IBRAHIM

Nonlinear resonances and some of their applications to information processing

Thèse présentée et soutenue à Dijon, le 6 Septembre 2021.
Composition du Jury :

BILBAULT Jean-Marie	Professeur à l'Université de Bourgogne	Président
ROUSSEAU David	Professeur à l'Université d'Angers	Rapporteur
TANG Tong Boon	Associate Professor Dr., Universiti Teknologi Petronas, Perak, Malaysia	Rapporteur
TSE VE KOON Kevin	Maître de Conférences à l'Université Lyon 1	Examinateur
MORFU Saverio	Maître de Conférences HDR à l'Université de Bourgogne	Directeur de thèse
MARQUIÉ Patrick	Professeur à l'Université de Bourgogne	Co-Directeur de thèse

N° 9 8 3 6 4

ACKNOWLEDGMENTS

I would like to most sincerely appreciate my supervisors: Saverio MORFU, Associate Professor, Université de Bourgogne Franche-Comté, and Patrick MARQUIÉ, University Professor, Université de Bourgogne Franche-Comté for their guidance and tireless support throughout this research journey. It was quite a pleasure having an opportunity to work with them as my supervisors. I appreciate their guidance, patience and most importantly the attention and the limitless time they gave to me throughout the years of this research. I am thankful for the huge knowledge I gained under their guidance from all aspects of research especially the skills of rigorous analysis, scientific result presentation and writing. It was luck and privilege having you as supervisors, I can't thank you enough.

I sincerely thank the reviewers of my thesis: David ROUSSEAU, University Professor, Université d'Angers, and Tong Boon TANG, Associate Professor, Universiti Teknologi PETRONAS for having time to review and provide very good comments and observations on my work and also for their participation in the jury of my defense. I also thank Jean-Marie BILBAULT, University Professor, Université de Bourgogne Franche-Comté, and Kevin TSE VE, Associate Professor, Polytech'Lyon - UCB Lyon1 for their participation in the jury of my defense as Examiners. My gratitude to all members of the jury for the roles they played during the thesis defense. Moreover, I can't forget to thank Professor Jean-Marie BILBAULT once more, the coordinator during my Master's program through whom I met my Ph.D. supervisors.

This thesis was only achievable in the presence of funding from the Kano State Government of Nigeria and the Embassy of France in Nigeria who jointly sponsored both my Master's and Doctoral studies. I thank both parties for the opportunity given to me. I also thank the management of the Kano University of Science and Technology Wudil especially the Vice-Chancellor, Professor Shehu Musa Alhaji, who initially nominated me for the scholarship. I can't forget to thank the management of the University of Burgundy Franche-Comté UBFC, SPIM doctoral school, and the ImViA laboratory for the opportunities and exceptional financial assistance rendered to me during the last year of this thesis when I encountered financial difficulties.

To my family, especially my parent: Alhaji Bello Ibrahim and Malama Salamatu Bello, your prayers have been so infectious on me, may God almighty reward you. To my elder brother Abdurrasheed Bello, I always remember your concern and sacrifices on me, thank you very much. I must thank my dear wife Hafsat Abdullahi Sansan and my little daughter Ummuhani Usama Bello for their patience in staying long without me.

To all that taught me right from my primary school to the University, thank you for training me morally and academically to achieve this higher feat, you are the citadel of my entire success. My best wishes and goodwill prayers for you and your families wherever you are.

CONTENTS

I State-of-the-art 1

1 Introduction and organization of the thesis 3

1.1 Motivations and aims 3

1.2 Organization of the thesis 5

2 Resonance phenomena in nonlinear systems 7

2.1 Random resonances 7

2.1.1 Coherence resonance 8

2.1.2 Stochastic resonance 9

2.1.3 Ghost-stochastic resonance 10

2.2 Deterministic resonances 11

2.2.1 Vibrational resonance 11

2.2.2 Ghost-vibrational resonance 12

II Main contributions 13

3 Analyses of VR in a damped nonlinear system 15

3.1 Description of the system 16

3.1.1 The potential $\Phi(x)$ 16

3.1.2 The damping coefficient $\Gamma(x)$ 18

3.1.3 The bichromatic driving of the system $e(t)$ 19

3.1.4 Numerical procedure 20

3.2 Case of a constant damping 21

3.2.1 Highlight of the classical VR effect 22

3.2.1.1 Temporal analyses 22

3.2.1.2 Frequency analysis 23

3.2.1.3 Highlight of the VR signature 25
3.2.2 Highlight of the Vibrational Multiresonance 26
3.2.2.1 Temporal analysis 27
3.2.2.2 Frequency analysis 28
3.2.3 Control of VR by the constant damping coefficient $\Gamma_0^{'}$ 30
3.2.4 The measuring tool indicating VR existence 32
3.2.5 Combined impact of the particle mass m and the constant damping amplitude $\Gamma_0^{'}$ on VR occurrence 33
3.3 Case of an inhomogeneous and space-dependent nonlinear damping 35
3.3.1 Response of the system 35
3.3.1.1 Temporal analyses 36
3.3.1.2 Frequency analyses 37
3.3.2 Control of VR by nonlinear damping parameters 39
3.3.2.1 Control of VR by the nonlinear damping amplitude Γ_0 39
3.3.2.2 Control of VR by the phase difference ϕ between the nonlinear damping and the periodic potential 41
3.3.2.3 Control of VR by the frictional inhomogeneity λ 42
3.3.3 Combined effect of the particle mass m and the nonlinear dissipation parameters on the VR occurrence 43
3.4 Conclusion 46

4 VR and GVR in Chua's model with specific nonlinearities 49

4.1 Introduction 50
4.2 Description of the Chua's model 50
4.2.1 The two considered nonlinearities of order n 51
4.2.2 Input perturbed excitation $e_p(t)$ 54
4.2.3 Numerical procedure 55
4.3 Vibrational resonance occurrence 55
4.3.1 Temporal analysis 56
4.3.2 Frequency analysis 57
4.3.3 Linear response analysis 58

4.3.4 Analysis by phase portraits . . . 64
4.4 Ghost-vibrational resonance . . . 67
4.5 Conclusion . . . 73

5 Applications of VR on subthreshold images perception 77
5.1 Introduction . . . 77
5.2 The detector and its set-up . . . 79
5.2.1 Input of the detector . . . 79
5.2.2 The resonant threshold detector . . . 80
5.3 Stochastic resonance based detector . . . 82
5.4 Vibrational resonance based detector . . . 85
5.4.1 Amplitude optimized VR-detector . . . 85
5.4.2 Frequency optimized VR-detector . . . 89
5.5 Conclusion . . . 94

III Conclusions and outlooks 97

6 Conclusions and outlooks 99
6.1 Conclusions . . . 99
6.2 Future perspectives . . . 101
6.3 Publications . . . 103

I

STATE-OF-THE-ART

1

INTRODUCTION AND ORGANIZATION OF THE THESIS

Contents

1.1 Motivations and aims 3
1.2 Organization of the thesis 5

My interest in the study of the dynamics of nonlinear systems and their applications started since during the days of my Master's degree program. I had Master's degree in advanced electronic systems engineering from university of Burgundy France through which I did my internship at Universitat Politecnica de Catalunya Spain, during 2016/2017 academic session. My internship concerned the design of Operational Transconductance Amplifiers (OTA) using Simulation Program with Integrated Circuit Emphasis (SPICE) and Python programming. This paved a way for me to this doctoral research which is also based on the applications of nonlinear systems to signal and image processing.

1.1/ MOTIVATIONS AND AIMS

Due to its counter-intuitive nature, understanding the dynamics of nonlinear systems has given rise to many challenges to overcome. This has brought about so many quests to answer because most systems are ubiquitously nonlinear in nature. For example, the information encoding by nonlinear neural systems brings about a rich variety of bio-inspired effects which are not yet comprehended. As a result, the study of the dynamics of nonlinear systems has drawn the attention of researchers in various fields such as for instance, engineering and cognitive sciences.

In particular, the famous nonlinear neuronal systems have received considerable attention from researchers due to their vast applications. Presently, there are many nonlinear neuronal models developed to describe the behavior of biological neurons. Indeed, these mathematical models are ruled by set of nonlinear differential equations. Abundant of literature reported different dynamical behaviors of nonlinear neuronal models. In most cases, the validity of the numerical models was proven by theoretical studies. Some models were realized as an electronic circuits to consistently comprehend the theoretical and numerical analyses. Apart from the biological behavior, these set of nonlinear differential equations can also model many other physical phenomena such as; motion of a particle in mechanical oscillators or follow of an electric charge/current in nonlinear circuits.

As a smallest unit of nervous system, neuron is an excitable electrical cell which is responsible for receiving information from external world, and which processes and transmits it through electrical signals. Biological neuron basically consists of dendrites, cell body and axon which are respectively analogous to the input, sum/threshold unit and output of the artificial neuron as depicted in the schematic of Fig. 1.1. Many mathematical models such as Integrate-and-Fire [1], McCulloch-Pitts [2], Hodgkin-Huxley (HH) [3], Leaky integrate-and-fire [4], FitzHugh-Nagumo (FHN) [5], Morris-Lecar [6] and Hindmarsh-Rose [7] models have been designed to predict the output behavior of biological neuron as a function of input stimulation. Hodgkin-Huxley (HH) and FitzHugh-Nagumo (FHN) models are still receiving attention of researchers from different fields.

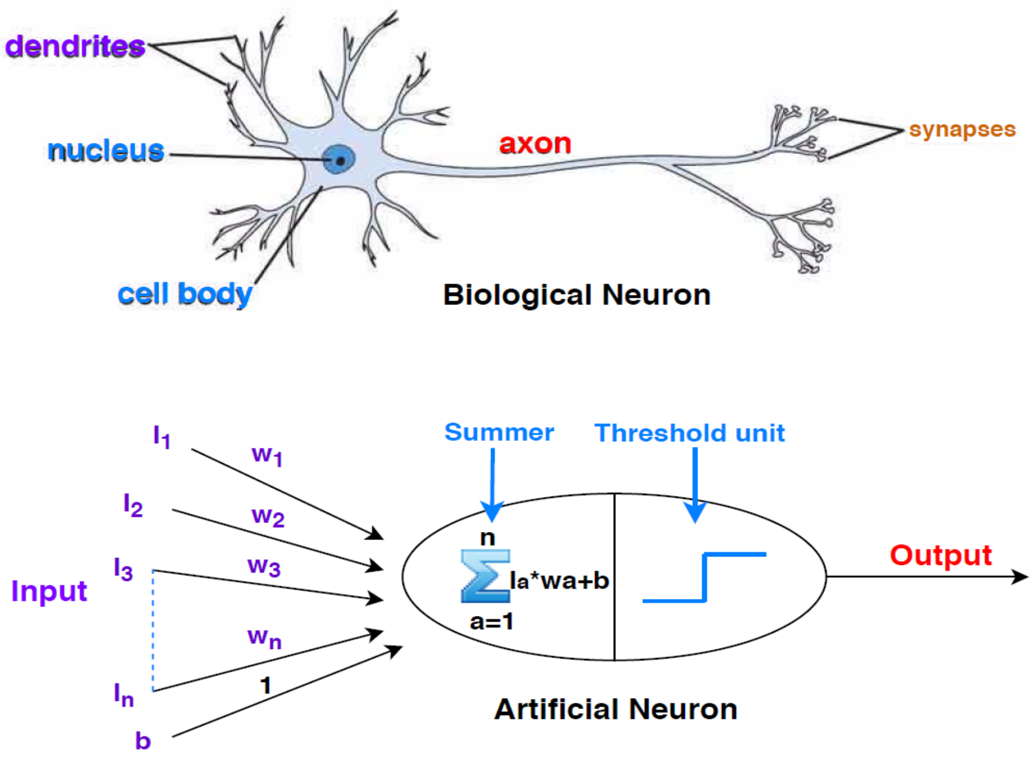

Figure 1.1: Biological and artificial neuron

Enormous nonlinear dynamical behaviors were investigated but there are yet arising challenges to address such as: understanding the information encoding by a single neuron, how neurons can collectively act to process information, how lattices of the coupled elementary neurons behave under the influence of various perturbations and how to carryout experiments with the nonlinear circuits to confirm the validity of theoretical results obtained from numerical simulations. For decades, variety of fascinating dynamical phenomena were explored in nonlinear systems. Among the most studied dynamical effects in nonlinear systems are resonance induced phenomena which mainly address how perturbing the input of nonlinear system can positively affect the system's output response. Occurrence of resonance induced effects can either be promoted by a noise perturbation or a high frequency perturbation. However, the later is now the most studied because it is easier to control without tedious mathematics and most importantly, it was reported to surpass the former in terms of performance in most scenarios.

In this thesis, out of the different dynamical properties reported in nonlinear systems, we focus on Vibrational Resonance (VR) effect, a phenomenon where high frequency perturbation enhances the output response of nonlinear systems at the low frequency [8]. VR was investigated in many systems and in different contexts both theoretically, numerically and experimentally. Moreover, VR was reported to have many applications such as in electronics to perform signal detection, signal amplification and subthreshold images perception to mention but just a few. However, with the advent of VR exploration in different systems and contexts, there are vast of arising issues to address. It constitutes the aims of this thesis since we consider: the impact of the particle's mass on VR occurrence in a mechanical system, the effect of a truncated sinusoidal nonlinearity on VR in the Chua's circuit model and the applications of VR in subthreshold images perception. We propose to carry out these studies numerically using Matlab scripts running on the computation cluster of the University of Burgundy.

1.2/ ORGANIZATION OF THE THESIS

The subsequent chapters of this thesis consist of the following: Chapter 2 provides an overview of literature on the most famous resonance phenomena in nonlinear systems. In chapter 3, we analyze vibrational resonance occurrence in a particular mechanical system describing the motion of a particle of mass m which is damped in two different cases. More precisely, the dynamics of the system is first studied with a constant damping and lastly with an inhomogeneous space dependent damping. Moreover, in each case, the influence of the particle mass on VR is highlighted. In chapter 4, we investigate the dynamics of a modified Chua's circuit model with a truncated sinusoidal nonlinearity. In particular, we study the impact of the system's nonlinearity on the occurrence of VR and GVR. Moreover, system's dynamics observed with our proposed truncated sinusoidal nonlinearity are compared with the existing dynamics of the system experiencing a sawtooth nonlinearity. In chapter 5, we investigate the application of VR in subthreshold noisy images perception. We first recall the existing SR-based detector for subthreshold images perception. Afterwards, we introduce a VR-based detector by replacing the noisy perturbation with a spatial high frequency signal. Lastly, chapter 6 comprises of the general conclusions and future works.

2

OVERVIEW OF THE MOST STUDIED NONLINEAR RESONANCE PHENOMENA

Contents

2.1 Random resonances . . . 7
  2.1.1 Coherence resonance . . . 8
  2.1.2 Stochastic resonance . . . 9
  2.1.3 Ghost-stochastic resonance . . . 10
2.2 Deterministic resonances . . . 11
  2.2.1 Vibrational resonance . . . 11
  2.2.2 Ghost-vibrational resonance . . . 12

This chapter presents a restrictive review of literature on the most famous resonance induced phenomena in nonlinear systems. These phenomena are of crucial importance due to their applications especially in the field of signal and image processing which constitute the topic of this thesis. In this chapter, depending on the nature of the external stimuli acting upon nonlinear systems, we choose to categorize these nonlinear resonance phenomena in nonlinear systems into random resonances and deterministic resonances.

2.1/ RANDOM RESONANCES

Random resonances in nonlinear systems refer to the resonance induced phenomena which take benefit of a noise perturbation to improve the output response of nonlinear systems. Noisy perturbations have aided the occurrence of very important phenomena in nonlinear systems which were reported to have applications in many fields of science and engineering.

Until late 19th century, it was usually considered that, noise which comes from an external environment or those that are generated by working systems/machines are nothing but disturbance to the systems. Presence of noise was then widely believed to negatively affect the performance of working systems and as a result, noise was generally accorded as something that has to be avoided.

Consequently, it was then very paramount to evacuate working systems from interaction with the noisy external environment and also to minimize the noise that the system may generate by its self.

With the continuous advent in nonlinear dynamics, it was later discovered that noise can play a constructive role in the dynamics of nonlinear systems, leading to interesting phenomena. In logistic systems, Mayer-Kress and Haken demonstrated that noise can induce transition from intermittent behavior to remarkable periodicities [9, 10]. Subsequently, Matsumoto and Tsuda revealed that external noise can induce a transition from chaotic behavior to ordered behavior [11]. Pikovsky used noisy dynamical systems to demonstrate the statistics of trajectory separation [12]. It was also shown that addition of small noise suppresses chaos and it leads to more pronounced periodicity than when the noise is larger [13]. Recently, Chapeau-Blondeau reported that noisy quantum bits (qubits) can enhance the estimation of quantum parameters [14–16].

On the other hand, the presence of an optimum noise amplitude was shown to made the oscillatory response of a non driven excitable system to be most coherent: this phenomenon is called Coherence Resonance (CR) [17]. Moreover, in a nonlinear system which is simultaneously driven by noisy perturbation and periodic signal, the noise was reported to improve the detection of the periodic signal in what was named Stochastic Resonance (SR) effect [18, 19]. Coherence and stochastic resonances are both noise-induced effects reported in nonlinear systems which have received considerable attentions especially from the fields of neuroscience and engineering. Particularly, stochastic resonance, which was studied in many systems including the neuronal models, has found to have many applications.

2.1.1/ COHERENCE RESONANCE

As it was pointed, the presence of noise in nonlinear systems is unavoidable. However, the effect of noisy perturbations in stochastic systems is not all the time trivial, noise does not always induce irregularities in systems. Indeed, in absence of external periodic force, noise can induce more coherence in the oscillatory response of certain nonlinear systems. This phenomenon termed Coherence Resonance (CR) was reported by Pikovsky and Kurths in excitable systems [17]. They also observed that, at an optimal noise intensity, the noise-induced oscillations present a maximum of regularity.

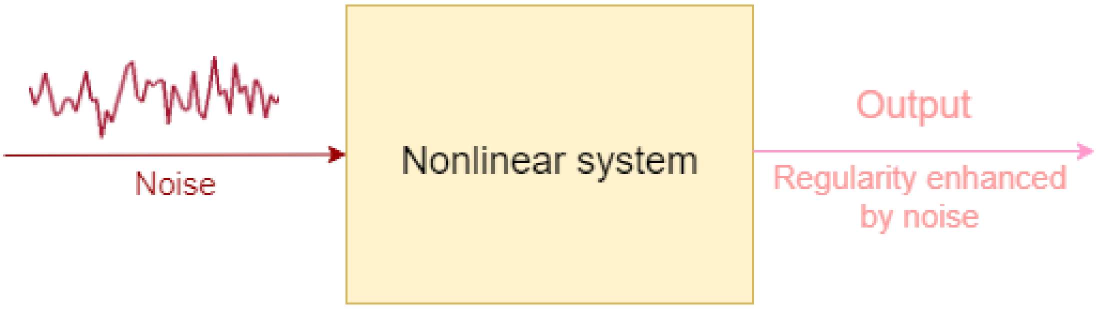

Figure 2.1: Coherence resonance phenomenon.

The schematic of Fig. 2.1 summarizes the coherence resonance effect. Basically, to observe this effect, the system must be tuned below a bifurcation which constitutes the subthreshold hypothesis. Moreover, the system must be driven without any external force but only with a random perturbation. In the absence of the noisy perturbation, the system remains in its rest state, that is the output does not reveal any activity. However, addition of certain amount of noise makes the response regular and most coherent at an optimal noise intensity. Coherence resonance is the typical example of the constructive role of noise in nonlinear systems.

Coherence resonance effect was first reported in the work of Gang *et al* as stochastic resonance phenomena without the external periodic force [20]. Later, Pikovsky and Kurths observed the same behavior in excitable system where it was named coherence resonance [17]. In the model of Hugkin-Huxley without external periodic force, the coherence of the system was found to be maximal at certain noise intensity [21]. Chua model submitted to chaotic medium exhibited regular oscillations in the presence of noise, whose intermediate value provided the best oscillatory response [22]. In the leaky integrate-and-fire model, it was demonstrated that the coherence of the spike train can be maximized or minimized depending on the noise intensity [23]. Other systems where coherence resonance was reported include: excitable FitzHugh-Nagumo models [24–27], plasma [28], optical systems [29–32], electromechanical systems [33–35] and in electronic circuits [36–38].

2.1.2/ STOCHASTIC RESONANCE

Unlike coherence resonance, the effect of Stochastic Resonance (SR) is normally studied in nonlinear systems driven by both periodic force and noise perturbation, as shown in the schematic of Fig. 2.2. Basically, an appropriate amount of a noise perturbation enhances the detection of the deterministic subthreshold low frequency signal at the system output.

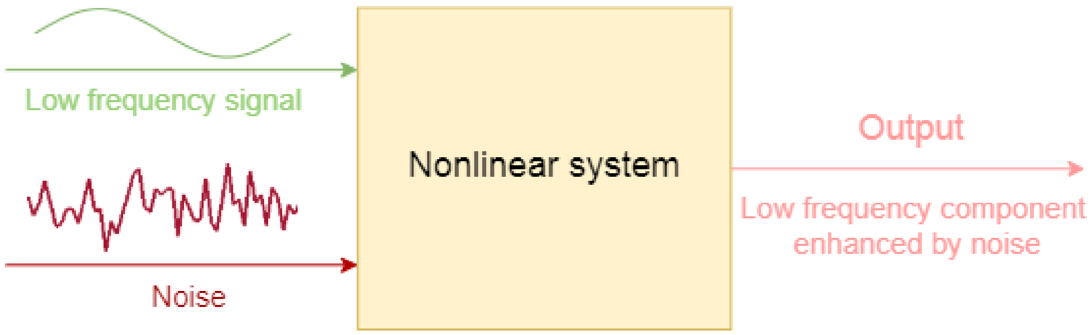

Figure 2.2: Stochastic resonance phenomenon.

The phenomenon of stochastic resonance, the famous of all the noise-induced effects, was first reported in 1980 by Benzi *et al* in climatic system to demonstrate the periodic behavior of the earth's ice age [19]. Here, a long-term alternation of temperature was induced when an external periodic forcing acted upon by a noise perturbation in the system. In dynamical systems, the authors observed in 1981 that external periodic forcing exhibits peak in the power spectrum (resonance) due to the noise perturbation [18]. Little attention was then devoted to the study of SR until 1989 when Gammaitoni *et al* reported the effect in bistable systems [39] and in 1990 when it was first examined in a single neuron model [40]. Henceforth, this noble effect became a subject of study in many fields, mainly in biological systems. In 1995, Dykman *et al* outlined the development of SR since its inception in 1980 [41]. Moreover, they also recall the concept of the linear response theory (LRT) previously described in [42, 43], which provides the simplest approach of understanding SR phenomenon than the tedious computational approaches previously available. In the year 2009, Gammaitoni *et al* reviewed the progress of SR investigations which comprise the applications and extensions reported as of that time [44].

Stochastic resonance was studied in variety of systems such as: optical systems [45–47], threshold systems [48–50], sensors [51–55], integrate-and-fire model [56], Hodkin-Huxley neuron [57, 58], FitzHugh-Nagumo model [59, 60] and electronics circuits [61, 62] to mention just a few. Moreover, SR was reported to have many applications in signal detection [63–77], optimal detection/estimation [63, 68, 78–91], quantum information processing/estimation [92–95], image perception [46, 96–99], signal/information transmission [51, 55, 61, 100–117] and neural signal transduction [118–121].

Note that, in the presence of other sources of perturbation instead of noise, other resonant-like behaviors can be observed. Indeed, it has been pointed out that the role of noise in noise-induced dynamics can also be played by a chaotic disturbance [122] or high frequency perturbation [8] instead of noise. More precisely, nonlinear system subjected to perturbation which is chaotic in nature can display a resonant-like behavior called chaotic resonance [122–125], whereas vibrational resonance, which is the center of our studies in this thesis, is analogous to the stochastic resonance which basically makes use of high frequency perturbation instead of noise to enhance the detection of an input low frequency signal. A part will be specifically devoted to VR in the deterministic resonance section of this chapter.

2.1.3/ GHOST-STOCHASTIC RESONANCE

In a nonlinear system driven by noisy perturbation and two close frequency signals, it was revealed that noise can induce resonance in the system output at a missing input frequency lower than the two frequencies which excite the system. This phenomenon named Ghost-Stochastic Resonance (GSR) was first observed by Chialvo *et al* in neuronal systems [126] to understand pitch perception by the auditory system in the complex sound signal and the mechanism for the missing fundamental illusion. Indeed, it was shown that neuron fires spikes at the rate similar to the perceived pitch for the complex tone [127–129]. Subsequently, GSR was studied in many contexts and in different systems including: FitzHugh Nagumo models/systems [130–132], Chua circuit [133], electronic neurons circuit [134–136] and in optical laser [137].

2.2/ DETERMINISTIC RESONANCES

Instead of random perturbations, nonlinear systems can also take benefit of deterministic high frequency perturbations to improve their response to an input subthreshold signal. The idea of using deterministic perturbations was first discovered after almost two decades of intensive breakthrough in the dynamics of nonlinear systems with random perturbations. However, much attention is now devoted to the investigation of dynamical responses with deterministic perturbations because it is easier to control. Moreover, studies confirmed that, the dynamical properties reported in nonlinear systems due to random perturbations can equally be obtained using deterministic perturbations. Indeed, deterministic resonances constitute the main area of study covered in this thesis.

2.2.1/ VIBRATIONAL RESONANCE

The same role played by noise perturbation in the study of Stochastic Resonance (SR) can however be induced by high frequency perturbations. This noble idea named Vibrational Resonance (VR) was initially reported in the year 2000 by Landa and McClintock in bistable systems [8]. The system in this setting is driven by a low frequency signal corrupted by a high frequency perturbation with relatively sharp difference between the two frequencies. They found that the response of the system at the low frequency is enhanced by an appropriate increase of the perturbation amplitude. Indeed, the maximum response is achieved for an intermediate perturbation amplitude, beyond which the system's response at the low frequency reduces. VR is analogous to the SR because the high frequency perturbation perform the same task of enhancing the detection of the low frequency signal as schematically depicted in Fig 2.3.

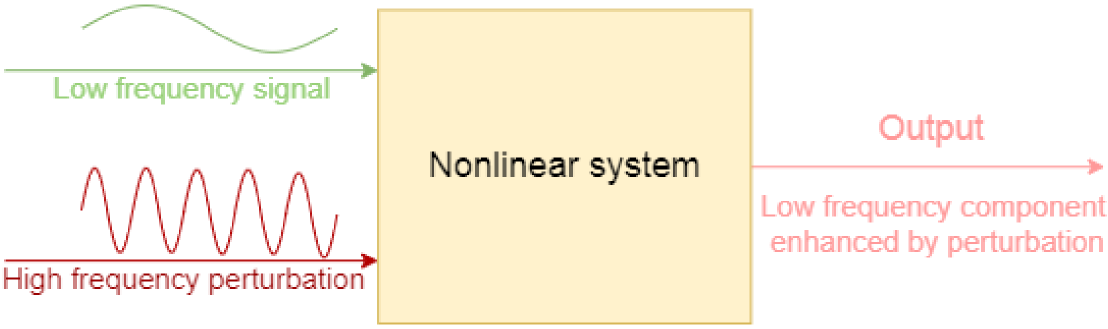

Figure 2.3: Vibrational resonance phenomenon.

VR phenomenon is deterministic and easier to control unlike SR where the system is described by stochastic process. In the year 2001, Gitterman proposed an analytical approach of analyzing VR occurrence which open way to more understanding of the paradigm [138]. Ulner *et al* experimentally reported the phenomena of VR in excitable electronic circuit and confirmed the effect numerically in FitzHugh-Nagumo model [139]. Moreover, Blekhman *et al* theoretically affirmed VR existence and showed that the resonance can also be induced not only by varying the amplitude of the high frequency excitation but also by either varying the low or high frequency [140]. Subsequently, VR has attracted the interest of many researchers in the last ten years and it was studied numerically, theoretically and experimentally in many systems and in different contexts. To mention but just a few, VR was reported in excitable neuronal systems [139, 141, 142], monostable systems [143, 144], bistable systems [8, 145–148], multistable systems [149, 150], Chua's circuit model [151, 152], FitzHugh-Nagumo model [131, 139, 153–155] optical system [156], biharmonically driven plasma [157] and in nonlinear dissipative systems [158]. Moreover, vibrational resonance was reported to have applications in signal detection [77, 159, 160] and signal amplification [161] among others.

2.2.2/ GHOST-VIBRATIONAL RESONANCE

Ghost-Vibrational Resonance (GVR) is a variant of Vibrational Resonance (VR) which occurs in nonlinear systems driven by a high frequency perturbation and low frequency signal consisting of more than one frequency. Basically, the system reveals resonance in its output signal at a missing frequency which is lower than the input low frequencies.

GVR was first reported by Rajamani *et al* in duffing oscillator [162] and in Chua's circuit model by Abirami *et al* [152]. Ghost-Vibrational Resonance (GVR) effect is analogous to the Ghost-Stochastic Resonance (GSR) where noise acts as a perturbation instead of high frequency signal. As more researchers are now interested in considering deterministic perturbation instead random perturbation, it will not come as surprise to anyone when GVR is revealed in the systems and contexts where GSR has been reported. Recently in this thesis, we reported the occurrence of GVR phenomenon in a Chua's circuit model with a truncated sinusoidal nonlinearity [163].

In this thesis, we numerically analyze the occurrence of VR in two different nonlinear systems and also investigate application of VR in subthreshold images perception [99, 163–165]. The two systems considered in this manuscript are: a nonlinear damped mechanical system [164] and a modified Chua's circuit model [163]. Concerning the mechanical system which was investigated with constant/linear and nonlinear damping [138, 140, 149, 158, 166, 167], none of these studies have focused on the possible impact of the particle mass on VR occurrence, which constitutes the subject considered in this thesis. In the analyses of Chua's circuit model, we mainly focus on the impact of the system's nonlinearity on VR and GVR occurrence which to our knowledge has not been yet addressed. Instead of the conventional SR-detector used for subthreshold noisy images perception [96, 98, 168, 169], in this thesis we report for the first time that VR can also enhance visual perception of subthreshold noisy images.

II

MAIN CONTRIBUTIONS

3

ANALYSES OF VIBRATIONAL RESONANCE (VR) OCCURRENCE IN A DAMPED PHYSICAL NONLINEAR SYSTEM

Contents

3.1 Description of the system 16
  3.1.1 The potential $\Phi(x)$ 16
  3.1.2 The damping coefficient $\Gamma(x)$ 18
  3.1.3 The bichromatic driving of the system $e(t)$ 19
  3.1.4 Numerical procedure 20
3.2 Case of a constant damping 21
  3.2.1 Highlight of the classical VR effect 22
  3.2.2 Highlight of the Vibrational Multiresonance 26
  3.2.3 Control of VR by the constant damping coefficient $\Gamma_0^{'}$ 30
  3.2.4 The measuring tool indicating VR existence 32
  3.2.5 Combined impact of the particle mass m and the constant damping amplitude $\Gamma_0^{'}$ on VR occurrence 33
3.3 Case of an inhomogeneous and space-dependent nonlinear damping 35
  3.3.1 Response of the system 35
  3.3.2 Control of VR by nonlinear damping parameters 39
  3.3.3 Combined effect of the particle mass m and the nonlinear dissipation parameters on the VR occurrence 43
3.4 Conclusion 46

In this chapter, we consider the dynamics of a particular nonlinear mechanical system experiencing a multistable potential well. The system is driven by a low frequency signal corrupted by a high frequency perturbation. We study the dynamics of this system with two different damping coefficients: first as constant damping coefficient and lastly, nonlinear space-dependent damping coefficient. In both the two cases of the damping, we begin by revealing vibrational resonance existence in the system by using temporal and frequency analyses. Subsequently, we study the impact of the damping coefficients for a unitary particle mass. Lastly, we consider the combined impact of varying the particle mass and the damping coefficients on vibrational resonance occurrence.

3.1/ DESCRIPTION OF THE SYSTEM

The system of our interest is similar to a multistable pendulum oscillator previously considered by Rajasekar *et al* when they first reported the phenomenon of vibrational resonance (VR) in multistable systems [149]. The system describes the motion of a single particle of mass m driven by an external excitation $e(t)$, experiencing a periodic potential $\Phi(x)$ and whose displacement x obeys to:

$$m\frac{d^2x}{dt^2}+\frac{d\Phi(x)}{dx}+\Gamma(x)\frac{dx}{dt}=e(t), \tag{3.1}$$

where $\Gamma(x)$ represents the damping coefficient.

3.1.1/ THE POTENTIAL $\Phi(x)$

In our system described by eq. (3.1), a particle of mass m is submitted to a nonlinear force $f(x)$ which derives from the potential $\Phi(x)$ via the relation:

$$\frac{d\Phi(x)}{dx}=-f(x), \tag{3.2}$$

with,

$$f(x)=-\Phi_0\sin kx,$$

where Φ_0 adjusts the potential height and the parameter k accounts for the periodicity of the potential. To obtain the expression of the periodic potential, we integrate the relation (3.2) in a boundary starting from position 0 to x which leads to

$$\int_{\Phi(0)}^{\Phi(x)} d\Phi(x)=\int_{u=0}^{u=x}\Phi_0\sin ku\,du,$$

that is

$$\Phi(x)-\Phi(0)=\left[-\frac{\Phi_0}{k}\cos ku\right]_{u=0}^{u=x}.$$

The potential is then defined by:

$$\Phi(x)=\Phi(0)-\frac{\Phi_0}{k}\cos kx+\frac{\Phi_0}{k}.$$

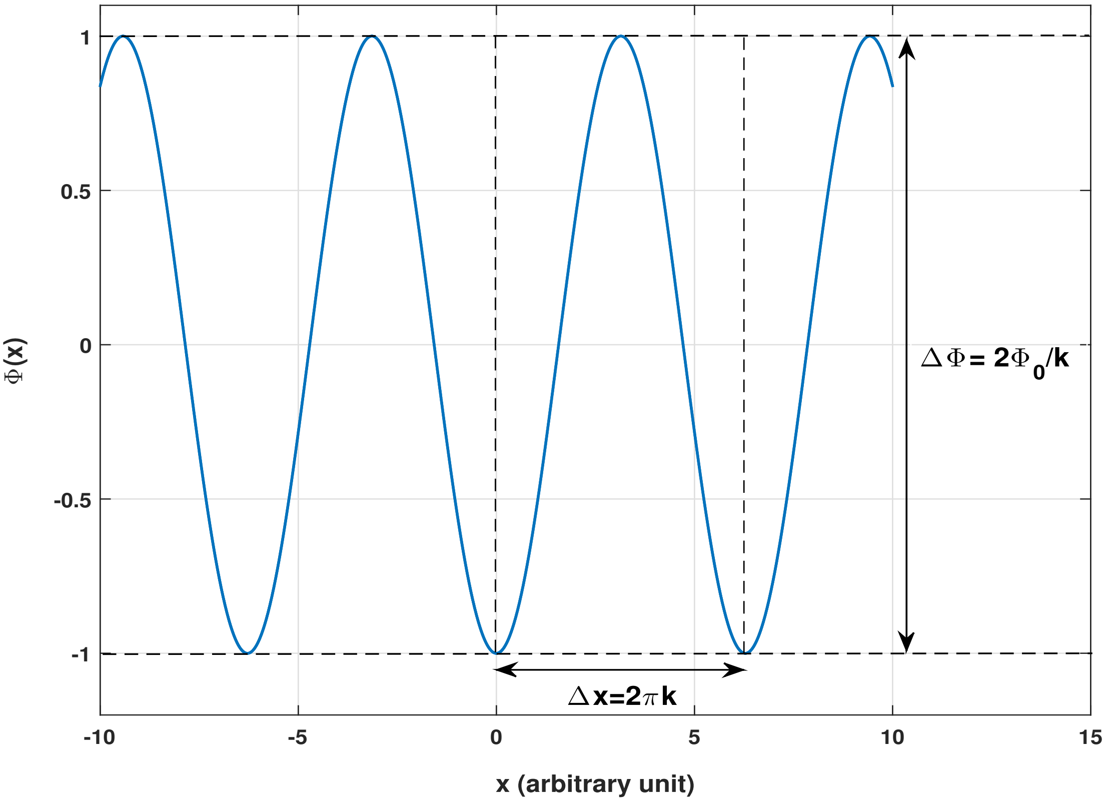

Figure 3.1: System's periodic potential $\Phi(x)$ defined by eq. (3.3) in the specific case considered in this chapter, namely $\Phi_0 = 1$ and $k = 1$. The height of the potential $\Delta\Phi$ and its width Δx are indicated with the double head arrows in this figure.

Assuming that the potential energy at the position $x = 0$ is

$$\Phi(x=0) = -\frac{\Phi_0}{k},$$

the expression of the potential reduces to

$$\Phi(x) = -\frac{\Phi_0}{k}\cos kx. \tag{3.3}$$

The symmetric periodic potential defined by eq. (3.3) is plotted at Fig. 3.1. The peak to peak amplitude of the potential corresponds to its height $\Delta\Phi$ which depends on parameters Φ_0 and k since $\Delta\Phi = \frac{2\Phi_0}{k}$. Moreover, the width Δx of the potential is defined by the distance between any two consecutive tops or bottoms of the potential, that is $\Delta x = 2\pi k$.

The symmetric periodic potential depicted in Fig. 3.1 has maxima at $X^*_{max,\ n} = \pm\frac{(2n+1)\pi}{k}$ and minima at $X^*_{min,\ n} = \pm\frac{2n\pi}{k}$, for $n = 0, 1, 2, \ldots$. Consequently, $X^*_{max,\ n}$ and $X^*_{min,\ n}$ are respectively the unstable and stable equilibrium positions of the system.

This multistable periodic potential was used in many systems for different purposes, including the pendulum system considered by Rajasekar *et al* [149] and the nonlinear dissipative system of Roy-

Layinde *et al* [158] where they highlighted the phenomenon of vibrational resonance. The property of multistability was used to study VR occurrence in many systems and also it was reported to have applications in image processing tasks. In fact, multistability property of the Cellular Neural Network (CNN) was used by Morfu *et al* to extract regions interest of a radiography of soldering [170]. Furthermore, multistability was used in chaotic systems to highlight different dynamical properties [152, 171–173] and also in memristors for information storage [174–176].

In this chapter, we use the multistable periodic potential $\Phi(x)$ to detect a subthreshold low frequency signal by the aid of a high frequency perturbation via vibrational resonance effect.

3.1.2/ THE DAMPING COEFFICIENT $\Gamma(x)$

In the particle motion ruled by eq. (3.1), the general parameter $\Gamma(x)$ characterizes the system's dissipation. In this chapter, we will consider this damping term $\Gamma(x)$ in two different cases: firstly with a constant damping and secondly, space-dependent inhomogeneous damping. More precisely,

$$\Gamma(x) = \Gamma_0^{'}, \tag{3.4}$$

will refer to constant damping, while

$$\Gamma(x) = \Gamma_0\left(1 - \lambda \sin(kx + \phi)\right), \tag{3.5}$$

will correspond to a space-dependent inhomogeneous damping. In eq. (3.5), the parameter λ sets the strength of the frictional inhomogeneity, the positive parameter Γ_0 is the whole amplitude of the nonlinear damping, k adjusts the same periodicity as in the periodic potential $\Phi(x)$, while ϕ denotes the phase difference between the periodic potential $\Phi(x)$ and the nonlinear dissipation $\Gamma(x)$.

The case of a constant damping $\Gamma(x) = \Gamma_0^{'}$ was initially analyzed by Rajasekar *et al* when they highlighted the occurrence of VR in multistable systems [149], whereas the case of the space-dependent inhomogeneous damping obeying to eq. (3.5) has been considered by Roy-Layinde *et al* [158].

In this chapter, for each case of the damping $\Gamma(x)$ defined by eq. (3.4) and (3.5), we first perform preliminary studies to highlight VR occurrence. Henceforth, we show how the parameters of the damping term $\Gamma(x)$ influence VR, which was not reported in the previous studies performed by Rajasekar *et al* in the case of a constant damping [149] and Roy-Layinde *et al* in the case of an inhomogeneous damping [158].

3.1.3/ THE BICHROMATIC DRIVING OF THE SYSTEM $e(t)$

In our model, the particle is driven by a bichromatic excitation $e(t)$ which consists of a low frequency signal corrupted by a high frequency perturbation, that is:

$$e(t) = G\cos\omega t + H\cos\Omega t, \tag{3.6}$$

where G and ω are respectively the amplitude of the low frequency component and its angular frequency. Moreover, H represents the high frequency perturbation amplitude and Ω its angular frequency. Throughout this thesis, we consider the perturbation angular frequency Ω to be much greater than the low angular frequency ω, that is $\Omega \gg \omega$. This corresponds to the usual setting of the excitation to observe vibrational resonance in nonlinear systems.

Many physical systems in engineering and science consist of this kind of two frequencies setup. This include: vertical cavity surface emitting laser used for experimental demonstration of VR [156], telecommunication signals where information carriers are usually high-frequency waves modulated by a low-frequency signal [177], ultrasonic two-frequency waves used to enhance cavity yield [178] and a two-frequency laser signal showing high stability and high efficiency [179]. In this thesis, we use the high frequency perturbation to enhance the detection of a low frequency signal.

Considering eq. (3.3) which described the periodic potential and eq. (3.6) that defined the system's external excitation, then eq. (3.1) can be rewritten as:

$$m\frac{d^2x}{dt^2} + \Gamma(x)\frac{dx}{dt} + \Phi_0 \sin kx = G\cos\omega t + H\cos\Omega t. \tag{3.7}$$

Note that, our system defined by eq. (3.7) can identically be adapted to describe many physical systems. For example, by considering noise instead of the high frequency perturbation in the model given by eq. (3.7), ratchet effect has been highlighted [180–184] as well as stochastic resonance [185]. Also, according to Rajasekar *et al* [149], this model described the dynamics of rf-driven Josephson junction and phase-locked voltage-controlled oscillators.

In this chapter, we perform two different studies on VR occurrence in our system ruled by eq. (3.7): first for the case of constant damping $\Gamma(x) = \Gamma_0'$ and secondly, with the space-dependent inhomogeneous damping $\Gamma(x) = \Gamma_0(1 - \lambda\sin(kx + \phi))$. In both cases, we first perform a preliminary study of VR effect for a fix value of the particle mass, namely $m = 1$. This is of great interest because unitary particle mass was mainly considered in the mechanical systems where VR was initially reported [149, 158]. Subsequently, we explore the effect of jointly varying the particle mass m and the damping parameters, on the occurrence of VR.

3.1.4/ NUMERICAL PROCEDURE

This section is devoted to the numerical procedure used in this chapter to carry out our numerical experiments. The numerical simulations performed throughout this research were launched on the University of Burgundy computation cluster. Particularly in this chapter, considering the number of samples we take, the simulation time step, number of iterations and the discretization of some parameters of the system, the simulations will take larger amount of time when they are carry out on the personal computer. Indeed, by using the university computation cluster, most of the resonance curves presented in this chapter rather took some few days before the results were produced.

To perform any analysis such as computing the system's response to the bichromatic excitation $e(t)$, the first step is to integrate the system by using any of the known numerical methods for solving nonlinear differential equations. In this chapter, we numerically integrate our system ruled by eq. (3.7) with a fourth order Runge-Kutta algorithm using a Matlab script. The system is integrated over a temporal window which corresponds to 2000 low frequency cycles and with a total number of samples sets to $N = 2^{22}$. Such temporal window sets the integrating time step to $dt = \frac{2000}{N} \times \frac{2\pi}{\omega}$ which will be sufficient for our numerical analyses. The corresponding spectral resolution is therefore $df = \frac{1}{Ndt}$. Also, we considered zero initial conditions, that is $x(t=0) = 0$ and $\dot{x}(t=0) = 0$.

While setting the algorithm, it is also convenient to transform our model given by eq. (3.7) into the system of two ordinary first order differential equations:

$$\begin{cases} \frac{dx}{dt} = y, \\ \\ \frac{dy}{dt} = -y\Gamma(x) - \Phi_0 \sin kx + G\cos\omega t + H\cos\Omega t. \end{cases} \tag{3.8}$$

Note that, the low frequency part of the excitation $G\cos\omega t$ constitutes the input of our system while $x(t)$ will then be considered as the system's output after integrating eq. (3.8). To analyze the system's behavior, we device the Fast Fourier Transform (FFT) which estimates the Fourier Transform $X(f)$ of the system's output $x(t)$ and which provides the bilateral magnitude spectrum defined by $|X(f)|$. Therefore, $2|X(f)|u(f)$ allows to compute the corresponding unilateral magnitude spectrum where $u(f)$ is the following Heaviside function:

$$u(f) = \begin{cases} 0 \;\; if \;\; f < 0, \\ \\ 1 \;\; if \;\; f \geq 0. \end{cases}$$

To quantize VR, it is important to evaluate the system's response amplitude at the low frequency $f_{Lf} = \frac{\omega}{2\pi}$ by determining the amplitude of the unilateral magnitude spectrum at this low frequency, namely $2|X(f=f_{Lf})|$. Indeed, this corresponds to the contribution of the low frequency component in the output unilateral magnitude spectrum $2|X(f)|$. The response amplitude provides an idea of how the low frequency component of the input signal is amplified by the high frequency perturbation.

Emergence of VR is usually revealed by the classical linear response Q, which was first defined by Landa and McClintock [8] as:

$$Q = \frac{2|X(f_{Lf})|}{G} . \tag{3.9}$$

Q allows to quantize VR effect since it represents the amplitude of the system's unilateral magnitude spectrum $2|X(f_{Lf})|$ at the low frequency normalized by the amplitude of the low frequency input signal G. Physically, the parameter Q can be viewed as the amplification factor of the nonlinear system for the specific low frequency component.

Throughout this thesis, as in the usual VR studies, we will consider the low angular frequency ω to be very small when compared to the perturbation angular frequency Ω. Indeed, we choose $\Omega = 20\omega$, and the low frequency amplitude G is set to $G=$0.05. Moreover, the parameters of the potential will also remain as $\Phi_0 = k = 1$ to provide a potential barrier $\frac{\Phi_0}{k} = 1$, as already illustrated in Fig. 3.1. This setting of parameters is to ensure that, the low frequency input excitation is subthreshold and that the potential barrier is never crossed without the help of the high frequency perturbation. This scenario constitutes the hypothesis commonly used to highlight VR.

3.2/ CASE OF A CONSTANT DAMPING

In this section, we first highlight VR signature from the temporal and frequency analyses points of view. Henceforth, by using the classical linear response of eq. (3.9), we study the effect of the constant damping coefficient on the VR occurrence, for the unitary particle mass ($m = 1$). Lastly, we study the combined effect of varying the particle mass m and the constant damping coefficient $\Gamma_0^{'}$ on the VR occurrence.

In the model of the system defined by eq. (3.7), the general damping parameter $\Gamma(x)$ becomes $\Gamma(x) = \Gamma_0^{'}$ for the case of constant damping, as defined by eq. (3.4). Therefore, the general equation of the system given by eq. (3.7) can now reduce to

$$m\frac{d^2x}{dt^2} + \Gamma_0^{'}\frac{dx}{dt} + \Phi_0 \sin kx = G\cos\omega t + H\cos\Omega t, \tag{3.10}$$

where $\Gamma_0^{'}$ stands for the constant damping amplitude which characterizes the system's dissipation. Therefore, it is maintained as a positive parameter throughout this chapter to stay in the dissipative mode else, it becomes an energy source to the system.

3.2.1/ HIGHLIGHT OF THE CLASSICAL VR EFFECT

This preliminary section highlights the classical VR signatures by means of temporal and frequency analyses for different perturbation amplitudes H. Moreover, by using the classical linear response Q, we study the influence of the constant damping amplitude $\Gamma_0^{'}$ on VR occurrence for a unitary mass $(m = 1)$.

3.2.1.1/ TEMPORAL ANALYSES

In this section, temporal behavior of the system's output $x(t)$ for different values of the perturbation amplitude H is examined by analyzing two different cases of the constant damping coefficient corresponding to $\Gamma_0^{'}$ =0.03 and $\Gamma_0^{'}$ =0.27. This temporal analysis of the system's output signal $x(t)$ is important because it allows to observe how the slow and fast oscillations are mixed and evolve through the system. This study is performed by integrating eq. (3.10) with the numerical procedure detailed in Sec. 3.1.4 to provide the temporal series of the system output.

For five different values of the perturbation amplitude H and for the specific value of the constant damping, namely $\Gamma_0^{'}$ =0.03, we present in Fig. 3.2, the temporal response of our linearly damped system defined by eq. (3.10). In each case presented at Figs. 3.2(a)–(e), the temporal series of the output signal reveals a low frequency component mixed with a high frequency perturbation component.

In particular, the temporal series of Fig. 3.2(a) corresponds to the instance of the smallest perturbation amplitude considered, namely $H = 30$. Here, we observed that the low frequency component in the system's output is very weak and the output signal is dominated by the high frequency perturbation. As shown in Fig. 3.2(b), when the perturbation amplitude increases to $H = 220$, the contribution of the low frequency component in the output signal is stronger than in Fig. 3.2(a). By contrast, in Fig. 3.2(c), the low frequency component in the output signal is best observed for an intermediate value of the perturbation $H = 245$. However, as the perturbation amplitude exceeds the intermediate value, the low frequency component in the output signal become less observable as depicted in Fig. 3.2(d) and Fig. 3.2(e) for $H = 300$ and $H = 405$ respectively.

Indeed, the temporal analysis of Fig. 3.2 shows that, varying the perturbation amplitude H enhances the detection of the low frequency component in the output signal. More precisely, the best response is obtained for an intermediate value of the perturbation amplitude H. This behavior is a typical signature of vibrational resonance effect.

We also study how the constant damping amplitude $\Gamma_0^{'}$ affects the contribution of the low frequency component in the output signal. Therefore at Fig. 3.3, the value of the damping coefficient is increased to $\Gamma_0^{'}$ =0.27 instead of $\Gamma_0^{'}$ =0.03. Despite increasing the constant damping coefficient $\Gamma_0^{'}$, VR signature is still observed from the temporal series of Fig. 3.3, which is obtained for specific values of the perturbation amplitude H. Indeed, as reported in Fig. 3.3(c), the low frequency com-

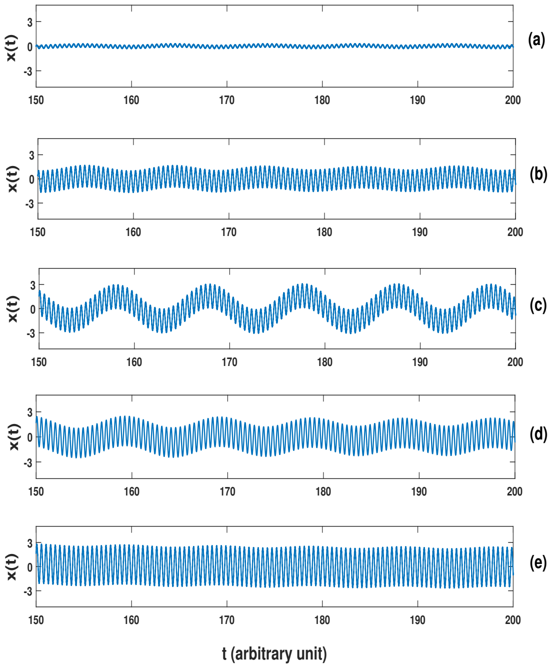

Figure 3.2: Time series of the system response revealing vibrational resonance effect for the specific constant damping coefficient Γ_0' =0.03. From top to bottom, the perturbation amplitude H increases as follows: (a) $H = 30$, (b) $H = 220$, (c) $H = 245$, (d) $H = 300$ and (e) $H = 405$. Parameters: $m = 1$, $k = 1$, $\Phi_0 = 1$, G =0.05, ω =0.65, $\Omega = 13$.

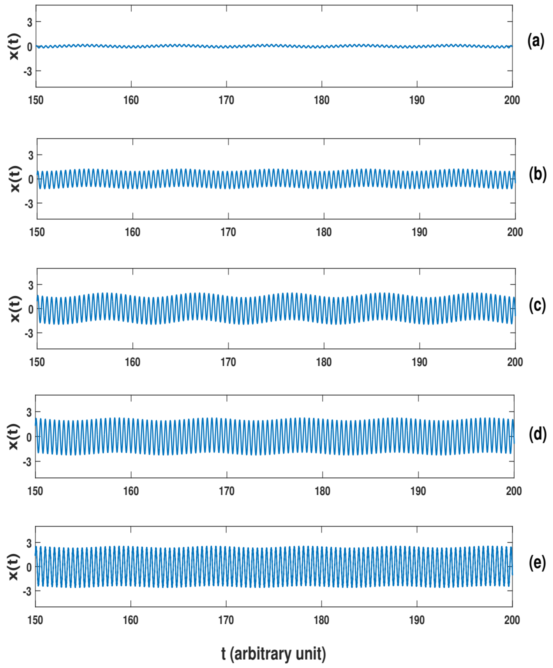

Figure 3.3: Time series of the system response revealing vibrational resonance effect for the specific constant damping coefficient Γ_0' =0.27. From top to bottom, the perturbation amplitude H increases as follows: (a) $H = 20$, (b) $H = 180$, (c) $H = 280$, (d) $H = 350$ and (e) $H = 405$. Parameters: $m = 1$, $k = 1$, $\Phi_0 = 1$, G =0.05, ω =0.65, $\Omega = 13$.

ponent of the output signal is best revealed for the intermediate value of the perturbation amplitude, namely $H = 280$.

Note that, the low frequency contributions in the temporal analyses of Fig. 3.3 are less pronounced when compared with the temporal series of Fig. 3.2. This implies that when the system is hugely damped, the low frequency signal detection in the system is lowered. Nevertheless, to have a better perception of the temporal series of Fig. 3.2 and Fig. 3.3, we therefore perform frequency analysis.

3.2.1.2/ FREQUENCY ANALYSIS

Temporal analysis is a good way of revealing the phenomenon of vibrational resonance but it is better to carry out frequency analysis to quantify this effect from the spectral point of view. Frequency analysis provides an alternative and better vision of how the low frequency component in the system's output signal $x(t)$ is affected by the perturbation amplitude H.

Therefore, we analyze the behavior of the unilateral magnitude spectrum of the system output $2|X(f)|u(f)$ versus the perturbation amplitude H for the two previously considered damping coefficients namely, Γ_0' =0.03 and Γ_0' =0.27. First, when Γ_0' =0.03, Figs. 3.4 (a)–(e) present the unilateral magnitude spectra corresponding to the same five values of the perturbation amplitude H used in the temporal analyses of Fig. 3.2. For the sake of clarity, we have made a zoom near

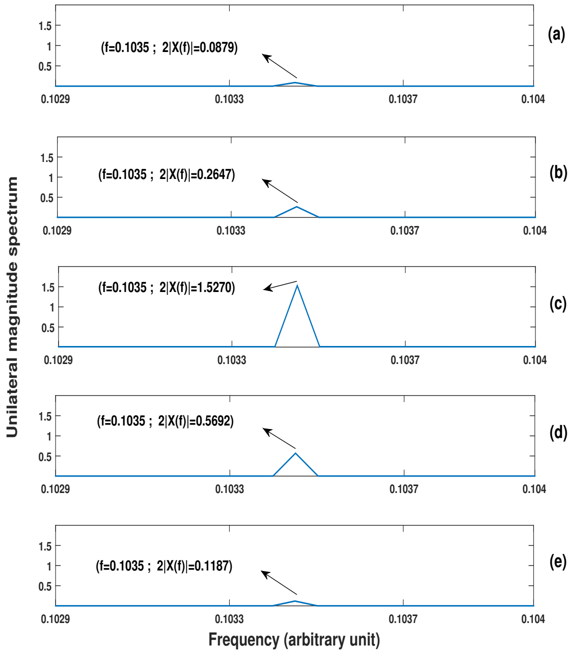

Figure 3.4: Unilateral magnitude spectra corresponding to the time series of Fig. 3.2. From top to bottom: (a) $H = 30$, (b) $H = 220$, (c) $H = 245$, (d) $H = 300$ and (e) $H = 405$. Parameters: $m = 1$, $\Gamma_0^{'}$ =0.03, $k = 1$, $\Phi_0 = 1$, G =0.05, ω =0.65, $\Omega = 13$.

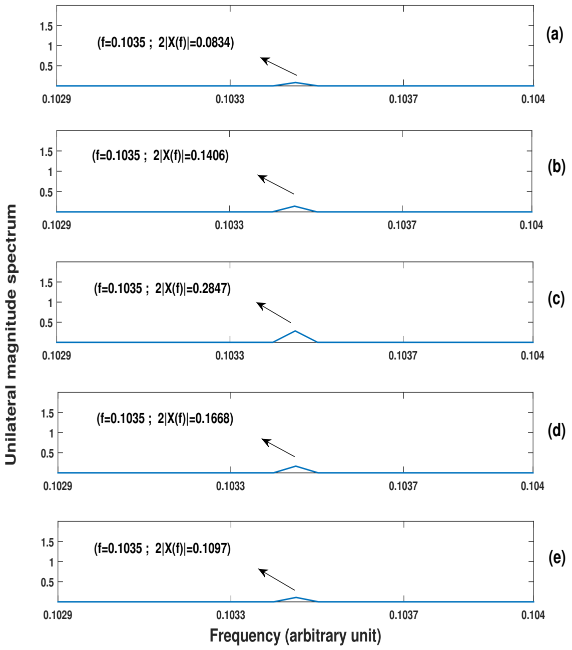

Figure 3.5: Unilateral magnitude spectra corresponding to the time series of Fig. 3.3. From top to bottom: (a) $H = 20$, (b) $H = 180$, (c) $H = 280$, (d) $H = 350$ and (e) $H = 405$. Parameters: $m = 1$, $\Gamma_0^{'}$ =0.27, $k = 1$, $\Phi_0 = 1$, G =0.05, ω =0.65, $\Omega = 13$.

the low frequency $f_{Lf} = \dfrac{\omega}{2\pi}$ in all the spectral responses presented at Fig. 3.4. It is obvious from the spectral response of Fig. 3.4(a) that, the amplitude of the unilateral magnitude spectrum at the low frequency f_{Lf} is weak for the smallest value of the perturbation amplitude, namely $H = 30$. Next, when the perturbation amplitude increases to $H = 220$, the spectral contribution of the low frequency increases at Fig. 3.4(b). As depicted at Fig. 3.4(c), the amplitude of the spectrum at the low frequency is best pronounced when the perturbation amplitude is tuned to the intermediate value $H = 245$. However, as shown at Figs. 3.4(d) and 3.4(e) for $H = 300$ and $H = 405$ respectively, increasing the perturbation amplitude H beyond the optimal value, the spectral contribution at the low frequency became weak again.

Consequently, the frequency analyses summarized at Fig. 3.4 confirm the temporal analyses presented at Fig. 3.2 which revealed that: the perturbation amplitude H can be optimally set to enhance the detection of the low frequency component. Especially, the best response is obtained for an intermediate value of the perturbation amplitude H, which is the typical signature of vibrational resonance effect.

Similarly, at Fig. 3.5, we report the spectral behavior of the system when the damping coefficient increases to $\Gamma_0^{'}$ =0.27, as we have observed in the temporal behavior for the same value of the damping coefficient at Fig. 3.3. Here, it is clearly obvious by comparing Fig. 3.5(a) and (b) that the amplitude of the spectrum at the low frequency is weak but it increases as the perturbation amplitude H increases from $H = 20$ to $H = 180$. As expected, the amplitude of the spectrum at the low frequency is more observable in Fig. 3.5(c), when the perturbation amplitude is optimally tuned to $H = 280$. Eventually, the amplitude of the spectrum at the low frequency became weak again as the perturbation amplitude increases to $H = 350$ and $H = 405$ in Fig. 3.5(d) and Fig. 3.5(e) respectively.

The spectral analyses of Fig. 3.5 clarify with better physical display than the temporal analyses of Fig. 3.3, how the perturbation amplitude H affects the system's response at the low frequency. This implies that the frequency analysis is also an important tool for our analysis despite the temporal analysis.

3.2.1.3/ HIGHLIGHT OF THE VR SIGNATURE

Having observed the behavior of the system from the perspectives of temporal and frequency analyses, it is now pertinent to quantize the spectral response of the system. It will allow to better investigate how the low frequency component of the output signal evolves when the high frequency perturbation amplitude H varies. Here, with the same set of parameter values used in our temporal and frequency analyses, we use the classical quantification tool Q defined by eq. (3.9) to highlight VR effect.

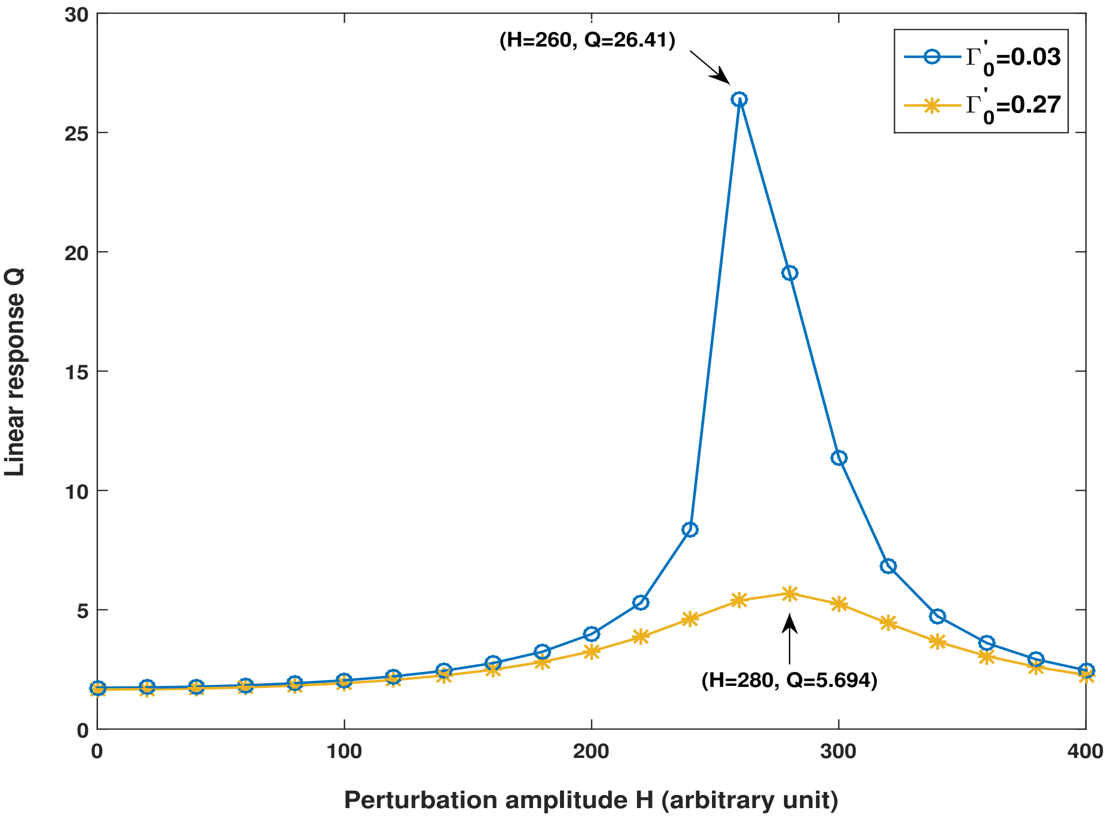

Figure 3.6: Typical VR signature observed in the system defined by eq. (3.10) for two values of the constant damping amplitude Γ_0'. Parameters: $m = 1$, $k = 1$, $\Phi_0 = 1$, G =0.05, ω =0.65, $\Omega = 13$.

Presented in Fig. 3.6 is the linear response Q as a function of the perturbation amplitude H for two values of the constant damping amplitude, namely $\Gamma_0^{'}$ =0.03 and $\Gamma_0^{'}$ =0.27. In both the two cases depicted at Fig. 3.6, we observed bell-shape curves which show that, the response amplitude Q is a non monotonous function of the perturbation amplitude H. Indeed, the linear response Q achieves its maximum for an optimal value of the perturbation amplitude H. This implies that the detection of the low frequency signal in this system can be optimized by an appropriate setting of the perturbation amplitude H, which is the typical VR signature. Moreover, it can be seen that decreasing the constant damping amplitude $\Gamma_0^{'}$ provides a better response since the maximum value of the linear response Q is greater in the case of weak damping amplitude, that is $\Gamma_0^{'}$ =0.03.

However, in the system with the space-dependent inhomogeneous damping, Roy-Layinde *et al* revealed that there are other resonances when the perturbation amplitude H is further increased [158]. Therefore, in this particular system, it is also important to find out if there are other resonances when the perturbation amplitude H increases.

3.2.2/ HIGHLIGHT OF THE VIBRATIONAL MULTIRESONANCE

It is now obvious that vibrational resonance signature is observed in our system and especially, that the low frequency component can be better detected when the perturbation amplitude H is tuned to an optimal value, as shown in Fig. 3.6. In the resonance curves of Fig. 3.6, the perturbation amplitude H varies from 0 to 400 as such, we obtained single resonance. However, we are interested in exploring the behavior of the system when the perturbation amplitude H increases beyond 400.

The linear response Q as a function of the perturbation amplitude H for the two values of the constant damping coefficients $\Gamma_0^{'}$ =0.03 and $\Gamma_0^{'}$ =0.27, is presented at Fig. 3.7 for a perturbation amplitude H ranging from 0 to 1500. For both the two constant damping amplitudes, we obtain multiple resonances as the perturbation amplitude H increases. Note that, in each case, the first resonance provides the global maximum which is obtained for an intermediate value of the perturbation amplitude H. Beyond the optimal value of the perturbation amplitude H, other resonances appear with local maxima which decrease as the perturbation amplitude H keeps increasing. Moreover, it can be seen from the resonance curves of Fig. 3.7 that increasing the constant damping amplitude from $\Gamma_0^{'}$ =0.03 to $\Gamma_0^{'}$ =0.27 decreases the performance of the system. Indeed, the amplitude of the local maxima is weakest for the strongest constant damping amplitude $\Gamma_0^{'}$.

Interestingly, our system reveals vibrational multiresonance effect with the resonances depending on the intensity of the perturbation amplitude H. This typical multiresonance signature was also reported in the study of vibrational resonance in pendulum systems [166,186,187], neuronal models with time delay [187–192] and in the study of stochastic resonance [193–196]. In the next section, we analyze the evolution of the second resonances depicted at Fig. 3.7, by means of temporal and frequency analyses.

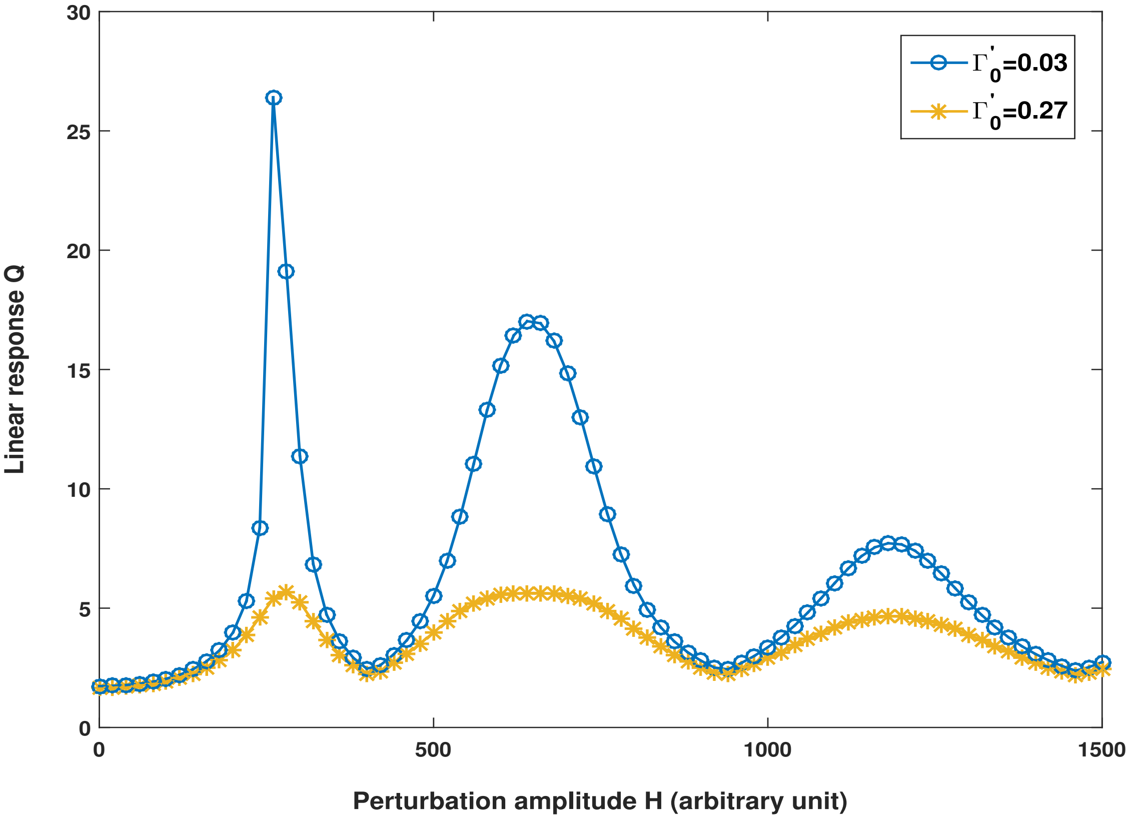

Figure 3.7: Vibrational multiresonance signature for two values of the constant damping amplitude Γ'_0. The linear response Q exhibits local maxima whose values decrease as the perturbation amplitude increases. Parameters: $m = 1$, $k = 1$, $\Phi_0 = 1$, G =0.05, ω =0.65, $\Omega = 13$.

3.2.2.1/ TEMPORAL ANALYSIS

In this subsection, we study the temporal behavior of the system near the second resonances of the linear response curves of Fig. 3.7, for both damping values Γ'_0 =0.03 and Γ'_0 =0.27. The temporal series of Fig. 3.8 correspond to the responses around the second resonance of Fig. 3.7 when the constant damping coefficient Γ'_0 is set to 0.03. We observe that for the two values of the perturbation amplitude H before the peak of the second resonance, namely $H = 430$ and $H = 500$, the low frequency component in the output signal is weak, as shown in Figs. 3.8(a) and 3.8(b). However, at the peak of the second resonance, corresponding to the time series of Fig. 3.8(c) when $H = 645$, the low frequency component reaches its highest intensity in this case. Also, for the values of perturbation amplitude H beyond the peak of the second resonance, $H = 770$ and $H = 935$, the low frequency component of the output signal decreases, as given in Fig. 3.8(d) and Fig. 3.8(e) respectively. The behavior revealed at Fig. 3.8 is similar to the temporal behavior previously observed for the first resonance in Fig. 3.2 and for the same value of the constant damping coefficient Γ'_0 =0.03.

Similarly, in Fig. 3.9, we study the temporal behavior of the second resonance of Fig. 3.7, for the corresponding value of the constant damping amplitude Γ'_0 =0.27. Our temporal studies of the

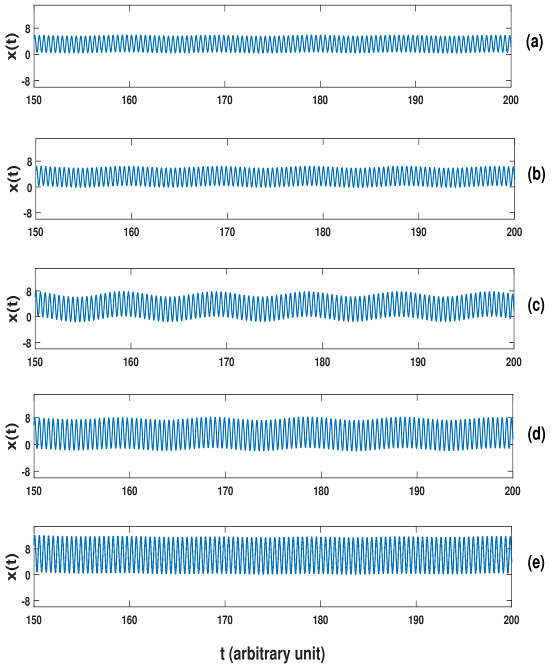

Figure 3.8: Time series of the system response revealing the second resonance of Fig. 3.7 for the specific constant damping coefficient Γ'_0 =0.03. From top to bottom, the perturbation amplitude H increases as follows: (a) $H = 430$, (b) $H = 500$, (c) $H = 645$, (d) $H = 770$ and (e) $H = 935$. Parameters: $m = 1$, $k = 1$, $\Phi_0 = 1$, G =0.05, ω =0.65, $\Omega = 13$.

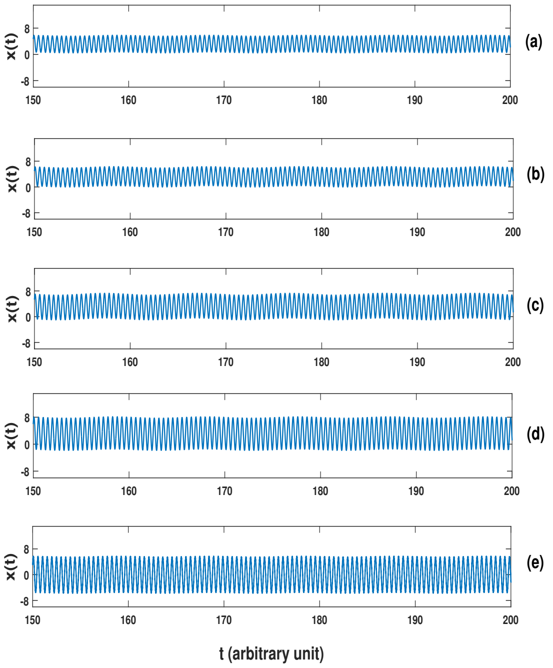

Figure 3.9: Time series of the system response revealing the second resonance of Fig. 3.7 for the specific constant damping coefficient Γ'_0 =0.27. From top to bottom, the perturbation amplitude H increases as follows: (a) $H = 430$, (b) $H = 500$, (c) $H = 650$, (d) $H = 810$ and (e) $H = 935$. Parameters: $m = 1$, $k = 1$, $\Phi_0 = 1$, G =0.05, ω =0.65, $\Omega = 13$.

second resonance in Fig. 3.9 also revealed vibrational resonance effect. Indeed, the detection of the low frequency component of the output signal is best achieved for an optimal perturbation amplitude H. By contrast, the temporal response of the second resonance at Fig. 3.9 is less pronounced than the temporal response of the first resonance at Fig. 3.3 for the same value of the constant damping amplitude, namely Γ'_0 =0.27. Comparing the temporal series for the second resonance when Γ'_0 =0.03 in Fig. 3.8 and when Γ'_0 =0.27 in Fig. 3.9, we can admit that the response decreases when the constant damping coefficient Γ'_0 increases. To clearly ascertain this fact, we study the frequency analysis for the same scenarios.

3.2.2.2/ FREQUENCY ANALYSIS

In the analysis of the second resonances, as with the study of the first resonance, temporal analysis is not enough to clearly visualize the impact of the perturbation amplitude H on the system's output signal. Especially, when the constant damping coefficient Γ'_0 became large. In this subsection, we study the spectral behavior of the second resonances of Fig. 3.7.

Increasing the perturbation amplitude from $H = 430$ to $H = 500$ below the peak of the second resonance for Γ'_0 =0.03, we can clearly observe how the amplitude of the spectrum at the low frequency increases from Fig. 3.10(a) to Fig. 3.10(b). Moreover, the amplitude of the spectrum at the low frequency is best observed at the peak of the second resonance, that is when $H = 645$ as reported at Fig. 3.10(c). When the perturbation amplitude H increases beyond the peak of this second resonance, the contribution of the low frequency in the system output spectra become weak again as shown in Figs. 3.10(d) and 3.10(e) for $H = 770$ and $H = 935$ respectively.

Meanwhile, for the second resonance in the case of $\Gamma_0^{'}$ =0.27 reported at Fig. 3.11, we obtain a better view of the resonance phenomenon with the spectral responses than with the equivalent temporal analyses presented at Fig. 3.9. Indeed, in the spectra of Figs. 3.11(a) and 3.11(b), it is obvious that the contribution of the low frequency is more pronounced when the perturbation amplitude H increases from $H = 430$ to $H = 500$. The amplitude of the spectrum at the low frequency is more evidently observed at the peak of the second resonance, that is when $H = 650$, as shown in Fig. 3.11(c). The response afterward decreases when the perturbation amplitude H is beyond the peak of the second resonance as shown in Fig. 3.11(d) and Fig. 3.11(e) when $H = 810$ and $H = 935$ respectively.

Having explored so much from the temporal and frequency analyses points of view, now we study the impact of the constant damping coefficient $\Gamma_0^{'}$ on the classical VR, for the unitary value of mass $m = 1$. The combined effect of the particle mass m and the constant damping coefficient $\Gamma_0^{'}$ will also be considered in the studies that follows.

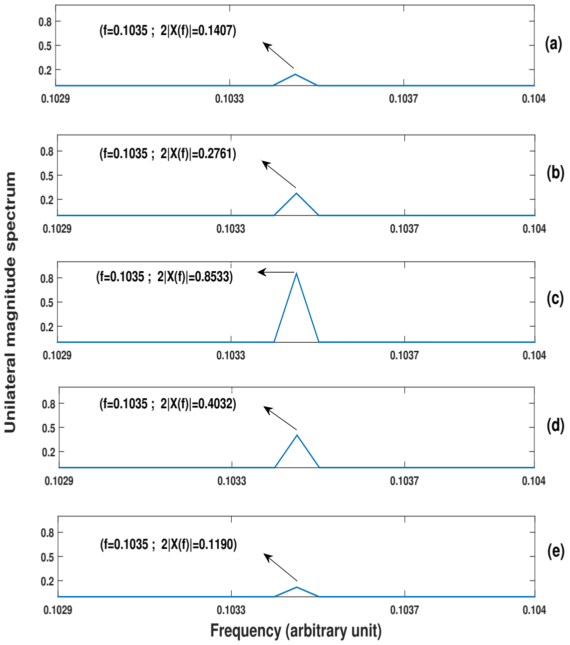

Figure 3.10: Unilateral magnitude spectra corresponding to the time series of Fig. 3.8. From top to bottom: (a) $H = 430$, (b) $H = 500$, (c) $H = 645$, (d) $H = 770$ and (e) $H = 935$. Parameters: $m = 1$, $\Gamma_0^{'}$ =0.03, $k = 1$, $\Phi_0 = 1$, G =0.05, ω =0.65, $\Omega = 13$.

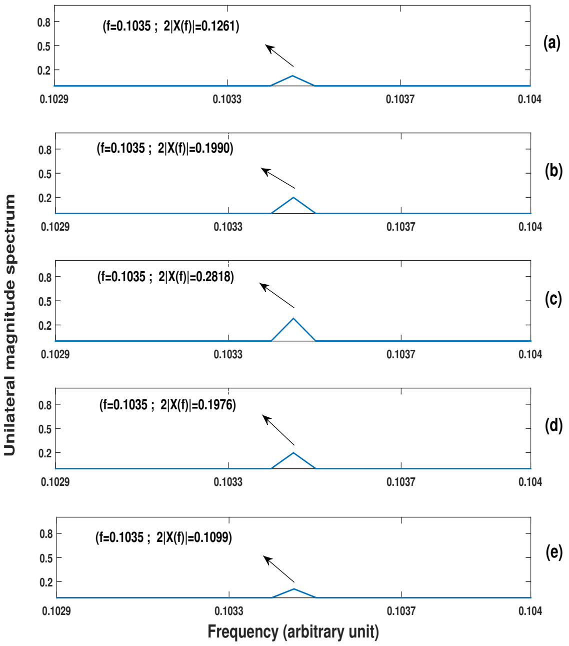

Figure 3.11: Unilateral magnitude spectra corresponding to the time series of Fig. 3.9. From top to bottom: (a) $H = 430$, (b) $H = 500$, (c) $H = 650$, (d) $H = 810$ and (e) $H = 935$. Parameters: $m = 1$, $\Gamma_0^{'}$ =0.27, $k = 1$, $\Phi_0 = 1$, G =0.05, ω =0.65, $\Omega = 13$.

3.2.3/ CONTROL OF VR BY THE CONSTANT DAMPING COEFFICIENT $\Gamma_0^{'}$

The temporal and frequency analyses performed in the previous sections highlighted the existence of VR phenomenon and also the impact of increasing the value of the constant damping coefficient $\Gamma_0^{'}$. Moreover, the presentation of the classical linear response Q in Fig. 3.7 shaded more light on the nature of the resonance curves obtained in our system and also on the effect of increasing the constant damping coefficient $\Gamma_0^{'}$. In this part, we use the classical VR measurement defined by eq. (3.9) to further investigate how the parameter of the constant damping $\Gamma_0^{'}$ can control the vibrational resonance occurrence for a unitary particle mass ($m = 1$).

Fig. 3.12 reveals the linear response Q as a function of the perturbation amplitude H for different values of the constant damping coefficient $\Gamma_0^{'}$. This shows that, increasing the perturbation amplitude H, there exist multiple resonances whatever the value of the constant damping coefficient $\Gamma_0^{'}$. In each case, the first resonance provides the best linear response Q which is achieved for an intermediate value of the perturbation amplitude H. Beyond the first resonance, which of course provided the global maximum, the local maxima afterward decrease as the perturbation amplitude H increases. Furthermore, the resonance curves of Fig. 3.12 also convey to us that the weakest constant dissipation $\Gamma_0^{'}$ provides the best response Q of the system.

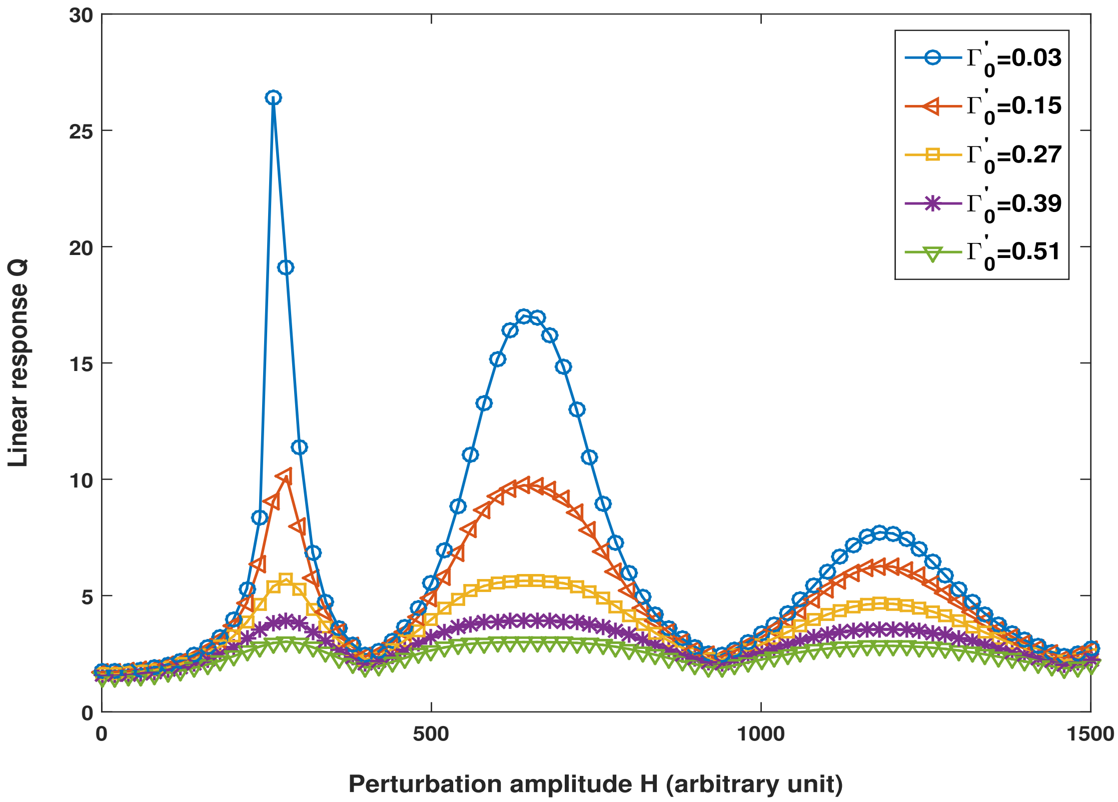

Figure 3.12: Control of VR with the constant damping amplitude $\Gamma_0^{'}$. Parameters: $m = 1$, $k = 1$, $\Phi_0 = 1$, G =0.05, ω =0.65, $\Omega = 13$.

From the mechanical point of view, one may conclude that the best linear response Q will be achieved without dissipation in the system ($\Gamma_0^{'} = 0$). In this chapter, we do not consider this case because there is always dissipation in the real systems therefore, the case $\Gamma_0^{'} = 0$ does not exist in reality.

The vibrational resonance behavior revealed in Fig. 3.12 shows that the linear response Q at which the global, second and third maxima are obtained depends on the constant damping amplitude $\Gamma_0^{'}$. For instance, the global maxima of Fig. 3.12 decreases as the constant damping amplitude $\Gamma_0^{'}$ increases. We have reported at Fig. 3.13 how the peak value Q_{max}^{n} of the resonance number n of Fig. 3.12 evolves versus the constant damping $\Gamma_0^{'}$. We restricted our analyses of Fig. 3.13 to the peak of the global, second and third maxima, that is Q_{max}^{1}, Q_{max}^{2} and Q_{max}^{3}. It is obvious in Fig. 3.13 that for smaller values of the constant damping amplitude $\Gamma_0^{'}$, the gaps between the global, second and third maxima are the greatest. By contrast, these gaps reduce and vanish as $\Gamma_0^{'}$ increases. Moreover, for larger $\Gamma_0^{'}$, the magnitudes of the three resonances become almost the same and the weakest one. This implies that controlling VR in this system is more efficient for the smaller value of the constant damping coefficient $\Gamma_0^{'}$.

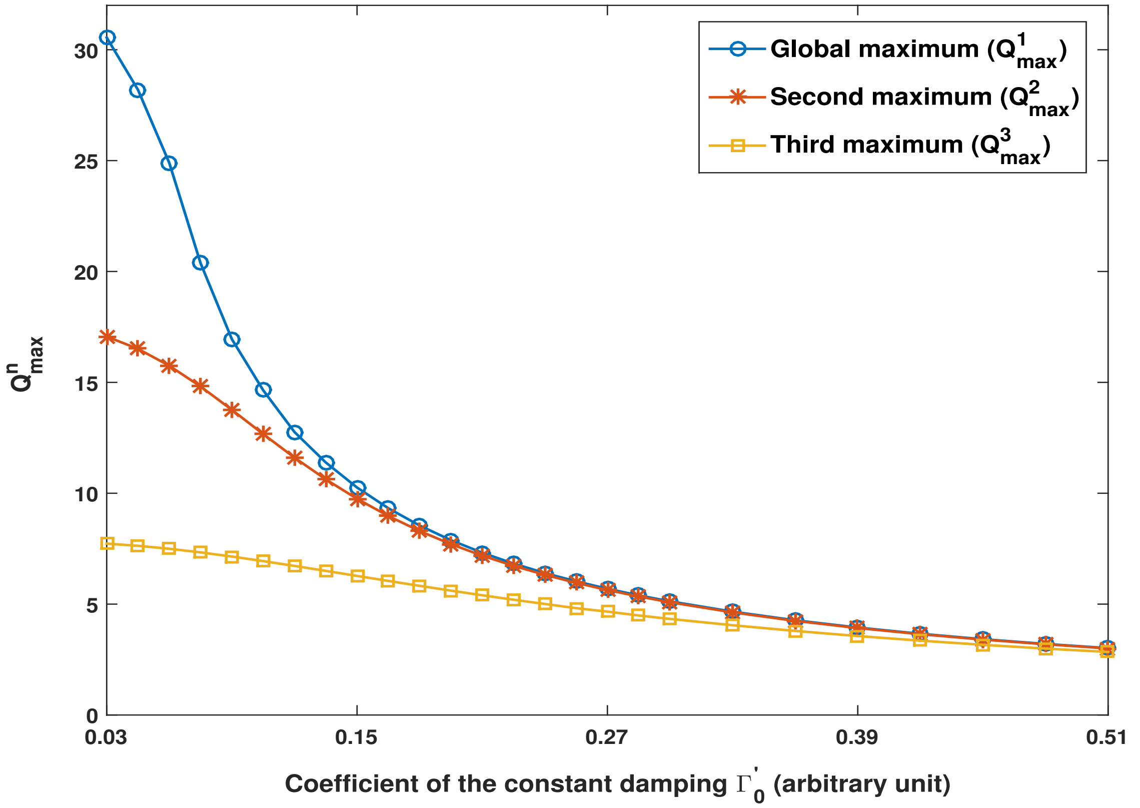

Figure 3.13: Dependence of the local maxima Q_{max}^{n} of Fig. 3.12 versus the constant damping amplitude $\Gamma_0^{'}$. Q_{max}^{n} donates the amplitude of the local maxima number n. Parameters: $m = 1$, $k = 1$, $\Phi_0 = 1$, G =0.05, ω =0.65, $\Omega = 13$.

3.2.4/ THE MEASURING TOOL INDICATING VR EXISTENCE

Until this end, our studies are restricted to the case of a particle of unitary mass, namely $m = 1$. Now, in this section, we investigate the combined impact of the particle mass m and the constant damping coefficient $\Gamma_0^{'}$ on the occurrence of VR phenomenon.

Depending on the particle mass m, our numerical investigations reveal two different behaviors. Fig. 3.14 highlights these two cases for different values of the constant damping coefficient $\Gamma_0^{'}$ and specific values of the particle mass, more precisely $m = 1$ and $m =$2.4. At Fig. 3.14(a), corresponding to $m = 1$, the system's performance can be optimized by an appropriate setting of the perturbation amplitude H since the linear response curves versus the perturbation amplitude exhibit multiresonance shapes. By contrast, for the case reported at Fig. 3.14(b), and corresponding to $m =$2.4, increasing the perturbation amplitude H can not maximized the system's response Q. Indeed, the maximum linear response in this case is obtained when the perturbation amplitude is $H = 0$, for all values of the constant damping coefficient $\Gamma_0^{'}$. Note that VR phenomenon failed to exist in this later case because, the maximum linear response Q is obtained without the perturbation, that is when $H = 0$.

The existence of these two behaviors highlighted in Fig. 3.14 makes it an interesting task for us to have a general view of the system's behavior when the particle mass m varies. For each value of

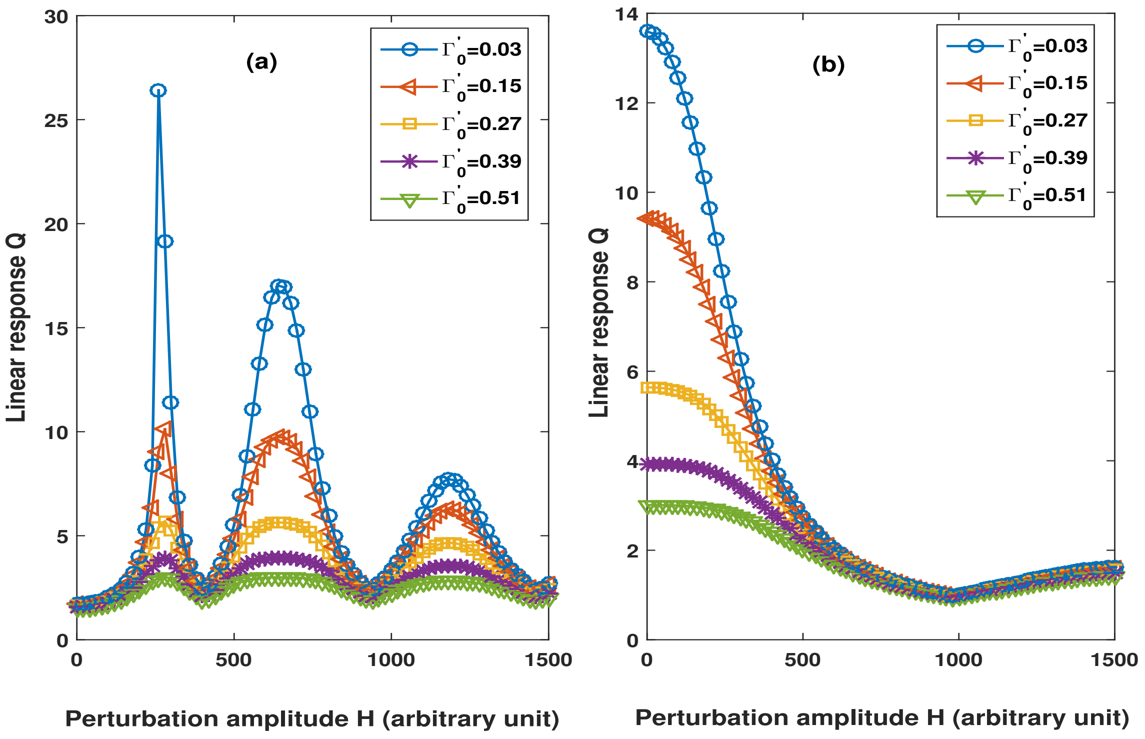

Figure 3.14: System's two different observed behaviors due to the change of the particle mass m. (a) $m = 1$, VR signature: A high frequency perturbation enhances the detection of the low frequency. (b) $m =$2.4, no enhancement of the low frequency detection. Parameters: $k = 1$, $\Phi_0 = 1$, $G =$0.05, $\omega =$0.65, $\Omega = 13$.

the mass m, to identify whether the perturbation can lead to an enhancement of the low frequency detection or not, we introduce an indicator, namely Q^*_{max}, which allows to classify the behavior belonging to each particle mass. We propose to define Q^*_{max} as the ratio of the maximum linear response Q_{max} to the linear response obtained without high frequency perturbation, that is when $H = 0$. We therefore define Q^*_{max} as:

$$Q^*_{max} = \frac{Q_{max}}{Q(H=0)} \; . \tag{3.11}$$

If the maximum response amplitude Q_{max} in whatever the case is obtained without the perturbation, our indicator Q^*_{max} equals $Q^*_{max} = 1$. This means for that particular value of the particle mass, no enhancement can be achieved by adding a high frequency perturbation, as in the case of Fig. 3.14(b). However, if Q_{max} is obtained for an appropriate increase of the perturbation, the indicator Q^*_{max} will exceed the value 1 as in the case of Fig. 3.14(a). Accordingly, $Q^*_{max} = 1$ implies no enhancement and $Q^*_{max} > 1$ signifies enhancement whereas the former corresponds to the case where VR phenomenon failed to exist while the latter matches the existence of VR. The indicator Q_{max} defined by eq. (3.11) will be used in this chapter to identify which of these two different behaviors occurs according to the particle mass m value.

3.2.5/ COMBINED IMPACT OF THE PARTICLE MASS m AND THE CONSTANT DAMPING AMPLITUDE $\Gamma_0^{'}$ ON VR OCCURRENCE

In this section, we investigate the influence of the particle mass m on the occurrence of vibrational resonance for different values of the constant damping amplitude $\Gamma_0^{'}$. For different values of the particle mass below and above $m = 1$, we study the evolution of the linear response Q. In each case, by using the indicator Q^*_{max} defined by eq. (3.11), we identify if the system's response can be optimized with the perturbation amplitude H, that is if $Q^*_{max} > 1$.

In Fig. 3.15, we present the indicator Q^*_{max} as a function of the particle mass m. This will give an idea of how the system changes its behavior, through VR effect, depending on the particle mass m. Our result in Fig. 3.15 revealed that there is a critical value of the particle mass m^* below which VR effect exists and beyond which VR effect ceases to exist. This critical value of mass m has been precisely calculated for our parameter settings as m^* =2.375, for all values of the constant damping amplitude $\Gamma_0^{'}$. Lastly, the best response Q^*_{max} is obtained for the smallest damping coefficient $\Gamma_0^{'}$ as previously reported, namely $\Gamma_0^{'}$=0.03.

The complete analyses conducted so far correspond to the case of a system with the constant damping $\Gamma(x) = \Gamma_0^{'}$ which will constitute a reference for our future studies of the system experiencing a nonlinear damping. Throughout these studies, we highlighted the occurrence of VR and the influence of the constant damping amplitude $\Gamma_0^{'}$ on VR. Our analyses were first for the case of the fixed unitary particle mass $m = 1$ and lastly for the case of varying the particle mass. In what

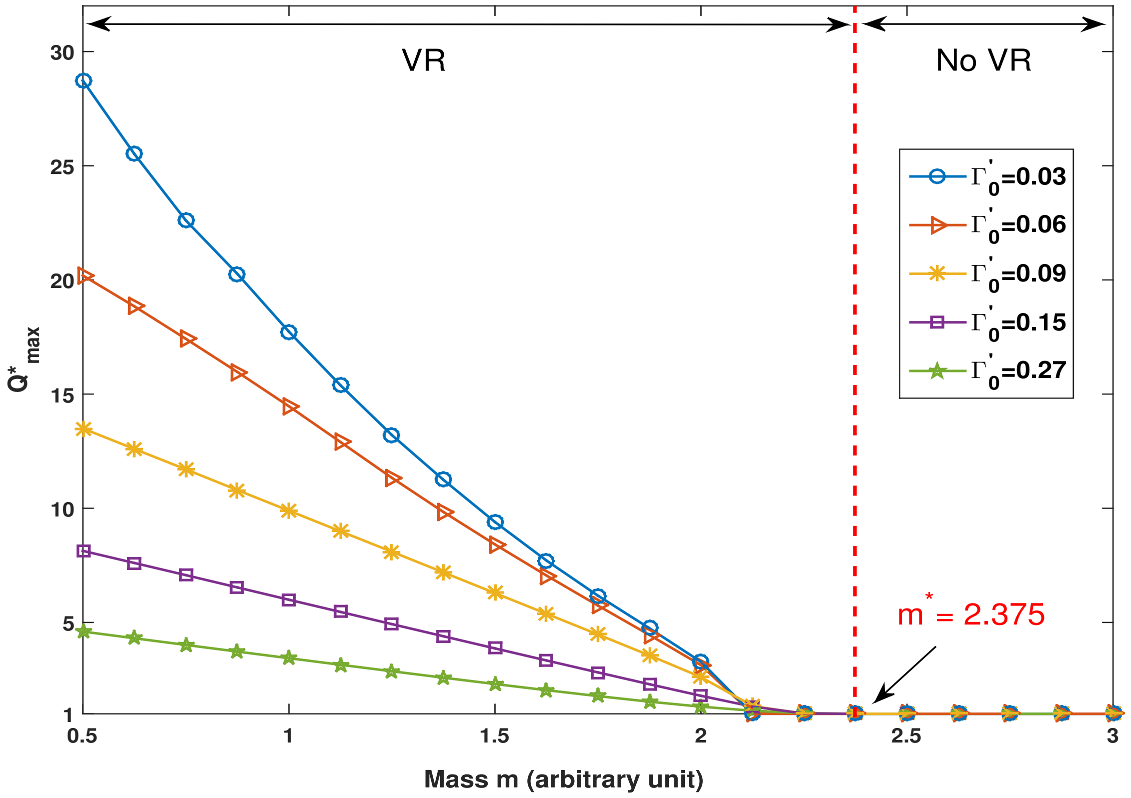

Figure 3.15: Selective response behavior controlled by the mass m of the particle. Summary of the system's two behaviors for different values of the constant damping amplitude Γ_0'. Values of mass m that correspond to $Q^*_{max} = 1$ define the region where VR ceases to exist whereas those that correspond to $Q^*_{max} > 1$ match the existence of VR. Parameters: $G =$0.05, $k = 1$, $\omega =$0.65, $\Omega = 13$, $\Phi_0 = 1$.

follows, we will study the behavior of a system experiencing a space-dependent inhomogeneous damping.

3.3/ CASE OF AN INHOMOGENEOUS AND SPACE-DEPENDENT NONLINEAR DAMPING

In the case of space-dependent nonlinear damping obeying to eq. (3.5), the equation (3.7) of the system describes the motion of a particle ruled by:

$$m\frac{d^2x}{dt^2}+\Gamma_0\left[1-\lambda\sin(kx+\phi)\right]\frac{dx}{dt}+\Phi_0\sin kx=G\cos\omega t+H\cos\Omega t. \tag{3.12}$$

Recall that, λ sets the strength of the frictional inhomogeneity, the positive parameter Γ_0 is the whole amplitude of the nonlinear damping, k adjusts the same periodicity as in the periodic potential $\Phi(x)$, while ϕ denotes the phase difference between the periodic potential $\Phi(x)$ and the nonlinear dissipation $\Gamma(x)$. The case $\lambda=0$ in eq. (3.12), which corresponds to the case of the constant damping studied in the previous section, has also been considered by Rajasekar *et al* when they first reported the phenomenon of VR in multistable systems [149]. Moreover, Roy-Layinde *et al* recently introduced nonlinear dissipative damping to the system and studied the role of its parameters on the occurrence of VR [158].

In fact, nonlinear dissipation [197] is a very interesting property due to its wide appearance and applications in many mechanical systems such as: aerospace structures [198], nanoelectromechanical systems [199–201], acoustic nonlinearity of an orifice [202], nonlinear suspension and isolation systems [203], cochlear amplifier [204], Kramers oscillator [205], Josephson junction [206,207] and in plasma science [157,208]. Despite its diverse occurrences and applications, there are very few investigations that focused on the impact of nonlinear damping/dissipation on the occurrence of vibrational resonance [157,158,209].

In this section, we numerically first study the role of the nonlinear dissipation parameters; Γ_0, λ and ϕ on the occurrence of VR for a fix unitary mass $(m=1)$. Especially, this preliminary studies allow to highlight the role of the mass m of the particle on the occurrence of VR, which to our knowledge, has not been yet reported.

3.3.1/ RESPONSE OF THE SYSTEM

In this section, we perform temporal and spectral analyses to study how the system with inhomogeneous damping defined by eq. (3.12) responds to an external input stimuli. Like in the case of constant damping, we subsequently study the influence of the nonlinear dissipation parameters on VR, first for unitary mass and lastly for other values of the particle mass.

3.3.1.1/ TEMPORAL ANALYSES

We analyze the temporal behavior of our dissipative system by examining the output signal $x(t)$ for different values of the perturbation amplitude H and for the specific values of nonlinear damping amplitude Γ_0 =0.03 and Γ_0 =0.27. Note that these two values of the inhomogeneous damping amplitude correspond to the values of constant damping amplitude Γ_0' previously considered in Sec. 3.2, when the damping was maintained constant. We carry out temporal analysis to qualitatively observe the slow and the fast oscillations in the system's output signal $x(t)$.

For five different values of the perturbation amplitude H and for the specific value of the nonlinear damping amplitude Γ_0 =0.03, we summarized at Fig. 3.16 the temporal response of the system with inhomogeneous damping. For all the perturbation amplitudes H of Fig. 3.16, the temporal series reveal a low frequency component mixed with the high frequency perturbation component. In particular, for the smallest value of the perturbation amplitude, namely $H = 20$, the low frequency component is weak as shown in Fig. 3.16(a). The contribution of the low frequency in the output signal is enhanced when the perturbation amplitude H increases to $H = 220$, as depicted in Fig. 3.16(b). By contrast, for an intermediate value of the perturbation amplitude, namely $H = 245$ presented at Fig. 3.16(c), the low frequency component in the output signal is best pronounced. In this latter case, we can see that the output signal is dominated by the low frequency signal,

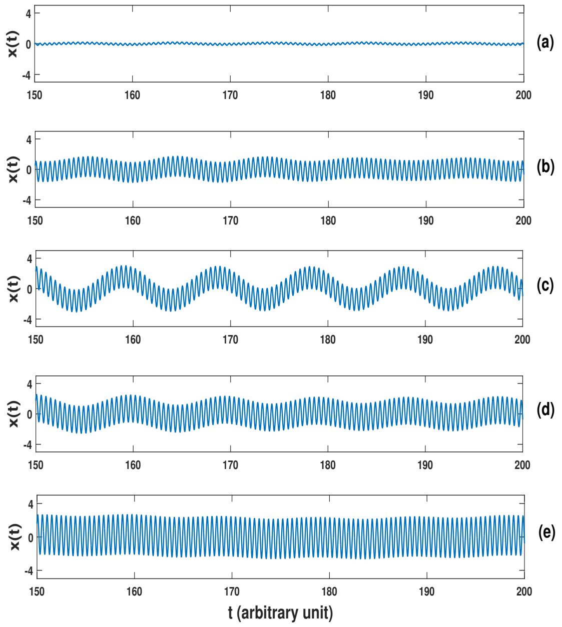

Figure 3.16: Time series of the system response revealing vibrational resonance effect for the specific nonlinear damping coefficient Γ_0 =0.03. From top to bottom, the perturbation amplitude H increases as follows: (a) $H = 20$, (b) $H = 220$, (c) $H = 245$, (d) $H = 300$ and (e) $H = 400$. Parameters: $m = 1$, λ =2.4, ϕ =0.2, $k = 1$, $\Phi_0 = 1$, G =0.05, ω =0.65, $\Omega = 13$.

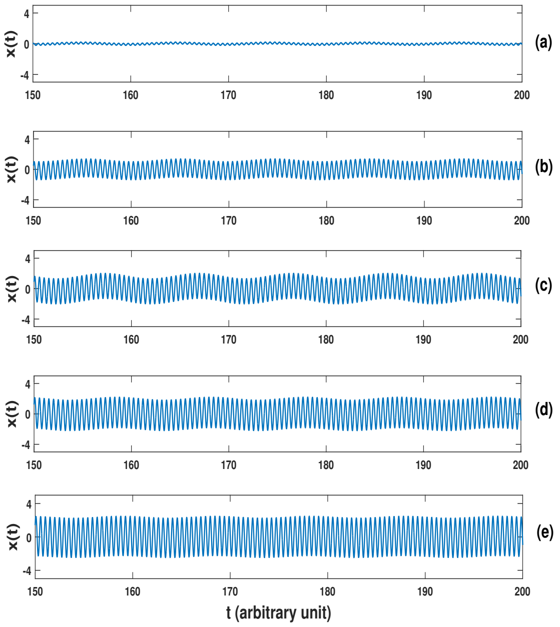

Figure 3.17: Time series of the system response revealing vibrational resonance effect for the specific nonlinear damping coefficient Γ_0 =0.27. From top to bottom, the perturbation amplitude H increases as follows: (a) $H = 20$, (b) $H = 200$, (c) $H = 280$, (d) $H = 340$ and (e) $H = 400$. Parameters: $m = 1$, λ =2.4, ϕ =0.2, $k = 1$, $\Phi_0 = 1$, G =0.05, ω =0.65, $\Omega = 13$.

which is contrary to the case of Fig. 3.16(a) when the perturbation amplitude H was very weak. Meanwhile, for the perturbation amplitudes beyond the intermediate value, $H = 300$ and $H = 400$ for example, the low frequency component becomes weak again as shown in Figs. 3.16(d) and 3.16(e) respectively. This implies that the detection of the low frequency signal in the system is enhanced when the perturbation amplitude H is tuned to an intermediate value. Consequently, the temporal series of Fig. 3.16 exhibit the signature of VR.

We have performed the same temporal analysis at Fig. 3.17 for a greater nonlinear damping amplitude, namely Γ_0 =0.27 instead of Γ_0 =0.03. This study gives an insight on the impact of the nonlinear damping amplitude Γ_0 on the dynamics of the dissipative system with inhomogeneous damping. Figs. 3.17(a)-(e) summarize the system temporal behavior, for five different values of the perturbation amplitudes. Fig. 3.17(a), which corresponds to the case of the smallest considered perturbation amplitude $H = 20$, shows that the low frequency component in the output signal is hardly detectable. Increasing the perturbation amplitude to $H = 200$ enhances the detection of the low frequency component in the output signal, as shown in Fig. 3.17(b). Moreover, for an intermediate value of the perturbation $H = 280$, the low frequency component in the output signal is best observed. The low frequency in the output signal becomes weak again for the values of perturbation amplitude beyond the intermediate value as shown in Figs. 3.17(d) and 3.17(e).

It is clear that, the responses obtained in Fig. 3.17 after increasing the nonlinear damping amplitude to Γ_0 =0.27 are less pronounced when compared with the responses obtained when the damping amplitude was Γ_0 =0.03 as given by Fig. 3.16. This implies that, when the nonlinear damping amplitude Γ_0 grows larger, the low frequency component in the system's output signal is less detectable. The responses obtained in these temporal analyses are in agreement with what has been observed from the system experiencing the constant damping, as such, this behavior can said to be general in both the two systems. To be more consistent with the temporal analyses of Figs. 3.16 and 3.17, we also perform the corresponding spectral analyses.

3.3.1.2/ FREQUENCY ANALYSES

We carry out frequency analyses as a complementary approach which allows to quantize the contribution of the low frequency component in the output signal corresponding to the chronograms presented at Figs. 3.16 and 3.17. Note that the spectra reported in this section at Figs. 3.18 and 3.19 correspond to the chronograms presented at Figs. 3.16 and 3.17 respectively.

In Fig. 3.18, we present the unilateral magnitude spectrum with the zoom only near the low frequency $f_{Lf} = \frac{\omega}{2\pi}$ for the lowest damping amplitude Γ_0 =0.03. Moreover, the same five values of the perturbation amplitude H are considered as in the temporal analysis of Fig 3.16. For the smallest perturbation amplitude, namely $H = 20$, the amplitude of the magnitude spectrum $2|X(f = f_{Lf})|$ at the low frequency $f_{Lf} = \frac{\omega}{2\pi}$ is weak as shown in Fig 3.18(a). As the perturbation amplitude increases to $H = 220$ in Fig 3.18(b), the amplitude of the spectrum at the low frequency $f_{Lf} = \frac{\omega}{2\pi}$

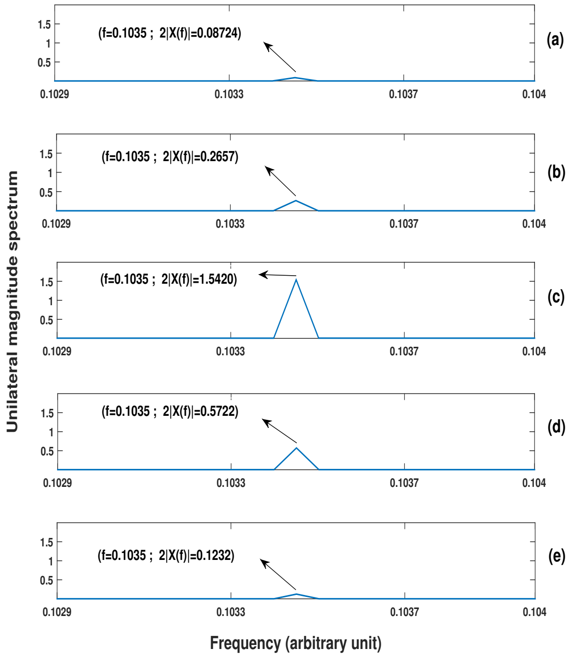

Figure 3.18: Unilateral magnitude spectra corresponding to the time series of Fig. 3.16. From top to bottom: (a) $H = 20$, (b) $H = 220$, (c) $H = 245$, (d) $H = 300$ and (e) $H = 400$. Parameters: $m = 1$, Γ_0 =0.03, λ =2.4, ϕ =0.2, $k = 1$, $\Phi_0 = 1$, G =0.05, ω =0.65, $\Omega = 13$.

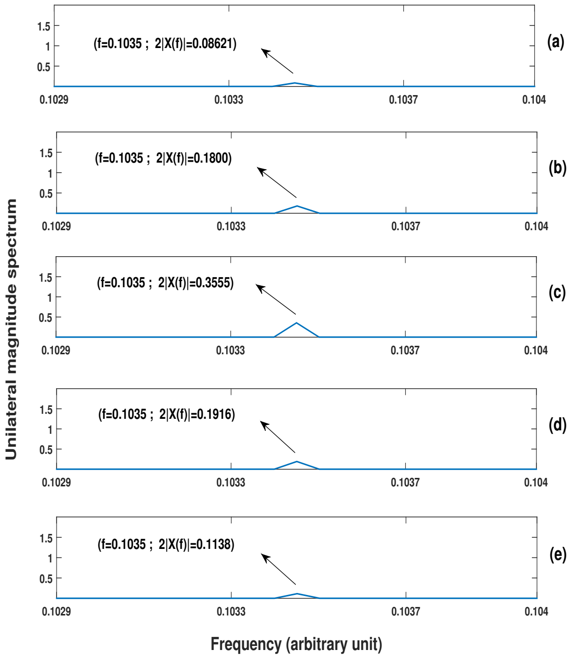

Figure 3.19: Unilateral magnitude spectra corresponding to the time series of Fig. 3.17. From top to bottom: (a) $H = 20$, (b) $H = 200$, (c) $H = 280$, (d) $H = 340$ and (e) $H = 400$. Parameters: $m = 1$, Γ_0 =0.27, λ =2.4, ϕ =0.2, $k = 1$, $\Phi_0 = 1$, G =0.05, ω =0.65, $\Omega = 13$.

also increases. However, the amplitude of the spectrum at the low frequency appears more evidently observable for the intermediate value of the perturbation amplitude $H = 245$, as shown in Fig 3.18(c). Eventually, the amplitude of the magnitude spectrum at the low frequency becomes weak again for the larger values of the perturbation amplitude, as displayed in Fig 3.18(d) and Fig 3.18(e) when $H = 300$ and $H = 400$ respectively. Therefore, the spectral analyses carried out at Fig. 3.18 confirm the observation of VR phenomenon revealed by the chronograms of Fig 3.16.

In the case when the nonlinear damping amplitude increases to Γ_0 =0.27, the spectral analysis is presented at Fig. 3.19. Unlike in the corresponding temporal analyses of Fig. 3.17, the influence of increasing the perturbation amplitude H is better perceived in the corresponding spectral analyses of Fig. 3.19. It is also obvious from Fig. 3.19(c) that, the amplitude of the spectrum at the low frequency is best pronounced for an intermediate perturbation amplitude, below and beyond which the response is lowered.

Having going far on the study of the temporal and spectral responses of our nonlinear dissipative system, next we pay attention to the influence of nonlinear dissipation parameters; Γ_0, λ and ϕ on VR. Emergence of VR effect can be revealed using the classical quantification tool defined by eq. (3.9) corresponding to the linear response Q. Indeed, the linear response Q is the amplitude of the unilateral magnitude spectrum $2|X(f_{Lf})|$ at the low frequency $f_{Lf} = \dfrac{\omega}{2\pi}$ normalized by the amplitude of the low frequency input signal G.

3.3.2/ CONTROL OF VR BY NONLINEAR DAMPING PARAMETERS

In this section, using the classical linear response Q, we conduct preliminary numerical investigations for a fix value of the particle mass $m = 1$, to study how VR phenomenon is controlled by the nonlinear dissipation parameters: damping amplitude Γ_0, frictional inhomogeneity λ and the phase ϕ between nonlinear damping and periodic potential. This preliminary study will constitute a reference to investigate the impact of the particle mass m on the occurrence of VR.

3.3.2.1/ CONTROL OF VR BY THE NONLINEAR DAMPING AMPLITUDE Γ_0

The study of the impact of nonlinear damping parameters on VR was initiated by Roy-Layinde *et al* [158]. However, their study was silent on the possible effect of nonlinear damping amplitude Γ_0 on VR. In this part, to complement the work of Roy-Layinde *et al* [158], we show how the damping amplitude Γ_0 affects VR, while the other dissipation parameters remain the same as those of Sec. 3.3.1, namely, λ =2.4, ϕ =0.2 and $k = 1$.

Fig. 3.20 depicts the linear response Q as a function of the perturbation amplitude H for different values of the nonlinear damping amplitude Γ_0. Here, increasing the perturbation amplitude H, we obtain multiple resonances, where the first resonance corresponds to the global maximum attained

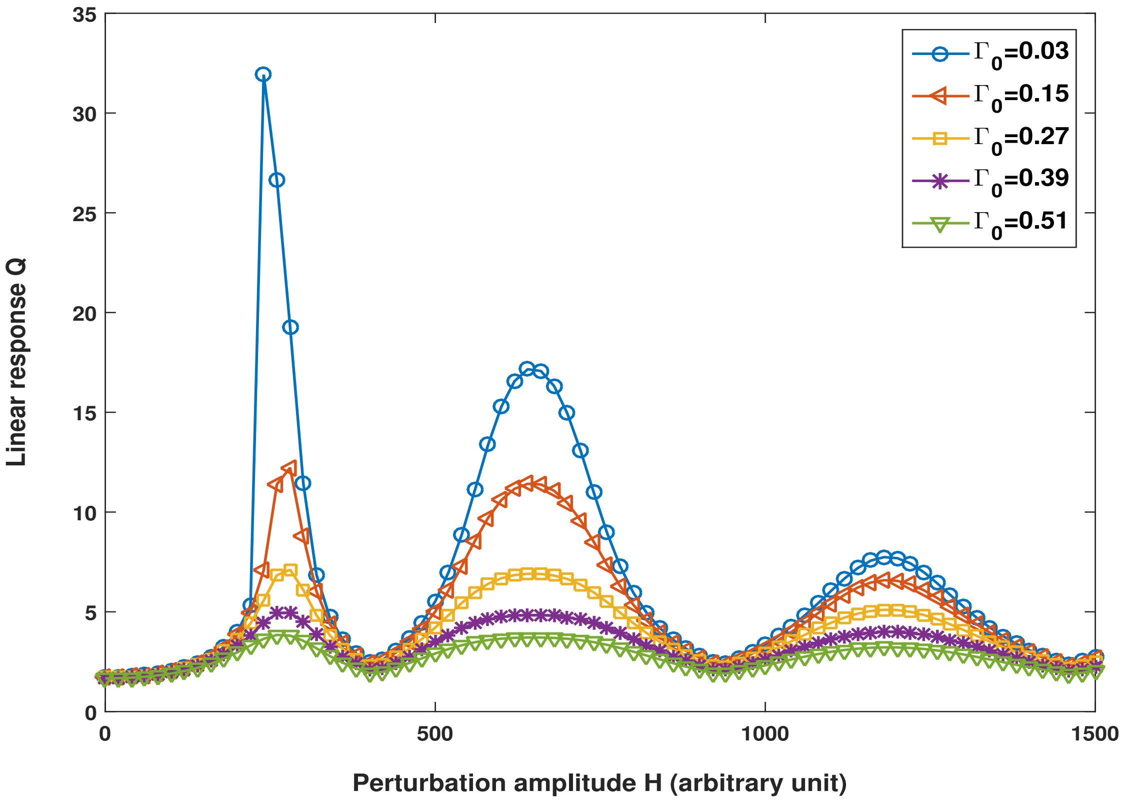

Figure 3.20: Control of VR with the nonlinear damping amplitude Γ_0 of the space-dependent damping coefficient $\Gamma(x)$. Parameters: $m = 1$, λ =2.4, ϕ =0.2, $k = 1$, $\Phi_0 = 1$, G =0.05, ω =0.65, $\Omega = 13$.

for an intermediate value of the perturbation amplitude H. For each value of the damping amplitude Γ_0, the local maxima decrease as the perturbation amplitude H increases. As well, it can be observed from Fig. 3.20 that reducing the nonlinear damping amplitude Γ_0 enhances the detection of the low frequency signal since the achieved maxima are greater for weak values of the damping amplitude Γ_0.

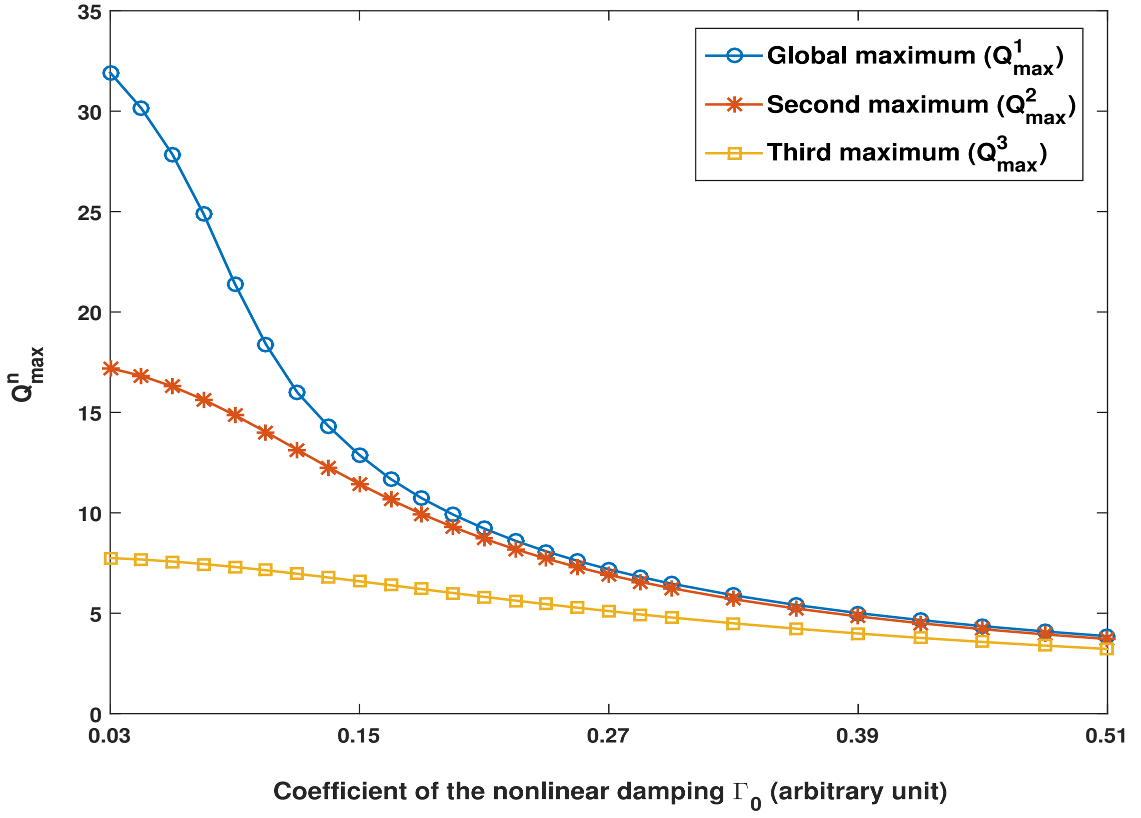

Figure 3.21: Dependence of the local maxima Q^n_{max} of Fig. 3.20 versus the nonlinear damping amplitude Γ_0. Q^n_{max} donates the amplitude of the local maxima number n. Parameters: $m = 1$, λ =2.4, ϕ =0.2, $k = 1$, $\Phi_0 = 1$, G =0.05, ω =0.65, $\Omega = 13$.

Comparing the result of Fig. 3.20 with the corresponding result for the case of constant damping in Fig. 3.12, one can conclude that including the nonlinearity in the system's damping is interesting because it enhances the response Q of the system. Indeed, the responses for the case of the nonlinear damping in Fig. 3.20 are better than those for the case of the constant damping presented at Fig. 3.12.

Lastly, Fig. 3.21 shows how the nonlinear damping amplitude Γ_0 affects the maximum amplitude of the local, second and third resonances of the linear response presented at Fig. 3.20. The results of Fig. 3.21 implies that varying the nonlinear damping is more significant for smaller values of the damping amplitude Γ_0 since for larger values of the nonlinear damping amplitude Γ_0, the response of all the maxima became less pronounced and approaches the same value.

3.3.2.2/ CONTROL OF VR BY THE PHASE DIFFERENCE ϕ BETWEEN THE NONLINEAR DAMPING AND THE PERIODIC POTENTIAL

The parameter ϕ was reported to have influenced the occurrence of VR by Roy-Layinde *et al* [158]. However, as they did not discuss the possibility for the phase ϕ to maximize VR, we addressed this particular point in this section. It may be recalled that, ϕ is the phase difference between the nonlinear damping $\Gamma(x)$ and the periodic potential $\Phi(x)$.

We carry out the study of the linear response Q versus the perturbation amplitude H, for different values of the phase ϕ. Our analyses in Fig. 3.22 reveal the same behavior as in Fig. 3.20 that is, varying the perturbation amplitude H, we obtain multiple resonances for each value of the phase ϕ, the first resonance gives the global maximum, followed by local maxima which decrease as the perturbation amplitude H increases. Note that, varying the phase ϕ enhances the performance of the system and the maximum response is obtained for the optimal value of the phase $\phi = \frac{\pi}{2}$. Indeed, beyond the optimal value $\phi = \frac{\pi}{2}$, for example for ϕ =2.1, the resonances of the linear response Q are less pronounced, as can be seen from Fig. 3.22.

Presented at Fig. 3.23 is the evolution of the local maxima Q^n_{max} of the linear response Q as a function of the phase ϕ, for the global, second and third maxima of the multiresonance curve

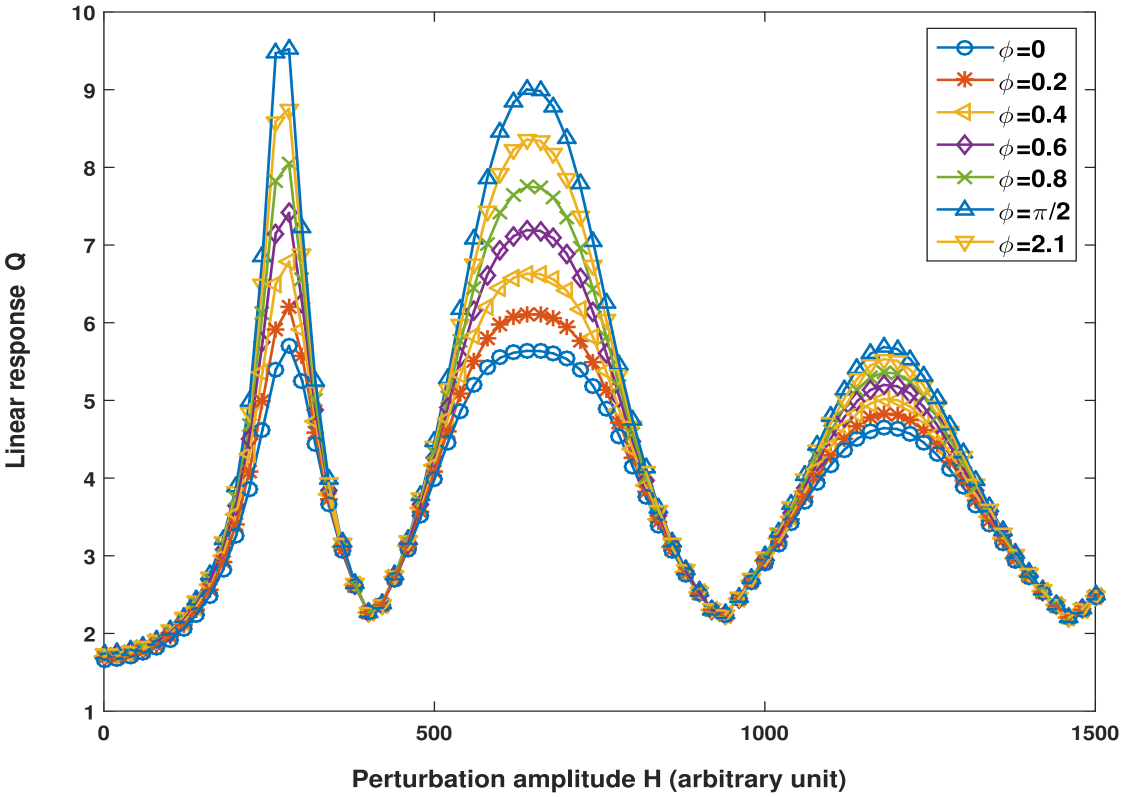

Figure 3.22: Control of VR by the phase ϕ of the space-dependent dissipation $\Gamma(x)$. Parameters taken as: $m = 1$, Γ_0 =0.27, $\lambda = 1$, $k = 1$, $\Phi_0 = 1$, G =0.05, ω =0.65, $\Omega = 13$.

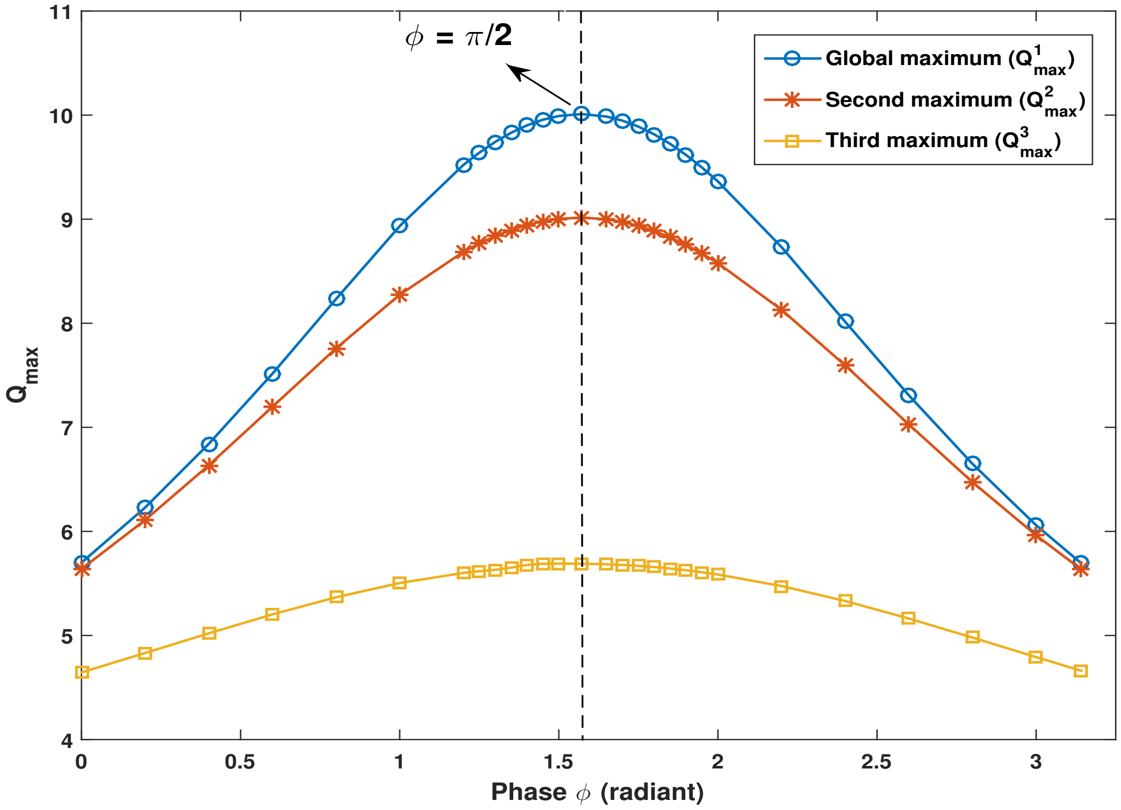

Figure 3.23: VR enhancement by the phase ϕ of the nonlinear damping $\Gamma(x)$. The three first local maxima Q^n_{max} of the resonance curves of Fig. 3.22, are plotted versus the phase ϕ. Parameters are: $m = 1$, Γ_0 =0.27, $\lambda = 1$, $k = 1$, $\Phi_0 = 1$, G =0.05, ω =0.65, $\Omega = 13$.

($n = 1$, 2 and 3) of Fig. 3.22. It appears from Fig. 3.23 that the largest resonances are obtained when the phase ϕ is optimally tuned to $\phi = \frac{\pi}{2} + 2\pi k$, with k being an integer.

In fact, when $\phi = \frac{\pi}{2}$, the *sine* function of the nonlinear damping term $\sin(kx + \frac{\pi}{2})$ in eq. (3.5) reduces to $\cos kx$ and it became perfectly in phase with the *cosine* function of the periodic potential defined by eq. (3.3). This implies that the maximum response is achieved when the modulation of the nonlinear damping force $\Gamma(x)$ and that of the periodic potential $\Phi(x)$ are in phase with each other.

3.3.2.3/ CONTROL OF VR BY THE FRICTIONAL INHOMOGENEITY λ

In this subsection, we briefly recall the effect of the frictional inhomogeneity λ on VR phenomenon. Indeed, it will provide a reference for our next study devoted to the influence of the particle mass m. The resonance curves of Fig. 3.24 summarized the behavior of the linear response Q as a function of the perturbation amplitude H for different values of the frictional inhomogeneity λ. Multiple resonances are once again observed for each value of λ, the first resonance corresponding to the global maximum which is obtained for an intermediate perturbation amplitude H. Moreover, increasing λ enhances the detection of the low frequency component of the signal. From the

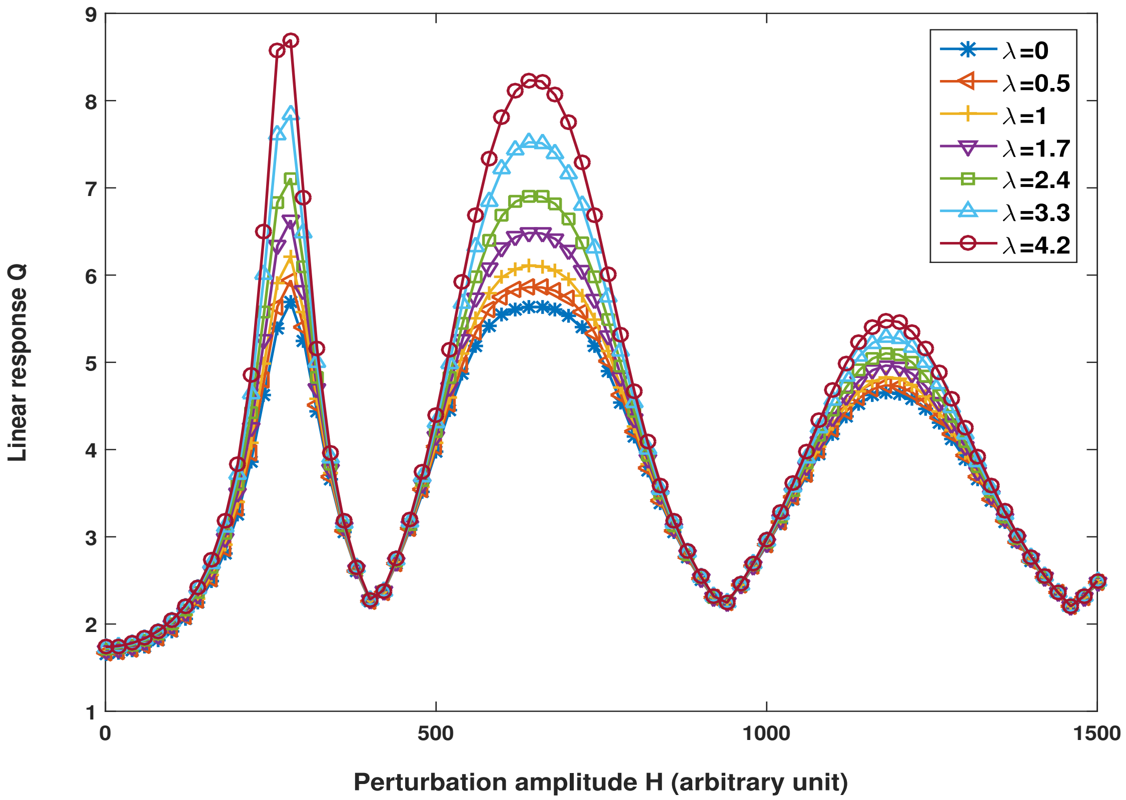

Figure 3.24: Control of VR with the modulation strength λ of the space-dependent dissipation $\Gamma(x)$. Parameters: $m = 1$, Γ_0 =0.27, ϕ =0.2, $k = 1$, $\Phi_0 = 1$, G =0.05, ω =0.65, $\Omega = 13$.

nonlinear damping coefficient given by eq. (3.5), we can interpret that the curve for $\lambda = 0$ in Fig. 3.24 corresponds to the case of constant damping which was reported in our previous studies of VR and also by Rajasekar *et al* [149].

As these typical vibrational multiresonance signatures were shown by Roy-Layinde *et al* in the case of a unitary particle mass [158], one may wonder if these signatures can persist for particles of different mass or if other behaviors may appear. This constitutes the subject of the next section.

3.3.3/ COMBINED EFFECT OF THE PARTICLE MASS m AND THE NONLINEAR DISSIPATION PARAMETERS ON THE VR OCCURRENCE

As with the previous case of the constant damping, depending on the mass of the particle, our numerical investigations for the case of nonlinear damping also reveal two different behaviors. Fig. 3.25 highlights these two cases for different values of the damping amplitude Γ_0 and specific mass values, more precisely $m = 1$ and m =2.4.

At Fig. 3.25(a) which corresponds to $m = 1$, the system's performance can be optimized by increasing the perturbation amplitude H and the maximum response is obtained for an intermediate value of the perturbation. By contrast, for the case reported at Fig. 3.25(b), and corresponding

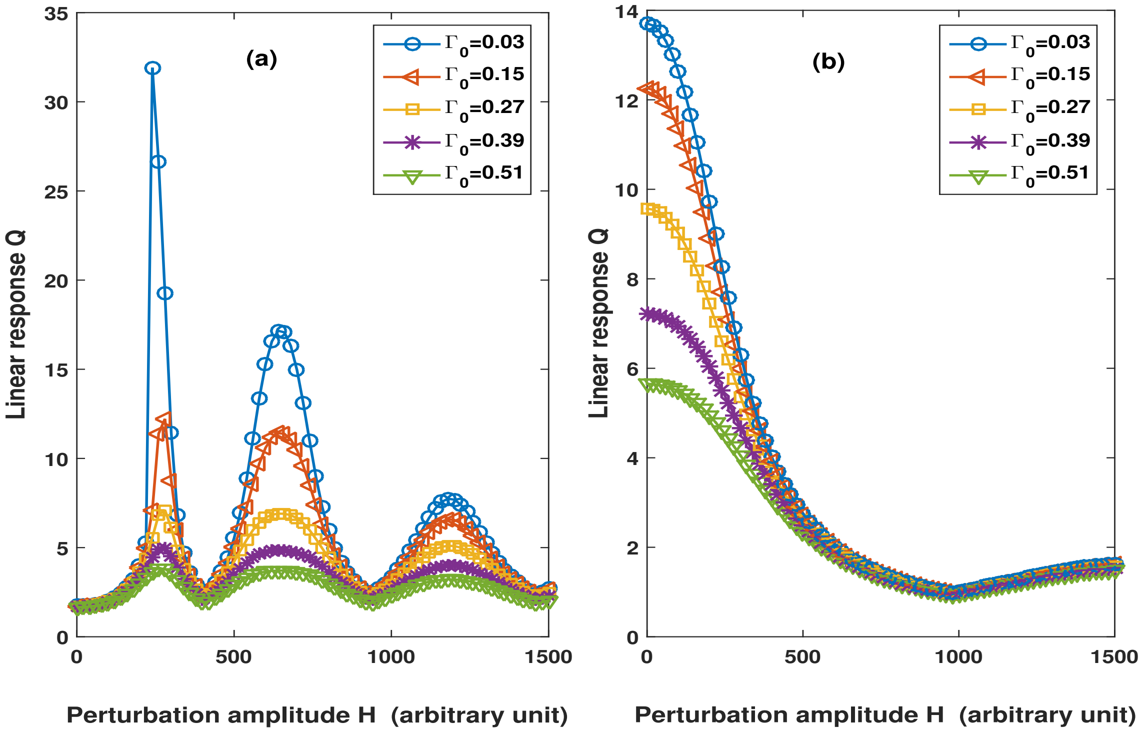

Figure 3.25: System's two different observed behaviors due to the change of the particle mass m. (a) $m = 1$, VR signature: A high frequency perturbation enhances the detection of the low frequency. (b) m =2.4, no enhancement of the low frequency detection. Parameters: λ =2.4, ϕ =0.2, $k = 1$, $\Phi_0 = 1$, G =0.05, ω =0.65, $\Omega = 13$.

to m =2.4, increasing the perturbation amplitude H can not optimize the system's response Q. Indeed, for m =2.4, the response Q of the system at $H = 0$ is the maximum response with the local maxima decreasing as the perturbation amplitude increasing. Note that VR phenomenon fails to exist in the case m =2.4 because, the maximum response amplitude is obtained without the perturbation, that is when $H = 0$.

Based on these two behaviors reported at Fig. 3.25, we perform the same study for different values of the mass below and above $m = 1$. For each value of the mass m, to identify whether the perturbation can lead to an enhancement of the low frequency detection or not, we use the indicator defined by eq. (3.11) in Sec. 3.2.4, namely Q^*_{max}. The indicator allows to classify the behavior belonging to each particle mass. Q^*_{max} is the ratio of the maximum response amplitude Q_{max} to the response amplitude obtained without the high frequency perturbation, namely when $H = 0$.

In the case of varying the amplitude of the nonlinear damping Γ_0, we present Q^*_{max} versus the particle mass m in Fig. 3.26. The curves presented in Fig. 3.26 reveal a critical value m^* of the mass around which we obtained the change of behavior, whatever the value of Γ_0. This value has been precisely determined and is equal to m^* =2.375. The first behavior occurs for particle masses below the critical mass m^*. For such particles, since Q^*_{max} exceeds 1, VR effect can be observed. By contrast, for particle masses beyond m^*, $Q^*_{max} = 1$ which indicates that VR ceases to exist.

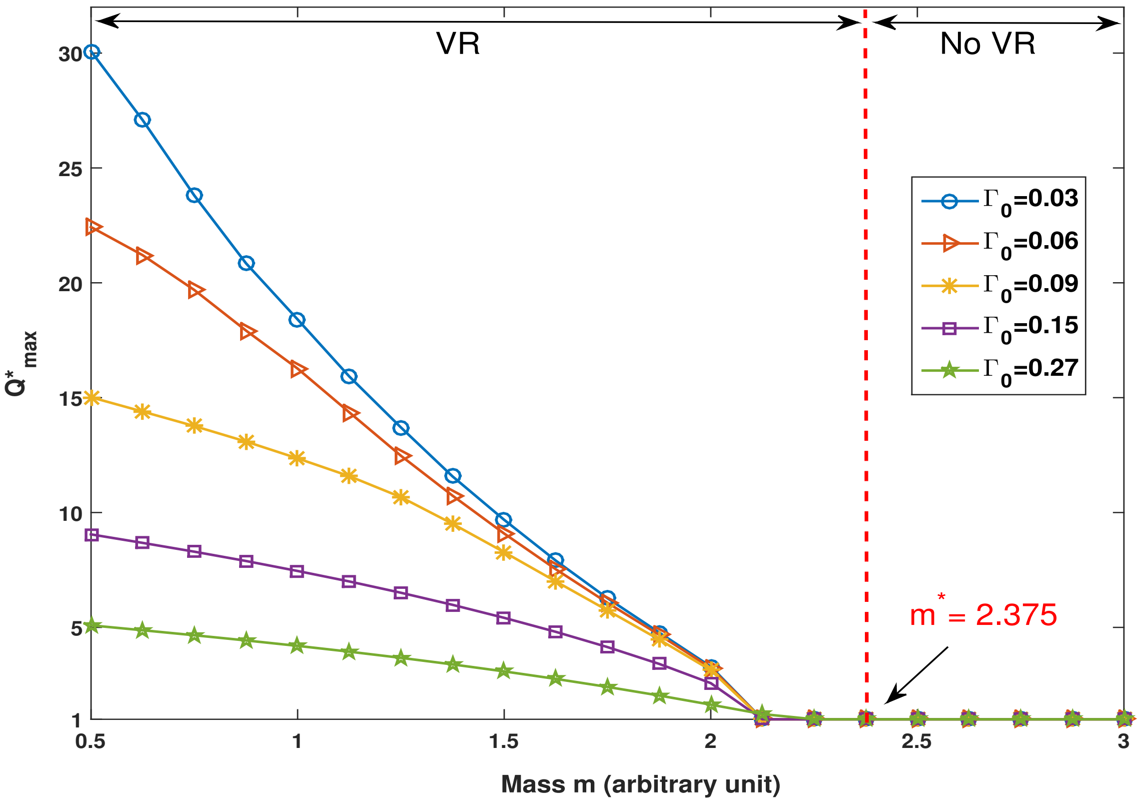

Figure 3.26: Selective response behavior controlled by the mass m of the particle. Summary of the system's two behaviors for different values of the nonlinear damping amplitude Γ_0. Values of mass m that correspond to $Q^*_{max} = 1$ define the region where VR ceases to exist whereas those that correspond to $Q^*_{max} > 1$ match the existence of VR. Parameters: $\lambda =$2.4, $\phi =$0.2, $k = 1$, $\Phi_0 = 1$, $G =$0.05, $\omega =$0.65, $\Omega = 13$.

Lastly, as previously shown, Fig. 3.26 also confirms that smaller value of Γ_0 yields the maximum response.

Consequently, particles with mass below m^* will experience VR, whereas for particles with a mass beyond m^*, no improvement of the system response can be expected by perturbing the system with a high frequency perturbation.

In a particular case of varying the phase ϕ, we also study Q^*_{max} as a function of the particle mass m at Fig. 3.27. For the parameter settings of Fig. 3.27, the critical mass m^* beyond which VR ceases to exist does not depend on the phase ϕ. Indeed, we have precisely measured this value as $m^* =$2.375. Lastly, we can also deduce from Fig. 3.27 that varying the phase ϕ improves the performance of the system, but the particular value $\phi = \frac{\pi}{2}$ gives the maximum response, as reported in the earlier preliminary study.

Similarly, at Fig. 3.28, we study how Q^*_{max} evolves versus the mass m of the particle for different values of the frictional inhomogeneity λ. There also exist a critical mass m^* below which VR occurs whatever the value of the frictional inhomogeneity λ. This critical mass m^* is determined to be invariably the same as the one obtained in the later cases of varying Γ_0 and ϕ, that is $m^* =$2.375. Moreover, we note that the maximum response amplitude is obtained for larger values of λ.

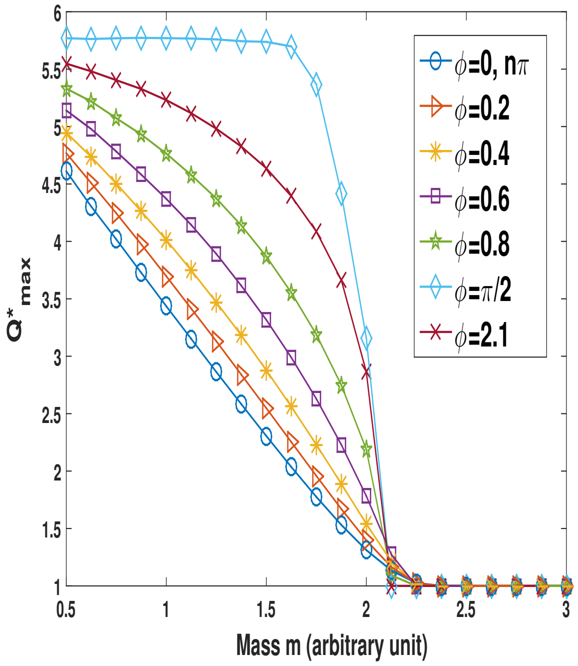

Figure 3.27: Selective response behavior controlled by the mass m of the particle for different values of the phase ϕ. Parameters: Γ_0 =0.27, $\lambda = 1$, $k = 1$, $\Phi_0 = 1$, G =0.05, ω =0.65, $\Omega = 13$.

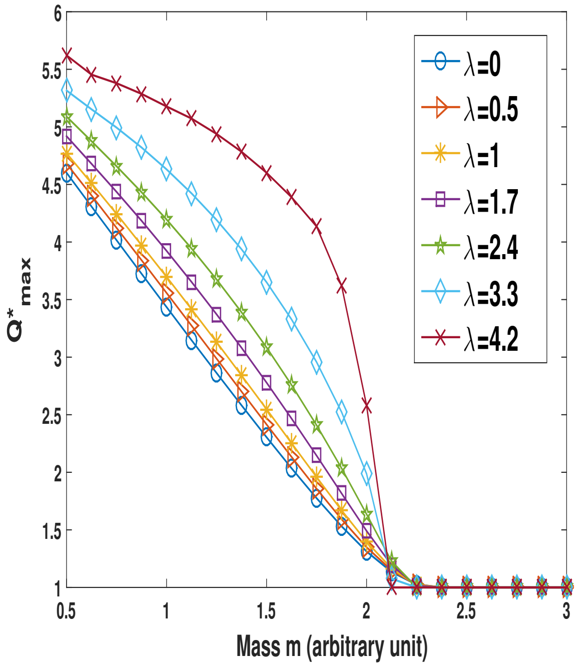

Figure 3.28: Selective response behavior controlled by the mass m of the particle for different values of the modulation strength λ. Parameters of the system: Γ_0 =0.27, ϕ =0.2, $k = 1$, $\Phi_0 = 1$, G =0.05, ω =0.65, $\Omega = 13$.

In summary, the simulation results presented at Figs. 3.26, 3.27 and 3.28 demonstrate that for all the nonlinear dissipation parameters considered, there exists a critical value of mass m^* below which the phenomenon of VR can be observed and beyond which no enhancement can be obtained by perturbing the system.

3.4/ CONCLUSION

In this chapter, we have considered the motion of a particle experiencing a periodic potential which is driven by a bichromatic excitation in two different cases of damping; constant damping and a space-dependent nonlinear damping. More precisely, our research has mainly addressed VR occurrence when the particle mass and the damping parameters are jointly considered as control parameters.

To accomplish these analyses, it was first useful to briefly precise the setting of the system and to introduce the classical tools necessary to highlight VR. In view of these, in both the two cases of the damping, we have therefore performed preliminary studies restricted to the case of a unitary particle mass.

In the first case of constant damping and for the unitary particle mass, we have numerically revealed by using temporal and spectral analyses that, VR effect exists in the system. We highlighted that VR can be controlled by the constant damping amplitude Γ_0' and that the best responses can be obtained for the smaller values of the constant damping amplitude $\Gamma_0^{'}$. Moreover, when the perturbation amplitude H evolves in a wide range, the obtained responses have exhibited vibrational multiresonance signature. More precisely, among the multiple observed resonances, the first resonance corresponds to the greatest one, while the magnitude of the next resonances decreases as the perturbation amplitude H keeps increasing.

Subsequently, we studied the combined impact of the particle mass m and the constant damping amplitude $\Gamma_0^{'}$ on VR occurrence. We demonstrated that the system exhibits two different behaviors that depend on the particle mass m, one of which VR phenomenon ceased to exist. The first behavior, which corresponds to the instance of the unitary particle mass, revealed that the system's response can be optimized by an appropriate increase of the perturbation amplitude H while in the latter, the system's maximum response is obtained without the perturbation, that is when $H = 0$. This change of behavior neither depends on the constant damping amplitude $\Gamma_0^{'}$ but on the variation of the particle mass m. Therefore, we then proposed an indicator, namely Q^*_{max}, which enabled us to classify the behavior belonging to each considered particle mass m. Indeed, for all values of the constant damping amplitude $\Gamma_0^{'}$, we have identified a critical value of mass m^* below which VR can be observed and beyond which it ceased to exist.

For the case of a system with nonlinear dissipation, the space-dependent nonlinear dissipation we have considered was first introduced by Roy-Layinde *et al*. This nonlinear dissipation can be tuned by its strength λ, its whole amplitude Γ_0 and its phase difference ϕ with the periodic potential of the system. We have first conducted a preliminary study for a unitary particle mass from the perspectives of temporal and frequency analyses to verify VR existence in the system. As previously pointed by Roy-Layinde *et al* [158], we have numerically verified that nonlinear dissipation parameters λ and ϕ allow to control VR. Indeed, as in the previous case of the constant damping, we obtained response curves that exhibited multiple resonances: the first resonance corresponds to the global maximum which is achieved for an intermediate value of the perturbation amplitude H while the other local maxima decrease as the perturbation amplitude increases. However, we highlighted that an optimal value of the phase difference between the potential and the nonlinear dissipation maximizes the VR effect. This optimal value of the phase ($\phi = \frac{\pi}{2}$) corresponds to the case when the modulation of the nonlinear damping and the modulation of the periodic potential are in phase with each other. In addition, we have enlarged this study by analyzing the impact of the dissipation amplitude Γ_0 which also allowed to control VR. In particular, we found that decreasing the amplitude of the nonlinear damping coefficient Γ_0 enhances the response Q of the system.

After these preparatory studies, our main results in this part concerned the joint effect of the nonlinear dissipation parameters and the particle mass m on VR occurrence. Especially, as in the case of the constant damping, we demonstrated that the system exhibits two different behaviors that depend on the particle mass m, one of which VR phenomenon ceased to exist.

By comparison, we understood that the responses achieved by the system experiencing nonlinear damping amplitude Γ_0 are better than those obtained for the case of the linear damping amplitude

$\Gamma_0^{'}$. Moreover, unlike linear damping, nonlinear damping allowed to control the response of the system from its multiple parameters: modulation strength λ and the phase difference ϕ between damping and potential.

We suspect that our finding concerning the existence of a critical mass m^* beyond which VR ceased to exist could be extended to other mechanical systems exhibiting different kinds of potential. Indeed, the depth and location of the potential wells [210], shape of the harmonically trapped potential [167] and the shape of an asymmetrical deformable potential were recently reported to have a significant impact on the occurrence of VR [211]. Moreover, it is interesting to note that the existence of the critical mass m^*, which is observed in our system with both constant and nonlinear damping, could allow to separate particles with different mass.

In the context of the so called ratchet effect, particle's trajectory was also studied in inhomogeneous systems experiencing symmetric periodic potential [180–184]. Frictional inhomogeneity λ and initial phase of the external periodic forcing ϕ_0 were reported to have an effect on the sensible generation of ratchet current for unitary particle masses [181]. We suggest that the phase difference ϕ, nonlinear damping amplitude Γ_0 and most especially the particle mass m may have significant impact on the directed particle transport. That is why the work presented in this chapter could be relevant in the context of ratchet effect.

4

VIBRATIONAL RESONANCE (VR) AND GHOST-VIBRATIONAL RESONANCE (GVR) OCCURRENCE IN CHUA'S CIRCUIT MODEL WITH SPECIFIC NONLINEARITIES

Contents

4.1 Introduction . . . 50

4.2 Description of the Chua's model . . . 50

4.2.1 The two considered nonlinearities of order n . . . 51

4.2.2 Input perturbed excitation $e_p(t)$ . . . 54

4.2.3 Numerical procedure . . . 55

4.3 Vibrational resonance occurrence . . . 55

4.3.1 Temporal analysis . . . 56

4.3.2 Frequency analysis . . . 57

4.3.3 Linear response analysis . . . 58

4.3.4 Analysis by phase portraits . . . 64

4.4 Ghost-vibrational resonance . . . 67

4.5 Conclusion . . . 73

In this chapter, we numerically investigate the dynamics of a multistable Chua's circuit model driven by an external perturbed excitation. We mainly study the impact of the system's nonlinearity, which provides the system's multistability, on the occurrence of Vibrational Resonance (VR) and Ghost-Vibrational Resonance (GVR) phenomena. Especially, we compare the well known dynamics obtained with the classical sawtooth nonlinearity [152] and the one produced with a truncated sinusoidal nonlinearity.

4.1/ INTRODUCTION

The nature of the nonlinearity have significant impact on the dynamical response of nonlinear systems. For instance, a multistable nonlinearity has proven to have applications in image processing [170]. In particular, Chua's circuit model, which was first introduced to study chaotic behavior in electronic circuits, is based on a multistable nonlinearity [212]. This model was used to study many nonlinear properties and phenomena such as the existence of multi-scroll chaotic attractors [172, 213], bifurcation analysis [171, 214], Stochastic Resonance (SR) [173], Vibrational Resonance (VR) [151, 152] and Ghost-Vibrational Resonance (GVR) [152].

Recently, Chua's circuit model was used with a multistable sawtooth force as form of nonlinearity to study the occurrence of VR and GVR [152]. However, we must admit that the dynamics of Chua's circuit model in the context of nonlinear resonances was not explored with a truncated sinusoidal force, which is also multistable. Indeed, nonlinear systems with the truncated sinusoidal force have revealed applications in image processing [170] and have also enabled information storage in memristors [174–176]. Owing to these promising applications, it is of crucial interest to characterize the impact of a truncated sinusoidal nonlinearity on VR and GVR occurrence. In this chapter, we study how a truncated sinusoidal force affects the occurrence of VR and GVR in a modified Chua's circuit model. Moreover, we especially compare the dynamics obtained with the well known classical sawtooth nonlinearity [152] and the one produced with our proposed truncated sinusoidal nonlinearity.

The subsequent sections of this chapter are arranged in the following order. Firstly, the system under consideration is described in Section 4.2 with its setup and the numerical procedure used throughout the chapter. Next, the analyses of the VR and GVR are presented in Sections 4.3 and 4.4 respectively for each considered nonlinearity, that is the sawtooth function and our propose truncated sinusoidal function. Lastly, section 4.5 is devoted to the conclusion and outlooks of this chapter.

4.2/ DESCRIPTION OF THE CHUA'S MODEL

Chua's circuit was first invented in 1983 by Chua to study the existence of double-scroll chaotic attractors [212]. These attractors were numerically confirmed in 1984 by Matsumotu [215] and the chaotic behavior of the circuit was experimentally shown one year later [216]. The modification of the initial nonlinearity of the system has also attracted attention since it has allowed to generate multi-scroll attractors [172]. In this chapter, we also focus on the impact of the nonlinearity on the dynamics of the following modified Chua's circuit model:

$$\begin{aligned}\frac{dx}{dt} &= \alpha y + \frac{d\Phi_n(x,\alpha)}{dx} + e_p(t) \\ \frac{dy}{dt} &= x - y + z \\ \frac{dz}{dt} &= -\beta y.\end{aligned} \tag{4.1}$$

This three dimensional system describes the evolution of three variables x, y and z, when it is driven by an input perturbed excitation $e_p(t)$. The term $\Phi_n(x,\alpha)$ represents the potential which provides the multistability and whose derivative will refer to a nonlinearity of order n in the whole chapter. Moreover, α is a constant parameter which also adjusts the height of the potential barrier. The corresponding nonlinear force $F_n(x,\alpha)$ is derived from the potential $\Phi_n(x,\alpha)$ by the relation

$$F_n(x,\alpha) = -\frac{d\Phi_n(x,\alpha)}{dx}. \tag{4.2}$$

4.2.1/ THE TWO CONSIDERED NONLINEARITIES OF ORDER n

The most crucial part of the Chua's circuit model defined by the set of eqs. (4.1) is the nonlinear force $F_n(x,\alpha)$ due to its significant impact on the dynamical response of the system. Indeed, variety of dynamical behaviors were studied while considering different nonlinear forces or nonlinearities $F_n(x,\alpha)$ such as: a sigmoid force [217], a piecewise linear force [218], a discontinuous force [219], a saturated force [220] and a sawtooth force [152, 172, 173] among others.

A recent study by Abirami *et al* reported the role of a sawtooth type nonlinearity on VR and GVR occurrence in a modified Chua's circuit model [152]. This sawtooth force is redefined here with our own notations for convenience and to allow direct comparison with the truncated sinusoidal nonlinearity proposed in this chapter. The sawtooth force of order n and parameter α is then redefined by the following expression:

$$\begin{aligned}F_n(x,\alpha) = & - \alpha\Bigg\{\frac{A_0}{A}x + \left(\frac{(-1)^n+1}{2}\right)A_0\,\mathrm{sgn}(x) \\ & - A_0\sum_{j=0}^{n}\Bigg[\mathrm{sgn}\left(x+\left(2j-\left(\frac{(-1)^n-1}{2}\right)\right)A\right) \\ & + \mathrm{sgn}\left(x-\left(2j-\left(\frac{(-1)^n-1}{2}\right)\right)A\right)\Bigg]\Bigg\},\end{aligned} \tag{4.3}$$

where sgn is a sign function, n is the order of nonlinearity and the constant parameters α, A and A_0 adjust the potential barrier. The sawtooth force $F_n(x,\alpha)$ described by eq. (4.3) is presented in Fig. 4.1 with its corresponding potential $\Phi_n(x,\alpha)$ for three values of the nonlinearity order, namely

$n = 0$, $n = 1$ and $n = 2$.

The number of stable and unstable states of the potential is controlled by n. Indeed, for each value of n, we obtain $n+1$ unstable states and $n+2$ stable states, whose positions are given by

$$X^*_{h,n} = \frac{h}{4A} \quad ,$$

where h is an integer value in the interval $[-(n+1); n+1]$, while the second index n refers to the nonlinearity order. The parameter n categorizes these stability positions in two cases:

- if n is odd, the positions $X^*_{h,n} = \dfrac{h}{4A}$ correspond to stable states for even values of h and unstable states for odd values of h.
- if n is even, the positions $X^*_{h,n} = \dfrac{h}{4A}$ correspond to stable states for odd values of h and unstable states for even values of h.

Moreover, for all values of n, the potential starts at the left with a stable state at the position $X^*_{-(n+1),n} = -\dfrac{n+1}{4A}$ and ends at the right with a stable state at position $X^*_{(n+1),n} = \dfrac{n+1}{4A}$. The potential barrier $\Delta\Phi$ associated to the sawtooth force is defined by $\Delta\Phi = \dfrac{\alpha A_0}{32A^3}$ and the spacing ΔX^* between any two consecutive stable or unstable states of the potential is given as $\Delta X^* = \dfrac{1}{2A}$.

In this chapter, we introduce another multistable nonlinearity to investigate its impact on the dynamics of the modified Chua's circuit model, especially in the context of VR and GVR. We choose to

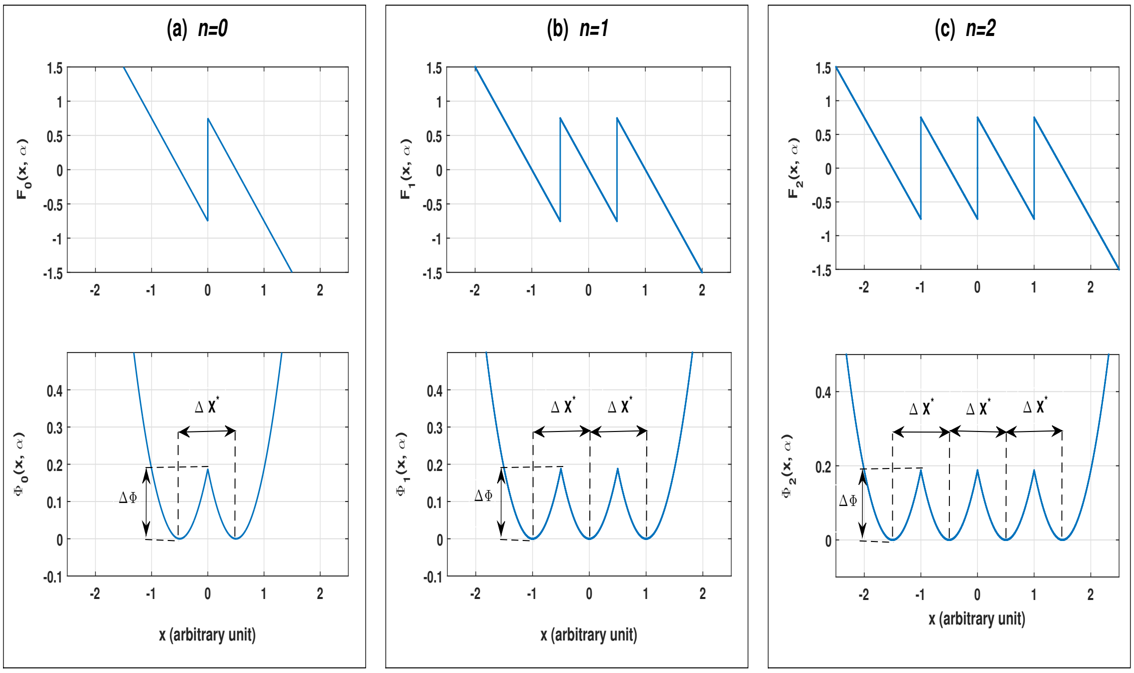

Figure 4.1: Sawtooth force $F_n(x,\alpha)$ and its corresponding potential $\Phi_n(x,\alpha)$ for three values of nonlinearity order n: (a) $n = 0$, (b) $n = 1$, (c) $n = 2$. Parameters: $\alpha = 6$, A =0.5, A_0 =0.125. ΔX^* represents the spacing between two consecutive stable or unstable states that is, the potential width and $\Delta\Phi$ is the potential barrier height.

use such nonlinearity because it can be implemented in electronic devices [221]. More precisely, we propose a truncated sinusoidal force which is expressed as:

$$F_n(x,\alpha) = \begin{cases} -\quad 2\pi\alpha V_0 k^2[x+X^*_{(n+1),n}], & \text{for } x < X^*_{-(n+1),n} \\ +\quad (-1)^n\alpha V_0 k[\sin(2\pi k x)], & \text{for } X^*_{-(n+1),n} \leq x \leq X^*_{(n+1),n} \\ -\quad 2\pi\alpha V_0 k^2[x+X^*_{-(n+1),n}], & \text{for } x > X^*_{(n+1),n} \end{cases} \quad (4.4)$$

In eq. (4.4), as for the potential driven from the sawtooth force, $X^*_{-(n+1),n}$ and $X^*_{(n+1),n}$ correspond to the respective positions of the two ends of the potential associated to our truncated sinusoidal force. Moreover, the truncated sinusoidal force defined in eq. (4.4) is also multistable owing to its sinusoidal behavior. Note also that, it is truncated because the force is replaced by the tangent of the sinusoidal function at both the two ends of the force as expressed in relation (4.4). Fig. 4.2 illustrates the form of the truncated sinusoidal force $F_n(x,\alpha)$ and its corresponding potential $\Phi_n(x,\alpha)$ for the orders of nonlinearity $n=0$, $n=1$ and $n=2$. In the definition of the truncated sinusoidal force given by eq. (4.4), the parameter k accounts for the periodicity and width of the potential ΔX^*. Moreover, α and V_0 adjust the potential barrier height $\Delta\Phi$.

Similarly, n sets the number of stable and unstable states of the potential. Furthermore, this poten-

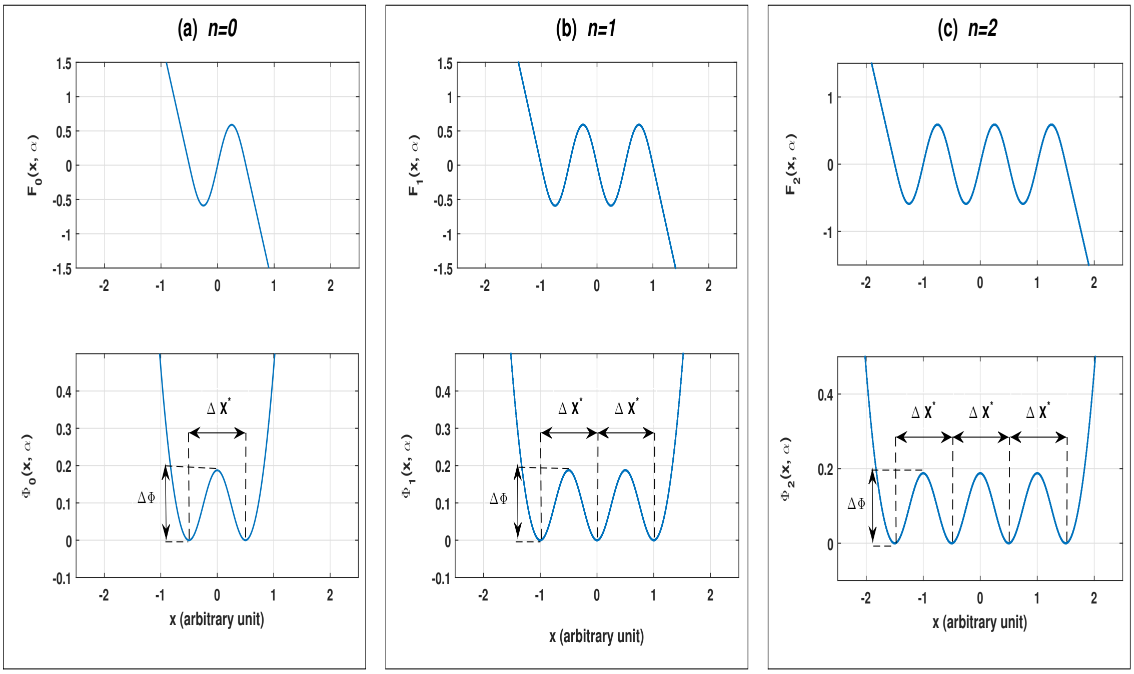

Figure 4.2: Truncated sinusoidal force $F_n(x,\alpha)$ and its corresponding potential $\Phi_n(x,\alpha)$ for three values of nonlinearity order n: (a) $n=0$, (b) $n=1$, (c) $n=2$. Parameters: $\alpha=6$, $V_0=\frac{\pi}{32}$, $k=1$. ΔX^* represents the spacing between two consecutive stable or unstable states and $\Delta\Phi$ is the potential barrier height.

tial still exhibits $n+1$ unstable states and $n+2$ stable states located at positions

$$X^*_{h,n} = \frac{h}{2k} \ ,$$

where h is an integer in the range $[-(n+1);(n+1)]$ and the second index n refers to the nonlinearity order. The stability of each of these positions depends on the parity of n:

- if n is odd, the positions $X^*_{h,n} = \frac{h}{2k}$ correspond to stable states for even values of h and unstable states for odd values of h.
- if n is even, the positions $X^*_{h,n} = \frac{h}{2k}$ correspond to stable states for odd values of h and unstable states for even values of h.

Lastly, whatever the value of n, the two ends of the potential correspond to stable states whose positions are given as $X^*_{-(n+1),n} = -\frac{(n+1)}{2k}$ and $X^*_{(n+1),n} = \frac{(n+1)}{2k}$. The barrier height of the potential driven from the truncated sinusoidal force, defined in eq. (4.4), is $\Delta\Phi = \frac{\alpha V_0}{\pi}$ and the spacing between any consecutive stable or unstable states of the truncated sinusoidal potential is given by $\Delta X^* = \frac{1}{k}$.

To compare the respective impact of the two nonlinearities defined by eqs. (4.3) and (4.4) on the system's response, it is necessary that the corresponding potentials share the same features in terms of barrier height $\Delta\Phi$ and width ΔX^*. This implies that, for our truncated sinusoidal force, the parameter V_0 must be tuned to $V_0 = \frac{\pi A_0}{32A^3}$ while the periodicity k of the truncated sinusoidal potential must be adjusted to $k = 2A$.

In the study of Abirami *et al* [152], the parameters A_0 and A of their sawtooth force were adjusted to A_0 =0.125 and A =0.5. Consequently, throughout this chapter, the parameters of our truncated sinusoidal nonlinearity are set to $V_0 = \frac{\pi}{32}$ and $k = 1$. With these parameters settings, both potentials of the two models share the same potential barrier height $\Delta\Phi$ and width ΔX^*, that is numerically $\Delta\Phi = \frac{\alpha}{32}$ and $\Delta X^* = 1$.

4.2.2/ INPUT PERTURBED EXCITATION $e_p(t)$

The system defined by eqs. (4.1) is driven by an input perturbed excitation $e_p(t)$ consisting of low frequency signal(s) $e(t)$, corrupted by an additive high frequency perturbation $p(t)$, that is,

$$e_p(t) = e(t) + p(t). \tag{4.5}$$

Here, $e(t)$ refers to the input low frequency signal(s) defined as

$$e(t) = b\cos(\omega_1 t)\delta + b\left[\cos(\omega_1 t) + \cos(\omega_2 t)\right](1-\delta), \tag{4.6}$$

where the boolean variable δ allows to select the appropriate stimuli to investigate VR ($\delta = 1$) or GVR ($\delta = 0$). In eq. (4.6), the parameter b represents the low frequency amplitude whereas ω_1 and ω_2 are two close low angular frequencies whose difference will define the ghost angular frequency ω_0. Therefore, in the whole chapter, we choose ω_1 and ω_2 so that they satisfy the classical setting to observe GVR, that is $\omega_1 = 2\omega_0$ and $\omega_2 = 3\omega_0$. Lastly, in the input perturbed excitation $e_p(t)$ defined by eq. (4.5), $p(t)$ stands for the high frequency perturbation which satisfies

$$p(t) = B\cos\Omega t. \tag{4.7}$$

In expression (4.7), B and Ω are the perturbation amplitude and its angular frequency respectively. Throughout this chapter, we consider the high angular frequency to be much greater than the low angular frequencies namely, $\Omega \gg \omega_1$ and $\Omega \gg \omega_2$, which corresponds to the commonly used condition for achieving VR and GVR phenomena.

4.2.3/ NUMERICAL PROCEDURE

To study the dynamics of the system described by the set of eqs. (4.1), it is pertinent to first detail the numerical procedure which was used by Abirami *et al* when they considered a sawtooth nonlinearity [152]. For each of the two types of nonlinearities defined by eqs. (4.3) and (4.4), taking into account zero initial conditions for all variables, namely $x(0) = y(0) = z(0) = 0$, we use a 4^{th} order Runge-Kutta algorithm in Matlab script to integrate the system of eqs. (4.1) which is driven by the input excitation of eq. (4.5). Considering first the zero perturbation case, that is $B = 0$, we perform simulations during a temporal window T which corresponds to 1000 low frequency cycles and 2^{22} total number of samples. The corresponding integrating time step is therefore $dt = (\frac{1000}{2^{22}})\frac{2\pi}{\omega_i}$, with ω_i taken according to the angular frequency to be analyzed, that is $\omega_i = \omega_1$ for the study of VR ($\delta = 1$) and $\omega_i = \omega_0$, ω_1 or ω_2 for the study of GVR ($\delta = 0$). When the perturbation amplitude B increases with step ΔB, last values of the system variables are considered as the initial conditions for the next simulation with amplitude $B + \Delta B$, that is $x(0) = x(T)$, $y(0) = y(T)$ and $z(0) = z(T)$. Lastly, the values of the output $x(t)$ corresponding to the last 500 driving cycles are considered for all computations whereas the first 500 cycles are discarded as transient.

4.3/ VIBRATIONAL RESONANCE OCCURRENCE

In order to study VR, the boolean variable δ in eq. (4.6) is set to $\delta = 1$. This reduces the input perturbed excitation $e_p(t)$ defined by eq. (4.5) to

$$e_p(t) = b\cos\omega_1 t + B\cos\Omega t. \tag{4.8}$$

In this section, we study how the multistable nonlinearities defined by eqs. (4.3) and (4.4) affect VR.

Three different analyses are presented namely: temporal, frequency and phase portraits analyses. In each of these analyses, responses of the system experiencing a truncated sinusoidal nonlinearity are compared with the responses of the system with a sawtooth nonlinearity. In this whole section, the constant parameters of the model α and β are taken as $\alpha = 6$ and $\beta = 16$. Moreover, we set the amplitude of the low frequency to b =0.1, the low angular frequency to $\omega_1 = 1$ and the perturbation angular frequency to $\Omega = 10\omega_1$.

4.3.1/ TEMPORAL ANALYSIS

In this subsection, we study how the temporal response $x(t)$ of the system experiencing the two different nonlinearities behave against the perturbation amplitude B. The time series analysis is conducted in such a way that, for each considered value of the perturbation amplitude B, we perform simulations starting from $B = 0$ with the step ΔB =0.01, saving the memory of the system each time until the chosen value of the perturbation B.

For the system experiencing the truncated sinusoidal force, we choose the perturbation amplitudes B =1.5, 4.13 and 6.8, to obtain the chronograms of Fig. 4.3(a), 4.3(b) and 4.3(c) respectively. The temporal series of Fig. 4.3 revealed that the low frequency signal is corrupted by the high frequency perturbation in all the three cases. For the smallest perturbation amplitude, that is B =1.5 at Fig. 4.3(a), the low frequency contribution in the output signal is weak. However, for the intermediate perturbation amplitude B =4.13 at Fig. 4.3(b), the low frequency component in the output signal is best revealed. The low frequency contribution in the output signal at Fig. 4.3(c) became less pronounced as the perturbation amplitude further increases to B =6.8. This implies that when the perturbation amplitude B is optimally tuned to the intermediate value B =4.13, the enhancement of the system response to the low frequency excitation is the best. This behavior signifies the occurrence of VR phenomenon in the system experiencing the truncated sinusoidal nonlinearity.

On the other hand, for the system experiencing the sawtooth force, we consider the perturbation amplitudes B =1.5, 4.72 and 9.79, to study its temporal response as presented at Fig. 4.4(a), 4.4(b) and 4.4(c) respectively. In fact, each of the temporal responses of Fig. 4.4 also revealed low frequency signal corrupted by a high frequency perturbation. For the weakest considered perturbation amplitude B =1.5, Fig. 4.4(a) shows that the low frequency contribution in the output signal is weak. However, for the intermediate perturbation B =4.72 depicted at Fig. 4.4(b), the low frequency in the output signal is best pronounced. Lastly, Increasing the perturbation amplitude to B =9.79, the low frequency component in the output signal became weak again as shown in Fig. 4.4(c). Indeed, varying the perturbation amplitude B, the best system response at the low frequency is achieved for an intermediate perturbation, namely B =4.72 in this case. This is the signature of VR also revealed by the system experiencing a sawtooth nonlinearity.

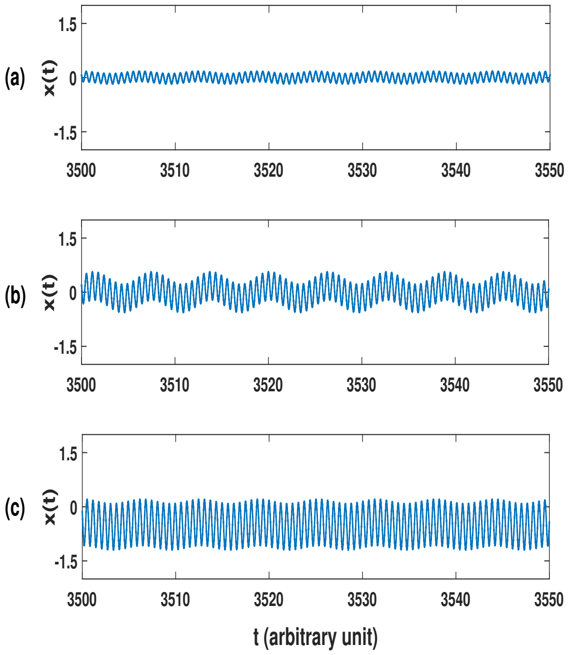

Figure 4.3: Typical time series of the Chua's model experiencing the truncated sinusoidal force defined by eq. (4.4) and driven by the excitation of eq. (4.8). The chronograms of x have been obtained by increasing the perturbation amplitude starting from $B=0$ with step ΔB =0.01 until (a) B =1.5, (b) B =4.13, (c) B =6.8. Model parameters: $n=1$, $k=1$, $V_0=\frac{\pi}{32}$, $\alpha=6$, $\beta=16$, b =0.1, $\omega_1=1$, $\Omega=10\omega_1$, numerical time step Δt =0.0015.

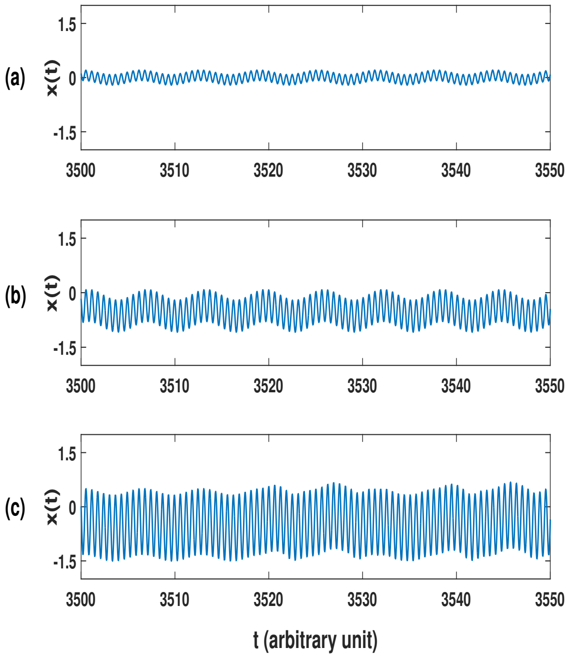

Figure 4.4: Typical time series of the Chua's model experiencing the sawtooth force defined by eq. (4.3) and driven by the excitation of eq. (4.8). The chronograms of x have been obtained by increasing the perturbation amplitude starting from $B=0$ with step ΔB =0.01 until (a) B =1.5, (b) B =4.72, (c) B =9.79. Parameters: $n=1$, A =0.5, A_0 =0.125, $\alpha=6$, $\beta=16$, b =0.1, $\omega_1=1$, $\Omega=10\omega_1$, ΔB =0.01, Δt =0.0015.

4.3.2/ FREQUENCY ANALYSIS

In this section, spectral analyses are first presented to confirm the observations made with the time series presented at Sec. 4.3.1. Afterwards, we study the impact of the two considered nonlinearities on VR occurrence by quantizing the spectral response. To better understand the time series of Figs. 4.3 and 4.4, we have computed their corresponding spectra at Figs. 4.5 and 4.6 respectively. As VR basically concerns the enhancement of a subthreshold low frequency signal by a high frequency perturbation, the unilateral magnitude spectra of Figs. 4.5 and 4.6 are presented with the zoom only near the low frequency $f_1=\frac{\omega_1}{2\pi}$ =0.1592.

The spectral responses of Fig. 4.5, which correspond to the case of the system experiencing the truncated sinusoidal force, are for the same values of the perturbation amplitude B considered to produce the chronograms of Fig. 4.3. It implies from Fig. 4.5 that, for the smallest perturbation B =1.5, the amplitude of the unilateral magnitude spectrum at the low frequency f_1 is weak. However, for the intermediate perturbation amplitude B =4.13, the amplitude of the spectrum at the low frequency f_1 is best pronounced. The spectral contribution at the low frequency f_1 is reduced again as the perturbation amplitude further increases to B =6.8. As expected, the spectral contribution at the low frequency f_1 is best pronounced for an intermediate value of the perturbation amplitude

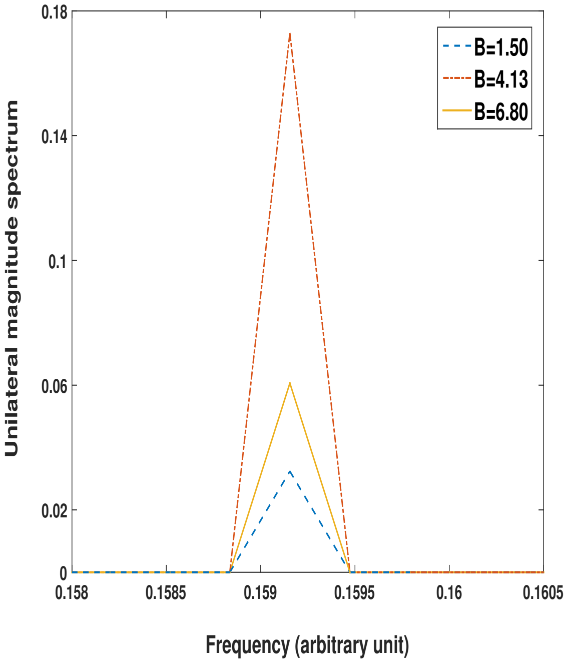

Figure 4.5: Spectral response of the system experiencing the truncated sinusoidal force corresponding to the time series of Fig. 4.3. Model parameters: $n=1$, $k=1$, $V_0=\frac{\pi}{32}$, $\alpha=6$, $\beta=16$, $b=$0.1, $\omega_1=1$, $\Omega=10\omega_1$, numerical time step $\Delta t=$0.0015.

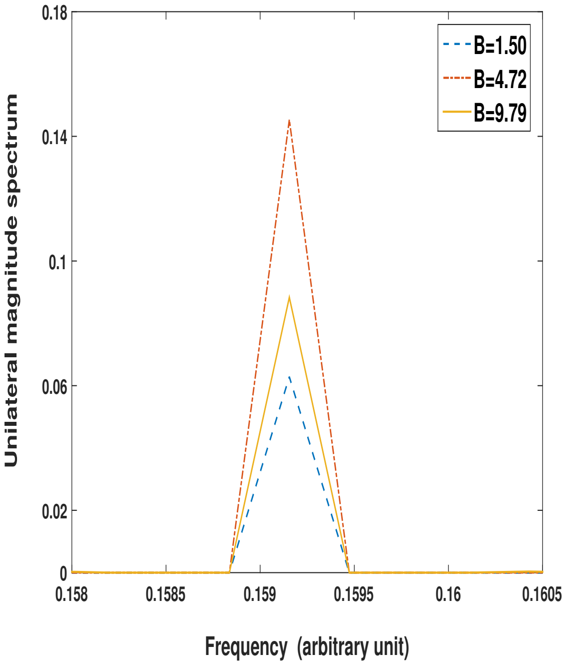

Figure 4.6: Spectral response of the system experiencing the sawtooth force corresponding to the time series of Fig. 4.4 Parameters: $n=1$, $A=$0.5, $A_0=$0.125, $\alpha=6$, $\beta=16$, $b=$0.1, $\omega_1=1$, $\Omega=10\omega_1$, $\Delta B=$0.01, $\Delta t=$0.0015.

B. This signifies VR occurrence is in agreement with the observation of the time series presented at Fig. 4.3.

Similarly, the spectral responses of Fig. 4.6, which correspond to the case of the system experiencing a sawtooth force, are for the same values of the perturbation amplitude considered to obtain the chronograms of Fig. 4.4. Analyses of Fig. 4.6 revealed that the amplitude of the spectrum at the low frequency f_1 is best pronounced for the intermediate perturbation amplitude $B=$4.72. This also agrees with the corresponding time series analyses previously presented at Fig. 4.4.

4.3.3/ LINEAR RESPONSE ANALYSIS

The time series and the spectral analyses presented so far both signified the occurrence of VR in our systems. However, in the majority of studies, VR is usually studied by quantizing the spectral response at the low frequency f_1 to compute the linear response Q previously defined by eq. (3.9) and recall hereafter:

$$Q=\frac{2|X(f_1)|}{b}. \tag{4.9}$$

In eq. (4.9), b is the amplitude of the low frequency signal at the system input while $2|X(f_1)|$ is its contribution at the system output. The definition (4.9) of the linear response Q expresses how a low frequency component in the output magnitude spectra is affected through the considered nonlinear systems by a high frequency perturbation. Therefore, through linear response Q, direct impact of a high frequency perturbation on a low frequency signal can be visualized more easily. Moreover, the analyses of the linear response Q will allow to better compare the impacts of the two proposed nonlinearities on VR occurrence.

Using the modus operandi given in Sec. 4.2.3, we integrate the system defined by the set of eqs. (4.1), first with our truncated sinusoidal force defined by eq. (4.3) and secondly, with the sawtooth force expressed by eq. (4.4). The resonance curve of Fig. 4.7 depicts the evolution of the linear response Q versus the perturbation amplitude B for the case of the system experiencing the truncated sinusoidal force with nonlinearity order $n = 1$. Here, we vary the perturbation amplitude B, first in the "forward direction", that is from $B = 0$ to $B = 20$, and then return in the "reverse direction" from $B = 20$ to $B = 0$. The resonance curves corresponding to the forward and reverse directions, for the system experiencing the truncated sinusoidal force are superimposed, as shown at Fig. 4.7. The system then follows the same path in both directions and the resonance curves reveal two resonances which correspond to the number of unstable states in the system's potential well, that is $n+1$. Increasing the perturbation amplitude B in the "forward direction", the first resonance gives the maximum response which decreases as the perturbation amplitude B keeps increasing.

In a similar way, considering the sawtooth nonlinearity with the order $n = 1$, we have obtained the

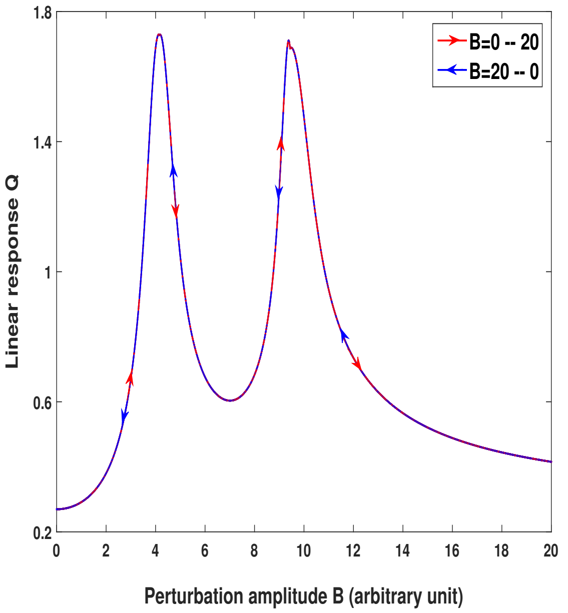

Figure 4.7: Linear response Q versus the perturbation amplitude B for a system experiencing the truncated sinusoidal force. The arrows indicate that increasing B from 0 to 20 or reducing B from 20 to 0 provide the same resonance curve. Parameters: $n = 1$, $k = 1$, $V_0 = \frac{\pi}{32}$, $\alpha = 6$, $\beta = 16$, b =0.1, $\omega_1 = 1$, $\Omega = 10\omega_1$, perturbation amplitude step ΔB =0.01, numerical time step Δt =0.0015.

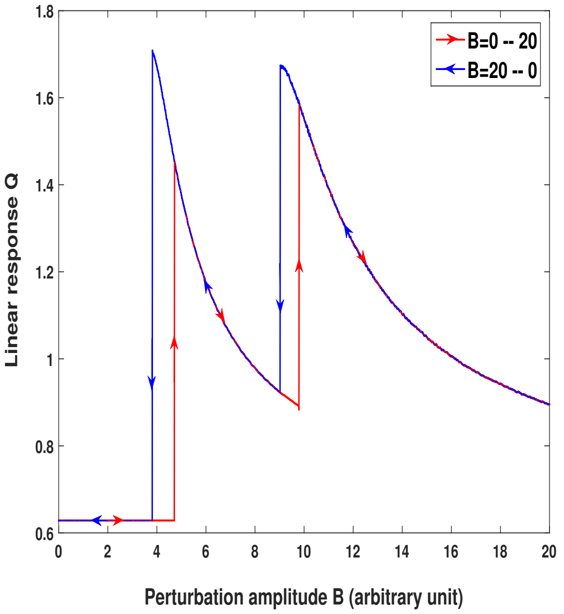

Figure 4.8: Linear response Q versus the perturbation amplitude B, for a system experiencing the sawtooth force. Our simulation results are in agreement with the one obtained by Abirami *et al* [152]. Parameters: $n = 1$, A =0.5, A_0 =0.125, $\alpha = 6$, $\beta = 16$, b =0.1, $\omega_1 = 1$, $\Omega = 10\omega_1$, ΔB =0.01, Δt =0.0015.

resonance curves of Fig. 4.8, which was first reported in the work of Abirami et al [152]. Fig. 4.8 confirms their work with our notation for the sawtooth force expressed in eq. (4.3): varying the perturbation amplitude B in the forward and returning in reverse direction, the system follows two different paths near the peak of each resonance. In the forward direction, the last resonance provides the system's maximum response contrary to the case of the truncated sinusoidal force presented in Fig. 4.7.

In comparison, the overall maximum response of our system with the truncated sinusoidal force in the forward direction is $Q^* =$1.729, achieved for the optimal perturbation amplitude $B^* =$4.10. This is better than the maximum response obtained with the sawtooth force in the forward direction, that is $Q^* =$1.587 at $B^* =$9.81. Indeed, at Fig. 4.7, the system with our truncated sinusoidal force needs smaller perturbation amplitude $B^* =$4.10 to reach its maximum response when compared to the system experiencing the sawtooth force at Fig. 4.8 which required $B^* =$9.81. Moreover, increasing the perturbation amplitude B in the forward and returning in the reverse direction, our system follows the same path at Fig. 4.7. Note that, hystereses at the breakpoints of each resonance are obtained only in the case of the system experiencing the sawtooth force as represented in Fig. 4.8. The presence of these hystereses around the jumps may be due to the discontinuities which are observed at the unstable positions of the sawtooth force in Fig. 4.1 and which does not exist for the truncated sinusoidal force of Fig. 4.2.

The nonlinearity order n controls the number of resonances obtained for both nonlinearities. Fig. 4.9(a) and 4.9(b) provide the overall resonance behavior of the system experiencing the truncated

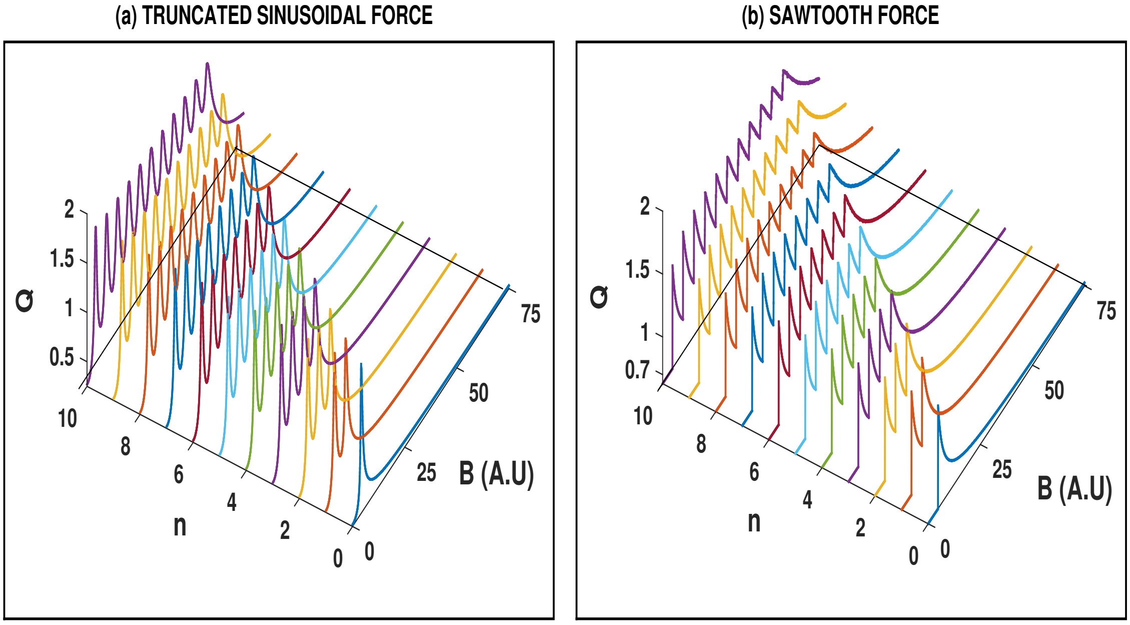
(a) TRUNCATED SINUSOIDAL FORCE

(b) SAWTOOTH FORCE

Figure 4.9: Overall resonance behavior of the system experiencing: (a) truncated sinusoidal force (b) Sawtooth force, in the perturbation amplitude B and nonlinearity order n parameters plane. The linear response Q is plotted versus B and n. Parameters: $k = 1$, $V_0 = \frac{\pi}{32}$, $A =$0.5, $A_0 =$0.125, $\alpha = 6$, $\beta = 16$, $b =$0.1, $\omega_1 = 1$, $\Omega = 10\omega_1$, $\Delta B =$0.01, $\Delta t =$0.0015.

sinusoidal force and the sawtooth force respectively. In each case of Fig. 4.9, linear response Q is presented as a function of the nonlinearity order n and the perturbation amplitude B. In fact, both Fig. 4.9(a) and 4.9(b) show that there are always $n+1$ resonances which correspond to the number of unstable states set by the system's potential. For each value of n in the case of the system experiencing the truncated sinusoidal force at Fig. 4.9(a), the first resonance always provides the maximum response, as depicted in Fig. 4.7 for $n=1$. After the first resonance, the amplitude of the other observed resonances decreases as the perturbation amplitude B increases. By contrast, at Fig. 4.9(b), for the system experiencing the sawtooth force, the first resonance is always the weakest one. Indeed, the response of the subsequent resonances increases with the perturbation amplitude B.

For the sake of clarity, we introduce $Q_m^{*,n}$ as the amplitude of the local maxima number m achieved by the linear response Q of a system with nonlinearity order n. Moreover, $B_m^{*,n}$ will refer to the amplitudes of the perturbation allowing to reach these local maxima $Q_m^{*,n}$.

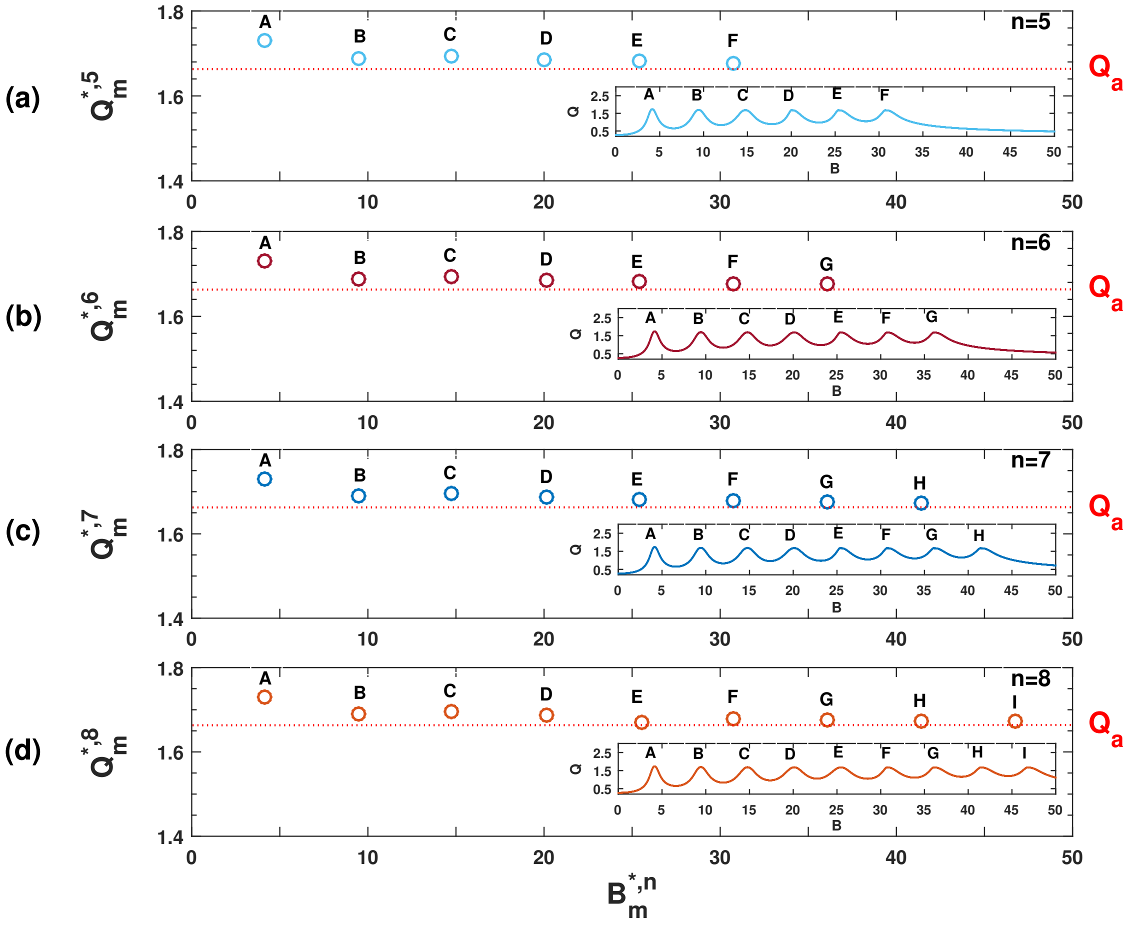

Figure 4.10: Locus of the linear response local maxima $Q_m^{*,n}$ versus the corresponding perturbation amplitude $B_m^{*,n}$ at which they occur. From top to bottom, we have considered a system experiencing a truncated sinusoidal force with order (a) $n=5$, (b) $n=6$, (c) $n=7$ and (d) $n=8$. The insets at each subfigure represent the classical linear response curves deduced from Fig. 4.9 where the maxima have been labeled with alphabetical capital letters. Parameters: $k=1$, $V_0=\frac{\pi}{32}$, $\alpha=6$, $\beta=16$, $b=0.1$, $\omega_1=1$, $\Omega=10\omega_1$, $\Delta B=0.01$, $\Delta t=0.0015$.

To have another look of the general behavior of the system for each nonlinearity order n, we analyze the evolution of the local maxima $Q_m^{*,n}$ that the linear response Q reaches and which corresponds to the response peak number m of Fig. 4.9(a) and 4.9(b). We therefore present at Figs. 4.10(a) – 4.10(d) the locus of the maximum response $Q_m^{*,n}$ at the resonance peaks of Fig. 4.9(a) for the truncated sinusoidal nonlinearity with order ranging from $n = 5$ to $n = 8$, versus the corresponding perturbation amplitude $B_m^{*,n}$ at which they occurred. For instance, in the inset of Fig. 4.10(a), the linear response Q exhibits $m = 6$ resonances for the nonlinearity order $n = 5$. These resonances are referred by capital letters A, B, C, D, E and F. Therefore, we can see from Fig. 4.10(a), the locus of the local maxima $Q_m^{*,5}$ of each of these six resonances A, B, C, D, E and F versus the corresponding optimal perturbation amplitude $B_m^{*,n}$ at which they occurred. Figs. 4.10(a) – 4.10(d) show that, whatever the nonlinearity order n, the first resonance is always the maximum response of our system after which, the magnitude of the m^{th} local maxima decreases as the nonlinearity order n increases. However, performing the same analyses on the system experiencing the sawtooth force, set of Figs. 4.11(a) – 4.11(d) show that the first resonance is always the weakest. Moreover,

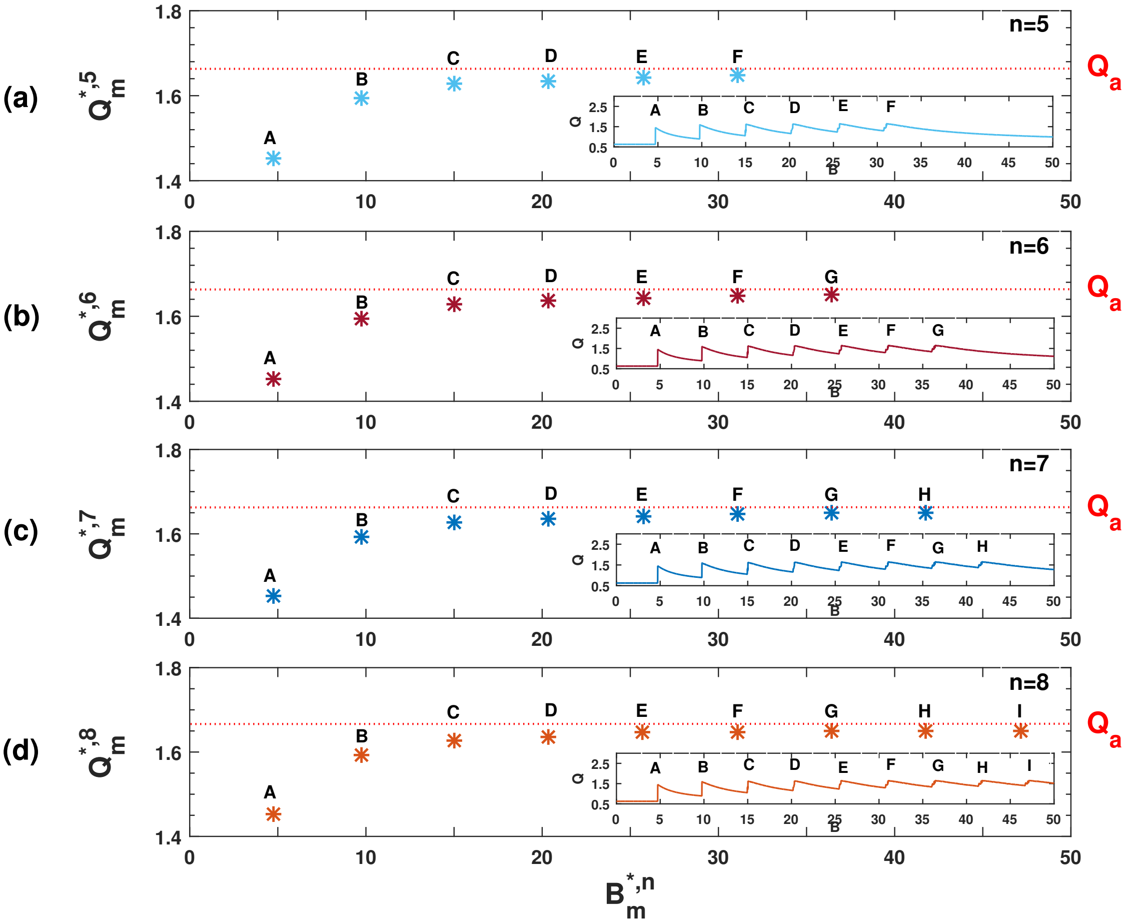

Figure 4.11: Locus of the linear response local maxima $Q_m^{*,n}$ versus the corresponding perturbation amplitude $B_m^{*,n}$ at which they occur. From top to bottom, we have considered a system experiencing a sawtooth force with order (a) $n = 5$, (b) $n = 6$, (c) $n = 7$ and (d) $n = 8$. The insets at each subfigure represent the classical linear response curves where the maxima have been labeled with alphabetical letters. Parameters: $A = 0\ 5$, $A_0 =$0.125, $\alpha = 6$, $\beta = 16$, $b =$0.1, $\omega_1 = 1$, $\Omega = 10\omega_1$, $\Delta B =$0.01, $\Delta t =$0.0015.

the intensity of the maximum linear response $Q_m^{*,n}$ at the peak of the m^{th} local resonance increases as the nonlinearity order n increases.

Note that, the maximum response $Q_m^{*,n}$ of the two systems from Figs. 4.10 and 4.11 tends to an asymptotic value Q_a as the nonlinearity order n keeps increasing. The asymptotic value of the two systems response, which is indicated with the dashed-line on both plots of Fig. 4.10 and Fig. 4.11, is rounded to Q_a =1.664. Therefore, it clearly appears that the advantage of the truncated sinusoidal nonlinearity is to provide the best response for the nonlinearity order $n = 0$, whereas to achieve the best resonance with the sawtooth force a greater nonlinearity order n must be considered.

The nonlinearity order n was shown to have directly controlled the number of resonances obtained in the two systems. However, we are now interested in exploring if n can enhance the system's local maximum response $Q_m^{*,n}$. We study the dependence of the two systems' local maximum responses $Q_m^{*,n}$ on the nonlinearity order n, corresponding to the first, second, third and fourth maxima in

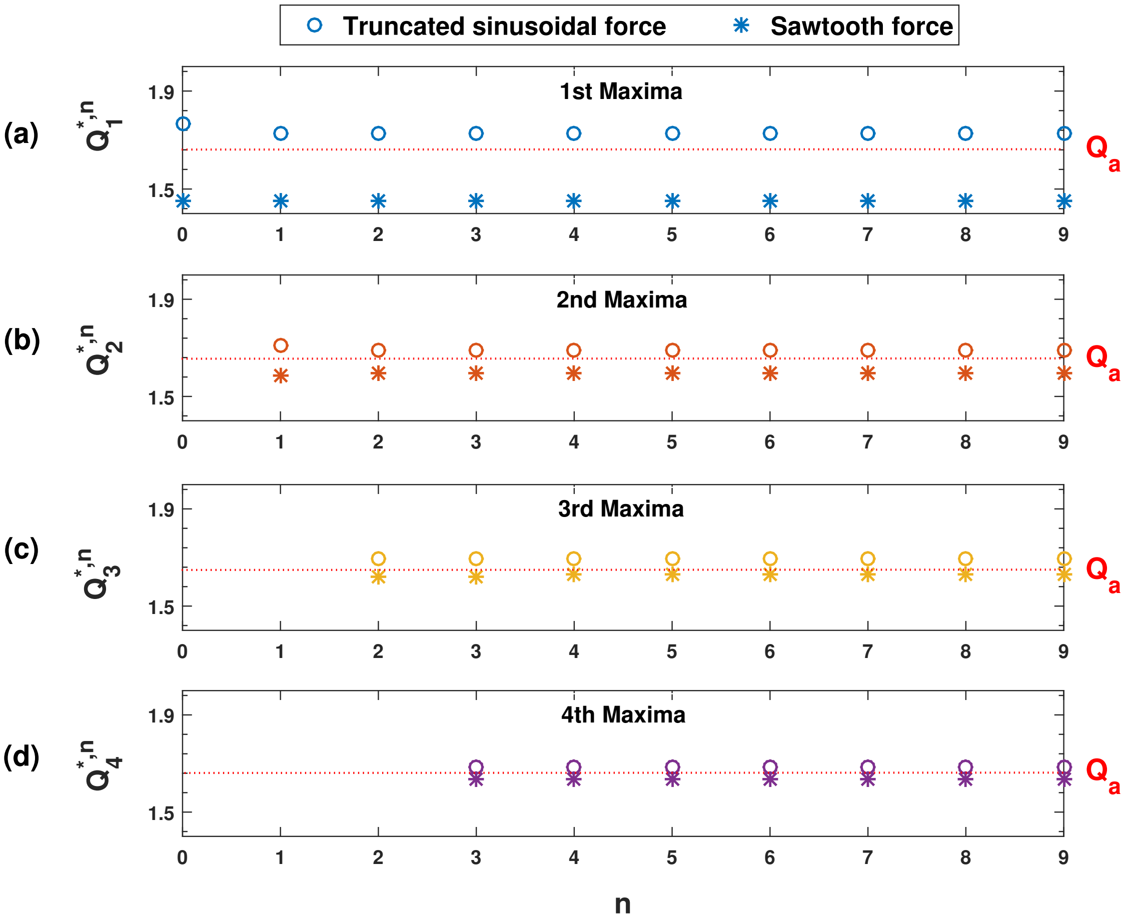

Figure 4.12: Evolution of each local maxima $Q_m^{*,n}$ reached by the linear response Q versus the nonlinearity order n. The performance obtained with the two nonlinear forces are compared when we consider: (a) The first maxima, (b) The second maxima, (c) The third maxima, (d) The fourth maxima. Circle-marked lines correspond to the truncated sinusoidal force whereas the star-marked lines refers to the sawtooth force. Parameters: $k = 1$, $V_0 = \frac{\pi}{32}$, A =0.5, A_0 =0.125, $\alpha = 6$, $\beta = 16$, b =0.1, $\omega_1 = 1$, $\Omega = 10\omega_1$, ΔB =0.01, Δt =0.0015.

Figs. 4.12(a), 4.12(b), 4.12(c) and 4.12(d) respectively. Circle-marked lines, which represent the response of the system submitted to the truncated sinusoidal force, are compared with the star-marked lines, which refer to the responses with the sawtooth force. As shown in all plots of Fig. 4.12, we understand that for each resonance, the maximum response $Q_m^{*,n}$ obtained in both the two systems does not significantly change due to the nonlinearity order n.

Furthermore, we can also understand from Fig. 4.12 that the responses of our system with the truncated sinusoidal force are more pronounced than those achieved with the sawtooth force. Lastly, as we are approaching the last maxima, the responses of the two systems tend to the asymptotic value Q_a, as indicated by the dashed-lines in all the plots of Fig. 4.12.

4.3.4/ ANALYSIS BY PHASE PORTRAITS

In this part, by means of phase portraits, we analyze the dynamical behavior of the system induced by each of the two different nonlinearities. In particular, we investigate the evolution of the resonance curves presented at Figs. 4.7 and 4.8, which correspond to the responses of the system submitted to the truncated sinusoidal and sawtooth forces of order $n = 1$ respectively. For this nonlinearity order $n = 1$, according to our notations, the truncated sinusoidal and sawtooth forces present three stable states located at positions $X^*_{-2,1} = -1$, $X^*_{0,1} = 0$, $X^*_{+2,1} = +1$ and two unstable states at positions $X^*_{-1,1} = -0.5$, $X^*_{+1,1} = +0.5$. We analyze the phase portraits behavior for six selected points on each resonance curve of Figs. 4.7 and 4.8. All simulations here start with the perturbation $B = 0$. The perturbation amplitude increases with step $\Delta B =0.01$ and the last values of the system variables from the previous simulation are maintained as the initial conditions for the next simulation. Moreover, for each selected point on Fig. 4.7 and 4.8, we perform five different simulations, each of them with one of the stable and unstable positions as initial condition for x, and zero for the remaining variables.

First, for the resonance curve obtained at Fig. 4.7 with the truncated sinusoidal force, we choose the perturbation amplitudes $B =1.5$, 3.5, 4.13, 6.86, 9.38 and 11 to analyze the corresponding phase portraits. For example, to obtain the phase portrait for each chosen perturbation B of Fig. 4.13, we start with $B = 0$ and perform five different simulations each of them starting with one of the initial conditions $x(0) = -1$, -0.5, 0, 0.5, 1 respectively, and $y(0) = z(0) = 0$. For each of these five simulations, the system exhibits periodic orbits which are centered around one of the stable or unstable positions of the system.

Therefore, setting the perturbation amplitude to $B =1.5$ at Fig. 4.13(a) gives rise to periodic orbits centered around the three stable positions $X^*_{-2,1} = -1$, $X^*_{0,1} = 0$ and $X^*_{+2,1} = +1$. This implies that the orbits for the two unstable positions: $X^*_{-1,1} = -0.5$ and $X^*_{+1,1} = +0.5$ are attracted to the neighboring stable states. Increasing the perturbation amplitude to $B =3.5$, the size of these periodic orbits increases, as shown at Fig. 4.13(b). At the peak of the first resonance of Fig. 4.7, which corresponds to $B =4.13$, the sizes of these three orbits increase further and the two

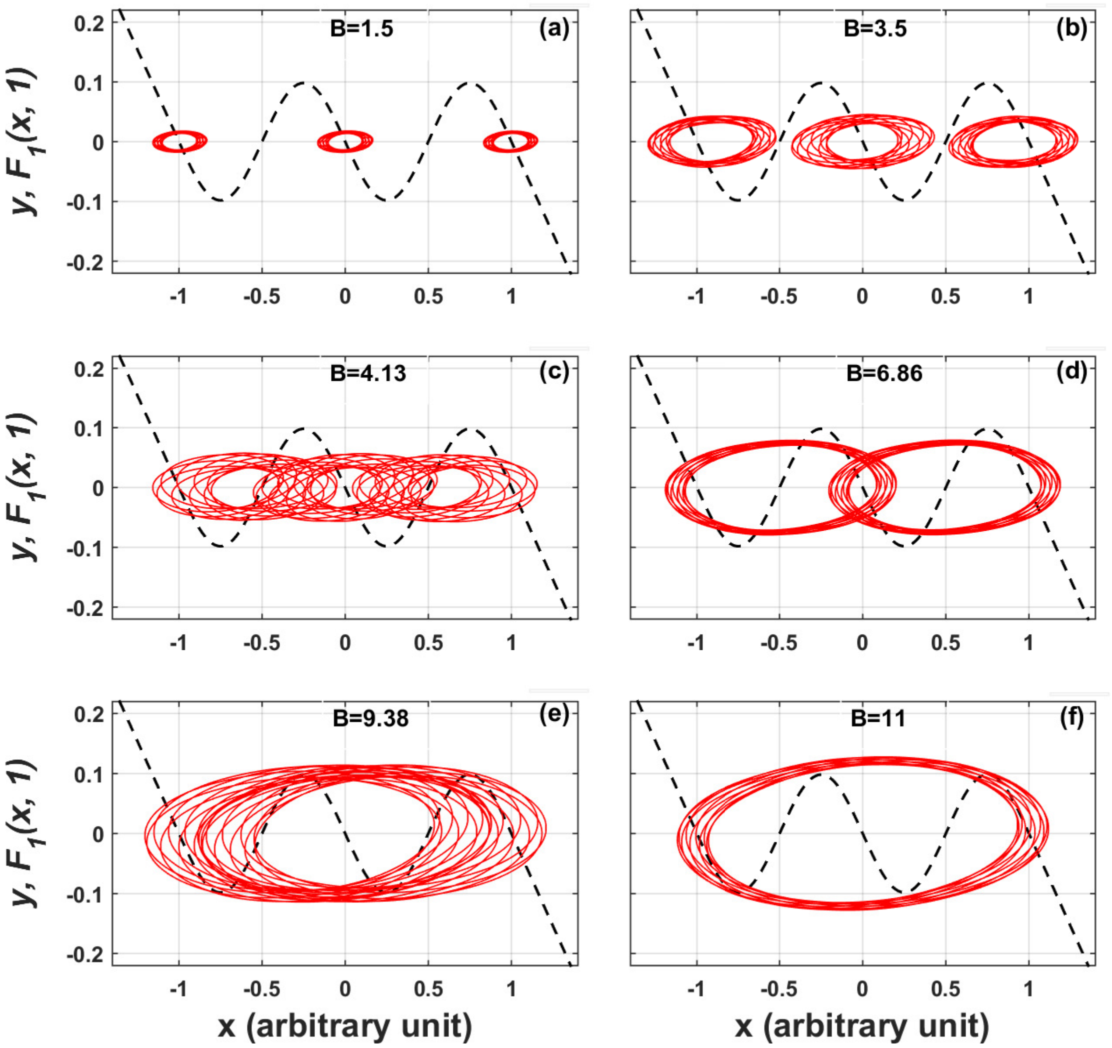

Figure 4.13: Phase portraits of the coexisting orbits for the resonance curve of Fig. 4.7. The perturbation amplitude is set to: (a) B =1.5, (b) B =3.5, (c) B =4.13, (d) B =6.86, (e) B =9.38 and (f) $B = 11$. The equivalent truncated sinusoidal force $F_1(x, 1)$ is also superimposed using a dashed-line in all the cases. Parameters: $n = 1$, $k = 1$, $V_0 = \frac{\pi}{32}$, $\alpha = 6$, $\beta = 16$, b =0.1, $\omega_1 = 1$, $\Omega = 10\omega_1$, Δt =0.0015.

adjacent orbits overlap the middle orbit. However, increasing the perturbation amplitude B beyond the peak of the first resonance, the linear response Q in Fig. 4.7 is decreasing. Consequently, we obtained two periodic orbits centered around the two unstable points. These orbits overlap at the bottom of the first resonance, that is when B =6.86, as presented in Fig. 4.13(d). The sizes of these two orbits keeps increasing as the perturbation amplitude B increases until at the peak of the second resonance when B =9.38, the orbits coincide with each other as shown in Fig. 4.13(e). Lastly, for perturbation amplitudes beyond the second resonance of Fig. 4.7, there will be no other resonance. This leads to the birth of one periodic orbit centered about the stable position at $X^*_{0,1} = 0$. The size of this orbit increases as the perturbation amplitude increases, as depicted for $B = 11$ at Fig. 4.13(f). The phase portrait analyses presented at Fig. 4.13 illustrate that our system with the truncated sinusoidal force exhibits resonance effect when the perturbation

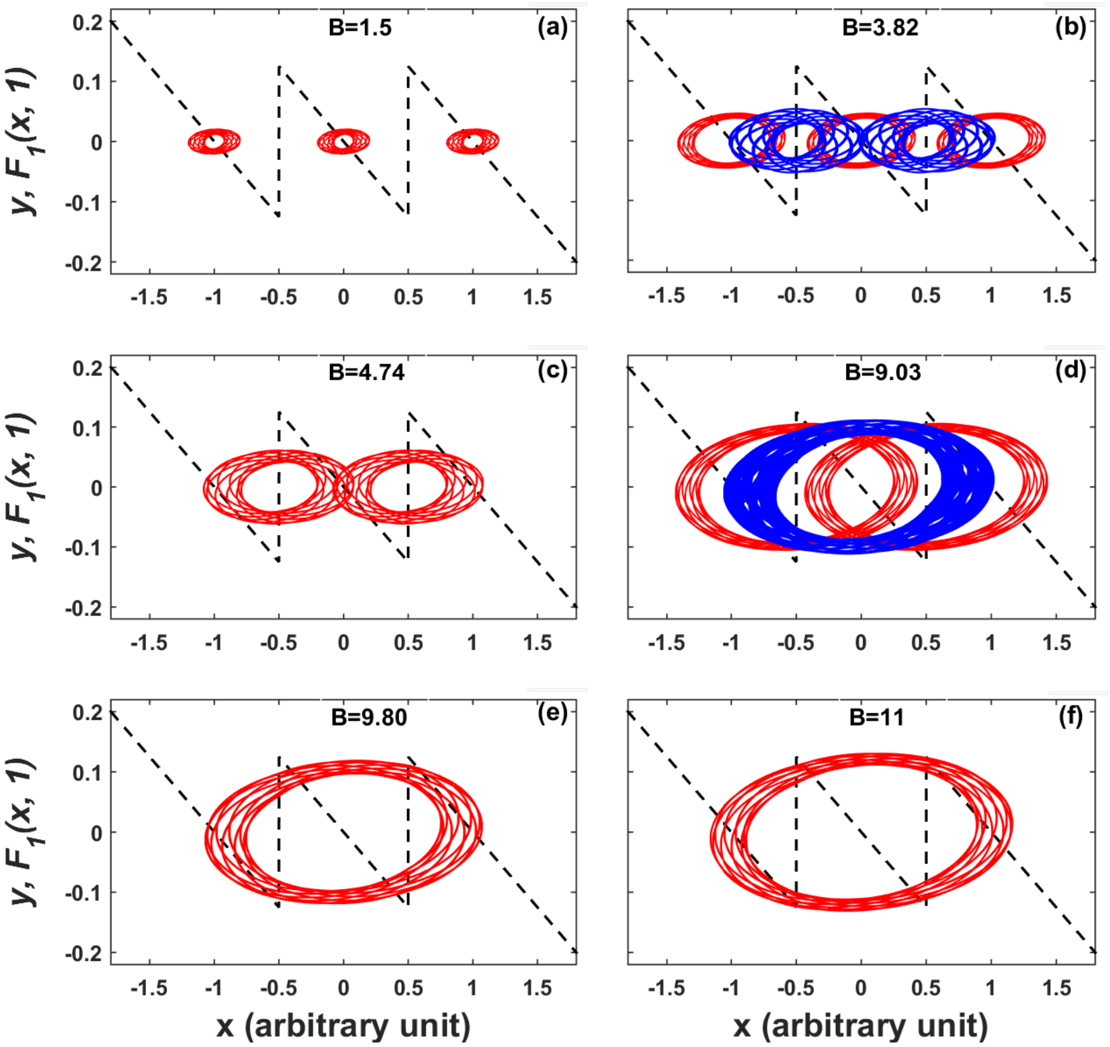

Figure 4.14: Phase portraits of the coexisting orbits for the resonance curve of Fig. 4.8. The perturbation amplitude is set to: (a) B =1.5, (b) B =3.5, (c) B =4.13, (d) B =6.86, (e) B =9.38 and (f) $B = 11$. The equivalent truncated sinusoidal force $F_1(x,1)$ is also superimposed using a dashed-line in all the cases. Parameters: $n = 1$, A =0.5, A_0 =0.125, $\alpha = 6$, $\beta = 16$, b =0.1, $\omega_1 = 1$, $\Omega = 10\omega_1$, Δt =0.0015.

amplitude B varies. This observed resonance is the VR phenomenon which was earlier identified using temporal and frequency analyses.

For the hysteretic response of the system submitted to the sawtooth force, which was previously presented at Fig. 4.8, we choose the perturbation amplitudes B =1.5, 3.82, 4.74, 9.03, 9.80 and 11 to propose the corresponding phase portraits of Fig. 4.14. In particular, B =1.5, 4.74, 9.80 and 11 whose phase portraits are presented at Fig. 4.14(a), 4.14(c), 4.14(e) and 4.14(f) respectively, are chosen to investigate the forward direction resonance of Fig. 4.8. The system reveals three small periodic orbits for B =1.5, each centered around the stable positions of the potential as depicted in Fig. 4.14(a). For the perturbation amplitude B =4.74, which corresponds to the first peak of the forward direction resonance of Fig. 4.8, the system reveals two orbits each centered around an unstable position as depicted at Fig. 4.14(c). At the second peak of the forward direction resonance of Fig. 4.8, which is achieved for B =4.74, there exists only one stable periodic orbit as shown at Fig. 4.14(e). Beyond the peak of the last resonance, the size of the remaining stable orbit increases with the perturbation amplitude B as at Fig. 4.14(f) for B =11.

To investigate the evolution of the hystereses depicted by the reverse direction resonance of Fig. 4.8, we present the phase portraits of Fig. 4.14(b) and 4.14(d). These phase portraits depict the orbits obtained from the forward and reverse simulations at the points of Fig. 4.8 where B =3.82 and B =9.03 respectively. For the perturbation B =3.82, which corresponds to the second peak of the reverse resonance of Fig. 4.8, forward simulation reveals three stable orbits (plotted in red) and reverse simulation reveals two unstable orbits (plotted in blue) as shown in Fig. 4.14(b). Moreover, two unstable orbits from the forward simulation and one additional stable orbit from the reverse simulation are also observed for B =9.03 as shown at Fig. 4.14(d). The additional orbits obtained in the reverse simulation for B =3.82 and B =9.03 signify the existence of hystereses in the system experiencing a sawtooth nonlinearity. Moreover, the phase portraits of Fig. 4.14 also illustrate VR effect induced by the perturbation amplitude B as previously revealed using the time series and frequency analyses in the system experiencing a sawtooth force.

4.4/ GHOST-VIBRATIONAL RESONANCE

In this section, we consider that the system is driven by two signals with close low angular frequencies ω_1 and ω_2, corrupted by a high frequency perturbation of amplitude B and angular frequency Ω. By setting the boolean variable δ of the excitation $e(t)$ defined by eq. (4.6) to $\delta = 1$, the input perturbed excitation $e_p(t)$ defined by eq. (4.5) reduces to

$$e_p(t) = b\left[\cos(\omega_1 t) + \cos(\omega_2 t)\right] + B\cos\Omega t, \tag{4.10}$$

with $\omega_1 = 2\omega_0$ and $\omega_2 = 3\omega_0$.

Especially, the gap ω_0 between the two input low angular frequencies ω_1 and ω_2 is fixed to $\omega_0 = \omega_2 - \omega_1$ =0.1 and it constitutes the system's ghost angular frequency. Moreover, the amplitude of the low frequencies is set to b =0.04 while the perturbation angular frequency is tuned to $\Omega = 20\omega_0$. Lastly, we take the following values for the constant parameters α and β of the Chua's model: $\alpha = 4$ and $\beta = 14$.

It is well known that VR and GVR effects consider a high frequency perturbation to enhance the detection of an input low frequency signals and a missing input low frequency signal respectively. These effects are induced when the perturbation amplitude B is considered as a control parameter while keeping the other parameters fixed. In this section, we propose to analyze the system response at the missing low angular frequency ω_0 and also at the two input low angular frequencies ω_1 and ω_2 to highlight GVR and VR phenomena in the Chua model experiencing the two proposed nonlinear forces. We first restrict our study to Chua model with nonlinearity order $n = 0$.

By using the simulation algorithm precised in Sec. 4.2.3, and considering the input perturbed excitation $e_p(t)$ defined by eq. (4.10), we integrate the system given by the set of eqs. (4.1) in the cases of the truncated sinusoidal and the sawtooth forces defined by eq. (4.3) and eq. (4.4) respectively.

For the system experiencing the truncated sinusoidal force, the resonance curves of Fig. 4.15 correspond to the evolution versus the perturbation amplitude B of the linear responses $Q(\omega_0)$, $Q(\omega_1)$ and $Q(\omega_2)$ estimated at the missing low angular frequency ω_0 and at the two input low angular frequencies ω_1 and ω_2. Without perturbation, namely $B = 0$, the system's linear response $Q(\omega_0)$ at the missing low angular frequency ω_0 is null, contrary to the linear responses $Q(\omega_1)$ and $Q(\omega_2)$ at the two input low angular frequencies. However, as the perturbation amplitude B increases, the system reveals resonances at the missing low angular frequency ω_0 and at the two input low angular frequencies (ω_1 and ω_2) whose predominance can be identified within different ranges of the perturbation amplitude B. In the first resonance region, where the perturbation amplitude B is in the range [0.560; 0.597], we observe an enhancement of the system's linear response $Q(\omega_i)$ at the three input angular frequencies ω_0, ω_1 and ω_2. Moreover, the linear response $Q(\omega_0)$ at the missing angular frequency ω_0 is the predominant one. However, for the perturbation amplitude B in the

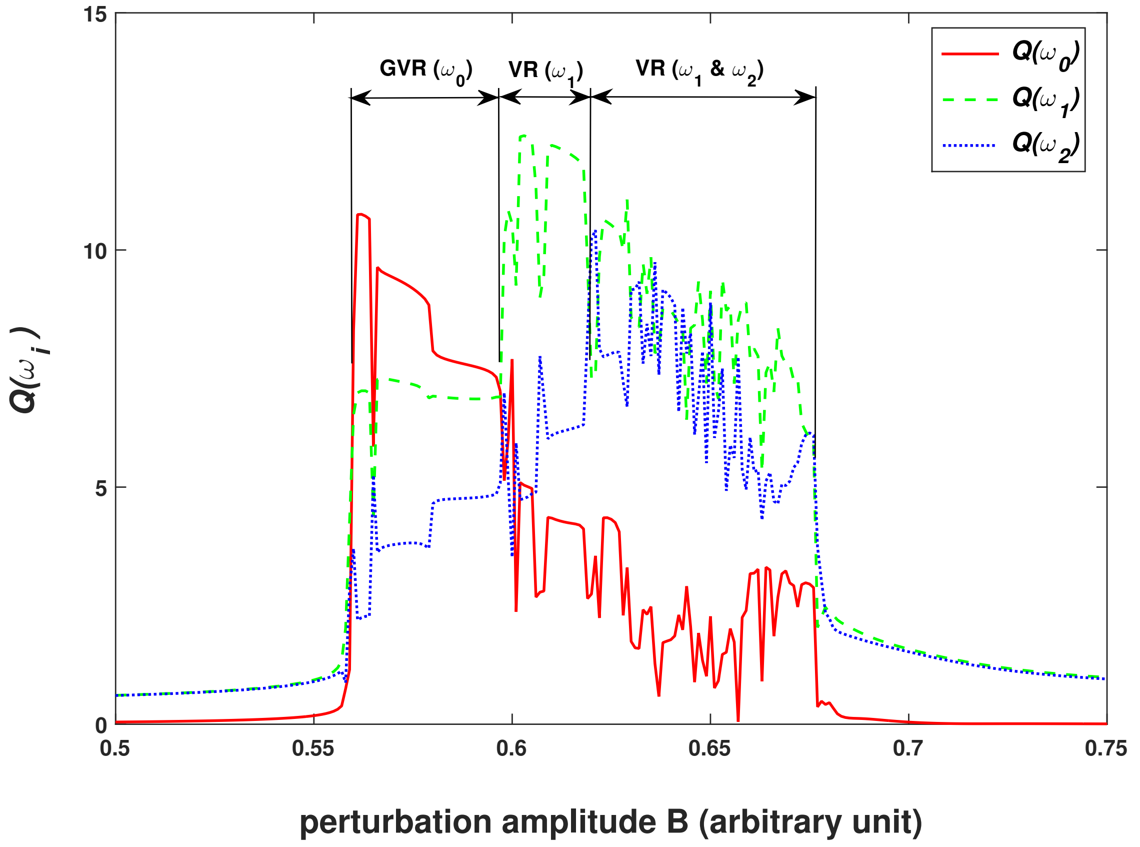

Figure 4.15: Linear response Q of the system estimated at the low angular frequencies ω_0, ω_1 and ω_2, versus the perturbation amplitude B, for the system experiencing the truncated sinusoidal force. Parameters: $n = 0$, $k = 1$, $V_0 = \frac{\pi}{32}$, $\alpha = 4$, $\beta = 14$, b =0.04, ω_0 =0.1, $\omega_1 = 2\omega_0$, $\omega_2 = 3\omega_0$, $\Omega = 20\omega_0$, ΔB =0.001, Δt =0.0015.

interval [0.598; 0.619], the system's linear response $Q(\omega_1)$ at the input low angular frequency ω_1 becomes predominant. Similarly, for the perturbation amplitude B in the interval [0.620; 0.676], the linear response at the two low angular frequencies ω_1 and ω_2 interchangeably dominates but each in a short interval of B. Lastly, as the perturbation amplitude B keeps increasing beyond $B =$0.676, the system's linear response $Q(\omega_0)$ at the missing angular frequency ω_0 approaches zero whereas the responses $Q(\omega_1)$ and $Q(\omega_2)$ at the two low angular frequencies ω_1 and ω_2 are amplified in the same way, none of the two being predominant.

To better understand the evolution of the resonances observed in Fig. 4.15, chronograms and their corresponding spectra are respectively presented at Figs. 4.16(a) – 4.16(d) and Figs. 4.17(a) – 4.17(d), for four specific values of the perturbation amplitude B, namely $B =$0.561, 0.603, 0.621

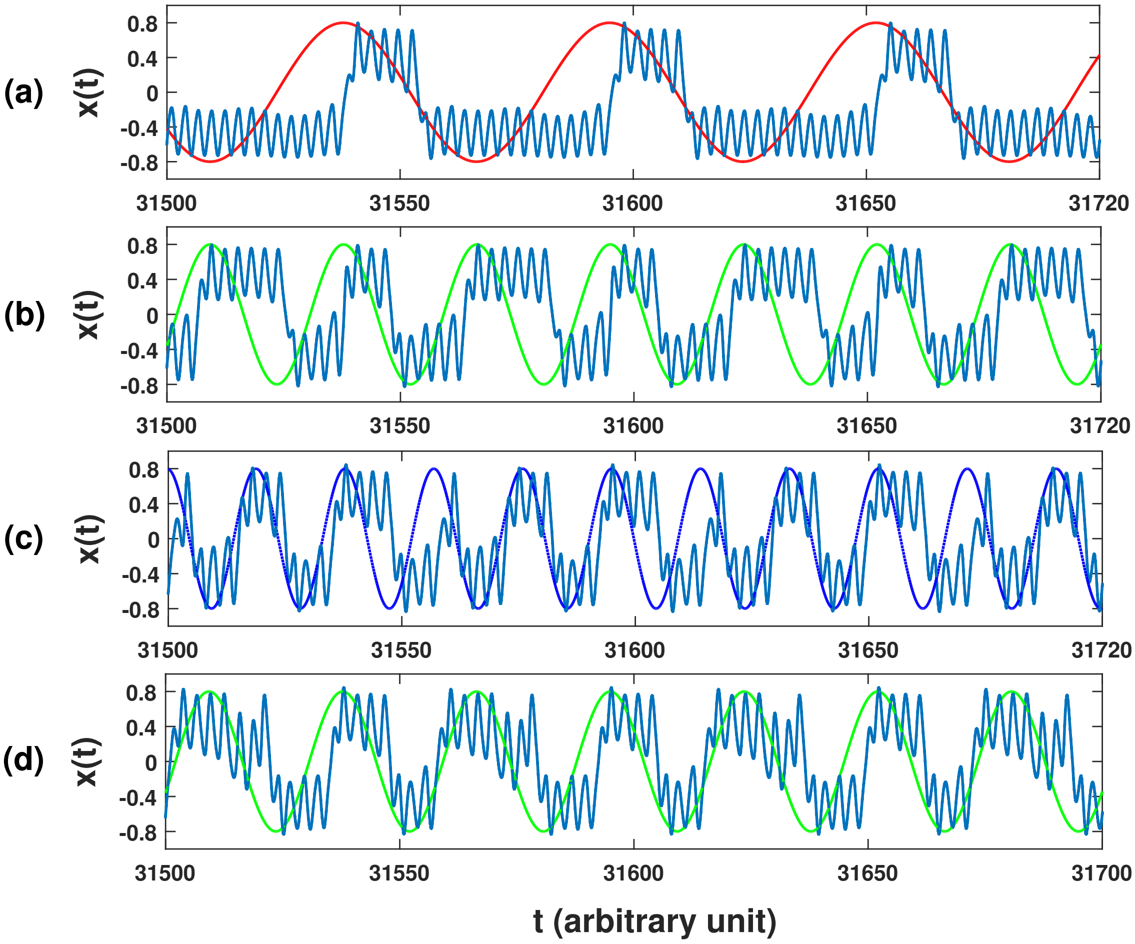

Figure 4.16: Chronograms summarizing the system's behavior for four specific values of the perturbation amplitude B taken in the different ranges identified at Fig. 4.15. The system synchronizes its response to the sinusoidal wave superimposed on each subfigure and which corresponds to the predominant angular frequency, that is, ω_0, ω_1, ω_2 and ω_1 for subfigures (a), (b), (c) and (d) respectively. From top to bottom, we observe the predominance of: (a) GVR at the ghost angular frequency ω_0 when $B =$0.561 (first resonance region of Fig. 4.15), (b) VR at the angular frequency ω_1 when $B =$0.603 (second resonance region of Fig. 4.15), (c) VR at the angular frequency ω_2 when $B =$0.621 (third resonance region of Fig. 4.15) and (d) VR at the angular frequency ω_1 when $B =$0.629 (third resonance region of Fig. 4.15). Parameters: $n = 0$, $k = 1$, $V_0 = \frac{\pi}{32}$, $\alpha = 4$, $\beta = 14$, $b =$0.04, $\omega_0 =$0.1, $\omega_1 = 2\omega_0$, $\omega_2 = 3\omega_0$, $\Omega = 20\omega_0$, $\Delta t =$0.0015.

and 0.629. We first choose the value B =0.561 to show the predominance of GVR at the ghost angular frequency ω_0 in the first resonance region of Fig. 4.15 defined by the range of the perturbation amplitude [0.560; 0.597]. Next, the value B =0.603 allows to observe the superiority of VR effect at the angular frequency ω_1 in the second resonance region of Fig. 4.15 defined by the perturbation range [0.598; 0.619]. Lastly, considering B =0.621 and B =0.629 allow to illustrate the predominance of VR respectively at the angular frequencies ω_2 and ω_1 in the last resonance region of Fig. 4.15, where B is in the range [0.620; 0.676]. Note that, to visualize at which frequency the system synchronizes its response, we have superimposed the corresponding predominant low frequency sinusoidal wave in each chronogram of Fig. 4.16. Additionally, for each spectrum of Fig. 4.17, we have labeled the value of the unilateral magnitude spectrum $2|X(f_i)|$ corresponding to each low frequency, namely $f_0 = \frac{\omega_0}{2\pi}$, $f_1 = \frac{\omega_1}{2\pi}$ and $f_2 = \frac{\omega_2}{2\pi}$.

In the first resonance region of Fig. 4.15 where GVR effect is predominant, that is for $B \in$ [0.560;

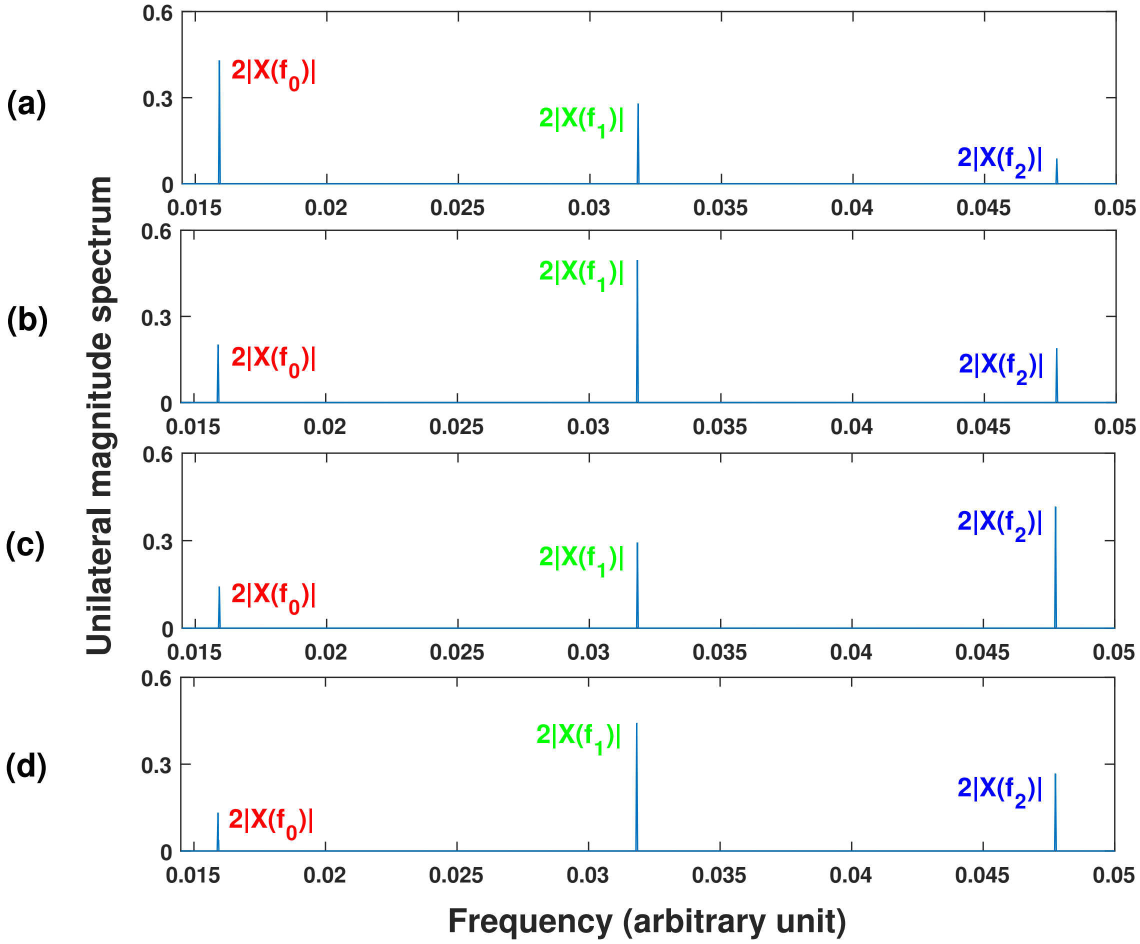

Figure 4.17: Unilateral magnitude spectra of the time series of Fig. 4.16. The spectral responses clearly indicate which frequency is dominant in each case. From top to bottom, we observe the predominance of: (a) GVR at the ghost angular frequency ω_0 when B =0.561 (first resonance region of Fig. 4.15), (b) VR at the angular frequency ω_1 when B =0.603 (second resonance region of Fig. 4.15), (c) VR at the angular frequency ω_2 when B =0.621 (third resonance region of Fig. 4.15) and (d) VR at the angular frequency ω_1 when B =0.629 (third resonance region of Fig. 4.15). Parameters: $n = 0$, $k = 1$, $V_0 = \frac{\pi}{32}$, $\alpha = 4$, $\beta = 14$, b =0.04, ω_0 =0.1, $\omega_1 = 2\omega_0$, $\omega_2 = 3\omega_0$, $\Omega = 20\omega_0$, B =0.561, Δt =0.0015.

0.597], Fig. 4.16(a) shows that the enclosed signal at the ghost angular frequency ω_0 synchronizes with the slow oscillations of the time series. In addition, the corresponding unilateral magnitude spectrum at Fig. 4.17(a) also confirms that the amplitude of the spectrum $2|X(f_0)|$ at the ghost angular frequency ω_0 is best pronounced in this particular region.

By contrast, the system's temporal response of Fig. 4.16(b) and its corresponding spectra of Fig. 4.17(b) have been obtained for the perturbation amplitude B from the second resonance region, where VR effect at the angular frequency ω_1 is the best pronounced resonance. In this resonance region, for which the perturbation amplitude B is in the range [0.598; 0.619], the chronogram of Fig. 4.16(b) shows that the slow oscillations of the temporal response are in phase with the superimposed sinusoidal wave of angular frequency ω_1. Moreover, the corresponding spectrum at Fig. 4.17(b) confirms that the response of the system at the angular frequency ω_1 is the predominant one.

In the last resonance region of Fig. 4.15 defined by the range of perturbation amplitude [0.620; 0.676], the chronograms of Figs. 4.16(c) and 4.16(d) with their corresponding spectra at Figs. 4.17(c) and 4.17(d) show that VR at the angular frequencies ω_2 and ω_1 interchangeably emerge as the best pronounced resonances. The chronogram of Fig. 4.16(c), obtained for B =0.621,

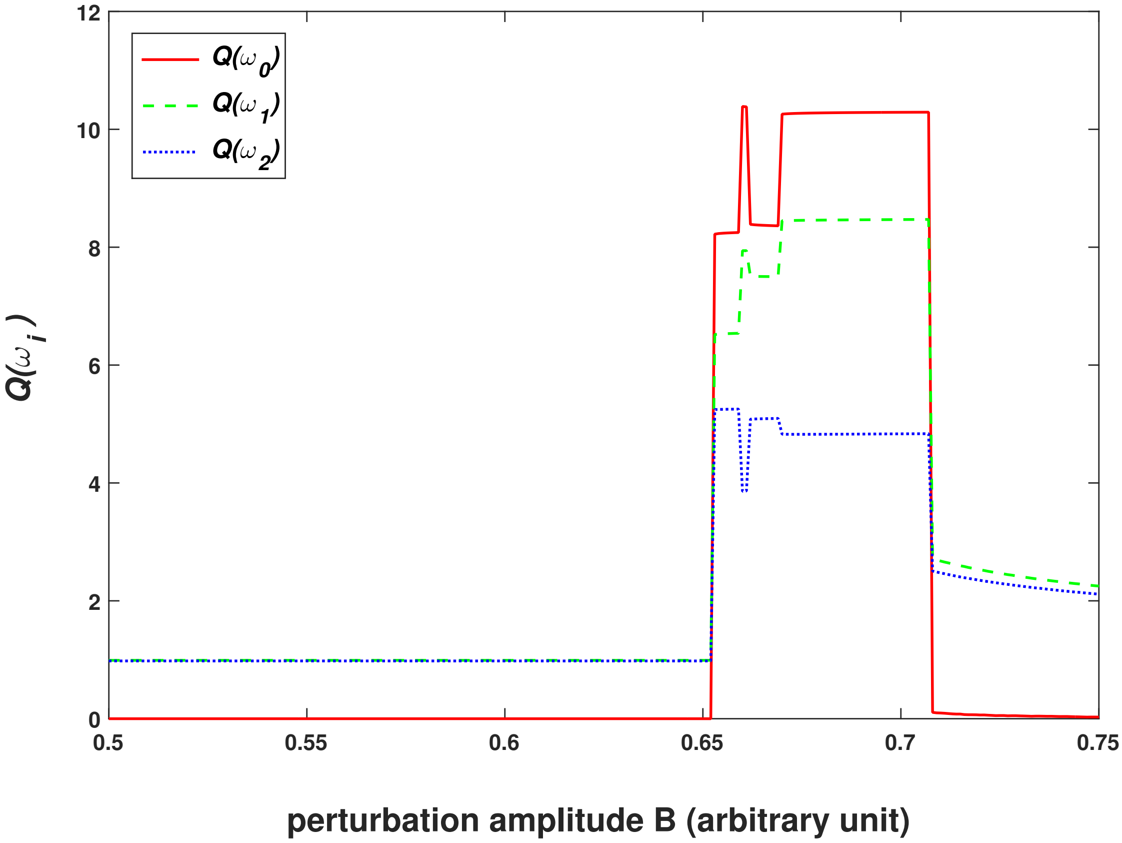

Figure 4.18: Linear response Q of the system at the angular frequencies ω_0, ω_1 and ω_2 versus the perturbation amplitude B, for the system experiencing the sawtooth force. Parameters: $n = 0$, A =0.5, A_0 =0.125, $\alpha = 4$, $\beta = 14$, b =0.04, ω_0 =0.1, $\omega_1 = 2\omega_0$, $\omega_2 = 3\omega_0$, $\Omega = 20\omega_0$, ΔB =0.001, Δt =0.0015.

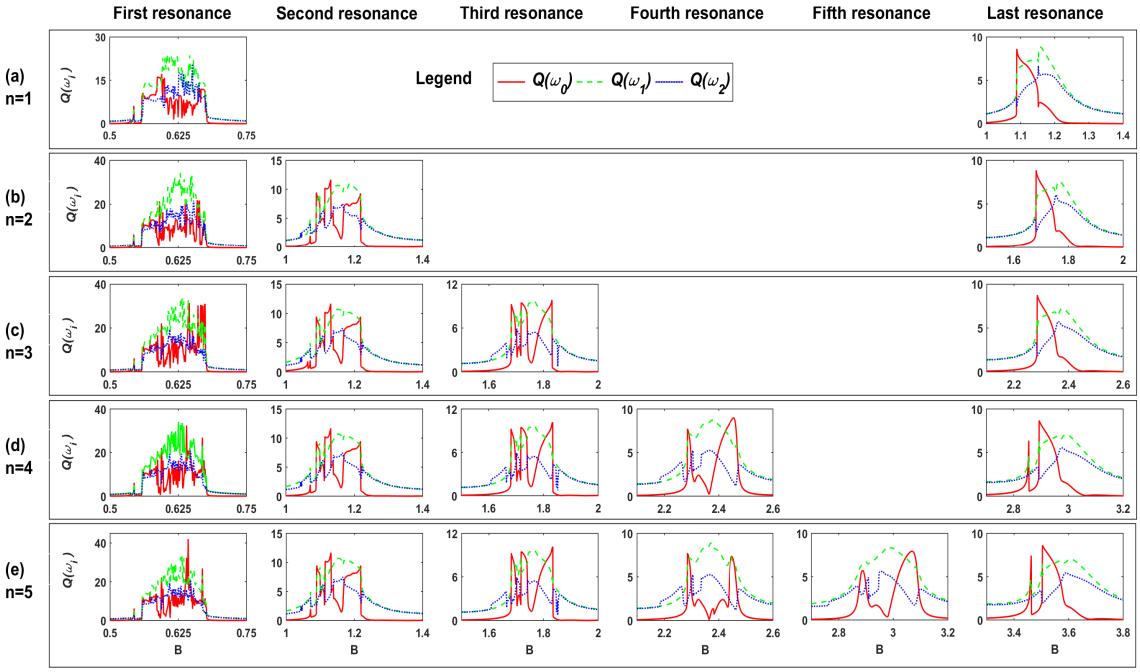

Figure 4.19: Impact of the nonlinearity order n of the truncated sinusoidal force on the resonances. The linear response Q estimated at the angular frequencies ω_0, ω_1 and ω_2 has been plotted versus the perturbation amplitude B, for the nonlinearity orders: (a) $n = 1$, (b) $n = 2$, (c) $n = 3$, (d) $n = 4$, (e) $n = 5$. Parameters: $k = 1$, $V_0 = \frac{\pi}{32}$, $\alpha = 4$, $\beta = 14$, b =0.04, ω_0 =0.1, $\omega_1 = 2\omega_0$, $\omega_2 = 3\omega_0$, $\Omega = 20\omega_0$, ΔB =0.01, Δt =0.0015.

illustrates the predominance of VR at the angular frequency ω_2, since the slow oscillations of the temporal response synchronize with the superimposed sinusoidal wave at the angular frequency ω_2. Furthermore, the corresponding spectrum at Fig. 4.17(c) proves that the system's response at the angular frequency ω_2 is the best pronounced one. Similarly, the time series of Fig. 4.16(d) and the associated spectrum at Fig. 4.17(d), obtained for B =0.629, refer to the predominance of VR effect at the angular frequency ω_1.

These resonance behaviors of the system submitted to the truncated sinusoidal force were not obtained in the case of the system experiencing a sawtooth force, for the considered parameter settings. Indeed, our simulation of the system with the sawtooth force reported at Fig. 4.18, confirms the behavior observed by Abirami *et al* [152] where: varying the perturbation amplitude B induces all the resonance effects in the same perturbation range [0.652; 0.708], with the linear response $Q(\omega_0)$ at the ghost angular frequency ω_0 predominant in the whole region. Note that, the system experiencing the sawtooth force can also exhibits the behavior which has been reported at Fig. 4.15 in the case of the truncated sinusoidal force. However, in this regard, it is necessary to change the system parameters such as the nonlinearity order n, the low frequencies amplitude b and the perturbation angular frequency Ω.

Concerning the system submitted to the truncated sinusoidal force, the separation of the different resonance effects in distinct ranges of perturbation amplitude B, is not restricted to the nonlinearity order $n = 0$. Indeed, for the nonlinearity orders n presented at Fig. 4.19, namely $n = 1, 2, 3, 4$

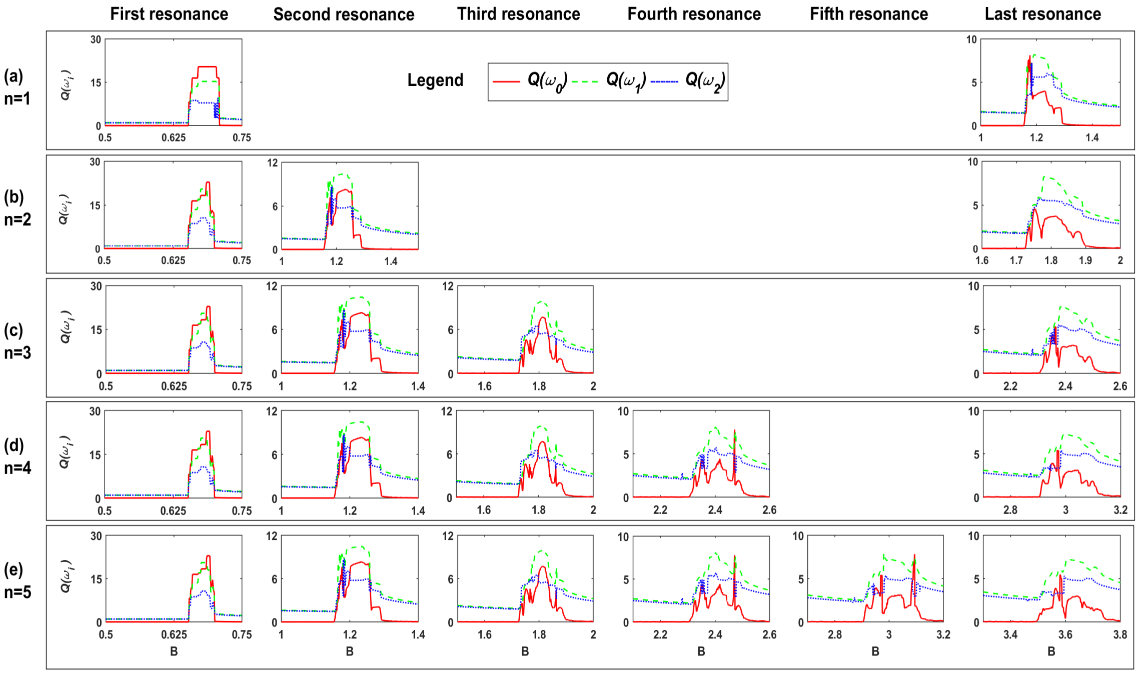

Figure 4.20: Impact of the nonlinearity order n of the sawtooth force on the resonances. The linear response Q estimated at the angular frequencies ω_0, ω_1 and ω_2 has been plotted versus the perturbation amplitude B, for the nonlinearity orders: (a) $n = 1$, (b) $n = 2$, (c) $n = 3$, (d) $n = 4$, (e) $n = 5$. Parameters: A =0.5, A_0 =0.125, $\alpha = 4$, $\beta = 14$, b =0.04, ω_0 =0.1, $\omega_1 = 2\omega_0$, $\omega_2 = 3\omega_0$, $\Omega = 20\omega_0$, ΔB =0.01, Δt =0.0015.

and 5, our system also follows the same behavior as achieved at Fig. 4.15 for $n = 0$. For each considered nonlinearity order n, we obtained $n+1$ resonances which have been plotted separately at Fig. 4.19 with an appropriate zoom near each resonance. Interestingly, we observe the same trend for each corresponding resonance, whatever the nonlinearity order n.

On the other hand, Fig. 4.20 reveals the system's response when submitted to the sawtooth force for the nonlinearity orders $n = 1$, 2, 3, 4 and 5. Contrary to the responses reported at Fig. 4.18 for $n = 0$, system's response at other input low frequencies can be predominant when the nonlinearity order n increases. Similarly, the same trend is observed for each corresponding resonance, whatever the nonlinearity order n.

4.5/ CONCLUSION

In this chapter, we have considered the dynamics of a modified Chua's circuit model, experiencing a truncated sinusoidal force and driven by a perturbed input excitations: low frequency signal(s) corrupted by a high frequency perturbation. In particular, we studied the impact of the system's nonlinearity on the occurrence of Vibrational Resonance (VR) and Ghost-Vibrational Resonance (GVR) phenomena. VR effect refers to the enhancement of an input low frequency signal at the system's output, by a high frequency perturbation. However, high frequency perturbation induces resonance at a missing (ghost) input low frequency in the case of GVR effect. In the previous work of Abirami et al devoted to this Chua system, VR and GVR were studied by considering a sawtooth nonlinearity [152]. In the present work, we analyzed the impact of the system's nonlinearity on the occurrence of VR and GVR, since we compared the system responses obtained with the truncated sinusoidal force and those with the sawtooth force. Consequently, we maintained the same parameters settings, namely, the same potential barrier height and potential periodicity in both the two systems.

Our VR studies in the system experiencing the truncated sinusoidal force revealed multiple resonances whose intensity reduces as the perturbation amplitude B increases. As initially reported by Abirami et al [152], our simulations with the sawtooth force also revealed multiple resonances. However, we have established that the intensity of the first resonance is the weakest one. More precisely, contrary to the truncated sinusoidal force, the intensity of the local maxima increases with the perturbation amplitude B. On the other hand, we have shown that the number of resonances obtained with both nonlinearities is controlled by their order n which also represents the number of unstable states in the system.

It is interesting to remark that, the system submitted to the truncated sinusoidal force requires smaller perturbation amplitude B to reach its maximum response. Consequently, it is less energy consuming when compared to the system experiencing a sawtooth force, which requires relatively larger perturbation amplitude B to attain its maximum response. In addition, as the nonlinearity order n in both the two systems keeps increasing, the response of the two systems approaches an asymptotic value Q_a which for our parameters setting has been rounded to $Q_a =$1.664.

Next, in the case of the truncated sinusoidal force, we have interpreted the multiple resonances observed by means of phase portraits analyses. For a weak value of the perturbation amplitude B, our system revealed orbits with small amplitudes, each centered around one of the stable positions of the system's potential. Increase in the size of the existing orbits refers to the enhancement in the system's linear response Q, when the perturbation B varies. At the peak of each resonance, the existing adjacent orbits overlap with each another. However, increasing the perturbation amplitude B beyond the peak of each resonance, one of the existing orbits disappeared. After the peak of the last resonance, the system revealed just one orbit whose size increases with the increase of the perturbation amplitude B. In a similar way, phase portraits corresponding to the system submitted to sawtooth force also followed the same trend as in the case of the system experiencing the truncated sinusoidal force. However, additional orbits were revealed at the peaks of the reverse direction resonances, which explained the existence of hystereses induced by the system experiencing a sawtooth force.

Exciting the system experiencing the truncated sinusoidal nonlinearity with two close low frequency signals, we have established that a high frequency perturbation can induce resonances at the two input low angular frequencies ω_1 and ω_2, together with another resonance at a missing input low angular frequency ω_0. The predominance of these resonances can be identified each in a specific range of the perturbation amplitude B. In the first range of the perturbation amplitude, the system's response at the missing low angular frequency ω_0 emerged as the best pronounced resonance which indicates a strong manifestation of GVR effect. Another resonance region is defined by a second range of the perturbation amplitude B where the system's linear response at the low angular frequency ω_1 is the strongest. It corresponds to the occurrence of VR effect at the low angular frequency ω_1. In the last region, obtained for a third range of perturbation amplitude B, VR effects at the low angular frequencies ω_2 and ω_1 interchangeably became the dominant resonances. Our temporal and spectral analyses also confirmed which resonance is the most pronounced one since the observed chronograms has revealed that the system can synchronize its response with the ghost frequency or one of the two input low frequencies. In fact, it depends on which of the previously established ranges the perturbation amplitude B is taken.

By contrast, for the system experiencing the sawtooth force, all the resonance effects occurred in only one specific range of the perturbation amplitude B, with the GVR as the predominant resonance throughout. As obtained from the study of the system with the truncated sinusoidal nonlinearity, the system experiencing a sawtooth nonlinearity can also reveal the predominance of different resonance effects in the distinct ranges of the perturbation amplitude B. However, this is possible through varying the system parameters such as the nonlinearity order n, the low frequencies amplitude b and the perturbation angular frequency Ω.

As we have shown that Chua's circuit model with the truncated sinusoidal nonlinearity provided a better response than with the sawtooth nonlinearity, we suspect that it could be interesting to analyze in the same way, the impact of the nonlinearities in other systems. It could lead to optimized application of signal detection in engineering fields.

5

APPLICATIONS OF VIBRATIONAL RESONANCE ON SUBTHRESHOLD IMAGES PERCEPTION

Contents

5.1 Introduction 77

5.2 The detector and its set-up 79

  5.2.1 Input of the detector 79

  5.2.2 The resonant threshold detector 80

5.3 Stochastic resonance based detector 82

5.4 Vibrational resonance based detector 85

  5.4.1 Amplitude optimized VR-detector 85

  5.4.2 Frequency optimized VR-detector 89

5.5 Conclusion 94

In the two previous chapters, we have studied the effect of Vibrational Resonance (VR) in the context of one-dimensional signals. This chapter extends the investigation to applications of VR in two-dimensional signals which consist of images. Precisely, we study the application of VR in subthreshold noisy images perception.

5.1/ INTRODUCTION

The analyses of the dynamics of nonlinear systems, especially their response to external input stimuli, has revealed a lot of fascinating applications. For instance, the famous Stochastic Resonance (SR) effect, where nonlinear systems take benefit of an external random perturbation to enhance their response [222], has drawn considerable attention and revealed applications in different contexts such as image processing, visual perception and signals dithering.

Indeed, parameter induced SR, which was first investigated in one-dimensional signals in the field of signal processing [49, 64], was later extended to two-dimensional signals to develop image processing tasks [223–227]. In the field of pattern recognition, potential applications of SR in biometric identification has been investigated, where the extraction of low-quality fingerprint images was enhanced [228]. Indirect techniques of noise induced improvement (SR) has revealed applications in images contrast enhancement [229, 230], in improving magnetic resonance as well as ultrasound images in the context of medical images analyses [231, 232]. It was also shown that, the noise enhanced properties of a nonlinear system can find applications in the context of image denoising and edge preserving [221, 233–235].

In another important scenario, it was revealed that adding an appropriate amount of noise to subthreshold images can enhance their perception through a simple threshold detector [96, 168, 169]. Moreover, at the acquisition process level of human vision, it has been established that spatio-temporal random fluctuations can enhance visual perception in a basic model of a retina [236, 237].

On the other hand, in the field of signal processing and during signal quantization, it is interesting to note that adding external perturbation was reported to reduce unavoidable loss of information and distortion which mainly occurred due to quantization error [238, 239]. This induced effect, rather called dithering, is normally applied to suprathreshold signals where the added dithering signal is often subtracted after the quantization, contrary to SR effect [240]. Concerning image quantization, among the dithering algorithms, ordered dithering, which consists of adding coherent patterns to the initial image before quantization, was reported to be more efficient than random dithering which uses noisy patterns [238]. Motivated by this fact, one may wonder if processes based on nonlinear resonances which use ordered perturbations, like VR, would be more efficient than processes which use noisy perturbations, like SR. This constitutes the content of this chapter which addresses the open question of the contribution of VR to subthreshold images perception through threshold detectors.

In this chapter, at Sec. 5.2, we first introduce a threshold detector which can be perturbed by noise to take benefit of stochastic resonance or by a high frequency spatial signal to take advantage of the enhancement induced by VR. Next, In Sec. 5.3, we highlight the limitations of stochastic resonance based detector in terms of subthreshold image perception. In Sec. 5.4, we introduce a particular spatial high frequency perturbation to show how VR overcomes the limitation of SR. Unlike classical studies which usually consider the amplitude of the perturbation as a control parameter, we also analyze the impact of the perturbation frequency in terms of image perception. We then close this chapter with concluding remarks and outlooks.

5.2/ THE DETECTOR AND ITS SET-UP

5.2.1/ INPUT OF THE DETECTOR

To perform our study, we use the noiseless images of size $N \times N$ pixels represented in Fig. 5.1 and whose gray levels evolve from 0 (black) to 1 (white). As shown in Fig. 5.1 where the scales of the images have been respected, we propose different image sizes N^2 ranging from $N^2 = 64^2$ pixels to $N^2 = 512^2$ pixels. Each of these images I is then corrupted by an additive white noise of root mean square σ to generate the noisy image I_b according to:

$$I_{b_{i,j}} = I_{i,j} + \sigma\eta_{i,j}, \text{ with } i = 1,2,\ldots,N \text{ and } j = 1,2,\ldots,N, \tag{5.1}$$

where $I_{i,j}$ denotes the gray level of the pixel of coordinates i, j and $\eta_{i,j}$ represents the unity gaussian variance stochastic process with autocorelation

$$\langle \eta_{i,j}, \eta_{i',j'} \rangle = \delta(i-i')\delta(j-j') \tag{5.2}$$

Each of the obtained noisy images I_b is represented at Fig. 5.2 in the case considered throughout this chapter, namely when the root mean square amplitude of the noise σ is set to σ =0.1. For a sake of clarity, we have chosen to zoom each image which fits the same size without changing the image resolution N^2 which remains $N^2 = 64^2$, $N^2 = 128^2$, $N^2 = 256^2$, $N^2 = 512^2$ pixels for images 1, 2, 3 and 4 respectively.

These noisy images I_b, which can have different resolutions N^2, will constitute the inputs of our resonant detector.

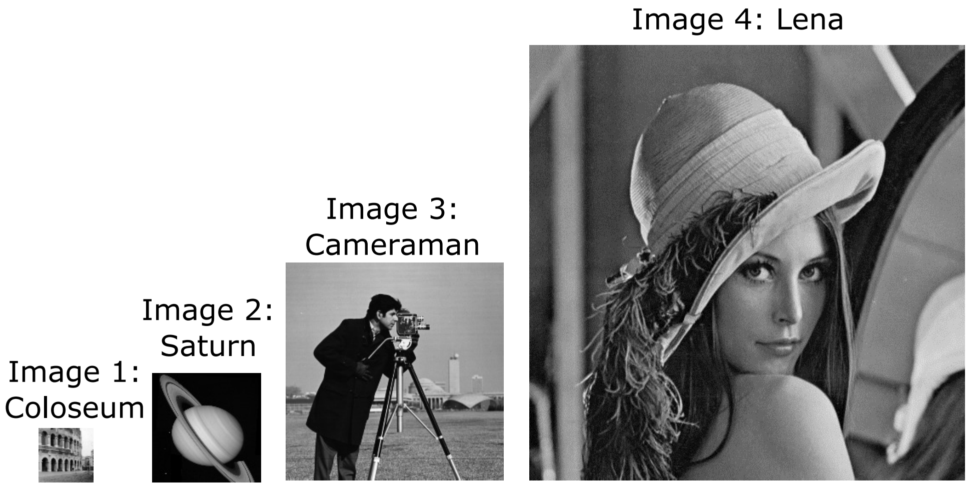

Figure 5.1: Images used throughout the chapter with different sizes $N \times N$. Images 1, 2, 3 and 4 represent the Roman Coloseum, Saturn, a Cameraman and Lena. The resolution of images 1, 2, 3 and 4 are $N^2 = 64^2$ pixels, $N^2 = 128^2$ pixels, $N^2 = 256^2$ pixels and $N^2 = 512^2$ pixels respectively.

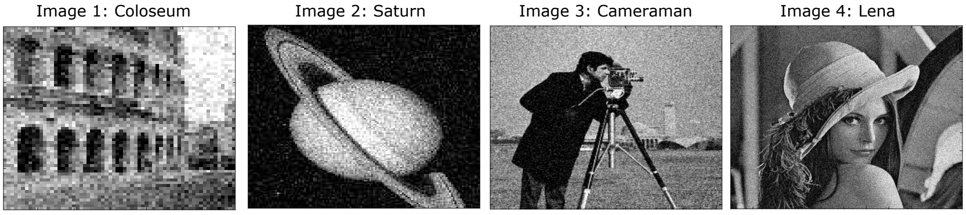

Image 1: Coloseum

Image 2: Saturn

Image 3: Cameraman

Image 4: Lena

Figure 5.2: The noisy images I_b with noise intensity σ =0.1. Each image has been zoomed even if they don't share the same resolution N^2. Coloseum: $N^2 = 64^2$ pixels, Saturn: $N^2 = 128^2$ pixels, Cameraman: $N^2 = 256^2$ pixels, Lena: $N^2 = 512^2$ pixels.

5.2.2/ THE RESONANT THRESHOLD DETECTOR

The resonant detector, which is simulated in this chapter, is described at Fig. 5.3. The noisy image input I_b of the threshold detector is first corrupted with an additive perturbation P which corresponds to noise in the case of a stochastic resonance based detector, while for a vibrational resonance based detector, P corresponds to an additive high frequency perturbation. Indeed, as shown at Fig. 5.3., a switch selects with a control c the appropriate perturbation between noise and high frequency sine spatial signal. The pixels gray levels $I_{P_{i,j}}$ of the perturbed image I_P are produced by adding the perturbation P to the noisy image I_b, thus they obey to:

$$I_{P_{i,j}} = P_{i,j} + I_{b_{i,j}}, \text{ with } i = 1,2, \quad ,N \text{ and } j = 1,2, \quad ,N \tag{5.3}$$

More precisely, if we introduce c as a switch control which takes the boolean value $c = 0$ for stochastic resonance or $c = 1$ for vibrational resonance, the perturbation added to each pixel of the noisy image I_b is defined by:

$$P_{i,j} = c \times A \cos\left(\frac{2\pi i j N_{HF}}{N^2} + \varphi_{i,j}\right) + (1-c) \times \gamma\eta'_{i,j} \text{ with } i = 1,2, \quad ,N \text{ and } j = 1,2, \quad ,N \tag{5.4}$$

According to the value of the switch command c, the device which has been designed corresponds to:

- A stochastic resonance based detector (SR-detector) when $c = 0$. Indeed, in eq. (5.4), the perturbation is the random term consisting of the unitary variance gaussian process $\eta'_{i,j}$ multiplied by the noise root mean square amplitude γ. In this case, the detector can be optimized by tuning the noise intensity γ of the perturbation.

- A vibrational resonance based detector (VR-detector) when the switch control is set to $c = 1$. In this case, the perturbation reduces to the high frequency cosine term of amplitude A, initial phase $\varphi_{i,j}$ and frequency adjusted with integer N_{HF}. In particular, the initial phase $\varphi_{i,j}$ is chosen randomly in a spatial gaussian distribution with standard deviation σ_φ =0.3π, that is $\varphi_{i,j} = \sigma_\varphi \zeta_{i,j}$ where $\zeta_{i,j}$ is a gaussian unitary variance process. Note that, in this chapter, we propose to investigate how the detector can be optimized by tuning the perturbation parameters, namely its amplitude A but also its spatial frequency which is adjusted with N_{HF}.

In Fig. 5.3, the detector processes the perturbed image I_P to produce the output black and white image T by performing a threshold filtering with threshold V_{th} according to the following rules:

$$\begin{aligned} &\text{if } I_{P_{i,j}} > V_{th}, && T_{i,j} = 1 \text{ (white level)} \\ &\text{else} && T_{i,j} = 0 \text{ (black level)} \end{aligned} \tag{5.5}$$

Moreover, the threshold detector used in eq. (5.5) is chosen such that the unperturbed image I_b remains subthreshold, that is not detectable by the detector without the help of the perturbation P. For all the results presented in this article, to ensure this condition, we use V_{th} =1.2.

Lastly the performance of the detector is quantified by a measurement of similarity between the initial image I and the black and white detected image T. More precisely, we use the cross-covariance which constitutes a fairly appropriate measurement of similarity between two images [97,221,227]. This cross-covariance between image I and T is defined by:

$$C_{I,T} = \frac{\Big\langle (I - \langle I \rangle)(T - \langle T \rangle) \Big\rangle}{\sqrt{\Big\langle (I - \langle I \rangle)^2 \Big\rangle \Big\langle (T - \langle T \rangle)^2 \Big\rangle}}, \tag{5.6}$$

where $\langle \; \rangle$ corresponds to an average over the whole image, that is an average across all the image pixels. Moreover, the cross-covariance defined by eq. (5.6) was numerically estimated

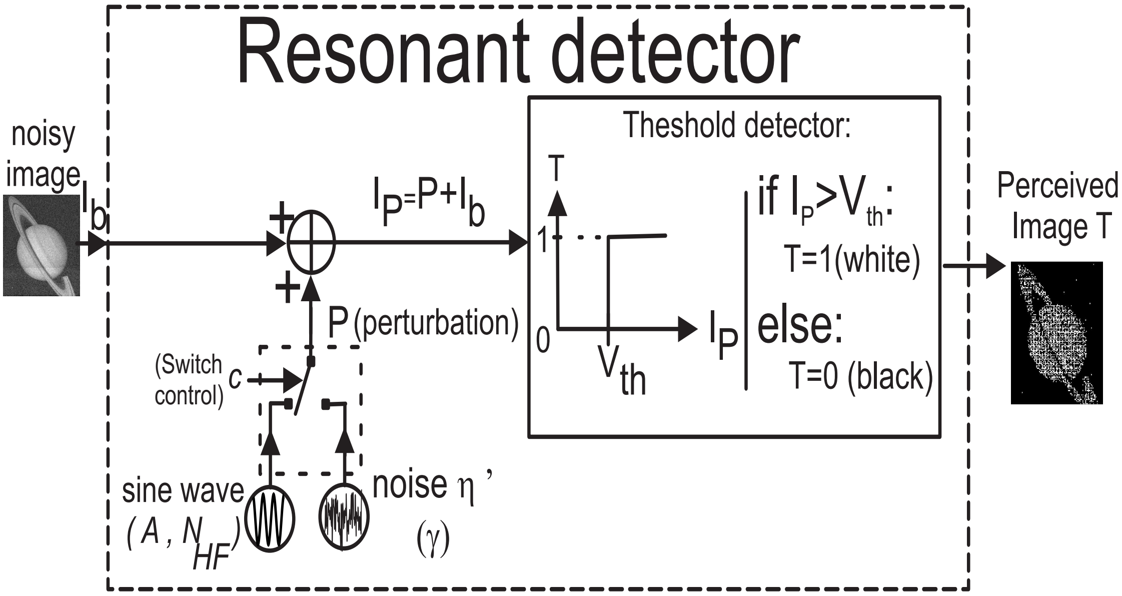

Figure 5.3: Sketch of the resonant detector which performs a threshold filtering of the perturbed image I_p and which perceives the black and white image T . The input of the resonant detector is the noisy image I_b which is perturbed by an additive perturbation P selected by a switch between noise or a sine perturbation. The switch command c chooses a noise perturbation η' of intensity γ in the case of a stochastic resonance based detector, while for a vibrational resonance based detector, a sine signal of amplitude A and spatial frequency N_{HF} is selected.

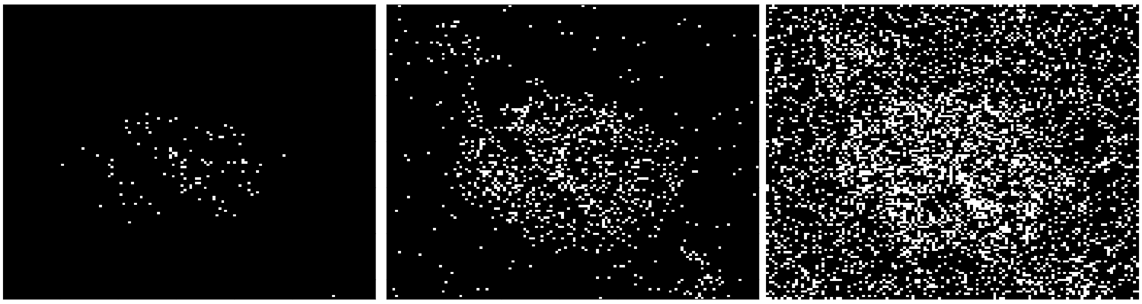

(a) (b) (c)

Figure 5.4: Images perceived by the SR-detector for different noise intensities γ. The initial noisy subthreshold image I_b of Saturn is corrupted with the increasing noise *RMS* amplitude γ and threshold filtered with threshold V_{th} =1.2 to produce the black and white images presented at subfigures $(a-c)$. (a): γ =0.2. (b): γ =0.5. (c): γ =1.2. The best perception of Saturn image is obtained for the optimal noise value γ^* =0.5 represented at subfigure (b).

by an average over a sufficient number of realizations of the noisy process.

5.3/ STOCHASTIC RESONANCE BASED DETECTOR

The switch of the detector of Fig. 5.3 takes the value $c=0$ such that the perturbation is a noise source of Root Mean Square *RMS* amplitude γ. Therefore, in the case of a SR-detector, the perturbation defined by expression (5.4) reduces to

$$P_{i,j}=\gamma\eta'_{i,j} \text{ with } i=1,2,\ldots,N \text{ and } j=1,2,\ldots,N \tag{5.7}$$

The black and white images T perceived by the detector are presented at Fig. 5.4 for growing values of the *RMS* amplitude of the noise perturbation, and in the case of the image 2 representing Saturn. For small noise intensities γ, as shown in Fig. 5.4.(a) for γ =0.2, threshold crossing events rarely occur. It results that they are not enough to allow the detector to retrieve the subthreshold information contained in the initial image. Next, for an intermediate value of the noise *RMS* amplitude, noise cooperates with the subthreshold image to reveal the coherent structure of the image. Indeed, the information is better perceived through the threshold detector for this optimal noise intensity γ =0.5 at Fig. 5.4.(b). Lastly, for greater noise intensities, the random nature of noise dominates the process of threshold crossing and hinders the perception of the image information through the detector. The resulting image at Fig. 5.4.(c) obtained for γ =1.2 seems completely noisy.

This is a qualitative signature of stochastic resonance, where an appropriate amount of noise enhances the response of a nonlinear system to a coherent input information. This effect is usually revealed by a quantitative performance measure of the system output which exhibits a resonance at an optimal *RMS* noise amplitude γ^*. The choice of the performance measure to highlight SR most often depends on the input signal and the context of applications. For instance, the signal to noise ratio is more appropriate for periodic signals, while for aperiodic signals the mutual infor-

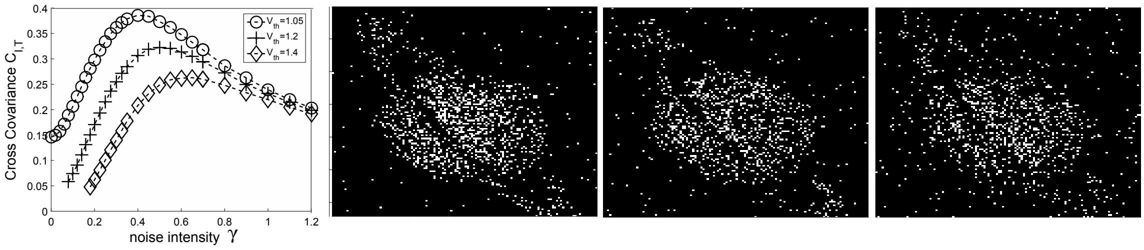

(a) *(b)* *(c)* *(d)*

Figure 5.5: Perception of the Saturn image through the SR-detector for different threshold levels V_{th}. Parameter: σ =0.1. (a): Cross-covariance $C_{I,T}$ versus the noise intensity γ for three different threshold values V_{th}. Dashed lines are guides to the eye. The best perceived images obtained for the optimal noise intensity γ^* are displayed for each considered threshold value V_{th} at subfigures $(b-d)$. (b): V_{th} =1.05 requires γ^* =0.4 to achieve $C_{I,T}(\gamma^*)$ =0.386. (c): V_{th} =1.2 requires γ^* =0.5 to achieve $C_{I,T}(\gamma^*)$ =0.322. (d): V_{th} =1.4 requires γ^* =0.65 to achieve $C_{I,T}(\gamma^*)$ =0.263.

mation, the channel capacity, the probability of error [102, 241–243] or the cross-covariance are rather preferred. In our case, we choose the cross-covariance $C_{I,T}$ defined by eq. (5.6) since it is commonly used in the context of image processing [97, 221] where images are rather aperiodic bidimensional signals. For the proposed image of Saturn, the cross-covariance C_{IT} is plotted with crosses against the noise level γ at Fig. 5.5.(a) when the detector threshold V_{th} is set to V_{th} =1.2. The curve exhibits a non monotonous behavior versus the noise intensity γ, which is a classical SR signature. Indeed, such a typical bell shaped curve indicates that there exists an optimal value of the noise γ^* which optimizes the system response. Note that, this optimal noise level γ^* is γ^* =0.5, and also corresponds to the noise level used in Fig. 5.4. (b) to obtain qualitatively the best image perception. Usually, the optimal performances of the system are strongly affected by the threshold of the detector. Especially, the gap between the subthreshold information signal and the threshold significantly affects the optimal performance that can be achieved by the system with the help of noise. To illustrate this feature, we have also plotted at Fig. 5.5. (a) the cross-covariance for two other values of the threshold V_{th}, namely V_{th} =1.05 plotted with circles and V_{th} =1.4 plotted with diamonds. When the threshold is reduced, we observe that the optimal noise γ^* =0.4 provides a better cross-covariance $C_{I,T}$, while increasing the threshold to V_{th}=1.4 involves a weaker cross-covariance. The curves presented for the three threshold values show that the more the image is far from the threshold, the less the perception of good quality image. Moreover, in the same time, a greater noise level is required to optimize the system.

This fact can be visually confirmed if we compare the images perceived through the detector for each optimal noise intensity γ^* corresponding to each of the three considered thresholds, namely γ^* =0.4 for V_{th} =1.05, γ^* =0.5 for V_{th} =1.2 and γ^* =0.65 for V_{th} =1.4. These images are reported at Fig. 5.5. (b), (c) and (d). It is clear that the best perception is achieved for the weakest threshold and that the quality of the perceived image decreases as the initial image is far from the threshold detector. Note that, in the whole article and in all that follows, we restrict our study to the intermediate value of the threshold V_{th} =1.2.

We have also analyzed the perception of the other initial images of Fig. 5.1 whose size N^2 ranges from $N^2 = 64^2$ pixels to $N^2 = 512^2$ pixels. Our results are summarized at Fig. 5.6. For all the considered initial images, a stochastic resonance type curve is observed for the evolution of the cross-covariance against the *RMS* noise level γ. Moreover, for each of the initial images of Fig. 5.1, we propose in subfigures 5.6. $(b-d)$ the best image perceived when the noise intensity is tuned to the noise level γ^* which maximizes the cross-covariance. Except for the first image of the Coloseum, stochastic resonance reveals quite fairly the information contained in each subthreshold initial image. In fact, the effect is less pronounced for the image of the Coloseum owing to its very low resolution of $N^2 = 64^2$ pixels which is not the most appropriate resolution to observe image details. Note that, we have reported in table 5.1 all the necessary features of our SR-detector, that is for each initial image: the image size , the optimal noise intensity γ^* and the best value of the cross-covariance $C_{I,T}$ achieved for $\gamma = \gamma^*$. This values will be of crucial interest to develop the VR-detectors presented in the next section.

Table 5.1: Features of the stochastic resonance based detector with threshold V_{th} =1.2. γ^* represents the optimal noise intensity which maximizes the cross-covariance $C_{I,T}$.

Image number	Image size N^2	Optimal noise γ^*	Best cross-covariance $C_{I,T}(\gamma = \gamma^*)$
Image 1: Coloseum	64^2	0.39	0.274
Image 2: Saturn	128^2	0.5	0.322
Image 3: Cameraman	256^2	0.59	0.199
Image 4: Lena	512^2	0.465	0.208

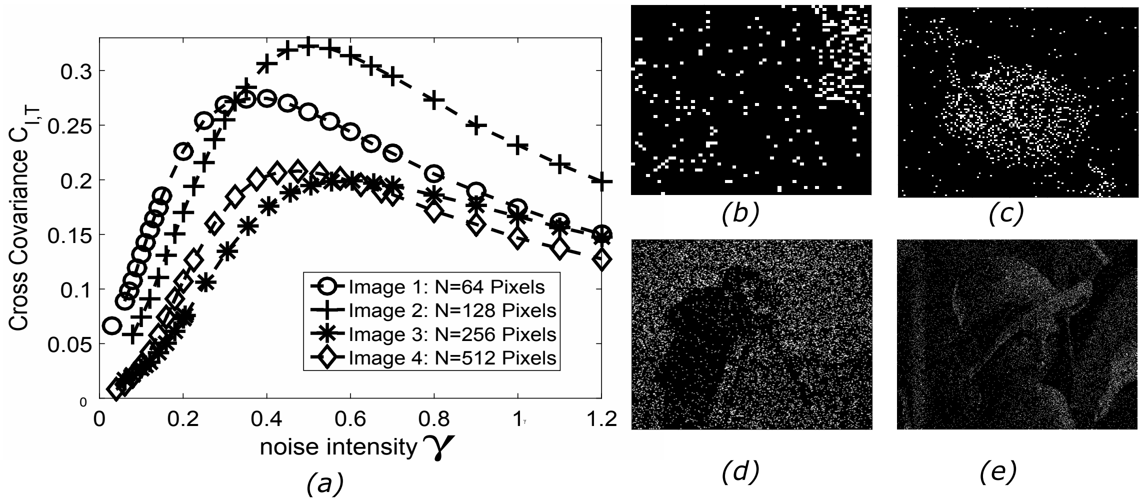

Figure 5.6: Perception of the different images through the SR-detector. Parameters: V_{th} =1.2 and σ =0.1. (a) Cross-covariance $C_{I,T}$ of each image against the noise intensity γ. Dashed lines are guides to the eye. The best perceived images are displayed for the optimal noise intensity γ^* at subfigures $(b-d)$. (b): image 1 requires γ^* =0.39 to achieve $C_{I,T}(\gamma^*)$ =0.274. (c): image 2 requires γ^* =0.5 to achieve $C_{I,T}(\gamma^*)$ =0.322. (d): image 3 requires γ^* =0.59 to achieve $C_{I,T}(\gamma^*)$ =0.199. (e): image 4 requires γ^* =0.465 to achieve $C_{I,T}(\gamma^*)$ =0.208.

5.4/ VIBRATIONAL RESONANCE BASED DETECTOR

By setting the switch control c of the detector to $c = 1$, the perturbation P of Fig. 5.3 defined by eq. (5.4) takes the form of the following sine function:

$$P_{i,j} = A\cos\left(\frac{2\pi i j N_{HF}}{N^2} + \varphi_{i,j}\right) \text{ with } i = 1,2,\ldots,N \text{ and } j = 1,2,\ldots,N \tag{5.8}$$

In this section, we analyze how the perception of the images presented in Fig. 5.1 through the VR-detector can be optimized by tuning the perturbation amplitude A and its spatial frequency N_{HF}. Therefore, it leads us to first define an amplitude optimized VR-detector obtained when the frequency N_{HF} of the perturbation remains constant while its amplitude A can be adjusted. Next, motivated by the work of Yao *et al* [147], which have obtained better resonances when the perturbation frequency can be tuned, we propose to develop a frequency optimized VR-detector: the amplitude of the perturbation will remain constant while its frequency will be adjusted.

5.4.1/ AMPLITUDE OPTIMIZED VR-DETECTOR

For each image of Fig 5.1, the spatial frequency N_{HF} of the perturbation is adjusted according to the image resolution N^2 to ensure that the normalized frequency N_{HF}/N^2 remains constant, while the perturbation amplitude A can be tuned. We arbitrarily choose the normalized value $N_{HF}/N^2 = 1/4$ which is not restrictive since the influence of the normalized frequency will be addressed in the next subsection. Like the SR-detector, we first consider the noisy image of Saturn whose resolution is $N^2 = 2^{14}$ pixels and whose level of noise is σ =0.1. It means that in this case, the frequency of the perturbation must be tuned to $N_{HF} = 2^{12}$ to ensure $N_{HF}/N^2 = 1/4$. Fig. 5.7 displays the different images perceived by the detector for growing values of the perturbation amplitude A.

For the weakest perturbation amplitude, namely A =0.3, the threshold triggerings induced by the

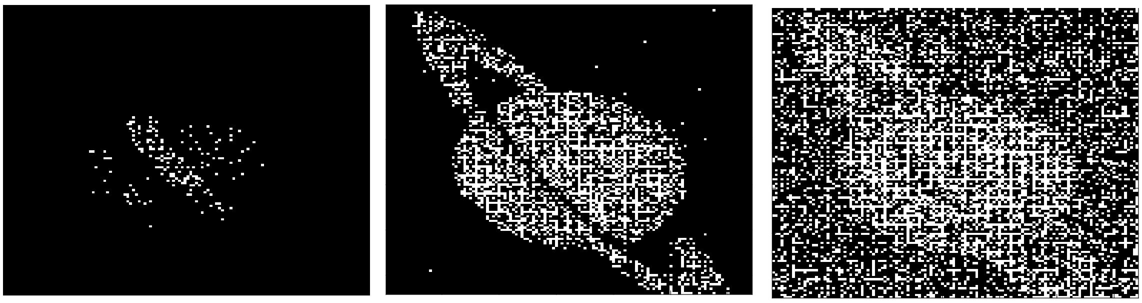
(a) (b) (c)

Figure 5.7: Images perceived by the VR-detector for different perturbation amplitudes A. The initial noisy subthreshold image I_b of Saturn is corrupted with increasing perturbation amplitude A and then threshold filtered with threshold V_{th} =1.2 to produce the black and white images presented at subfigures (a-c) . (a): A =0.3. (b): A =0.95. (c): A =1.4. The best perception of Saturn image is obtained for the optimal perturbation amplitude A =0.95 at subfigure (b).

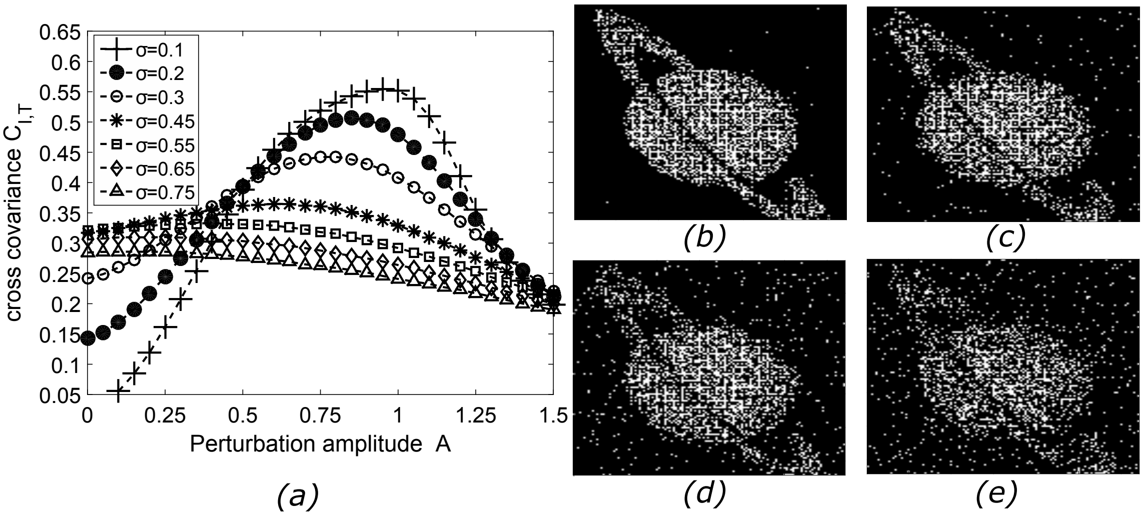

Figure 5.8: Perception through the VR-detector of the saturn image with different noise intensities σ. Parameter: V_{th} =1.2. (a): Cross-covariance $C_{I,T}$ against the perturbation amplitude A for different levels of noise σ. Dashed lines are guides to the eye. For each noise intensity σ where a resonance of the cross-covariance occurs, we have displayed the best perceived image obtained for the optimal perturbation amplitude A^* at subfigures $(b-e)$. (b): σ =0.1 requires A^* =0.95 to achieve $C_{I,T}(A^*)$ =0.554. (c): σ =0.2 requires A^* =0.85 to achieve $C_{I,T}(A^*)$ =0.506. (d): σ =0.3 requires $A = 0\ 8$ to achieve $C_{I,T}(A^*)$ =0.442. (e): σ =0.45 requires A^* =0.6 to achieve $C_{I,T}(A^*)$ =0.365.

addition of perturbation are not sufficient to enable the perception of the initial image with a good quality. However, in the case of Fig. 5.7. (b), for the intermediate amplitude value A =0.95, the perturbation positively helps the initial subthreshold image to cross the threshold. The perception of the initial image details is then the best and qualitatively exceeds the quality reported with the SR-detector at Fig. 5.4.(b). By contrast, for the greatest perturbation amplitude considered at Fig. 5.7.(c), the information contained in the initial image is not well retrieved by the detector because the threshold triggerings are rather ruled by the perturbation than by the initial image. It results that the perceived image is dominated by the high frequency perturbation.

To quantify the performance of the VR-detector, we have plotted at Fig. 5.8.(a) the cross-covariance $C_{I,T}$ against the perturbation amplitude A for different levels of noise σ ranging from σ =0.1 to σ =0.75. First, to compare the VR-detector and the SR-detector, it is necessary to consider the same level of noise in the input initial image I_b for both detectors. Therefore, since we used a noise level σ =0.1 for the SR-detector, we can first comment the curve plotted with crosses at Fig. 5.8.(a) which corresponds to the same noise intensity σ =0.1. This curve, which shows the evolution of the cross-covariance $C_{I,T}$ versus the perturbation amplitude A, presents a non monotonous behavior with a maximum value $C_{I,T}$ =0.554 achieved for a perturbation amplitude A^* =0.95. Such resonance curve constitutes the classical signature of the vibrational resonance phenomenon. Moreover, the optimal value of the cross-covariance exceeds the one obtained with the SR-detector which was $C_{I,T}$ =0.322 for the same noisy Saturn image. It quantitatively confirms that VR-detector perceives noisy images with a better quality than SR-detectors.

The same resonant behaviors of the cross-covariance are reported at Fig. 5.8.(a) for the noise intensity σ =0.2 (filled circles), σ =0.3 (empty circles) and σ =0.45 (stars). The corresponding

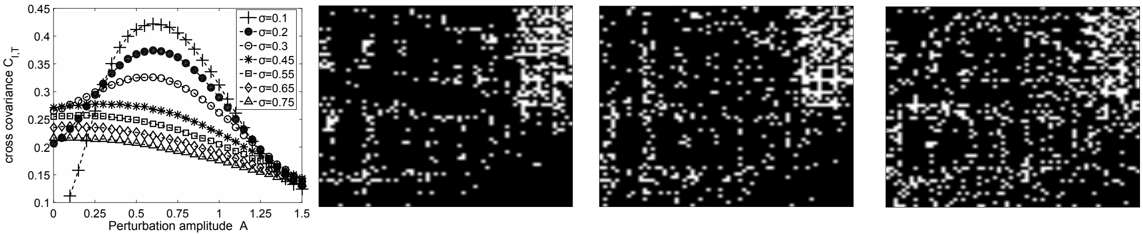

(a) (b) (c) (d)

Figure 5.9: Perception through the VR-detector of the Coloseum image with different noise intensities σ. Parameter: V_{th} =1.2. (a): Cross-covariance $C_{I,T}$ against the perturbation amplitude A for different levels of noise σ. Dashed lines are guides to the eye. For each noise intensity σ where a resonance of the cross-covariance occurs, we have displayed the best perceived image obtained for the optimal perturbation amplitude A^* at subfigures $(b-d)$. (b): σ =0.1 requires A^* =0.6 to achieve $C_{I,T}(A^*)$ =0.422. (c) σ =0.2 requires A^* =0.6 to achieve $C_{I,T}(A^*)$ =0.374. (d): σ =0.3 requires A^* =0.6 to achieve $C_{I,T}(A^*)$ =0.325.

optimal images are proposed at Fig. 5.8.(c), (d) and (e) respectively. In addition, we have recalled at Fig. 5.8.(b), the optimal image obtained with the VR-detector when the noise level is σ =0.1. We observe that the quality of the perceived image decreases as the noise level of the initial image increases. In fact, it is not surprising since the maxima of the cross-covariance also reduces with increasing values of noise at Fig. 5.8.(a).

On the other hand, Fig. 5.8.(a) also reveals that vibrational resonance ceases to exist when the noise level σ of the initial image exceeds the optimal noise *RMS* value γ^* of the SR-detector. Indeed, the cross-covariance is a monotonous decreasing function of the perturbation amplitude for the noise intensity σ =0.55 (squares), σ =0.65 (diamonds) and σ =0.75 (triangles) which are beyond the critical noise value γ^* =0.5 of the SR-detector. It results that there exists a critical value of noise beyond which no perception enhancement can be expected with vibrational resonance.

We also propose to analyze if the image resolution N^2 impacts the performances of the VR-detector. Therefore, we consider the other images of Fig. 5.1 with the same level of noise ranging from σ =0.1 to σ =0.75. The cross-covariances have been estimated against the amplitude of the perturbation A, while the spatial normalized perturbation frequency remains $N_{HF}/N^2 = 1/4$. Our results for the first image representing the Coloseum are reported at Fig. 5.9 with $N_{HF} = 2^{10}$ since $N^2 = 2^{12}$. First, we recall from Table 5.1 that the optimal noise value γ^* which maximized the SR-detector was γ^* =0.39 with a maximal value of the cross-covariance $C_{I,T}(\gamma^*)$ =0.274. Fig. 5.9. (a) confirms that vibrational resonance ceases to exist for noise intensities σ exceeding γ^*. Indeed, only the curves corresponding to the noise levels σ =0.1, σ =0.2 and σ =0.3 exhibit a resonant behavior, while for the other noise values, namely σ =0.45, σ =0.55, σ =0.65, σ =0.75, the cross-covariance $C_{I,T}$ monotonously decreases against the perturbation amplitude A. Nevertheless, for the noise intensity σ =0.1, the VR-detector perceives the initial image better than the SR-detector since a cross-covariance $C_{I,T}$ =0.422 is reached for the optimal perturbation amplitude A^* =0.6. Comparing Figs. 5.6.(b) and 5.9.(b), which display the perceived image through each detector, there is no doubt that the VR-detector outperforms the SR-detector. However, when the noise level of the initial image increases at Figs. 5.9.(c) and (d), the quality of the retrieved image reduces.

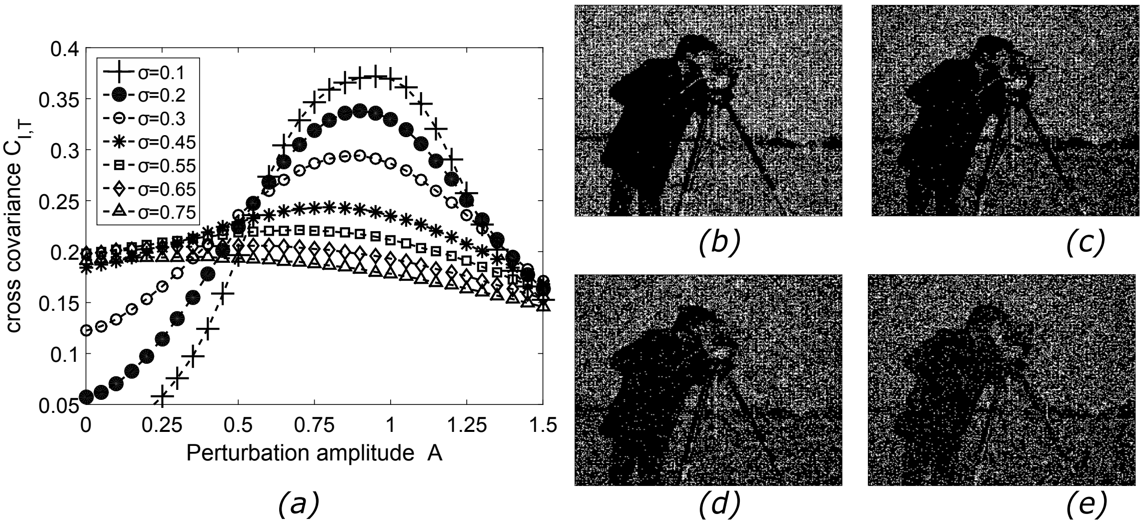

(a) (b) (c) (d) (e)

Figure 5.10: Perception through the VR-detector of the Cameraman image with different noise intensities σ. Parameter: V_{th} =1.2. (a): Cross-covariance $C_{I,T}$ against the perturbation amplitude A for different levels of noise σ. Dashed lines are guides to the eye. For each noise intensity σ where a resonance of the cross-covariance occurs, we have displayed the best perceived image obtained for the optimal perturbation amplitude A^* at subfigures $(b-e)$. (b): σ =0.1 requires A^* =0.95 to achieve $C_{I,T}(A^*)$ =0.372. (c): σ =0.2 requires A^* =0.9 to achieve $C_{I,T}(A^*)$ =0.342. (d): σ =0.3 requires A^* =0.9 to achieve $C_{I,T}(A^*)$ =0.292. (e): σ =0.45 requires A =0.8 to achieve $C_{I,T}$ =0.243.

The results obtained with the third image representing the Cameraman with a resolution of $N^2 = 256^2$ pixels are available at Fig. 5.10. Note that the perturbation frequency is now tuned to $N_{HF} = 2^{14}$ to satisfy the condition $N_{HF}/N^2 = 1/4$. According to table 5.1, vibrational resonance is expected to occur for noise levels σ below the critical value γ^* =0.59. It is verified at Fig. 5.10.(a), where the evolution of the cross-covariance versus the perturbation amplitude exhibits a resonance only for the noise intensities σ =0.1, σ =0.2, σ =0.3, σ =0.45 and σ =0.55. Note that in the later case, the resonance is less pronounced since the noise level σ =0.55 is close to the critical value γ^* =0.59. The corresponding images perceived through the VR-detector are also presented at Figs. 5.10.$(b-e)$ to provide a qualitative overview of the optimal achieved performances according to the noise level.

Lastly, the fourth image representing Lena with a resolution of $N^2 = 512^2$ pixels is used as the input subthreshold image. It leads to consider a spatial perturbation frequency $N_{HF} = 2^{16}$ since we fit the condition $N_{HF}/N^2 = 1/4$. Once again, the cross-covariance $C_{I,T}$ can be maximized for an optimal amplitude A^* of the high frequency perturbation if the noise level of the input image σ remains below the critical noise value γ^* defined by the SR-detector. For the image of Lena, we have established at table 5.1 that this critical value is γ^* =0.465. Therefore, the curves of cross-covariance, which correspond to the noise intensities σ =0.1, σ =0.2, σ =0.3 and σ =0.45, exhibit a behavior with a resonance at Fig. 5.11.(a). It indicates that an appropriate tuning of the perturbation amplitude to A^* allows to enhance the perception of the subthreshold noisy image. The perceived images for each noise level are reported at Fig. 5.11.$(b-e)$ when the perturbation amplitude has been optimally set to A^*. Especially, the perceived image of Fig. 5.11.(b) can be compared with the one obtained with the SR-detector at Fig. 5.6.(e) since they share the same input noise level σ =0.1. It

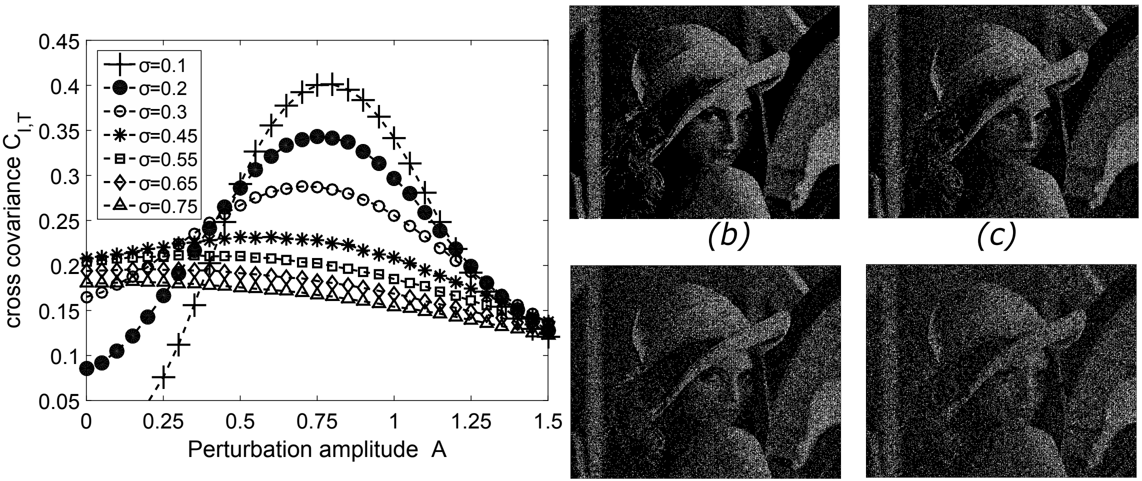

(a) (b) (c) (d) (e)

Figure 5.11: Perception through the VR-detector of the Lena image with different noise intensities σ. Parameter: V_{th} =1.2. (a): Cross-covariance $C_{I,T}$ against the perturbation amplitude A for different levels of noise σ. Dashed lines are guides to the eye. For each noise intensity σ where a resonance of the cross-covariance occurs, we have displayed the best perceived image obtained for the optimal perturbation amplitude A^* at subfigures $(b-e)$. (b): σ =0.1 requires A^* =0.8 to achieve $C_{I,T}(A^*)$ =0.401. (c): σ =0.2 requires A^* =0.75 to achieve $C_{I,T}(A^*)$ =0.343. (d): σ =0.3 requires A^* =0.7 to achieve $C_{I,T}(A^*)$ =0.288. (e): σ =0.45 requires A^* =0.6 to achieve $C_{I,T}(A^*)$ =0.232.

is clearly established that, whatever the considered image, a better enhancement of image perception is achieved with the VR-detector than with the SR-detector. By contrast, the cross-covariance monotonously decreases for the noise intensities σ =0.55, σ =0.65 and σ =0.75 revealing that no enhancement of perception through the VR-detector can be obtained if the noise of the input image exceeds the critical value γ^*.

The main features of the VR-detector are summarized in table 5.2 when the normalized spatial frequency of the perturbation remains $N_{HF}/N^2 = 1/4$. First, we have specified the critical noise level γ^* beyond which the detector fails to enhance image perception. Next, for each noise intensity σ below γ^*, we provide the value A^* of the perturbation amplitude which gives the best image perception and the corresponding maximum value of the cross-covariance $C_{I,T}(A^*)$. This table shows that as the noise intensity increases, the performance of the vibrational resonance reduces, whatever the considered images. Moreover, except for the first image of the Coloseum whose resolution N^2 is very poor, it requires a weaker amplitude of the perturbation A^* for greater noise intensity σ to achieve the best performance. One may wonder if the normalized spatial frequency N_{HF}/N^2 of the perturbation would have an impact on the performances achieved by the detector. It is the aim of the next subsection for which table 5.2 will constitute a reference.

5.4.2/ FREQUENCY OPTIMIZED VR-DETECTOR

We now consider that the spatial normalized frequency N_{HF}/N^2 of the perturbation evolves, while the amplitude of the perturbation A remains constant. Our study concerning the effect of the perturbation frequency has been carried out for the five following constant perturbation amplitudes A:

0.1, 0.6, 0.8, 0.95 and 1.4. It is an appropriate choice to obtain a fairly good overview of the system behavior. Indeed, these values include the optimal amplitudes A^* which have been introduced in the previous subsection at table 5.2 to maximize the perception of the images when the normalized spatial frequency was set to $N_{HF}/N^2 = 1/4$. To complete the general set-up, the noise intensity σ of the noisy image I_b at the input of the VR-detector is adjusted to the value which was used at the input of the SR-detector, namely σ =0.1. It allows to directly compare the performance between the two detectors in terms of image perception.

First, we analyze how the perturbation frequency influences the perception of the Saturn image through the VR-detector. For each value of the perturbation amplitude, the cross-covariance has been computed versus the normalized perturbation frequency N_{HF}/N^2. For a sake of clarity, our results are presented at Fig. 5.12.(a) where we have used a log_2 scale for the horizontal axis.

We remark that the curve plotted with circles and which has been obtained with the perturbation amplitude A =0.95 always remains beyond the other curves. It means that for this amplitude of the perturbation, the detector provides the best performance whatever the frequency of the perturbation. Of course, this specific value of the perturbation amplitude also corresponds to the optimal value A^* which was introduced in the previous section in table 5.2 to optimize the VR-detector versus the amplitude at constant frequency. Moreover, for the perturbation amplitudes below A^*, namely A =0.8 (squares), A =0.6 (crosses) and A =0.1 (diamonds), the corresponding cross-covariance curves are ranked one on top of the others from the weakest amplitude A to the greatest one. By contrast, when the perturbation amplitude is set to A =1.4 and exceeds A^*, the cross-covariance curve plotted with stars is always below the curve obtained with the optimal setting $A = A^*$. This specific behavior indicates that irrespective of the perturbation frequency, the evolution of the cross-covariance versus the perturbation amplitude A follows the typical bell shaped curves presented in the previous section and which constitutes the signature of vibrational resonance.

On the other hand, the perturbation frequency directly impacts the quality of the perceived image since all cross-covariance curves share the same feature: whatever the considered amplitude A of the perturbation, the cross-covariance monotonously grows with the frequency until it saturates to a maximum value reached for the optimal normalized frequency $N^*_{HF}/N^2 = 1$. The perturbation frequency N_{HF} is then optimally set to $N^*_{HF} = N^2$ which corresponds to the value of the image resolution. Note that, when the perturbation frequency N_{HF} exceeds this optimal frequency N^*_{HF},

Table 5.2: Features of the VR-detector with spatial normalized frequency $N_{HF}/N^2 = 1/4$ and threshold V_{th} =1.2. A^* represents the optimal amplitude of the perturbation which maximizes the cross-covariance $C_{I,T}$ and γ^* the critical noise value beyond which the detector cannot recover the subthreshold image.

Image number	critical noise γ^*	$C_{I,T}(A^*)$ for σ =0.1	$C_{I,T}(A^*)$ for σ =0.2	$C_{I,T}(A^*)$ for σ =0.3
1: Coloseum $N^2 = 2^{12}$	0.39	0.422 for A^* =0.6	0.374 for A^* =0.6	0.325 for A^* =0.6
2: Saturn $N^2 = 2^{14}$	0.5	0.554 for A^* =0.95	0.506 for A^* =0.85	0.442 for A^* =0.8
3: Cameraman $N^2 = 2^{16}$	0.59	0.372 for A^* =0.95	0.342 for A^* =0.9	0.292 for A^* =0.9
4: Lena $N^2 = 2^{18}$	0.465	0.401 for A^* =0.8	0.343 for A^* =0.75	0.288 for A^* =0.7

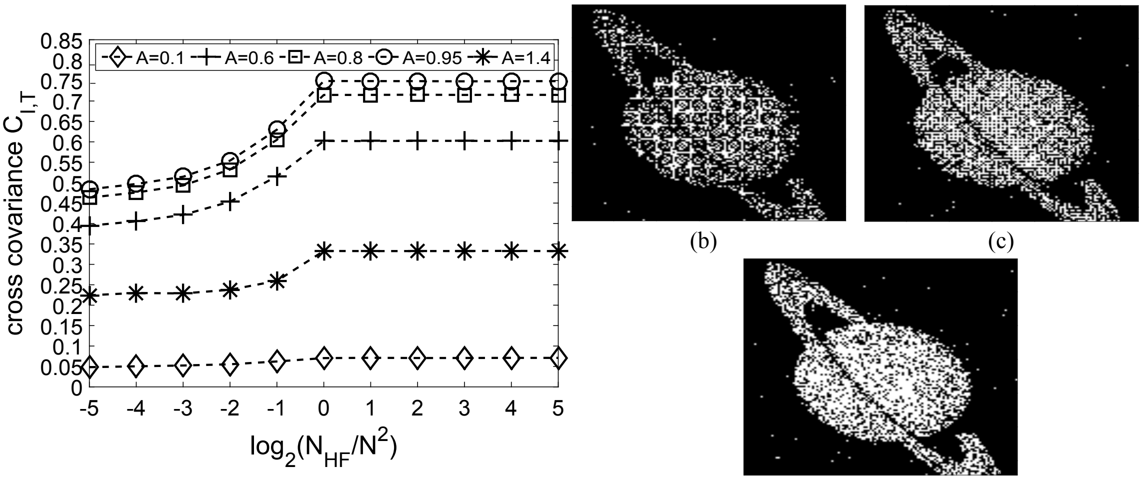

(a) (b) (c) (d)

Figure 5.12: Effect of the perturbation frequency on the perception of Saturn through the VR-detector. Parameters: $N^2 = 2^{14}$, V_{th} =1.2 and σ =0.1. (a): Cross-covariance $C_{I,T}$ against the normalized perturbation frequency N_{HF}/N^2 for different amplitudes A of the perturbation. Dashed lines are guides to the eye. For the optimal perturbation amplitude A^* =0.95, we have displayed the images perceived through the detector for three specific frequencies at subfigures $(b-d)$. (b): $N_{HF} = 2^{11}$. (c): $N_{HF} = 2^{13}$. (d): $N_{HF} = 2^{14}$. The best perception of the Saturn image is achieved when the cross-covariance saturates to $C_{I,T}$ =0.749, that is when the perturbation is tuned to the optimal amplitude A^* =0.95 and when its frequency is greater than the optimal value $N_{HF}^* = N^2 = 2^{14}$.

the wavelength of the perturbation becomes shorter than the interpixel distance leading to the saturation of the cross-covariance. In summary, the best perception of the Saturn image is achieved when the perturbation amplitude A matches A^* =0.95 and when the perturbation frequency exceeds $N_{HF}^* = N^2 = 2^{14}$. Indeed, if we visually analyze the images obtained for the optimal amplitude A^* =0.95, and presented for various frequencies at Figs. 5.12.$(b-d)$, there is no doubt that tuning the detector with the optimal frequency N_{HF}^* better enhances the image perception. Moreover, for the other frequencies chosen below the optimal value N_{HF}^* at Figs 5.12.$(b-c)$, we can note that the information can also be perceived. However, as observed for the weakest frequency at Fig. 5.12.(b), the perturbation also dominates the threshold crossing events and induces the lost of some image details.

Next, we have performed the test bench of our VR-detector by using the other images. The frequency analysis is reported at Fig. 5.13 for the image of the Coloseum whose resolution is the weakest, namely $N^2 = 64^2$ pixels. To comment the results, it is necessary to recall that in the previous section, we have established the exact value of the optimal perturbation amplitude A^* that maximizes the cross-covariance at constant frequency. This value, A^* =0.6, is one of the considered amplitudes used to plot the cross-covariance versus the perturbation frequency at Fig. 5.13.(a). This curve, plotted with crosses, is always over the others indicating that the amplitude A^* maximizes the image perception independently from the considered frequency. Moreover, the curves obtained for the amplitude exceeding A^*, namely A =0.8, A =0.95 and A =1.4, are located underneath each other and sorted from the weakest amplitude to the others. It shows that vibrational resonance occurs whatever the frequency, with a more or less pronounced resonance, which is defined by the curve corresponding to the optimal amplitude A^* =0.6 at Fig. 5.13.(a). In

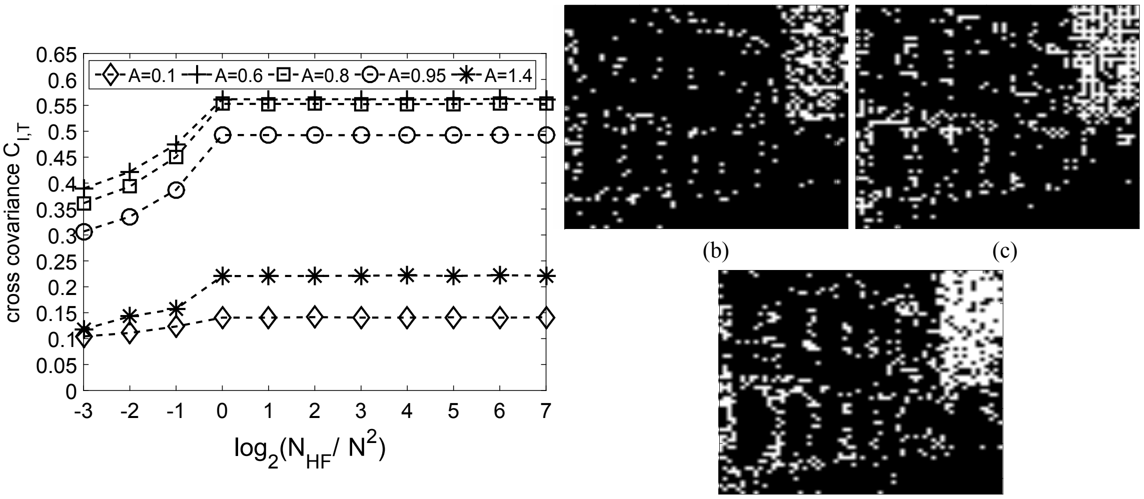

(a) (b) (c) (d)

Figure 5.13: Effect of the perturbation frequency on the perception of the Coloseum through the VR-detector. Parameters: $N^2 = 2^{12}$, V_{th} =1.2 and σ =0.1. (a): Cross-covariance $C_{I,T}$ against the normalized perturbation frequency N_{HF}/N^2 for different amplitudes A of the perturbation. Dashed lines are guides to the eye. For the optimal perturbation amplitude A^* =0.6, we have displayed the images perceived through the detector for three specific frequencies at subfigures $(b-d)$. (b): $N_{HF} = 2^9$. (c): $N_{HF} = 2^{11}$. (d): $N_{HF} = 2^{12}$. The best perception of the Coloseum image is achieved when the cross-covariance saturates to $C_{I,T}$ =0.562, that is when the perturbation is tuned to the optimal amplitude A^* =0.6 and when its frequency is greater than the optimal value $N^*_{HF} = N^2 = 2^{12}$.

the case of the Coloseum image, the cross-covariance saturation occurs for all perturbation amplitudes, when the frequency N_{HF} exceeds the optimal value $N^*_{HF} = 2^{12}$ which exactly matches the image resolution $N^2 = 2^{12}$ pixels. Therefore, as visually presented at Fig 5.13.$(b-d)$ for different perturbation frequencies, the best quality of perception is achieved when the perturbation of the VR-detector is optimally tuned with the amplitude A^* =0.6 and the frequency $N^*_{HF} = 2^{12}$.

Lastly, for the images of the Cameraman and Lena, which are displayed at Fig. 5.14 and 5.15, the cross-covariance follows the same trend and, therefore, do not alter the conclusion previously drawn with the images of Saturn and the Coloseum. Indeed, in the case of the Cameraman picture with resolution $N^2 = 2^{16}$ pixels, the cross-covariance saturates for the optimal frequency $N^*_{HF} = 2^{16}$ whatever the perturbation amplitude. Similarly, for the Lena image of resolution $N^2 = 2^{18}$ pixels, the saturation of the cross-covariance appears at frequencies $N^*_{HF} = 2^{18}$. Moreover, for both images, the cross-covariance obtained for the optimal amplitude A^* always remains the greatest irrespective of the perturbation frequency. Therefore, the existence of the classical vibrational resonance phenomenon for all the considered frequencies is clearly established whatever the considered image. Lastly, as shown by the images presented for various perturbation frequencies at Figs. 5.14.$(b-d)$ and 5.15.$(b-d)$, to obtain the best perception enhancement of subthreshold images, it is confirmed that the perturbation must be adjusted with the optimal amplitude A^* and the optimal frequency $N^*_{HF} = N^2$. Indeed, the more the frequency is far from the optimal value $N^*_{HF} = N^2$, the more the crossing threshold events are governed by the perturbation rather than the subthreshold image. It involves a qualitative lost of the image details when the frequency is too weak compared to the optimal value $N^*_{HF} = N^2$. Lastly, we quantitatively compare at table 5.3 the performances

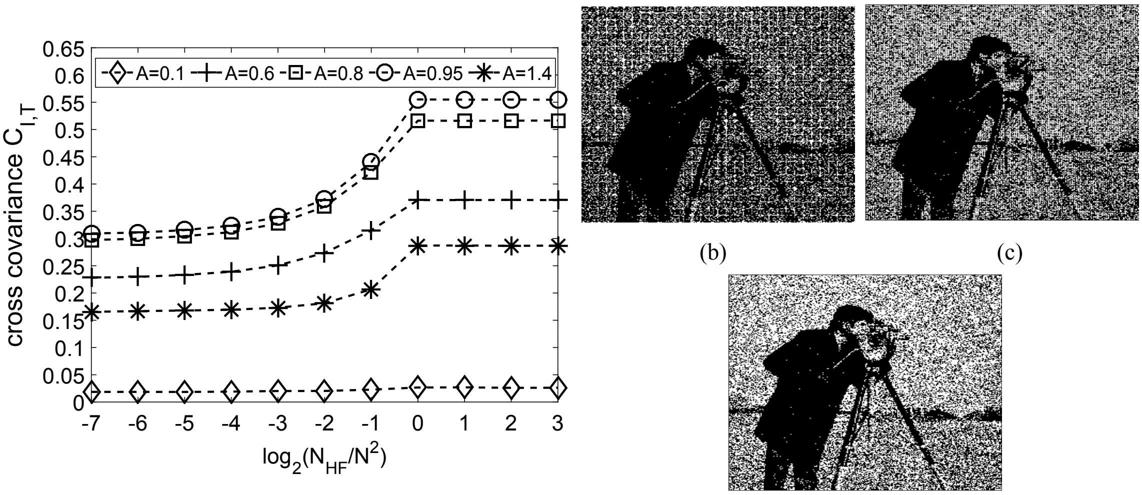

(b) (c)

(a) (d)

Figure 5.14: Effect of the perturbation frequency on the perception of the Cameraman through the VR-detector. Parameters: $N^2 = 2^{16}$, V_{th} =1.2 and σ =0.1. (a): Cross-covariance $C_{I,T}$ against the normalized perturbation frequency N_{HF}/N^2 for different amplitudes A of the perturbation. Dashed lines are guides to the eye. For the optimal perturbation amplitude A^* =0.95, we have displayed the images perceived through the detector for three specific frequencies at subfigures $(b-d)$. (b): $N_{HF} = 2^{13}$. (c): $N_{HF} = 2^{15}$. (d): $N_{HF} = 2^{16}$. The best perception of the Cameraman image is achieved when the cross-covariance saturates to $C_{I,T}$ =0.565, that is when the perturbation is tuned to the optimal amplitude A^* =0.95 and when its frequency is greater than the optimal value $N^*_{HF} = N^2 = 2^{16}$.

of the VR-detector and SR-detector. The cross-covariance is given for the SR-detector tuned with its optimal noise level γ^* and for the optimally tuned VR-detector with optimal perturbation amplitude A^* and optimal frequency N^*_{HF}. We have also added the cross-covariance of the VR-detector whose perturbation frequency obeys to $N_{HF} = N^2/4$ and whose amplitude is optimally set to A^*.

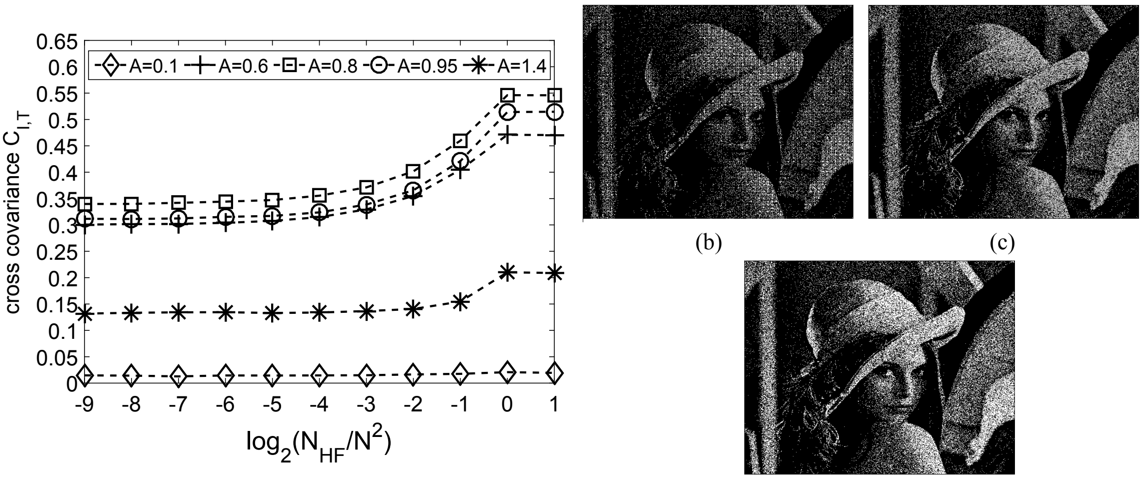

(b) (c)

(a) (d)

Figure 5.15: Effect of the perturbation frequency on the perception of Lena through the VR-detector. Parameters: $N^2 = 2^{18}$, V_{th} =1.2 and σ =0.1. (a): Cross-covariance $C_{I,T}$ against the normalized perturbation frequency N_{HF}/N^2 for different amplitudes A of the perturbation. Dashed lines are guides to the eye. For the optimal perturbation amplitude A^* =0.8, we have displayed the images perceived through the detector for three specific frequencies at subfigures $(b-d)$. (b): $N_{HF} = 2^{15}$. (c): $N_{HF} = 2^{17}$. (d): $N_{HF} = 2^{18}$. The best perception of the Lena image is achieved when the cross-covariance saturates to $C_{I,T}$ =0.546, that is when the perturbation is tuned to the optimal amplitude A^* =0.8 and when its frequency is greater than the optimal value $N^*_{HF} = N^2 = 2^{18}$.

Whatever the image and its resolution, the VR-detector clearly outperforms the SR-detector even if the perturbation frequency is not optimally tuned to N^*_{HF} but to $N_{HF} = N^2/4$.

Table 5.3: Features of the VR and SR detectors when the noise level of the input subthreshold image is σ =0.1 and when the detector threshold is V_{th} =1.2.

Image number and size N^2	Best cross-covariance of VR-detector with $N_{HF} = N^2/4$ $C_{I,T}(A^*, N_{HF} = N^2/4)$	Best cross-covariance of VR-detector $C_{I,T}(A^*, N^*_{HF})$	Best cross-covariance of SR-detector $C_{I,T}(\gamma^*)$
1: Coloseum $N^2 = 2^{12}$	0.422 for A^* =0.6 and $N_{HF} = 2^{10}$	0.562 for A^* =0.6 and $N^*_{HF} = 2^{12}$	0.274 for γ^* =0.39
2: Saturn $N^2 = 2^{14}$	0.554 for A^* =0.95 and $N_{HF} = 2^{12}$	0.749 for A^* =0.95 and $N^*_{HF} = 2^{14}$	0.322 for γ^* =0.5
3: Cameraman $N^2 = 2^{16}$	0.372 for A^* =0.95 and $N_{HF} = 2^{12}$	0.565 for A^* =0.95 and $N^*_{HF} = 2^{16}$	0.199 for γ^* =0.59
4: Lena $N^2 = 2^{18}$	0.401 for $A^* = 0\ 8$ and $N_{HF} = 2^{14}$	0.546 for A^* =0.8 and $N^*_{HF} = 2^{18}$	0.208 for γ^* =0.465

5.5/ CONCLUSION

In this chapter, we have first reviewed some applications of nonlinear resonances in the context of image processing and visual perception. Next, we have focused our study on the perception through a threshold detector of subthreshold noisy images which have different resolutions. The main feature of this detector is to use a perturbation whose parameters can be tuned to provide the best perception of the input subthreshold image whose noise level is σ.

When the perturbation corresponds to noise, the well-known stochastic resonance phenomenon takes place: there exists an optimal intensity of noise γ^* which optimizes the perception of the information contained in the noisy subthreshold input image. Indeed, using the cross-covariance $C_{I,T}$ as a measure of the similarity between the initial image I and the perceived image T, we have determined this optimal level of noise γ^*. We have shown that this specific noise value also corresponds to the critical noise intensity of the input image beyond which a spatial high frequency perturbation fails to retrieve the information of the subthreshold image. However, for images with a noise level below the critical value γ^*, considering a high frequency perturbation instead of noise gives rise to the vibrational resonance phenomenon: similar to stochastic resonance, there exists an appropriate setting of the perturbation parameters which provides the best perception of the subthreshold image. We have first characterized this VR-detector at constant frequency versus the amplitude of the perturbation to highlight that an optimal amplitude A^* of the perturbation maximizes the cross-covariance. It has led to a better enhancement of the visual perception through the detector than with the SR-detector. Next, we have analyzed the impact of the spatial frequency N_{HF} of the perturbation when its amplitude A remains constant. It has been established that whatever the perturbation frequency N_{HF}, the amplitude which provides the best visual perception through the detector is always the same, namely A^*. Therefore, we have set the perturbation amplitude to this optimal value and considered different spatial frequencies of the perturbation. By considering different input subthreshold images with different sizes N^2, we have established that the cross-correlation coefficient $C_{I,T}$, which quantizes the quality of the perceived image, saturates when the frequency exceeds the image resolution, namely N^2. Therefore, we have clearly established that the vibrational resonance detector must be tuned with a perturbation of optimal amplitude A^* and spatial frequency N_{HF} greater than the image resolution N^2. Using this optimal setting, the vibrational resonance detector clearly outperforms the stochastic resonance detector provided that the noise of the input images is below γ^*.

In our work, we have restricted our study to spatial perturbations. It could be also interesting to consider spatio-temporal perturbations, i.e. perturbations which also evolve versus time. Indeed, as reviewed in the case of stochastic resonance, such spatio-temporal perturbations have revealed a rich variety of applications in perceptual decision-making [237,244,245] and have also accounted for the process of perception by the retina [236]. More generally, as reported in the case of our detector, we trust that vibrational resonance based strategies could provide better results in various fields where stochastic resonance is used. Lastly, this work might constitute a starting point for further investigations of more complex detectors which could induce applications in the area of image processing.

III

CONCLUSIONS AND OUTLOOKS

6

CONCLUSIONS AND OUTLOOKS

Contents

6.1 Conclusions 99
6.2 Future perspectives 101
6.3 Publications 103

6.1/ CONCLUSIONS

In this thesis, we have numerically investigated resonance induced phenomena in nonlinear systems and their applications to information processing. In particular, this thesis focused on Vibrational Resonance (VR), Ghost-Vibrational Resonance (GVR) and Stochastic Resonance (SR). Consequently, the introductory part of this manuscript consists of a brief overview on the most famous resonance induced effects in nonlinear systems. Our first two analyses studied VR and VR/GVR in mechanical oscillators and Chua's circuit model respectively. Moreover, our last analysis concerned the study of the application of VR in subthreshold noisy images perception. Indeed, the major takeaway and the findings of each study are concluded as follows:

- In our first analysis, we considered the dynamics of a particular nonlinear mechanical system describing the motion of a particle of a given mass experiencing a multistable potential and driven by a low frequency signal corrupted by a high frequency perturbation. More precisely, our research has mainly addressed VR occurrence when the particle mass and the damping parameters are jointly considered as control parameters. We studied the dynamics of the system with two different damping coefficients: firstly, constant damping coefficient and secondly, nonlinear space-dependent damping coefficient. In both the two cases of the damping, we begin by studying the impact of the damping coefficients on VR occurrence for a unitary particle mass. Lastly, we studied the combined impact of varying the particle mass and parameters of the damping coefficients on VR occurrence.

  In the first case of constant damping and for the unitary particle mass, vibrational multiresonance effect controlled by the constant damping amplitude is revealed. Best system's responses are achieved by the first resonances and for the smallest constant damping amplitude. Moreover, considering the particle mass as a control parameter, the system revealed two different behaviors one of which VR ceased to exist because the best system's response is obtained when the perturbation is null. Therefore, we have highlighted the existence of a critical value of the particle mass below which VR phenomenon occurred and beyond which it failed to exist.

For the case of the system experiencing nonlinear dissipation and unitary particle mass, vibrational multiresonance controlled by the nonlinear dissipation parameters is revealed. Similarly, considered dissipation parameters revealed best response at the first resonance which are better than the responses obtained in the same system but with the constant dissipation. Furthermore, considering the particle mass as a control parameter for each considered nonlinear dissipation parameters, the system revealed two different behaviors, one of which VR phenomenon ceased to exist.

By comparison, we found that, responses obtained in the case of the system experiencing nonlinear damping are better than those achieved for the case of the system experiencing constant damping. Moreover, the considered nonlinear damping allowed to control the response of the system from its multiple parameters unlike the case of constant damping where only the damping amplitude can control the system.

- In another nonlinear system, we numerically investigated the dynamics of a Chua's circuit model experiencing a truncated sinusoidal nonlinearity and driven by an external perturbed excitation. We mainly study the impact of the system's nonlinearity on the occurrence of VR and GVR phenomena. In all the studies carried out, we compared the responses achieved with our proposed truncated sinusoidal nonlinearity and the existing sawtooth nonlinearity.

  VR studies in the system with the two different nonlinearities both revealed multiple resonances whose number is controlled by the nonlinear force parameter named “nonlinearity order”. The system experiencing a truncated sinusoidal force attained its maximum response always at the first resonance which required smaller perturbation amplitude to be achieved. This is contrary to the system experiencing a sawtooth force as it attained its maximum response always at the last resonance which required relatively larger perturbation amplitude to be realized. Moreover, the overall maximum responses of the system experiencing our proposed truncated sinusoidal force are better than those achieved with the existing sawtooth force. However, the responses of the two systems both approach an asymptotic value as the nonlinearity order keeps increasing.

  Exciting the system with a weak signal consisting of two close low frequencies corrupted by a high frequency perturbation, we observed for both the two different nonlinearities that, varying the perturbation amplitude induced resonances at the two input low frequencies and at a missing (ghost) frequency lower than the two input low frequencies. The observed VR and GVR effects can each become predominant resonance in a distinct range of the perturbation amplitude.

- In the last chapter, we studied the application of Vibrational Resonance (VR) in subthreshold noisy images perception. We first reviewed the nonlinear resonances applications in the context of image processing and visual perception. Next, to quantify the perception of subthreshold images of different resolution through a threshold detector, we employed the Cross-Covariance as a measure of similarity between the input and perceived images.

  When noise perturbed the system, we briefly revisited the well-known Stochastic Resonance (SR) threshold detector, whose best performances are achieved when the noise intensity of the random perturbation is tuned to an optimal value. Next, we introduce a VR-based detector which uses a tunable spatial high frequency perturbation instead of noise to provide a much better visual perception of the input subthreshold noisy images.

  However, we have shown that to take advantage of this new VR-based detector, the noise level of the input subthreshold images must be below the optimal noise intensity of the SR-based detector. Under this condition, we have established that VR-based detector clearly outperforms SR-based detector. Especially when the amplitude of the spatial perturbation tuned to its optimal value and the spatial perturbation frequency exceeded the images resolution, we have shown that the VR-based detector alloweds the best perception of the subthreshold noisy images.

6.2/ FUTURE PERSPECTIVES

Since the inception of vibrational resonance in the year 2000, a lot of advances have been reported especially in the field of sciences and engineering. In particular, this thesis has analyzed the occurrence of VR in two different nonlinear systems and also studied application of VR in subthreshold images perception.

- Our studies of VR in a mechanical system experiencing a periodic potential has revealed the existence of a critical mass beyond which VR ceased to exist. Extending this analysis to other mechanical systems experiencing different potentials, including modifications in the shape and location of the potential wells, may lead to discovery of more interesting features. Moreover, the existence of this critical mass might provide an opportunity of sorting particles based on VR, for instance in micro/nanofluidic devices.
- In the crucial model of Chua's circuit, different nonlinearities have reported significant advances especially, sawtooth nonlinearity which was reported to exhibits multiple resonances on VR studies. However, our proposed truncated sinusoidal nonlinearity was shown to outperformed the sawtooth nonlinearity in this thesis. We suspect that our proposed truncated sinusoidal nonlinearity may report more promising applications in the dynamical fields where sawtooth nonlinearity is usually considered.

- In our studies of the application of VR in subthreshold images perception, our proposed VR-based detector has clearly outperformed the conventional SR-based detector in terms of visual perception. We suspect that further investigations of VR applications in this fields could be developed, especially in the context of cognitive sciences.

6.3/ PUBLICATIONS

1. **International publications:**

   [P-1] S. Morfu, B.I. Usama, and P. Marquié. **Perception enhancement of subthreshold noisy image with Vibrational Resonance**. Electron. Lett., 55 :650–652, 2019. doi:10.1049/el.2018.8059

   [P-2] B. I. Usama, S. Morfu, and P. Marquié. **Numerical analyses of the vibrational resonance occurrence in a nonlinear dissipative system**. Chaos, Solitons & Fractals, 127 :31–37, 2019. doi:10.1016/j.chaos.2019.06.028

   [P-3] S.Morfu, B.I. Usama, and P.Marquié. **On some applications of vibrational resonance on image perception : The role of the perturbation parameters**. Phil. Trans. R. Soc. A, 379 :20200240, 2021. doi:10.1098/rsta.2020.0240

2. **Submitted publications:**

   [P-4] B. I. Usama, S. Morfu, and P. Marquié. **Vibrational resonance and ghost-vibrational resonance occurrence in Chua's circuit models with specific nonlinearities**. Chaos, Solitons & Fractals, 2021. (Currently on minor revision)

3. **International conferences:**

   [Ci-1] B.I.Usama, S.Morfu,M. Rossé, P.Marquié and J.M. Bilbault, **"Vibrational Resonance in inhomogeneous and space-dependent nonlinear damped systems"**, The 13^{th} Chaos 2020 international conference, 9-12 June 2020 Florence, Italy. p55.

4. **National conferences:**

   [Cn-1] S. Morfu, B.I. Usama and P. Marquié **"Perception d'images subliminales utilisant la Résonance vibrationnelle"** p.66 des résumés de la 23^{eme} Rencontre du non-linéaire Paris 25-27 Mars 2020.

5. **Commlunications in the ImViA laboratory:**

   [Cl-1] Séminaire inter-équipe **"Ma Thése en 180 secondes"**,08 March 2018.

   [Cl-2] Cores seminar of ImViA Laboratory **"Vibrational resonance in an inhomogeous and space-dependent nonlinear damped systems"**, 18 May 2021.

BIBLIOGRAPHY

[1] L. É. Lapicque. Recherches quantitatives sur l'excitation électronique des nerfs traitée comme une polarization. *J. physiol. Pathol. Gen.*, 9:620–635, 1907.

[2] W. S. McCulloch and W. Pitts. A logical calculus of the ideas immanent in nervous activity. *Bull. Math. Biophys.*, 5(4):115–133, 1943.

[3] A. L. Hodgkin and A. F. Huxley. A quantitative description of membrane current and its application to conduction and excitation in nerve. *J. Physiol. Paris*, 117(4):500–544, 1952.

[4] C. D. Geisler and J. M. Goldberg. A stochastic model of the repetitive activity of neurons. *Biophys. J.*, 6(1):53–69, 1966.

[5] R. FitzHugh. Impulses and physiological states in theoretical models of nerve membrane. *Biophys. J.*, 1(6):445–466, 1961.

[6] C. Morris and H. Lecar. Voltage oscillations in the barnacle giant muscle fiber. *Biophys. J.*, 35(1):193–213, 1981.

[7] J. L. Hindmarsh and R. M. Rose. A model of the nerve impulse using two first-order differential equations. *Nature*, 296(5853):162–164, 1982.

[8] P. S. Landa and P. V. E. McClintock. Vibrational resonance. *J. Phys. A*, 33(45):L433, 2000.

[9] G. Mayer-Kress and H. Haken. The influence of noise on the logistic model. *J. Stat. Phys.*, 26(1):149–171, 1981.

[10] G. Mayer-Kress and H. Haken. Intermittent behavior of the logistic system. *Phys. Lett. A.*, 82(4):151–155, 1981.

[11] K. Matsumoto and I. Tsuda. Noise-induced order. *J. Stat. Phys.*, 31(1):87–106, 1983.

[12] A. S. Pikovsky. Statistics of trajectory separation in noisy dynamical systems. *Phys. Lett. A*, 165(1):33–36, 1992.

[13] V. Hakim and W. J. Rappel. Noise-induced periodic behaviour in the globally coupled complex ginzburg-landau equation. *EPL*, 27(9):637, 1994.

[14] F. Chapeau-Blondeau. Qubit state estimation and enhancement by quantum thermal noise. *Electron. Lett.*, 51(21):1673–1675, 2015.

[15] F. Chapeau-Blondeau. Entanglement-assisted quantum parameter estimation from a noisy qubit pair: A Fisher information analysis. *Phys. Lett. A*, 381(16):1369–1378, 2017.

[16] F. Chapeau-Blondeau. Optimized entanglement for quantum parameter estimation from noisy qubits. *Int. J. Quantum Inf.*, 16(07):1850056, 2018.

[17] A. S. Pikovsky and J. Kurths. Coherence resonance in a noise-driven excitable system. *Phys. Rev. Lett.*, 78:775–778, 1997.

[18] R. Benzi, A. Sutera, and A. Vulpiani. The mechanism of stochastic resonance. *J. Phys. A*, 14(11):L453, 1981.

[19] R. Benzi, G. Parisi, A. Sutera, and A. Vulpiani. Stochastic resonance in climatic change. *Tellus*, 34(1):10–16, 1982.

[20] H. Gang, T. Ditzinger, C. Z. Ning, and H. Haken. Stochastic resonance without external periodic force. *Phys. Rev. Lett.*, 71(6):807, 1993.

[21] S. G. Lee, A. Neiman, and S. Kim. Coherence resonance in a Hodgkin–Huxley neuron. *Phys. Rev. E*, 57(3):3292, 1998.

[22] C. Palenzuela, R. Toral, C. R. Mirasso, O. Calvo, and J. D. Gunton. Coherence resonance in chaotic systems. *EPL*, 56(3):347, 2001.

[23] B. Lindner, L. Schimansky-Geier, and A. Longtin. Maximizing spike train coherence or incoherence in the LEAKY integrate-and-fire model. *Phys. Rev. E*, 66(3):031–916, 2002.

[24] B. Lindner and L. Schimansky-Geier. Coherence and stochastic resonance in a two-state system. *Phys. Rev. E*, 61(6):6103, 2000.

[25] Y. Shinohara, T. Kanamaru, H. Suzuki, T. Horita, and K. Aihara. Array-enhanced coherence resonance and forced dynamics in coupled FitzHugh–Nagumo neurons with noise. *Phys. Rev. E*, 65(5):051–906, 2002.

[26] X. Feng and Z. Zheng. Coherent resonance and phase locking in noise-driven excitable systems. *Int. J. Mod. Phys. B*, 19(22):3501–3509, 2005.

[27] M. E. Yamakou and J. Jost. Control of coherence resonance by self-induced stochastic resonance in a multiplex neural network. *Phys. Rev. E*, 100(2):022313, 2019.

[28] P. K. Shaw, D. Saha, S. Ghosh, M. S. Janaki, and A. N. S. Iyengar. Intrinsic noise induced coherence resonance in a glow discharge plasma. *Chaos*, 25(4):043–101, 2015.

[29] J. L. A. Dubbeldam, B. Krauskopf, and D. Lenstra. Excitability and coherence resonance in lasers with saturable absorber. *Phys. Rev. E*, 60(6):65–80, 1999.

[30] G. Giacomelli, M. Giudici, S. Balle, and J. R. Tredicce. Experimental evidence of coherence resonance in an optical system. *Phys. rev. lett.*, 84(15):32–98, 2000.

[31] J. M. Buldú, J. García-Ojalvo, C. R. Mirasso, M. C. Torrent, and J. M. Sancho. Effect of external noise correlation in optical coherence resonance. *Phys. Rev. E*, 64(5):051–109, 2001.

[32] O. V. Ushakov, H. J. Wünsche, F. Henneberger, I. A. Khovanov, L. Schimansky-Geier, and M. A. Zaks. Coherence resonance near a Hopf bifurcation. *Phys. Rev. Lett.*, 95:123903, 2005.

[33] I. Z. Kiss, J. L. Hudson, G. J. E. Santos, and P. Parmananda. Experiments on coherence resonance: Noisy precursors to Hopf bifurcations. *Phys. Rev. E*, 67(3):035–201, 2003.

[34] G. J. E. Santos, M. Rivera, and P. Parmananda. Experimental evidence of coexisting periodic stochastic resonance and coherence resonance phenomena. *Phys. rev. lett.*, 92(23):230–601, 2004.

[35] V. Beato, I. Sendina-Nadal, I. Gerdes, and H. Engel. Coherence resonance in a chemical excitable system driven by coloured noise. *Philos. Trans. Royal Soc. A*, 366(1864):381–395, 2007.

[36] S. K. Han, T. G. Yim, D. E. Postnov, and O. V. Sosnovtseva. Interacting coherence resonance oscillators. *Phys. Rev. Lett.*, 83(9):1771, 1999.

[37] D. E. Postnov, S. K. Han, T. G. Yim, and O. V. Sosnovtseva. Experimental observation of coherence resonance in cascaded excitable systems. *Phys. Rev. E*, 59(4):R3791, 1999.

[38] O. Calvo, C. R. Mirasso, and R. Toral. Coherence resonance in chaotic electronic circuits. *Electron. Lett.*, 37(17):1062–1063, 2001.

[39] L. Gammaitoni, F. Marchesoni, E. Menichella-Saetta, and S. Santucci. Stochastic resonance in bistable systems. *Phys. Rev. Lett.*, 62(4):349, 1989.

[40] A. Bulsara, E. W. Jacobs, T. Zhou, F. Moss, and L. Kiss. Stochastic resonance in a single neuron model: Theory and analog simulation. *J. Theor. Biol.*, 152(4):531–555, 1991.

[41] M. I. Dykman, D. G. Luchinsky, R. Mannella, P. V. E. McClintock, N. D. Stein, and N. G. Stocks. Stochastic resonance in perspective. *Il Nuovo Cimento D*, 17(7-8):661–683, 1995.

[42] M. I. Dykman, R. Mannella, P. V. E. McClintock, and N. G. Stocks. Comment on “stochastic resonance in bistable systems”. *Phys. rev. lett.*, 65(20):2606, 1990.

[43] M. I. Dykman, P. V. E. McClintock, R. Mannella, and N. G. Stocks. Stochastic resonance in the linear and nonlinear responses of a bistable system to a periodic field. *JETP Lett.*, 52(3):141–144, 1990.

[44] L. Gammaitoni, P. Hänggi, P. Jung, and F. Marchesoni. Stochastic resonance: a remarkable idea that changed our perception of noise. *Eur. Phys. J. B*, 69(1):1–3, 2009.

[45] B. McNamara, K. Wiesenfeld, and R. Roy. Observation of stochastic resonance in a ring laser. *Phys. Rev. Lett.*, 60(25):2626, 1988.

[46] S. Blanchard, D. Rousseau, D. Gindre, and F. Chapeau-Blondeau. Constructive action of the speckle noise in a coherent imaging system. *Opt. Lett.*, 32(14):1983–1985, 2007.

[47] F. Chapeau-Blondeau, D. Gindre, R. Barillé, and D. Rousseau. Optical coherence of a scalar wave influenced by first-order and second-order statistics of its random phase. *Fluct. Noise Lett.*, 8(02):L107–L123, 2008.

[48] F. Chapeau-Blondeau. Periodic and aperiodic stochastic resonance with output signal-to-noise ratio exceeding that at the input. *Int. J. Bifurc. Chaos*, 9(01):267–272, 1999.

[49] B. Xu, F. Duan, and F. Chapeau-Blondeau. Comparison of aperiodic stochastic resonance in a bistable system realized by adding noise and by tuning system parameters. *Phys. Rev. E*, 69(6):061110, 2004.

[50] F. Duan, F. Chapeau-Blondeau, and D. Abbott. Encoding efficiency of suprathreshold stochastic resonance on stimulus-specific information. *Phys. Lett. A*, 380(1-2):33–39, 2016.

[51] D. Rousseau, J. R. Varela, and F. Chapeau-Blondeau. Stochastic resonance for nonlinear sensors with saturation. *Phys. Rev. E*, 67(2):021102, 2003.

[52] F. Chapeau-Blondeau and D. Rousseau. Enhancement by noise in parallel arrays of sensors with power-law characteristics. *Phys. Rev. E*, 70(6):060101, 2004.

[53] F. Chapeau-Blondeau, S. Blanchard, and D. Rousseau. Noise-enhanced fisher information in parallel arrays of sensors with saturation. *Phys. Rev. E*, 74(3):031102, 2006.

[54] F. Chapeau-Blondeau and D. Rousseau. Noise-aided snr amplification by parallel arrays of sensors with saturation. *Phys. lett. A*, 351(4-5):231–237, 2006.

[55] F. Duan, L. Duan, F. Chapeau-Blondeau, Y. Ren, and D. Abbott. Binary signal transmission in nonlinear sensors: Stochastic resonance and human hand balance. *Instru. Meas. Mag.*, 23(1):44–49, 2020.

[56] F. Chapeau-Blondeau, X. Godivier, and N. Chambet. Stochastic resonance in a neuron model that transmits spike trains. *Phys. Rev. E*, 53(1):1273, 1996.

[57] X. Godivier and F. Chapeau-Blondeau. Noise-enhanced transmission of spike trains in the neuron. *EPL*, 35(6):473, 1996.

[58] S. G. Lee and S. Kim. Parameter dependence of stochastic resonance in the stochastic Hodgkin–Huxley neuron. *Phys. Rev. E*, 60(1):826, 1999.

[59] D. Nozaki and Y. Yamamoto. Enhancement of stochastic resonance in a FitzHugh–Nagumo neuronal model driven by colored noise. *Phys. Lett. A*, 243(5-6):281–287, 1998.

[60] F. Duan, F. Chapeau-Blondeau, and D. Abbott. Enhancing array stochastic resonance in ensembles of excitable systems. *J. Stat. Mech. Theory Exp.*, 2009(08):P08017, 2009.

[61] X. Godivier and F. Chapeau-Blondeau. Noise-assisted signal transmission in a nonlinear electronic comparator: Experiment and theory. *Signal Process.*, 56(3):293–303, 1997.

[62] D. G. Luchinsky, R. Mannella, P. V. E. McClintock, and N. G. Stocks. Stochastic resonance in electrical circuits. I. conventional stochastic resonance. *IEEE Trans. Circuits. Syst. II*, 46(9):1205–1214, 1999.

[63] F. Chapeau-Blondeau and D. Rousseau. Noise improvements in stochastic resonance: From signal amplification to optimal detection. *Fluct. noise lett.*, 2(03):L221–L233, 2002.

[64] B. Xu, F. Duan, R. Bao, and J. Li. Stochastic resonance with tuning system parameters: the application of bistable systems in signal processing. *Chaos Solitons Fract.*, 13(4):633–644, 2002.

[65] D. Rousseau and F. Chapeau-Blondeau. Constructive role of noise in signal detection from parallel arrays of quantizers. *Signal Process.*, 85(3):571–580, 2005.

[66] D. Rousseau, J. R. Varela, F. Duan, and F. Chapeau-Blondeau. Evaluation of a nonlinear bistable filter for binary signal detection. *Chaos*, 15(02):667–679, 2005.

[67] F. Duan and D. Abbott. Signal detection for frequency-shift keying via short-time stochastic resonance. *Phys. Lett. A*, 344(6):401–410, 2005.

[68] D. Rousseau and F. Chapeau-Blondeau. Stochastic resonance and improvement by noise in optimal detection strategies. *Digit. Signal Process.*, 15(1):19–32, 2005.

[69] J. Fiorina, D. Rousseau, and F. Chapeau-Blondeau. Interferer rejection improved by noise in ultra-wideband telecommunications. *Fluct. Noise Lett.*, 6(03):L317–L328, 2006.

[70] D. Rousseau, G. V. Anand, and F. Chapeau-Blondeau. Noise-enhanced nonlinear detector to improve signal detection in non-gaussian noise. *Signal Process.*, 86(11):3456–3465, 2006.

[71] F. Duan and D. Abbott. Binary modulated signal detection in a bistable receiver with stochastic resonance. *Physica A*, 376:173–190, 2007.

[72] F. Duan, F. Chapeau-Blondeau, and D. Abbott. Fisher-information condition for enhanced signal detection via stochastic resonance. *Phys. Rev. E*, 84(5):051107, 2011.

[73] F. Duan, F. Chapeau-Blondeau, and D. Abbott. Exploring weak-periodic-signal stochastic resonance in locally optimal processors with a Fisher information metric. *Signal Process.*, 92(12):3049–3055, 2012.

[74] F. Duan, F. Chapeau-Blondeau, and D. Abbott. Weak signal detection: condition for noise induced enhancement. *Digit. Signal Process.*, 23(5):1585–1591, 2013.

[75] F. Duan, F. Chapeau-Blondeau, and D. Abbott. Stochastic resonance with colored noise for neural signal detection. *PLoS One*, 9(3):e91345, 2014.

[76] F. Duan, F. Chapeau-Blondeau, and D. Abbott. Non-gaussian noise benefits for coherent detection of narrowband weak signal. *Phys. Lett. A*, 378(26-27):1820–1824, 2014.

[77] Y. Ren, Y. Pan, F. Duan, F. Chapeau-Blondeau, and D. Abbott. Exploiting vibrational resonance in weak-signal detection. *Phys. Rev. E*, 96(2):022141, 2017.

[78] F. Chapeau-Blondeau. Stochastic resonance and optimal detection of pulse trains by threshold devices. *Digit. Signal Process.*, 9(3):162–177, 1999.

[79] F. Chapeau-Blondeau. Noise-aided nonlinear Bayesian estimation. *Phys. Rev. E*, 66(3):032101, 2002.

[80] F. Chapeau-Blondeau. Stochastic resonance for an optimal detector with phase noise. *Signal process.*, 83(3):665–670, 2003.

[81] D. Rousseau, F. Duan, and F. Chapeau-Blondeau. Suprathreshold stochastic resonance and noise-enhanced Fisher information in arrays of threshold devices. *Phys. Rev. E*, 68(3):031107, 2003.

[82] F. Chapeau-Blondeau and D. Rousseau. Noise-enhanced performance for an optimal Bayesian estimator. *IEEE Trans. Signal Process.*, 52(5):1327–1334, 2004.

[83] F. Chapeau-Blondeau and D. Rousseau. Constructive action of additive noise in optimal detection. *Chaos*, 15(09):2985–2994, 2005.

[84] F. Chapeau-Blondeau and D. Rousseau. Injecting noise to improve performance of optimal detector. *Electron. Lett.*, 43(16):897–898, 2007.

[85] D. Rousseau and F. Chapeau-Blondeau. Noise-improved Bayesian estimation with arrays of one-bit quantizers. *IEEE Trans. Instrum. Meas.*, 56(6):2658–2662, 2007.

[86] F. Chapeau-Blondeau, S. Blanchard, and D. Rousseau. Fisher information and noise-aided power estimation from one-bit quantizers. *Digit. Signal Process.*, 18(3):434–443, 2008.

[87] F. Chapeau-Blondeau and D. Rousseau. Raising the noise to improve performance in optimal processing. *J. Stat. Mech. Theory Exp*, 2009(01):P01003, 2009.

[88] F. Duan, F. Chapeau-Blondeau, and D. Abbott. Fisher information as a metric of locally optimal processing and stochastic resonance. *PLoS One*, 7(4):e34282, 2012.

[89] Y. Pan, F. Duan, F. Chapeau-Blondeau, and D. Abbott. Noise enhancement in robust estimation of location. *IEEE Trans. Signal Process.*, 66(8):1953–1966, 2018.

[90] F. Duan, Y. Pan, F. Chapeau-Blondeau, and D. Abbott. Noise benefits in combined nonlinear Bayesian estimators. *IEEE Trans. Signal Process.*, 67(17):4611–4623, 2019.

[91] Y. Pan, F. Duan, L. Xu, and F. Chapeau-Blondeau. Benefits of noise in M-estimators: Optimal noise level and probability density. *Physica A*, 534:120835, 2019.

[92] F. Chapeau-Blondeau. Quantum state discrimination and enhancement by noise. *Phys. Lett. A*, 378(30-31):2128–2136, 2014.

[93] N. Gillard, É. Belin, and F. Chapeau-Blondeau. Stochastic antiresonance in qubit phase estimation with quantum thermal noise. *Phys. Lett. A*, 381(32):2621–2628, 2017.

[94] N. Gillard, É. Belin, and F. Chapeau-Blondeau. Enhancing qubit information with quantum thermal noise. *Physica A*, 507:219–230, 2018.

[95] N. Gillard, É. Belin, and F. Chapeau-Blondeau. Stochastic resonance with unital quantum noise. *Fluct. Noise Lett.*, 18(03):1950015, 2019.

[96] E. Simonotto, M. Riani, C. Seife, M. Roberts, J. Twitty, and F. Moss. Visual perception of stochastic resonance. *Phys. Rev. lett.*, 78(6):1186, 1997.

[97] D. Rousseau, A. Delahaies, and F. Chapeau-Blondeau. Structural similarity measure to assess improvement by noise in nonlinear image transmission. *IEEE Signal Process. Lett.*, 17(1):36–39, 2010.

[98] A. Delahaies, D. Rousseau, J. B. Fasquel, and F. Chapeau-Blondeau. Local-feature-based similarity measure for stochastic resonance in visual perception of spatially structured images. *JOSA A*, 29(7):1211–1216, 2012.

[99] S. Morfu, B. I. Usama, and P. Marquié. Perception enhancement of subthreshold noisy image with vibrational resonance. *Electron. Lett.*, 2019.

[100] P. Jung and G. Mayer-Kress. Stochastic resonance in threshold devices. *Il Nuovo Cimento D*, 17(7-8):827–834, 1995.

[101] F. Chapeau-Blondeau. Input-output gains for signal in noise in stochastic resonance. *Phys. Lett. A*, 232(1-2):41–48, 1997.

[102] F. Chapeau-Blondeau. Noise-enhanced capacity via stochastic resonance in an asymmetric binary channel. *Phys. Rev. E*, 55(2):2016, 1997.

[103] F. Chapeau-Blondeau and X. Godivier. Theory of stochastic resonance in signal transmission by static nonlinear systems. *Phys. Rev. E*, 55(2):1478, 1997.

[104] X. Godivier and F. Chapeau-Blondeau. Stochastic resonance in the information capacity of a nonlinear dynamic system. *Int. J. Bifurc. Chaos*, 8(03):581–589, 1998.

[105] F. Vaudelle, J. Gazengel, G. Rivoire, X. Godivier, and F. Chapeau-Blondeau. Stochastic resonance and noise-enhanced transmission of spatial signals in optics: The case of scattering. *J. Opt. Soc. Am. B*, 15(11):2674–2680, 1998.

[106] F. Chapeau-Blondeau. Noise-assisted propagation over a nonlinear line of threshold elements. *Electron. Lett*, 35(13):1055–1056, 1999.

[107] F. Chapeau-Blondeau. Stochastic resonance at phase noise in signal transmission. *Phys. Rev. E*, 61(1):940, 2000.

[108] F. Chapeau-Blondeau and J. Rojas-Varela. Nonlinear signal propagation enhanced by noise via stochastic resonance. *Chaos*, 10(08):1951–1959, 2000.

[109] F. Duan and B. Xu. Parameter-induced stochastic resonance and baseband binary PAM signals transmission over an awgn channel. *Int. J. Bifurc. Chaos*, 13(02):411–425, 2003.

[110] F. Duan, D. Rousseau, and F. Chapeau-Blondeau. Residual aperiodic stochastic resonance in a bistable dynamic system transmitting a suprathreshold binary signal. *Phys. Rev. E*, 69(1):011109, 2004.

[111] D. Rousseau and F. Chapeau-Blondeau. Suprathreshold stochastic resonance and signal-to-noise ratio improvement in arrays of comparators. *Phys. Lett. A*, 321(5-6):280–290, 2004.

[112] S. Blanchard, D. Rousseau, D. Gindre, and F. Chapeau-Blondeau. Benefits from a speckle noise family on a coherent imaging transmission. *Opt. Commun.*, 281(17):4173–4179, 2008.

[113] F. Chapeau-Blondeau, D. Rousseau, S. Blanchard, and D. Gindre. Optimizing the speckle noise for maximum efficacy of data acquisition in coherent imaging. *JOSA A*, 25(6):1287–1292, 2008.

[114] D. Rousseau, A. Delahaies, and F. Chapeau-Blondeau. Structural similarity measure to assess improvement by noise in nonlinear image transmission. *Signal Process. Lett.*, 17(1):36–39, 2009.

[115] F. Chapeau-Blondeau, David Rousseau, and A. Delahaies. Renyi entropy measure of noise-aided information transmission in a binary channel. *Phys. Rev. E*, 81(5):051112, 2010.

[116] A. Delahaies, F. Chapeau-Blondeau, D. Rousseau, and F. Franconi. Tuning the noise in magnetic resonance imaging to maximize nonlinear information transmission. *Fluct. Noise Lett.*, 12(01):1350005, 2013.

[117] L. Duan, F. Duan, F. Chapeau-Blondeau, and D. Abbott. Stochastic resonance in Hopfield neural networks for transmitting binary signals. *Phys. Lett. A*, 384(6):126–143, 2020.

[118] D. Rousseau and F. Chapeau-Blondeau. Neuronal signal transduction aided by noise at threshold and at saturation. *Neural Process. Lett.*, 20(2):71–83, 2004.

[119] S. Blanchard, D. Rousseau, and F. Chapeau-Blondeau. Noise enhancement of signal transduction by parallel arrays of nonlinear neurons with threshold and saturation. *Neurocomputing*, 71(1-3):333–341, 2007.

[120] F. Chapeau-Blondeau, F. Duan, and D. Abbott. Synaptic signal transduction aided by noise in a dynamical saturating model. *Phys. Rev. E*, 81(2):021124, 2010.

[121] F. Duan, F. Chapeau-Blondeau, and D. Abbott. Neural signal transduction aided by noise in multisynaptic excitatory and inhibitory pathways with saturation. *Physica A*, 390(16):2855–2862, 2011.

[122] E. Ippen, J. Lindner, and W. L. Ditto. Chaotic resonance: A simulation. *J. stat. phys.*, 70(1-2):437–450, 1993.

[123] R. Kozma and W. J. Freeman. Chaotic resonance—methods and applications for robust classification of noisy and variable patterns. *Int. J. Bifurc. Chaos*, 11(06):1607–1629, 2001.

[124] S. Zambrano, J. M. Casado, and M. A. F. Sanjuán. Chaos-induced resonant effects and its control. *Phys. Lett. A*, 366(4-5):428–432, 2007.

[125] I. T. Tokuda, C. E. Han, K. Aihara, M. Kawato, and N. Schweighofer. The role of chaotic resonance in cerebellar learning. *Neural Networks*, 23(7):836–842, 2010.

[126] D. R. Chialvo, O. Calvo, D. L. Gonzalez, O. Piro, and G. V. Savino. Subharmonic stochastic synchronization and resonance in neuronal systems. *Phys. Rev. E*, 65(5):050902, 2002.

[127] D. R. Chialvo. How we hear what is not there: A neural mechanism for the missing fundamental illusion. *Chaos*, 13(4):1226–1230, 2003.

[128] P. Balenzuela and J. García-Ojalvo. Neural mechanism for binaural pitch perception via ghost stochastic resonance. *Chaos*, 15(2):023903, 2005.

[129] P. Balenzuela, H. Braun, and D. R. Chialvo. The ghost of stochastic resonance: an introductory review. *Contemp. Phys.*, 53(1):17–38, 2012.

[130] M. Bordet, S. Morfu, and P. Marquié. Ghost stochastic resonance in FitzHugh–Nagumo circuit. *Electron. lett.*, 50(12):861–862, 2014.

[131] M. Bordet, S. Morfu, and P. Marquié. Ghost responses of the FitzHugh–Nagumo system induced by colored noise. *Chaos, Solitons Fract.*, 78:205–214, 2015.

[132] I. G. Silva, O. A. Rosso, M. V. D. Vermelho, and M. L. Lyra. Ghost stochastic resonance induced by a power-law distributed noise in the fitzhugh–nagumo neuron model. *Commun. Nonlinear Sci. Numer. Simul.*, 22(1-3):641–649, 2015.

[133] I. Gomes, M. V. D. Vermelho, and M. L. Lyra. Ghost resonance in the chaotic chua's circuit. *Phys. Rev. E*, 85(5):056201, 2012.

[134] O. Calvo and D. R. Chialvo. Ghost stochastic resonance in an electronic circuit. *Int. J. Bifurc. Chaos*, 16(03):731–735, 2006.

[135] A. Lopera, J. M. Buldú, M. C. Torrent, D. R. Chialvo, and J. García-Ojalvo. Ghost stochastic resonance with distributed inputs in pulse-coupled electronic neurons. *Phys. Rev. E*, 73(2):021101, 2006.

[136] T. Noguchi and H. Torikai. Ghost stochastic resonance from an asynchronous cellular automaton neuron model. *IEEE Trans. Circuits. Syst. II: Express Briefs*, 60(2):111–115, 2013.

[137] G. Van der Sande, G. Verschaffelt, J. Danckaert, and C. R. Mirasso. Ghost stochastic resonance in vertical-cavity surface-emitting lasers: Experiment and theory. *Phys. Rev. E*, 72(1):016113, 2005.

[138] M. Gitterman. Bistable oscillator driven by two periodic fields. *J. Phys. A*, 34(24):L355, 2001.

[139] E. Ullner, A. Zaikin, J. García-Ojalvo, R. Bascones, and J. Kurths. Vibrational resonance and vibrational propagation in excitable systems. *Phys. Lett. A*, 312(5-6):348–354, 2003.

[140] I. I. Blekhman and P. S. Landa. Conjugate resonances and bifurcations in nonlinear systems under biharmonical excitation. *Int. J. Nonlinear Mech.*, 39(3):421–426, 2004.

[141] H. Yu, J. Wang, C. Liu, B. Deng, and X. Wei. Vibrational resonance in excitable neuronal systems. *Chaos*, 21(4):043101, 2011.

[142] L. Ning and Z. Chen. Vibrational resonance analysis in a gene transcriptional regulatory system with two different forms of time-delays. *Physica D*, 401:132164, 2020.

[143] S. Jeyakumari, V. Chinnathambi, S. Rajasekar, and M. A. F. Sanjuán. Single and multiple vibrational resonance in a quintic oscillator with monostable potentials. *Phys. Rev. E*, 80(4):046608, 2009.

[144] S. Rajasekar and M. A. F. Sanjuán. Vibrational resonance in monostable systems. In *Nonlinear Resonances*, pages 83–117. Springer, 2016.

[145] J. P. Baltanás, L. Lopez, I. I. Blechman, P. S. Landa, A. Zaikin, J. Kurths, and M. A. F. Sanjuán. Experimental evidence, numerics, and theory of vibrational resonance in bistable systems. *Phys. Rev. E*, 67(6):066119, 2003.

[146] C. Yao and M. Zhan. Signal transmission by vibrational resonance in one-way coupled bistable systems. *Phys. Rev. E*, 81(6):061129, 2010.

[147] C. Yao, Y. Liu, and M. Zhan. Frequency-resonance-enhanced vibrational resonance in bistable systems. *Phys. Rev. E*, 83(6):061122, 2011.

[148] R. Gui, Y. Wang, Y. Yao, and G. Cheng. Enhanced logical vibrational resonance in a two-well potential system. *Chaos Solitons Fract.*, 138:109952, 2020.

[149] S. Rajasekar, K. Abirami, and M. A. F. Sanjuán. Novel vibrational resonance in multistable systems. *Chaos*, 21(3):033106, 2011.

[150] V. N. Chizhevsky. Experimental evidence of vibrational resonance in a multistable system. *Phys. Rev. E*, 89(6):062914, 2014.

[151] R. Jothimurugan, K. Thamilmaran, S. Rajasekar, and M. A. F. Sanjuán. Experimental evidence for vibrational resonance and enhanced signal transmission in Chua's circuit. *Int. J. Bifurc. Chaos*, 23(11):1350189, 2013.

[152] K. Abirami, S. Rajasekar, and M. A. F. Sanjuán. Vibrational and ghost-vibrational resonances in a modified Chua's circuit model equation. *Int. J. Bifurc. Chaos*, 24(11):1430031, 2014.

[153] M. Bordet and S. Morfu. Experimental and numerical study of noise effects in a FitzHugh–Nagumo system driven by a biharmonic signal. *Chaos Solitons Fract.*, 54:82–89, 2013.

[154] S. Morfu and M. Bordet. On the propagation of a low frequency excitation in a perturbed FitzHugh–Nagumo system: Simulation and experiments. *Chaos Solitons Fract.*, 103:205–212, 2017.

[155] S. Morfu and M. Bordet. On the correlation between phase-locking modes and vibrational resonance in a neuronal model. *Commun Nonlinear Sci. Numer. Simul.*, 55:277–286, 2018.

[156] V. N. Chizhevsky, E. Smeu, and G. Giacomelli. Experimental evidence of "vibrational resonance" in an optical system. *Phys. Rev. lett.*, 91(22):220602, 2003.

[157] T. O. Roy-Layinde, J. A. Laoye, O. O. Popoola, and U. E. Vincent. Analysis of vibrational resonance in bi-harmonically driven plasma. *Chaos*, 26(9):093117, 2016.

[158] T. O. Roy-Layinde, J. A. Laoye, O. O. Popoola, U. E. Vincent, and P. V. E. McClintock. Vibrational resonance in an inhomogeneous medium with periodic dissipation. *Phys. Rev. E*, 96(3):032209, 2017.

[159] H. G. Liu, X. L. Liu, J. H. Yang, M. A. F. Sanjuán, and G Cheng. Detecting the weak high-frequency character signal by vibrational resonance in the Duffing oscillator. *Nonlinear Dyn.*, 89(4):2621–2628, 2017.

[160] Y. Ren, Y. Pan, and F. Duan. Generalized energy detector for weak random signals via vibrational resonance. *Phys. Lett. A*, 382(12):806–810, 2018.

[161] V. N. Chizhevsky. Amplification of an autodyne signal in a bistable vertical-cavity surface-emitting laser with the use of a vibrational resonance. *Tech. Phys. Lett.*, 44(1):17–19, 2018.

[162] S. Rajamani, S. Rajasekar, and M. A. F. Sanjuán. Ghost-vibrational resonance. *Commun Nonlinear Sci. Numer. Simul.*, 19(11):4003–4012, 2014.

[163] B. I. Usama, S. Morfu, and P. Marquié. Vibrational resonance and ghost-vibrational resonance occurrence in Chua's circuit models with specific nonlinearities. *Chaos Solitons Fract.*, 2021, submitted.

[164] B. I. Usama, S. Morfu, and P. Marquié. Numerical analyses of the vibrational resonance occurrence in a nonlinear dissipative system. *Chaos Solitons Fract.*, 127:31–37, 2019.

[165] S. Morfu, B. I. Usama, and P. Marquié. On some applications of vibrational resonance on image perception: The role of the perturbation parameters. *submitted to: Phil. Trans. R. Soc. A*, 2020.

[166] S. Jeyakumari, V. Chinnathambi, S. Rajasekar, and M. A. F. Sanjuán. Analysis of vibrational resonance in a quintic oscillator. *Chaos*, 19(4):043128, 2009.

[167] K. Abirami, S. Rajasekar, and M. A. F. Sanjuán. Vibrational resonance in a harmonically trapped potential system. *Comm. Nonlinear Sci. Numer. Simulat.*, 47:370–378, 2017.

[168] T. Ditzinger, M. Stadler, D. Strüber, and J. A. S. Kelso. Noise improves three-dimensional perception: Stochastic resonance and other impacts of noise to the perception of autostereograms. *Phys. rev. E*, 62(2):2566, 2000.

[169] M. Piana, M. Canfora, and M. Riani. Role of noise in image processing by the human perceptive system. *Phys. rev. E*, 62(1):1104, 2000.

[170] S. Morfu, B. Nofiele, and P. Marquié. On the use of multistability for image processing. *Phys. Lett. A*, 367(3):192–198, 2007.

[171] A. I. Khibnik, D. Roose, and L. O. Chua. On periodic orbits and homoclinic bifurcations in Chua's circuit with a smooth nonlinearity. *Int. J. Bifurc. Chaos*, 3(02):363–384, 1993.

[172] S. Yu, W. K. S. Tang, and G. Chen. Generation of n× m-scroll attractors under a Chua-circuit framework. *Chaos*, 17(11):3951–3964, 2007.

[173] S. Arathi, S. Rajasekar, and J. Kurths. Stochastic and coherence resonances in a modified Chua's circuit system with multi-scroll orbits. *Int. J. Bifurc. Chaos*, 23(08):1350132, 2013.

[174] A. G. Radwan, M. A. Zidan, and K. N. Salama. Hp memristor mathematical model for periodic signals and DC. In *2010 53rd IEEE International Midwest Symposium on Circuits and Systems*, pages 861–864. IEEE, 2010.

[175] C. Yakopcic, T. M. Taha, G. Subramanyam, R. E. Pino, and S. Rogers. A memristor device model. *IEEE Electron Device Lett.*, 32(10):1436–1438, 2011.

[176] H. Kim, M. P. Sah, C. Yang, S. Cho, and L. O. Chua. Memristor emulator for memristor circuit applications. *IEEE Trans. Circuits. Syst. I: Regular Papers*, 59(10):2422–2431, 2012.

[177] V. A. Mironov and V. M. Sokolov. Detection of broadband phase-code-modulated two-frequency signals through calculation of their cross-correlation function. *J. commun. tech. electron.*, 41(16):1406–1409, 1996.

[178] R. Feng, Y. Zhao, C. Zhu, and T. J. Mason. Enhancement of ultrasonic cavitation yield by multi-frequency sonication. *Ultrasonics sonochemistry*, 9(5):231–236, 2002.

[179] D. C. Su, M. H. Chiu, and C. D. Chen. Simple two-frequency laser. *Precision engineering*, 18(2-3):161–163, 1996.

[180] S. Saikia and M. C. Mahato. Dispersionless motion and ratchet effect in a square-wave-driven inertial periodic potential system. *J. Phys. Cond. Matt.*, 21(17):175409, 2009.

[181] S. Saikia and M. C. Mahato. Deterministic inhomogeneous inertia ratchets. *Physica A*, 389(19):4052–4060, 2010.

[182] C. Mulhern. Persistence of uphill anomalous transport in inhomogeneous media. *Phys. Rev. E*, 88(2):022906, 2013.

[183] D. Kharkongor, W. L. Reenbohn, and M. C. Mahato. Particle dynamics in a symmetrically driven underdamped inhomogeneous periodic potential system. *Phys. Rev. E*, 94(2):022148, 2016.

[184] S. Saikia. Ratchet effect in an underdamped periodic potential and its characterisation. *Physica A*, 468:219–227, 2017.

[185] S. Saikia, A. M. Jayannavar, and M. C. Mahato. Stochastic resonance in periodic potentials. *Phys. Rev. E*, 83(6):061121, 2011.

[186] C. Jeevarathinam, S. Rajasekar, and M. A. F. Sanjuán. Theory and numerics of vibrational resonance in Duffing oscillators with time-delayed feedback. *Phys. Rev. E*, 83(6):066205, 2011.

[187] C. Jeevarathinam, S. Rajasekar, and M. A. F. Sanjuán. Effect of multiple time-delay on vibrational resonance. *Chaos*, 23(1):013136, 2013.

[188] J. H. Yang and X. B. Liu. Controlling vibrational resonance in a delayed multistable system driven by an amplitude-modulated signal. *Phys. Scr.*, 82(2):025006, 2010.

[189] J. H. Yang and X. B. Liu. Controlling vibrational resonance in a multistable system by time delay. *Chaos*, 20(3):033124, 2010.

[190] J. H. Yang and X. B. Liu. Delay induces quasi-periodic vibrational resonance. *J. Phys. A*, 43(12):122001, 2010.

[191] D. Hu, J. Yang, and X. Liu. Delay-induced vibrational multiresonance in FitzHugh–Nagumo system. *Commun. Nonlinear Sci. Numer. Simulat.*, 17(2):1031–1035, 2012.

[192] D. Hu, J. H. Yang, and X. B. Liu. Vibrational resonance in the FitzHugh–Nagumo system with time-varying delay feedback. *Comput. Biol. Med.*, 45:80–86, 2014.

[193] J. M. G. Vilar and J. M. Rubi. Stochastic multiresonance. *Phys. Rev. Lett.*, 78(15):2882, 1997.

[194] E. I. Volkov, E. Ullner, and J. Kurths. Stochastic multiresonance in the coupled relaxation oscillators. *Chaos*, 15(2):023105, 2005.

[195] F. Duan, F. Chapeau-Blondeau, and D. Abbott. Double-maximum enhancement of signal-to-noise ratio gain via stochastic resonance and vibrational resonance. *Phys. Rev. E.*, 90(2):022134, 2014.

[196] H. Li, X. Sun, and J. Xiao. Stochastic multiresonance in coupled excitable FHN neurons. *Chaos*, 28(4):043113, 2018.

[197] S. J. Elliott, M. G. Tehrani, and R. S. Langley. Nonlinear damping and quasi-linear modelling. *Phil. Trans. R. Soc. A*, 373(2051):20140402, 2015.

[198] J. R. Wright and J. E. Cooper. *Introduction to aircraft aeroelasticity and loads*, volume 20. John Wiley & Sons, 2008.

[199] A. Eichler, J. Moser, J. Chaste, M. Zdrojek, I. Wilson-Rae, and A. Bachtold. Nonlinear damping in mechanical resonators made from carbon nanotubes and graphene. *Nat. Nanotechnol.*, 6(6):339, 2011.

[200] M. Imboden, O. Williams, and P. Mohanty. Nonlinear dissipation in diamond nanoelectromechanical resonators. *Appl. Phys. Lett.*, 102(10):103502, 2013.

[201] M. Imboden and P. Mohanty. Dissipation in nanoelectromechanical systems. *Phys. Rep.*, 534(3):89–146, 2014.

[202] U. Ingard and H. Ising. Acoustic nonlinearity of an orifice. *J. Acoust. Soc. Am.*, 42(1):6–17, 1967.

[203] C. Surace, K. Worden, and G. R. Tomlinson. An improved nonlinear model for an automotive shock absorber. *Nonlinear Dyn.*, 3(6):413–429, 1992.

[204] E. De Boer. Mechanics of the cochlea: modeling efforts. In *The cochlea*, pages 258–317. Springer, 1996.

[205] V. V. Semenov, A. B. Neiman, T. E. Vadivasova, and V. S. Anishchenko. Noise-induced transitions in a double-well oscillator with nonlinear dissipation. *Phys. Rev. E*, 93(5):052210, 2016.

[206] P. Silvestrini. Effects of the phase-dependent dissipative term on the supercurrent decay of Josephson junctions. *Phys. Rev. B*, 46(9):5470, 1992.

[207] P. Silvestrini. Effects of nonlinear dissipation on the supercurrent decay of a Josephson junction. *J. Appl. Phys.*, 68(2):663–667, 1990.

[208] H. G. Enjieu Kadji, B. R. Nana Nbendjo, J. B. Chabi Orou, and P. K. Talla. Nonlinear dynamics of plasma oscillations modeled by an anharmonic oscillator. *Phys. Plasmas*, 15(3):032308, 2008.

[209] T. L. M. D. Mbong, M. S. Siewe, and C. Tchawoua. The effect of nonlinear damping on vibrational resonance and chaotic behavior of a beam fixed at its two ends and prestressed. *Commun. Nonlinear Sci. Numer. Simulat.*, 22(1-3):228–243, 2015.

[210] Z. Chen and L. Ning. Impact of depth and location of the wells on vibrational resonance in a triple-well system. *Pramana*, 90(4):49, 2018.

[211] U. E. Vincent, T. O. Roy-Layinde, O. O. Popoola, P. O. Adesina, and P. V. E. McClintock. Vibrational resonance in an oscillator with an asymmetrical deformable potential. *Phys. Rev. E*, 98(6):062203, 2018.

[212] L. O. Chua. *The genesis of Chua's circuit*. Electronics Research Laboratory, College of Engineering, University of California, 1992.

[213] J. A. K. Suykens and J. Vandewalle. Generation of n-double scrolls (n= 1, 2, 3, 4,...). *IEEE Trans. on Circuits and Syst. - I*, 40(11):861–867, 1993.

[214] J. Yang and L. Zhao. Bifurcation analysis and chaos control of the modified Chua's circuit system. *Chaos Solitons Fract.*, 77:332–339, 2015.

[215] T. Matsumoto. A chaotic attractor from Chua's circuit. *IEEE Trans. Circuits Syst.*, 31(12):1055–1058, 1984.

[216] G. Q. Zhong and F. Ayrom. Experimental confirmation of chaos from Chua's circuit. *Int. J. Circuit Theory Appl.*, 13(1):93–98, 1985.

[217] A. I. Mahla and Á. G. Badan Palhares. Chua's circuit with a discontinuous nonlinearity. *J. Circuit. Syst. Comp.*, 3(01):231–237, 1993.

[218] M. A Aziz-Alaoui. Differential equations with multispiral attractors. *Int. J. Bifurc. Chaos*, 9(06):1009–1039, 1999.

[219] C. H. Lamarque, O. Janin, and J. Awrejcewicz. Chua systems with discontinuities. *Int. J. Bifurc. Chaos*, 9(04):591–616, 1999.

[220] J. Lu, G. Chen, X. Yu, and H. Leung. Design and analysis of multiscroll chaotic attractors from saturated function series. *IEEE Trans. Circuits Syst. - I*, 51(12):2476–2490, 2004.

[221] S. Morfu, P. Marquié, B. Nofiele, and D. Ginhac. Nonlinear systems for image processing. *Adv. Imaging Electron Phys.*, 152:79–151, 2008.

[222] L. Gammaitoni, P. Hänggi, P. Jung, and F. Marchesoni. Stochastic resonance. *Rev. Mod. Phys*, 70(1):223, 1998.

[223] Y. Yang, Z. Jiang, B. Xu, and D. W. Repperger. An investigation of two-dimensional parameter-induced stochastic resonance and applications in nonlinear image processing. *J. Phys. A: Math. Theor.*, 42(14):145207, 2009.

[224] D. V. Dylov and J. W. Fleischer. Nonlinear self-filtering of noisy images via dynamical stochastic resonance. *Nat. Photonics*, 4(5):323–328, 2010.

[225] D. V. Dylov, L. Waller, and J. W. Fleischer. Nonlinear restoration of diffused images via seeded instability. *IEEE. J. Quantum. Electron.*, 18(2):916–925, 2011.

[226] Q. Sun, H. Liu, N. Huang, Z. Wang, J. Han, and S. Li. Nonlinear restoration of pulse and high noisy images via stochastic resonance. *Scientific reports*, 5:16183, 2015.

[227] X. Feng, H. Liu, N. Huang, Z. Wang, and Y. Zhang. Reconstruction of noisy images via stochastic resonance in nematic liquid crystals. *Scientific reports*, 9(1):1–9, 2019.

[228] Ch. Ryu, S. G. Kong, and H. Kim. Enhancement of feature extraction for low-quality fingerprint images using stochastic resonance. *Pattern Recognit. Lett.*, 32(2):107–113, 2011.

[229] R. Chouhan, R. K. Jha, and P. K. Biswas. Enhancement of dark and low-contrast images using dynamic stochastic resonance. *IET Image Process.*, 7(2):174–184, 2013.

[230] R. Chouhan, P. K. Biswas, and R. K. Jha. Enhancement of low-contrast images by internal noise-induced fourier coefficient rooting. *Signal Image Video Process.*, 9(1):255–263, 2015.

[231] V. P. S. Rallabandi. Enhancement of ultrasound images using stochastic resonance-based wavelet transform. *Comput. Med. Imaging Graph.*, 32(4):316–320, 2008.

[232] V. P. S. Rallabandi and P. K. Roy. Magnetic resonance image enhancement using stochastic resonance in Fourier domain. *Magn. Reson. Imaging*, 28(9):1361–1373, 2010.

[233] P. Perona and J. Malik. Scale-space and edge detection using anisotropic diffusion. *IEEE Trans. Pattern Anal. Machine Intell.*, 12(7):629–639, 1990.

[234] A. Histace and D. Rousseau. Noise-enhanced nonlinear PDE for edge restoration in scalar images. In *IEEE 2010 International Conference of Soft Computing and Pattern Recognition*, pages 458–461. IEEE, 2010.

[235] A. Histace and D. Rousseau. Useful noise effect for nonlinear PDE based restoration of scalar images. *International Journal of Computer Information Systems and Industrial Management Applications*, 4:411–419, 2012.

[236] S. Zozor, P. O. Amblard, and C. Duchêne. Does eye tremor provide the hyperacuity phenomenon? *J. Stat. Mech. Theory Exp.*, 2009(01):P01015, 2009.

[237] E. Itzcovich, M. Riani, and W. G. Sannita. Stochastic resonance improves vision in the severely impaired. *Scientific reports*, 7(1):1–8, 2017.

[238] J. O. Limb. Design of dither waveforms for quantized visual signals. *Bell Syst. Tech.*, 48(7):2555–2582, 1969.

[239] N. S. Jayant and L. R. Rabiner. The application of dither to the quantization of speech signals. *Bell Syst. Tech.*, 51(6):1293–1304, 1972.

[240] M. D. McDonnell, N. G. Stocks, C. E. M. Pearce, and D. Abbott. Stochastic resonance: from suprathreshold stochastic resonance to stochastic signal quantization. *Cambridge University Press*, 2008.

[241] A. R. Bulsara and A. Zador. Threshold detection of wideband signals: A noise-induced maximum in the mutual information. *Phys. Rev. E*, 54(3):R2185, 1996.

[242] L. B. Kish, G. P. Harmer, and D. Abbott. Information transfer rate of neurons: stochastic resonance of shannon's information channel capacity. *Fluct. Noise Lett.*, 1(01):L13–L19, 2001.

[243] P. O. Amblard, O. J. J. Michel, and S. Morfu. Revisiting the asymmetric binary channel: joint noise-enhanced detection and information transmission through threshold devices. In *Noise in Complex Systems and Stochastic Dynamics III*, volume 5845, pages 50–60. International Society for Optics and Photonics, 2005.

[244] O. van der Groen and N. Wenderoth. Transcranial random noise stimulation of visual cortex: stochastic resonance enhances central mechanisms of perception. *J. Neurosci.*, 36(19):5289–5298, 2016.

[245] B. Moret, R. Camilleri, A. Pavan, G. L. Giudice, A. Veronese, R. Rizzo, and G. Campana. Differential effects of high-frequency transcranial random noise stimulation (hf-tRNS) on contrast sensitivity and visual acuity when combined with a short perceptual training in adults with amblyopia. *Neuropsychologia*, 114:125–133, 2018.

LIST OF FIGURES

1.1 Biological and artificial neuron 4

2.1 Coherence resonance phenomenon. 8

2.2 Stochastic resonance phenomenon. 9

2.3 Vibrational resonance phenomenon. 11

3.1 System's periodic potential $\Phi(x)$ defined by eq. (3.3) in the specific case considered in this chapter, namely $\Phi_0 = 1$ and $k = 1$. The height of the potential $\Delta\Phi$ and its width Δx are indicated with the double head arrows in this figure. 17

3.2 Time series of the system response revealing vibrational resonance effect for the specific constant damping coefficient $\Gamma_0^{'}$ =0.03. From top to bottom, the perturbation amplitude H increases as follows: (a) $H = 30$, (b) $H = 220$, (c) $H = 245$, (d) $H = 300$ and (e) $H = 405$. Parameters: $m = 1$, $k = 1$, $\Phi_0 = 1$, G =0.05, ω =0.65, $\Omega = 13$. . . 23

3.3 Time series of the system response revealing vibrational resonance effect for the specific constant damping coefficient $\Gamma_0^{'}$ =0.27. From top to bottom, the perturbation amplitude H increases as follows: (a) $H = 20$, (b) $H = 180$, (c) $H = 280$, (d) $H = 350$ and (e) $H = 405$. Parameters: $m = 1$, $k = 1$, $\Phi_0 = 1$, G =0.05, ω =0.65, $\Omega = 13$. . . 23

3.4 Unilateral magnitude spectra corresponding to the time series of Fig. 3.2. From top to bottom: (a) $H = 30$, (b) $H = 220$, (c) $H = 245$, (d) $H = 300$ and (e) $H = 405$. Parameters: $m = 1$, $\Gamma_0^{'}$ =0.03, $k = 1$, $\Phi_0 = 1$, G =0.05, ω =0.65, $\Omega = 13$. 24

3.5 Unilateral magnitude spectra corresponding to the time series of Fig. 3.3. From top to bottom: (a) $H = 20$, (b) $H = 180$, (c) $H = 280$, (d) $H = 350$ and (e) $H = 405$. Parameters: $m = 1$, $\Gamma_0^{'}$ =0.27, $k = 1$, $\Phi_0 = 1$, G =0.05, ω =0.65, $\Omega = 13$. 24

3.6 Typical VR signature observed in the system defined by eq. (3.10) for two values of the constant damping amplitude $\Gamma_0^{'}$. Parameters: $m = 1$, $k = 1$, $\Phi_0 = 1$, G =0.05, ω =0.65, $\Omega = 13$. 25

3.7 Vibrational multiresonance signature for two values of the constant damping amplitude $\Gamma_0^{'}$. The linear response Q exhibits local maxima whose values decrease as the perturbation amplitude increases. Parameters: $m = 1$, $k = 1$, $\Phi_0 = 1$, G =0.05, ω =0.65, $\Omega = 13$. 27

3.8 Time series of the system response revealing the second resonance of Fig. 3.7 for the specific constant damping coefficient $\Gamma_0^{'}$ =0.03. From top to bottom, the perturbation amplitude H increases as follows: (a) $H = 430$, (b) $H = 500$, (c) $H = 645$, (d) $H = 770$ and (e) $H = 935$. Parameters: $m = 1$, $k = 1$, $\Phi_0 = 1$, G =0.05, ω =0.65, $\Omega = 13$. 28

3.9 Time series of the system response revealing the second resonance of Fig. 3.7 for the specific constant damping coefficient $\Gamma_0^{'}$ =0.27. From top to bottom, the perturbation amplitude H increases as follows: (a) $H = 430$, (b) $H = 500$, (c) $H = 650$, (d) $H = 810$ and (e) $H = 935$. Parameters: $m = 1$, $k = 1$, $\Phi_0 = 1$, G =0.05, ω =0.65, $\Omega = 13$. 28

3.10 Unilateral magnitude spectra corresponding to the time series of Fig. 3.8. From top to bottom: (a) $H = 430$, (b) $H = 500$, (c) $H = 645$, (d) $H = 770$ and (e) $H = 935$. Parameters: $m = 1$, $\Gamma_0^{'}$ =0.03, $k = 1$, $\Phi_0 = 1$, G =0.05, ω =0.65, $\Omega = 13$. 29

3.11 Unilateral magnitude spectra corresponding to the time series of Fig. 3.9. From top to bottom: (a) $H = 430$, (b) $H = 500$, (c) $H = 650$, (d) $H = 810$ and (e) $H = 935$. Parameters: $m = 1$, $\Gamma_0^{'}$ =0.27, $k = 1$, $\Phi_0 = 1$, G =0.05, ω =0.65, $\Omega = 13$. 29

3.12 Control of VR with the constant damping amplitude $\Gamma_0^{'}$. Parameters: $m = 1$, $k = 1$, $\Phi_0 = 1$, G =0.05, ω =0.65, $\Omega = 13$. 30

3.13 Dependence of the local maxima Q^n_{max} of Fig. 3.12 versus the constant damping amplitude $\Gamma_0^{'}$. Q^n_{max} donates the amplitude of the local maxima number n. Parameters: $m = 1$, $k = 1$, $\Phi_0 = 1$, G =0.05, ω =0.65, $\Omega = 13$. 31

3.14 System's two different observed behaviors due to the change of the particle mass m. (a) $m = 1$, VR signature: A high frequency perturbation enhances the detection of the low frequency. (b) m =2.4, no enhancement of the low frequency detection. Parameters: $k = 1$, $\Phi_0 = 1$, G =0.05, ω =0.65, $\Omega = 13$. 32

3.15 Selective response behavior controlled by the mass m of the particle. Summary of the system's two behaviors for different values of the constant damping amplitude $\Gamma_0^{'}$. Values of mass m that correspond to $Q^*_{max} = 1$ define the region where VR ceases to exist whereas those that correspond to $Q^*_{max} > 1$ match the existence of VR. Parameters: G =0.05, $k = 1$, ω =0.65, $\Omega = 13$, $\Phi_0 = 1$. 34

3.16 Time series of the system response revealing vibrational resonance effect for the specific nonlinear damping coefficient Γ_0 =0.03. From top to bottom, the perturbation amplitude H increases as follows: (a) $H = 20$, (b) $H = 220$, (c) $H = 245$, (d) $H = 300$ and (e) $H = 400$. Parameters: $m = 1$, λ =2.4, ϕ =0.2, $k = 1$, $\Phi_0 = 1$, G =0.05, ω =0.65, $\Omega = 13$. 36

3.17 Time series of the system response revealing vibrational resonance effect for the specific nonlinear damping coefficient Γ_0 =0.27. From top to bottom, the perturbation amplitude H increases as follows: (a) $H = 20$, (b) $H = 200$, (c) $H = 280$, (d) $H = 340$ and (e) $H = 400$. Parameters: $m = 1$, λ =2.4, ϕ =0.2, $k = 1$, $\Phi_0 = 1$, G =0.05, ω =0.65, $\Omega = 13$. 36

3.18 Unilateral magnitude spectra corresponding to the time series of Fig. 3.16. From top to bottom: (a) $H = 20$, (b) $H = 220$, (c) $H = 245$, (d) $H = 300$ and (e) $H = 400$. Parameters: $m = 1$, Γ_0 =0.03, λ =2.4, ϕ =0.2, $k = 1$, $\Phi_0 = 1$, G =0.05, ω =0.65, $\Omega = 13$. 38

3.19 Unilateral magnitude spectra corresponding to the time series of Fig. 3.17. From top to bottom: (a) $H = 20$, (b) $H = 200$, (c) $H = 280$, (d) $H = 340$ and (e) $H = 400$. Parameters: $m = 1$, Γ_0 =0.27, λ =2.4, ϕ =0.2, $k = 1$, $\Phi_0 = 1$, G =0.05, ω =0.65, $\Omega = 13$. 38

3.20 Control of VR with the nonlinear damping amplitude Γ_0 of the space-dependent damping coefficient $\Gamma(x)$. Parameters: $m = 1$, λ =2.4, ϕ =0.2, $k = 1$, $\Phi_0 = 1$, G =0.05, ω =0.65, $\Omega = 13$. 39

3.21 Dependence of the local maxima Q^n_{max} of Fig. 3.20 versus the nonlinear damping amplitude Γ_0. Q^n_{max} donates the amplitude of the local maxima number n. Parameters: $m = 1$, λ =2.4, ϕ =0.2, $k = 1$, $\Phi_0 = 1$, G =0.05, ω =0.65, $\Omega = 13$. 40

3.22 Control of VR by the phase ϕ of the space-dependent dissipation $\Gamma(x)$. Parameters taken as: $m = 1$, Γ_0 =0.27, $\lambda = 1$, $k = 1$, $\Phi_0 = 1$, G =0.05, ω =0.65, $\Omega = 13$. . . . 41

3.23 VR enhancement by the phase ϕ of the nonlinear damping $\Gamma(x)$. The three first local maxima Q^n_{max} of the resonance curves of Fig. 3.22, are plotted versus the phase ϕ. Parameters are: $m = 1$, Γ_0 =0.27, $\lambda = 1$, $k = 1$, $\Phi_0 = 1$, G =0.05, ω =0.65, $\Omega = 13$. 42

3.24 Control of VR with the modulation strength λ of the space-dependent dissipation $\Gamma(x)$. Parameters: $m = 1$, Γ_0 =0.27, ϕ =0.2, $k = 1$, $\Phi_0 = 1$, G =0.05, ω =0.65, $\Omega = 13$. 43

3.25 System's two different observed behaviors due to the change of the particle mass m. (a) $m = 1$, VR signature: A high frequency perturbation enhances the detection of the low frequency. (b) m =2.4, no enhancement of the low frequency detection. Parameters: λ =2.4, ϕ =0.2, $k = 1$, $\Phi_0 = 1$, G =0.05, ω =0.65, $\Omega = 13$. 44

3.26 Selective response behavior controlled by the mass m of the particle. Summary of the system's two behaviors for different values of the nonlinear damping amplitude Γ_0. Values of mass m that correspond to $Q^*_{max} = 1$ define the region where VR ceases to exist whereas those that correspond to $Q^*_{max} > 1$ match the existence of VR. Parameters: λ =2.4, ϕ =0.2, $k = 1$, $\Phi_0 = 1$, G =0.05, ω =0.65, $\Omega = 13$. 45

3.27 Selective response behavior controlled by the mass m of the particle for different values of the phase ϕ. Parameters: Γ_0 =0.27, $\lambda = 1$, $k = 1$, $\Phi_0 = 1$, G =0.05, ω =0.65, $\Omega = 13$. 46

3.28 Selective response behavior controlled by the mass m of the particle for different values of the modulation strength λ. Parameters of the system: Γ_0 =0.27, ϕ =0.2, $k = 1$, $\Phi_0 = 1$, G =0.05, ω =0.65, $\Omega = 13$. 46

4.1 Sawtooth force $F_n(x,\alpha)$ and its corresponding potential $\Phi_n(x,\alpha)$ for three values of nonlinearity order n: (a) $n = 0$, (b) $n = 1$, (c) $n = 2$. Parameters: $\alpha = 6$, A =0.5, A_0 =0.125. ΔX^* represents the spacing between two consecutive stable or unstable states that is, the potential width and $\Delta\Phi$ is the potential barrier height. 52

4.2 Truncated sinusoidal force $F_n(x,\alpha)$ and its corresponding potential $\Phi_n(x,\alpha)$ for three values of nonlinearity order n: (a) $n = 0$, (b) $n = 1$, (c) $n = 2$. Parameters: $\alpha = 6$, $V_0 = \frac{\pi}{32}$, $k = 1$. ΔX^* represents the spacing between two consecutive stable or unstable states and $\Delta\Phi$ is the potential barrier height. 53

4.3 Typical time series of the Chua's model experiencing the truncated sinusoidal force defined by eq. (4.4) and driven by the excitation of eq. (4.8). The chronograms of x have been obtained by increasing the perturbation amplitude starting from $B = 0$ with step ΔB =0.01 until (a) B =1.5, (b) B =4.13, (c) B =6.8. Model parameters: $n = 1$, $k = 1$, $V_0 = \frac{\pi}{32}$, $\alpha = 6$, $\beta = 16$, b =0.1, $\omega_1 = 1$, $\Omega = 10\omega_1$, numerical time step Δt =0.0015. 57

4.4 Typical time series of the Chua's model experiencing the sawtooth force defined by eq. (4.3) and driven by the excitation of eq. (4.8). The chronograms of x have been obtained by increasing the perturbation amplitude starting from $B = 0$ with step ΔB =0.01 until (a) B =1.5, (b) B =4.72, (c) B =9.79. Parameters: $n = 1$, A =0.5, A_0 =0.125, $\alpha = 6$, $\beta = 16$, b =0.1, $\omega_1 = 1$, $\Omega = 10\omega_1$, ΔB =0.01, Δt =0.0015. . . . 57

4.5 Spectral response of the system experiencing the truncated sinusoidal force corresponding to the time series of Fig. 4.3. Model parameters: $n = 1$, $k = 1$, $V_0 = \frac{\pi}{32}$, $\alpha = 6$, $\beta = 16$, b =0.1, $\omega_1 = 1$, $\Omega = 10\omega_1$, numerical time step Δt =0.0015. 58

4.6 Spectral response of the system experiencing the sawtooth force corresponding to the time series of Fig. 4.4 Parameters: $n = 1$, A =0.5, A_0 =0.125, $\alpha = 6$, $\beta = 16$, b =0.1, $\omega_1 = 1$, $\Omega = 10\omega_1$, ΔB =0.01, Δt =0.0015. 58

4.7 Linear response Q versus the perturbation amplitude B for a system experiencing the truncated sinusoidal force. The arrows indicate that increasing B from 0 to 20 or reducing B from 20 to 0 provide the same resonance curve. Parameters: $n = 1$, $k = 1$, $V_0 = \frac{\pi}{32}$, $\alpha = 6$, $\beta = 16$, b =0.1, $\omega_1 = 1$, $\Omega = 10\omega_1$, perturbation amplitude step ΔB =0.01, numerical time step Δt =0.0015. 59

4.8 Linear response Q versus the perturbation amplitude B, for a system experiencing the sawtooth force. Our simulation results are in agreement with the one obtained by Abirami *et al* [152]. Parameters: $n = 1$, $A =$0.5, $A_0 =$0.125, $\alpha = 6$, $\beta = 16$, $b =$0.1, $\omega_1 = 1$, $\Omega = 10\omega_1$, $\Delta B =$0.01, $\Delta t =$0.0015. 59

4.9 Overall resonance behavior of the system experiencing: (a) truncated sinusoidal force (b) Sawtooth force, in the perturbation amplitude B and nonlinearity order n parameters plane. The linear response Q is plotted versus B and n. Parameters: $k = 1$, $V_0 = \frac{\pi}{32}$, $A =$0.5, $A_0 =$0.125, $\alpha = 6$, $\beta = 16$, $b =$0.1, $\omega_1 = 1$, $\Omega = 10\omega_1$, $\Delta B =$0.01, $\Delta t =$0.0015. 60

4.10 Locus of the linear response local maxima $Q_m^{*,n}$ versus the corresponding perturbation amplitude $B_m^{*,n}$ at which they occur. From top to bottom, we have considered a system experiencing a truncated sinusoidal force with order (a) $n = 5$, (b) $n = 6$, (c) $n = 7$ and (d) $n = 8$. The insets at each subfigure represent the classical linear response curves deduced from Fig. 4.9 where the maxima have been labeled with alphabetical capital letters. Parameters: $k = 1$, $V_0 = \frac{\pi}{32}$, $\alpha = 6$, $\beta = 16$, $b =$0.1, $\omega_1 = 1$, $\Omega = 10\omega_1$, $\Delta B =$0.01, $\Delta t =$0.0015. 61

4.11 Locus of the linear response local maxima $Q_m^{*,n}$ versus the corresponding perturbation amplitude $B_m^{*,n}$ at which they occur. From top to bottom, we have considered a system experiencing a sawtooth force with order (a) $n = 5$, (b) $n = 6$, (c) $n = 7$ and (d) $n = 8$. The insets at each subfigure represent the classical linear response curves where the maxima have been labeled with alphabetical letters. Parameters: $A = 0\,5$, $A_0 =$0.125, $\alpha = 6$, $\beta = 16$, $b =$0.1, $\omega_1 = 1$, $\Omega = 10\omega_1$, $\Delta B =$0.01, $\Delta t =$0.0015. 62

4.12 Evolution of each local maxima $Q_m^{*,n}$ reached by the linear response Q versus the nonlinearity order n. The performance obtained with the two nonlinear forces are compared when we consider: (a) The first maxima, (b) The second maxima, (c) The third maxima, (d) The fourth maxima. Circle-marked lines correspond to the truncated sinusoidal force whereas the star-marked lines refers to the sawtooth force. Parameters: $k = 1$, $V_0 = \frac{\pi}{32}$, $A =$0.5, $A_0 =$0.125, $\alpha = 6$, $\beta = 16$, $b =$0.1, $\omega_1 = 1$, $\Omega = 10\omega_1$, $\Delta B =$0.01, $\Delta t =$0.0015. 63

4.13 Phase portraits of the coexisting orbits for the resonance curve of Fig. 4.7. The perturbation amplitude is set to: (a) $B =$1.5, (b) $B =$3.5, (c) $B =$4.13, (d) $B =$6.86, (e) $B =$9.38 and (f) $B = 11$. The equivalent truncated sinusoidal force $F_1(x,1)$ is also superimposed using a dashed-line in all the cases. Parameters: $n = 1$, $k = 1$, $V_0 = \frac{\pi}{32}$, $\alpha = 6$, $\beta = 16$, $b =$0.1, $\omega_1 = 1$, $\Omega = 10\omega_1$, $\Delta t =$0.0015. 65

4.14 Phase portraits of the coexisting orbits for the resonance curve of Fig. 4.8. The perturbation amplitude is set to: (a) $B=$1.5, (b) $B=$3.5, (c) $B=$4.13, (d) $B=$6.86, (e) $B=$9.38 and (f) $B=11$. The equivalent truncated sinusoidal force $F_1(x,1)$ is also superimposed using a dashed-line in all the cases. Parameters: $n=1, A=$0.5, $A_0=$0.125, $\alpha=6$, $\beta=16$, $b=$0.1, $\omega_1=1$, $\Omega=10\omega_1$, $\Delta t=$0.0015. 66

4.15 Linear response Q of the system estimated at the low angular frequencies ω_0, ω_1 and ω_2, versus the perturbation amplitude B, for the system experiencing the truncated sinusoidal force. Parameters: $n=0$, $k=1$, $V_0=\frac{\pi}{32}$, $\alpha=4$, $\beta=14$, $b=$0.04, $\omega_0=$0.1, $\omega_1=2\omega_0$, $\omega_2=3\omega_0$, $\Omega=20\omega_0$, $\Delta B=$0.001, $\Delta t=$0.0015. 68

4.16 Chronograms summarizing the system's behavior for four specific values of the perturbation amplitude B taken in the different ranges identified at Fig. 4.15. The system synchronizes its response to the sinusoidal wave superimposed on each subfigure and which corresponds to the predominant angular frequency, that is, ω_0, ω_1, ω_2 and ω_1 for subfigures (a), (b), (c) and (d) respectively. From top to bottom, we observe the predominance of: (a) GVR at the ghost angular frequency ω_0 when $B=$0.561 (first resonance region of Fig. 4.15), (b) VR at the angular frequency ω_1 when $B=$0.603 (second resonance region of Fig. 4.15), (c) VR at the angular frequency ω_2 when $B=$0.621 (third resonance region of Fig. 4.15) and (d) VR at the angular frequency ω_1 when $B=$0.629 (third resonance region of Fig. 4.15). Parameters: $n=0$, $k=1$, $V_0=\frac{\pi}{32}$, $\alpha=4$, $\beta=14$, $b=$0.04, $\omega_0=$0.1, $\omega_1=2\omega_0$, $\omega_2=3\omega_0$, $\Omega=20\omega_0$, $\Delta t=$0.0015. 69

4.17 Unilateral magnitude spectra of the time series of Fig. 4.16. The spectral responses clearly indicate which frequency is dominant in each case. From top to bottom, we observe the predominance of: (a) GVR at the ghost angular frequency ω_0 when $B=$0.561 (first resonance region of Fig. 4.15), (b) VR at the angular frequency ω_1 when $B=$0.603 (second resonance region of Fig. 4.15), (c) VR at the angular frequency ω_2 when $B=$0.621 (third resonance region of Fig. 4.15) and (d) VR at the angular frequency ω_1 when $B=$0.629 (third resonance region of Fig. 4.15). Parameters: $n=0$, $k=1$, $V_0=\frac{\pi}{32}$, $\alpha=4$, $\beta=14$, $b=$0.04, $\omega_0=$0.1, $\omega_1=2\omega_0$, $\omega_2=3\omega_0$, $\Omega=20\omega_0$, $B=$0.561, $\Delta t=$0.0015. 70

4.18 Linear response Q of the system at the angular frequencies ω_0, ω_1 and ω_2 versus the perturbation amplitude B, for the system experiencing the sawtooth force. Parameters: $n=0$, $A=$0.5, $A_0=$0.125, $\alpha=4$, $\beta=14$, $b=$0.04, $\omega_0=$0.1, $\omega_1=2\omega_0$, $\omega_2=3\omega_0$, $\Omega=20\omega_0$, $\Delta B=$0.001, $\Delta t=$0.0015. 71

4.19 Impact of the nonlinearity order n of the truncated sinusoidal force on the resonances. The linear response Q estimated at the angular frequencies ω_0, ω_1 and ω_2 has been plotted versus the perturbation amplitude B, for the nonlinearity orders: (a) $n=1$, (b) $n=2$, (c) $n=3$, (d) $n=4$, (e) $n=5$. Parameters: $k=1$, $V_0=\frac{\pi}{32}$, $\alpha=4$, $\beta=14$, b =0.04, ω_0 =0.1, $\omega_1=2\omega_0$, $\omega_2=3\omega_0$, $\Omega=20\omega_0$, ΔB =0.01, Δt =0.0015. 72

4.20 Impact of the nonlinearity order n of the sawtooth force on the resonances. The linear response Q estimated at the angular frequencies ω_0, ω_1 and ω_2 has been plotted versus the perturbation amplitude B, for the nonlinearity orders: (a) $n=1$, (b) $n=2$, (c) $n=3$, (d) $n=4$, (e) $n=5$. Parameters: A =0.5, A_0 =0.125, $\alpha=4$, $\beta=14$, b =0.04, ω_0 =0.1, $\omega_1=2\omega_0$, $\omega_2=3\omega_0$, $\Omega=20\omega_0$, ΔB =0.01, Δt =0.0015. 73

5.1 Images used throughout the chapter with different sizes $N\times N$. Images 1, 2, 3 and 4 represent the Roman Coloseum, Saturn, a Cameraman and Lena. The resolution of images 1, 2, 3 and 4 are $N^2=64^2$ pixels, $N^2=128^2$ pixels, $N^2=256^2$ pixels and $N^2=512^2$ pixels respectively. 79

5.2 The noisy images I_b with noise intensity σ =0.1. Each image has been zoomed even if they don't share the same resolution N^2. Coloseum: $N^2=64^2$ pixels, Saturn: $N^2=128^2$ pixels, Cameraman: $N^2=256^2$ pixels, Lena: $N^2=512^2$ pixels. 80

5.3 Sketch of the resonant detector which performs a threshold filtering of the perturbed image I_p and which perceives the black and white image T . The input of the resonant detector is the noisy image I_b which is perturbed by an additive perturbation P selected by a switch between noise or a sine perturbation. The switch command c chooses a noise perturbation η' of intensity γ in the case of a stochastic resonance based detector, while for a vibrational resonance based detector, a sine signal of amplitude A and spatial frequency N_{HF} is selected. 81

5.4 Images perceived by the SR-detector for different noise intensities γ. The initial noisy subthreshold image I_b of Saturn is corrupted with the increasing noise *RMS* amplitude γ and threshold filtered with threshold V_{th} =1.2 to produce the black and white images presented at subfigures $(a-c)$. (a): γ =0.2. (b): γ =0.5. (c): γ =1.2. The best perception of Saturn image is obtained for the optimal noise value γ^* =0.5 represented at subfigure (b). 82

5.5 Perception of the Saturn image through the SR-detector for different threshold levels V_{th}. Parameter: σ =0.1. (a): Cross-covariance $C_{I,T}$ versus the noise intensity γ for three different threshold values V_{th}. Dashed lines are guides to the eye. The best perceived images obtained for the optimal noise intensity γ^* are displayed for each considered threshold value V_{th} at subfigures $(b-d)$. (b): V_{th} =1.05 requires γ^* =0.4 to achieve $C_{I,T}(\gamma^*)$ =0.386. (c): V_{th} =1.2 requires γ^* =0.5 to achieve $C_{I,T}(\gamma^*)$ =0.322. (d): V_{th} =1.4 requires γ^* =0.65 to achieve $C_{I,T}(\gamma^*)$ =0.263. 83

5.6 Perception of the different images through the SR-detector. Parameters: V_{th} =1.2 and σ =0.1. (a) Cross-covariance $C_{I,T}$ of each image against the noise intensity γ. Dashed lines are guides to the eye. The best perceived images are displayed for the optimal noise intensity γ^* at subfigures $(b-d)$. (b): image 1 requires γ^* =0.39 to achieve $C_{I,T}(\gamma^*)$ =0.274. (c): image 2 requires γ^* =0.5 to achieve $C_{I,T}(\gamma^*)$ =0.322. (d): image 3 requires γ^* =0.59 to achieve $C_{I,T}(\gamma^*)$ =0.199. (e): image 4 requires γ^* =0.465 to achieve $C_{I,T}(\gamma^*)$ =0.208. 84

5.7 Images perceived by the VR-detector for different perturbation amplitudes A. The initial noisy subthreshold image I_b of Saturn is corrupted with increasing perturbation amplitude A and then threshold filtered with threshold V_{th} =1.2 to produce the black and white images presented at subfigures (a-c) . (a): A =0.3. (b): A =0.95. (c): A =1.4. The best perception of Saturn image is obtained for the optimal perturbation amplitude A =0.95 at subfigure (b). 85

5.8 Perception through the VR-detector of the saturn image with different noise intensities σ. Parameter: V_{th} =1.2. (a): Cross-covariance $C_{I,T}$ against the perturbation amplitude A for different levels of noise σ. Dashed lines are guides to the eye. For each noise intensity σ where a resonance of the cross-covariance occurs, we have displayed the best perceived image obtained for the optimal perturbation amplitude A^* at subfigures $(b-e)$. (b): σ =0.1 requires A^* =0.95 to achieve $C_{I,T}(A^*)$ =0.554. (c): σ =0.2 requires A^* =0.85 to achieve $C_{I,T}(A^*)$ =0.506. (d): σ =0.3 requires $A = 0\ 8$ to achieve $C_{I,T}(A^*)$ =0.442. (e): σ =0.45 requires A^* =0.6 to achieve $C_{I,T}(A^*)$ =0.365. 86

5.9 Perception through the VR-detector of the Coloseum image with different noise intensities σ. Parameter: V_{th} =1.2. (a): Cross-covariance $C_{I,T}$ against the perturbation amplitude A for different levels of noise σ. Dashed lines are guides to the eye. For each noise intensity σ where a resonance of the cross-covariance occurs, we have displayed the best perceived image obtained for the optimal perturbation amplitude A^* at subfigures $(b-d)$. (b): σ =0.1 requires A^* =0.6 to achieve $C_{I,T}(A^*)$ =0.422. (c) σ =0.2 requires A^* =0.6 to achieve $C_{I,T}(A^*)$ =0.374. (d): σ =0.3 requires A^* =0.6 to achieve $C_{I,T}(A^*)$ =0.325. 87

5.10 Perception through the VR-detector of the Cameraman image with different noise intensities σ. Parameter: V_{th} =1.2. (a): Cross-covariance $C_{I,T}$ against the perturbation amplitude A for different levels of noise σ. Dashed lines are guides to the eye. For each noise intensity σ where a resonance of the cross-covariance occurs, we have displayed the best perceived image obtained for the optimal perturbation amplitude A^* at subfigures $(b-e)$. (b): σ =0.1 requires A^* =0.95 to achieve $C_{I,T}(A^*)$ =0.372. (c): σ =0.2 requires A^* =0.9 to achieve $C_{I,T}(A^*)$ =0.342. (d): σ =0.3 requires A^* =0.9 to achieve $C_{I,T}(A^*)$ =0.292. (e): σ =0.45 requires A =0.8 to achieve $C_{I,T}$ =0.243. 88

5.11 Perception through the VR-detector of the Lena image with different noise intensities σ. Parameter: V_{th} =1.2. (a): Cross-covariance $C_{I,T}$ against the perturbation amplitude A for different levels of noise σ. Dashed lines are guides to the eye. For each noise intensity σ where a resonance of the cross-covariance occurs, we have displayed the best perceived image obtained for the optimal perturbation amplitude A^* at subfigures $(b-e)$. (b): σ =0.1 requires A^* =0.8 to achieve $C_{I,T}(A^*)$ =0.401. (c): σ =0.2 requires A^* =0.75 to achieve $C_{I,T}(A^*)$ =0.343. (d): σ =0.3 requires A^* =0.7 to achieve $C_{I,T}(A^*)$ =0.288. (e): σ =0.45 requires A^* =0.6 to achieve $C_{I,T}(A^*)$ =0.232. 89

5.12 Effect of the perturbation frequency on the perception of Saturn through the VR-detector. Parameters: $N^2 = 2^{14}$, V_{th} =1.2 and σ =0.1. (a): Cross-covariance $C_{I,T}$ against the normalized perturbation frequency N_{HF}/N^2 for different amplitudes A of the perturbation. Dashed lines are guides to the eye. For the optimal perturbation amplitude A^* =0.95, we have displayed the images perceived through the detector for three specific frequencies at subfigures $(b-d)$. (b): $N_{HF} = 2^{11}$. (c): $N_{HF} = 2^{13}$. (d): $N_{HF} = 2^{14}$. The best perception of the Saturn image is achieved when the cross-covariance saturates to $C_{I,T}$ =0.749, that is when the perturbation is tuned to the optimal amplitude A^* =0.95 and when its frequency is greater than the optimal value $N^*_{HF} = N^2 = 2^{14}$. 91

5.13 Effect of the perturbation frequency on the perception of the Coloseum through the VR-detector. Parameters: $N^2 = 2^{12}$, V_{th} =1.2 and σ =0.1. (a): Cross-covariance $C_{I,T}$ against the normalized perturbation frequency N_{HF}/N^2 for different amplitudes A of the perturbation. Dashed lines are guides to the eye. For the optimal perturbation amplitude A^* =0.6, we have displayed the images perceived through the detector for three specific frequencies at subfigures $(b-d)$. (b): $N_{HF} = 2^9$. (c): $N_{HF} = 2^{11}$. (d): $N_{HF} = 2^{12}$. The best perception of the Coloseum image is achieved when the cross-covariance saturates to $C_{I,T}$ =0.562, that is when the perturbation is tuned to the optimal amplitude A^* =0.6 and when its frequency is greater than the optimal value $N^*_{HF} = N^2 = 2^{12}$. 92

5.14 Effect of the perturbation frequency on the perception of the Cameraman through the VR-detector. Parameters: $N^2 = 2^{16}$, V_{th} =1.2 and σ =0.1. (a): Cross-covariance $C_{I,T}$ against the normalized perturbation frequency N_{HF}/N^2 for different amplitudes A of the perturbation. Dashed lines are guides to the eye. For the optimal perturbation amplitude A^* =0.95, we have displayed the images perceived through the detector for three specific frequencies at subfigures $(b-d)$. (b): $N_{HF} = 2^{13}$. (c): $N_{HF} = 2^{15}$. (d): $N_{HF} = 2^{16}$. The best perception of the Cameraman image is achieved when the cross-covariance saturates to $C_{I,T}$ =0.565, that is when the perturbation is tuned to the optimal amplitude A^* =0.95 and when its frequency is greater than the optimal value $N^*_{HF} = N^2 = 2^{16}$. 93

5.15 Effect of the perturbation frequency on the perception of Lena through the VR-detector. Parameters: $N^2 = 2^{18}$, V_{th} =1.2 and σ =0.1. (a): Cross-covariance $C_{I,T}$ against the normalized perturbation frequency N_{HF}/N^2 for different amplitudes A of the perturbation. Dashed lines are guides to the eye. For the optimal perturbation amplitude A^* =0.8, we have displayed the images perceived through the detector for three specific frequencies at subfigures $(b-d)$. (b): $N_{HF} = 2^{15}$. (c): $N_{HF} = 2^{17}$. (d): $N_{HF} = 2^{18}$. The best perception of the Lena image is achieved when the cross-covariance saturates to $C_{I,T}$ =0.546, that is when the perturbation is tuned to the optimal amplitude A^* =0.8 and when its frequency is greater than the optimal value $N^*_{HF} = N^2 = 2^{18}$. 93

LIST OF TABLES

5.1 Features of the stochastic resonance based detector with threshold V_{th} =1.2. γ^* represents the optimal noise intensity which maximizes the cross-covariance $C_{I,T}$. . . 84

5.2 Features of the VR-detector with spatial normalized frequency $N_{HF}/N^2 = 1/4$ and threshold V_{th} =1.2. A^* represents the optimal amplitude of the perturbation which maximizes the cross-covariance $C_{I,T}$ and γ^* the critical noise value beyond which the detector cannot recover the subthreshold image. 90

5.3 Features of the VR and SR detectors when the noise level of the input subthreshold image is σ =0.1 and when the detector threshold is V_{th} =1.2. 94

Document generated with LaTeX and:
the LaTeX style for PhD Thesis created by S. Galland — http://www.multiagent.fr/ThesisStyle
the `tex-upmethodology` package suite — http://www.arakhne.org/tex-upmethodology/

école doctorale **sciences pour l'ingénieur et microtechniques**

Title: Nonlinear resonances and some of their applications to information processing

Keywords: Nonlinear dynamics, vibrational resonance, ghost-vibrational resonance, subthreshold images perception

Abstract:

The study of resonance phenomena in nonlinear dynamical systems has drawn considerable attention for years. The most studied nonlinear resonance is undoubtedly the famous stochastic resonance, which consists of perturbing a nonlinear system with an appropriate amount of noise to enhance the detection of a subthreshold input signal. Since the introduction of stochastic resonance in the context of climate dynamics, it was later observed that a deterministic high frequency perturbation can replace noise leading to vibrational resonance. Even if this latter resonance was investigated in many areas of science for more than two decades now, it is still receiving attentions. It is the subject of this thesis, which numerically analyzes the occurrence of this phenomenon in two different nonlinear systems, and which suggests applications in the context of subthreshold images perception. First, we analyze the motion of a particle with a given mass which is submitted to a nonlinear force deriving from a double-well potential. For both considered cases of linear and nonlinear space-dependent damping, we establish that there exists a critical mass beyond which vibrational resonance ceases to exist. Next, we analyze how the nonlinearity affects vibrational resonance in the Chua's circuit model. Especially, we show that better resonances can be achieved when Chua's system experiences a truncated sinusoidal nonlinearity instead of the conventional sawtooth nonlinearity. Moreover, when the system driving consists of two close low frequencies, we observe that the high frequency perturbation can induce resonances at the two input low frequencies but also at a lower frequency via the mechanisms of vibrational resonance and ghost-vibrational resonance. Lastly, we consider the perception of subthreshold images through perturbed threshold detectors. In terms of image perception, we show that detectors which are based on vibrational resonance clearly outperform detectors based on stochastic resonance.

Titre : Résonances non linéaires et certaines de leurs applications en traitement de l'information

Mots-clés : Dynamiques non linéaires, résonance vibrationnelle, résonance vibrationnelle-fantôme, perception d'images subliminales.

Résumé :

Ces dernières années, un intérêt considérable a été consacré à l'étude des phénomènes de résonance dans les systèmes dynamiques non linéaires. Parmi les résonances non linéaires, la plus étudiée est sans aucun doute la résonance stochastique, qui traduit la particularité des systèmes non linéaires à utiliser une quantité appropriée de bruit pour améliorer leur réponse à une excitation subliminale. Plus tardivement, il a été observé qu'une perturbation haute fréquence pouvait remplacer le bruit, ce qui donna naissance à l'effet de résonance vibrationnelle. Même si cette forme de résonance a été mise en évidence dans de nombreux systèmes et dans différents contextes depuis plus de deux décennies maintenant, l'étude de ce phénomène continue de susciter l'intérêt des chercheurs. C'est l'objectif de cette thèse, qui analyse numériquement l'apparition de cette résonance dans deux systèmes non linéaires, ainsi que ses applications dans le cadre de la perception d'images subliminales. Notre première étude numérique porte ainsi sur un système mécanique représentant une particule de masse donnée. Que ce soit dans le cas d'un amortissement linéaire ou spatialement non linéaire, nous avons mis en évidence l'existence d'une masse critique au-delà de laquelle la résonance vibrationelle cesse d'exister. Notre seconde étude porte sur l'impact de la non linéarité sur la résonance d'un modèle de circuit de Chua. Nous avons principalement montré numériquement qu'une non linéarité du type sinusoïdale tronquée permettait d'obtenir une résonance vibrationnelle plus marquée que la non linéarité usuelle du type dent de scie. Par ailleurs, quand deux fréquences proches excitent le système, en plus d'une résonance à chacune de ces fréquences, il apparait une résonance à une fréquence plus faible, qualifiée de fantôme. Enfin, nous avons établi qu'il était possible d'obtenir une bien meilleure perception d'images subliminales au travers d'un dispositif à seuil tirant profit de la résonance vibrationnelle plutôt que d'un dispositif basé sur la résonance stochastique.

Université Bourgogne Franche-Comté
32, avenue de l'Observatoire
25000 Besançon, France